State of Oregon
Department of Geology and Mineral Industries
Vicki S. McConnell, State Geologist

Special Paper 41

TSUNAMI HAZARD ASSESSMENT OF THE NORTHERN OREGON COAST: A MULTI-DETERMINISTIC APPROACH TESTED AT CANNON BEACH, CLATSOP COUNTY, OREGON

By
George R. Priest[1], Chris Goldfinger[2], Kelin Wang[3], Robert C. Witter[1],
Yinglong Zhang[4], and António M. Baptista[4]

2009

[1]Oregon Department of Geology and Mineral Industries, Coastal Field Office, 313 SW 2nd Street, Suite D, Newport, Oregon 97365
[2]College of Oceanic and Atmospheric Sciences, 104 Ocean Administration Building, Oregon State University, Corvallis, Oregon 97331-3212
[3]Pacific Geoscience Centre, Room 4714m, 9860 West Saanich Road, Sidney, British Columbia, Canada
[4]P.O. Box 91000, OGI School of Science and Engineering, Oregon Health and Science University, Portland, Oregon

NOTICE

THE RESULTS AND CONCLUSIONS OF THIS REPORT ARE NECESSARILY BASED ON LIMITED GEOLOGIC AND GEOPHYSICAL DATA. AT ANY GIVEN SITE IN ANY MAP AREA, SITE-SPECIFIC DATA COULD GIVE RESULTS THAT DIFFER FROM THOSE SHOWN IN THIS REPORT. **THIS REPORT CANNOT REPLACE SITE-SPECIFIC INVESTIGATIONS.** THE HAZARDS OF AN INDIVIDUAL SITE SHOULD BE ASSESSED THROUGH GEOTECHNICAL OR ENGINEERING GEOLOGY INVESTIGATION BY QUALIFIED PRACTITIONERS.

Oregon Department of Geology and Mineral Industries Special Paper 41
Published in conformance with ORS 516.030

For copies of this publication or other information about Oregon's geology and natural resources, contact:

Nature of the Northwest Information Center
800 NE Oregon Street #28, Suite 965
Portland, Oregon 97232
(971) 673-1555
http://www.naturenw.org

For additional information:
Administrative Offices
800 NE Oregon Street #28, Suite 965
Portland, OR 97232
Telephone (971) 673-1555
Fax (971) 673-1562
http://www.oregongeology.com
http://egov.oregon.gov/DOGAMI/

TABLE OF CONTENTS

ABSTRACT 1

INTRODUCTION 2

Objectives and Intended Audience for the Report 2

Largest Historical Tsunami 3

Approach 3

General Findings 4

RELATIONSHIP TO PREVIOUS TSUNAMI MODELING STUDIES 5

METHODS 6

Geological Constraints on Cascadia Earthquake Source Parameters 6

Paleoseismicity and Recurrence Model 6

Offshore Turbidite Record 6

Cascadia Megathrust Slip Inferred from Offshore Turbidites 11

Geologic Evidence of Interplate Locking 13

Updip Limit of Interplate Locking 13

Downdip Limit of Interplate Coupling 18

Splay Fault 24

Fault Deformation Modeling 25

Logic Tree Evaluation of Cascadia Earthquake Source Parameters 27

Earthquake Size and Coseismic Slip 28

Slip Partitioned to a Splay Fault 31

Rupture Model 31

Slip Distribution 32

Distant Tsunami Sources 32

Hydrodynamic Tsunami Modeling 32

Tides 34

Comparison of Simulated Tsunami to Observations 34

Observations of the March 27, 1964, Tsunami 34

Paleotsunami Deposits 34

Reconstructing the Prehistoric Landscape 36

Comparison of Simulated Coseismic Deformation to Observations 36

RESULTS 37

Cascadia Earthquake Sources 37

Source Scenarios Eliminated from the Analyses 37

Source Parameters Eliminated from the Analyses 37

Tsunami Elevation and Inundation for Final Cascadia Scenarios 37

Effect on Inundation and Runup of Slip, Splay Faulting, and Slip patches 46

Alaska 1964 Tsunami Simulation 48

Theoretical Maximum Considered Distant Tsunami Simulation 48

Local Amplification of Open Coastal Runup 48

Tsunami Arrival Time and Velocities 48

Correspondence of Cascadia Simulations to Paleotsunami Inundation 52

Coseismic Subsidence 60

Data Files 60

COMPARISON OF RESULTS TO PREVIOUS STUDIES 63
Relationship to Probabilistic Tsunami Hazard Assessments 63
Comparison to Previous Tsunami Hazard Assessments for Oregon 64
Comparison to Cascadia Scenarios of Tsunami Pilot Study Working Group 66
COMPARISON OF CASCADIA TSUNAMI TO THE 2004 SUMATRA TSUNAMI 67
DISTANT TSUNAMI SCENARIOS 68
UNCERTAINTIES 69
Uncertainty of Cascadia Fault Slip Estimated from Turbidite Data 69
Uncertainty in Paleoseismic Estimates of Coseismic Subsidence 71
Uncertainty in the Hydrodynamic Model 71
Uncertainty in the Fault Dislocation Model 71
Uncertainty in the Local Basin and Bank Slip Patch Sources 72
MINIMUM TSUNAMI SCENARIOS FOR INUNDATION MAPS 72
TSUNAMI SCENARIOS FOR OREGON EVACUATION MAPS 76
SUMMARY AND CONCLUSIONS 76
RECOMMENDATIONS FOR FUTURE WORK 78
ACKNOWLEDGMENTS 79
REFERENCES 80
APPENDIX A: FAULT DISLOCATION MODELING OF CASCADIA EARTHQUAKE SCENARIOS A1
FAULT SOURCE MODELING APPROACH A1
FAULT SLIP DIRECTION AND MAGNITUDE A1
FAULT GEOMETRY AND FAULT MESHES — CASCADIA SCENARIOS A2
FAULT PATCHES AND SLIP DISTRIBUTION — CASCADIA SCENARIOS A2

LIST OF FIGURES

Figure 1 Location of the Cannon Beach study area relative to major offshore tectonic plates and plate boundaries 2
Figure 2 Photographs showing the impact of the 1964 Alaska tsunami at Cannon Beach, Oregon 4
Figure 3 Cascadia margin turbidite canyons, channels, and 1999 and 2002 core locations; synchroneity test at channel confluence 7
Figure 4 Preliminary rupture modes identified using turbidite correlation 8
Figure 5 Correlation details from two representative pairs of cores on the Cascadia margin 10
Figure 6 Relationship between turbidite mass per event at Juan de Fuca and Cascadia channels, and interseismic time, north-central Cascadia margin 14
Figure 7 Plot of interseismic intervals versus mass per event for time-predictable and slip-predictable models for the northern and central Cascadia margin. 15
Figure 8 Shaded bathymetry of the Oregon margin, with structural map overlain 16
Figure 9 Decoupled regions of the central Cascadia margin mapped from multiple proxies for interplate coupling 17
Figure 10 Sumatra forearc shown by single-channel profile Sumatra Earthquake and Tsunami Offshore Survey line 1 19
Figure 11 Cross section across Heceta Bank, Oregon from Chevron line HOG-15 and Western Geco siesmic line WO-18 20
Figure 12 Evidence of extension of the Washington shelf 22
Figure 13 Poststack depth-migrated multichannel seismic profiles showing the splay fault off the Kii peninsula, Nankai subduction zone 24

List of Figures, continued

Figure 14 Unmigrated USGS reflection profile L-5-WO77-12 across the mid slope off north central Oregon 25
Figure 15 Logic tree for "Average" source scenarios and trunk branches of "Small," "Large," and "Largest" scenarios for Cascadia tsunami simulations 27
Figure 16 Vertical coseismic deformation patterns for release of 525 years of convergence on the Cascadia subduction zone 29
Figure 17 Coseismic deformation from the 1964 Prince William Sound earthquake from Johnson and others (1996) 33
Figure 18 Maximum considered distant tsunami source from the Tsunami Pilot Study Working Group analysis for Seaside, Oregon 33
Figure 19 Unstructured computational grid used in tsunami simulations 35
Figure 20 Grid resolution expressed as the equivalent radius of each numerical grid element plotted against bathymetric depth 35
Figure 21 West-to-east cross sections of coseismic deformation for all Cascadia earthquake source scenarios 38
Figure 22 Logic tree weights for 32 versus 25 tsunami source scenarios 39
Figure 23 Difference at Cannon Beach, Oregon, between inundation for regional splay fault slip patch scenarios with differing rupture width and skew 40
Figure 24 Sensitivity of wave arrival at Cannon Beach, Oregon, to Cascadia fault rupture width and slip distribution for splay fault scenarios with "average" slip of ~15 m 41
Figure 25 Observation lines and points for inundation, maximum wave elevations, and time histories of wave arrivals 42
Figure 26 Cumulative percent confidence that tsunami water depth will be less than the scenario depth for a Cascadia tsunami (~500-yr event) 43
Figure 27 Water depth data as in Figure 26 but in terms of cumulative logic tree weight instead of percent confidence 44
Figure 28 Inundation up the Ecola Creek channel versus cumulative logic tree weight versus scenarios of the Tsunami Pilot Study Working Group 44
Figure 29 Relationship between inundation for selected regional slip patch scenarios, minimum and maximum inundation for Tsunami Pilot Study Working Group (TPSW, 2006) scenarios, and isolines of percent confidence . . . 45
Figure 30 Linear relationship between fault slip and tsunami inundation or tsunami elevation at the shoreline 46
Figure 31 Percent amplification by the splay fault relative to buried rupture source of water level at the shoreline and inundation up Ecola Creek versus percent amplification of seafloor uplift by the splay fault 47
Figure 32 Simulated versus observed inundation from the 1964 teletsunami at Cannon Beach. Steidel House and Bell Harbor Motel are localities with high-quality estimates of tsunami flow depth 49
Figure 33 Inundation from the 1964 and maximum considered distant tsunami compared to isolines of percent confidence for capturing all variability in Cascadia inundation 50
Figure 34 South-north (S-N) variation of open coastal tsunami wave elevations for scenario Largest 14, approximating the 99 percent isoline for all potential Cascadia tsunamis 51
Figure 35 Tsunami arrival times for splay fault sources at observation point cb009 in Figure 25 53
Figure 36 Tsunami arrival times for buried rupture sources at Station cb009 in Figure 25 53
Figure 37 Time histories of wave elevation for key regional slip patch scenarios; observation point at Station cb009 in Figure 25 54
Figure 38 Time history of wave elevation for the maximum considered Alaska tsunami scenario; 5-hour simulation at Station cb009 in Figure 25 54
Figure 39 Time history of wave elevation for the 1964 Alaska tsunami scenario; 8-hour simulation at Station cb009 in Figure 25 55
Figure 40 Time histories of tsunami velocity for key tsunami scenarios at the open coastal shoreline (Station cb009 in Figure 25) 55
Figure 41 Maximum velocity map for the Average 14 (preferred) tsunami scenario, approximating the ~70 percent confidence level for all variability in velocity for Cascadia tsunami 56
Figure 42 Time history of 1964 tsunami velocities at the open coastal shoreline (Station cb009 in Figure 25) 57
Figure 43 Time history of velocity changes for the maximum distant tsunami scenario at Station cb009 in Figure 25; 5-hour simulation 57

(List of Figures, continued)

Figure 44 Map of core sites used for the paleoseismic investigation and tsunami deposits versus tsunami inundation simulated on a paleolandscape with a foredune and without a foredune 59
Figure 45 Correspondence at the outer coast of scenario coseismic deformation to paleosubsidence data for the AD 1700 Cascadia earthquake of Leonard and others (2004) and Nelson and others (2008) 61
Figure 46 Correspondence from Youngs Bay east along the Columbia River of scenario coseismic deformation to paleosubsidence data of Leonard and others (2004) for the AD 1700 Cascadia earthquake 62
Figure 47 Relationship between isolines of percent confidence and key inundation boundaries. 65
Figure 48 Cross sections of selected coseismic deformation of Cascadia earthquake scenarios of this investigation most similar to inferred deformation for the 2004 Sumatra–Andaman earthquake near the latitude of Banda Aceh, Indonesia 67
Figure 49 Comparison of data from 2007 and 2009 on frequency of inter-turbidite time intervals for turbidites deposited in the last ~10,000 years compared to recurrence scenarios and weights from the basal four branches of the logic tree. 69
Figure 50 Key scenario inundation scenarios at Cannon Beach, Oregon 73
Figure 51 Inundation map as in Figure 50 but for the Arch Cape area immediately south of Cannon Beach, Oregon. 74
Figure 52 Maximum depth map for Average 14 scenario (preferred), approximating the ~70 percent confidence level for all variability in flow depth for Cascadia tsunami. 75
Figure 53 2008 tsunami evacuation map for Cannon Beach, Oregon, based on theoretical worst-case local and distant tsunami inundation 77
Figure A1 Structural boundaries relevant to this study A2
Figure A4 Coastal subsidence predicted by no-splay-fault, regional asperity models and comparison with AD 1700 coseismic subsidence data using 500 years of slip release A4
Figure A2 Model results of regional asperity models along an east-west profile at the Cannon Beach, Oregon, latitude. A5
Figure A3 Coastal subsidence predicted by buried rupture, regional slip patch models and comparison with 1700 coseismic subsidence data using 500 years of slip release A5
Figure A7 Fault slip distribution and resultant surface vertical deformation for the no-splay-fault "bank asperity" model (p3 patch) A6
Figure A8 Fault slip distribution and resultant surface vertical deformation for the splay-fault "bank asperity" model (p3 patch) A6
Figure A5 Fault slip distribution (left) and resultant surface vertical deformation (right) for the no-splay-fault model of medium p2a patch with modified symmetric fb76 slip distribution. A7
Figure A6 Fault slip distribution (left) and resultant surface vertical deformation (right) for the splay-fault model of medium p2a patch with symmetric fb76 slip distribution using 500 years of plate convergence to simulate coseismic slip A7

LIST OF TABLES

Table 1 Turbidite mass versus interevent time, either time following or preceding each turbidite 11
Table 2 Pearson product-moment correlation matrix: Turbidite mass versus prior and following interevent time 14
Table 3 Earthquake source parameters and weighting factors used in logic tree for Cascadia tsunami sources 28
Table 4 Four scenario time intervals and resulting coseismic slips and logic tree weights used in 2007 compared to similar data from 2009 follow time data of Table 1. 30
Table 5 Tsunami water elevation and inundation differences resulting from changes in rupture width and skew 41
Table 6 Tsunami water elevation and inundation differences between regional versus local (bank or basin) slip patches and splay fault versus buried rupture scenarios. 47
Table 7 Comparison of observed water depths and elevations during the 1964 Alaska tsunami at Cannon Beach, Oregon, to results of tsunami simulations. 51
Table 8 Preferred radiocarbon ages for three sand layers identified as tsunami sands at Cannon Beach, Oregon. 58

ABSTRACT

To update the tsunami hazard assessment method for Oregon, we (1) evaluate geologically reasonable variability of the earthquake rupture process on the Cascadia megathrust, (2) compare those scenarios to geological and geophysical evidence for plate locking, (3) specify 25 deterministic earthquake sources, and (4) use the resulting vertical coseismic deformations as initial conditions for simulation of Cascadia tsunami inundation at Cannon Beach, Oregon. Because of the Cannon Beach focus, the north-south extent of source scenarios is limited to the region from Neah Bay, Washington to Florence, Oregon. We use the marine paleoseismic record to establish recurrence intervals from the 10,000-year event record and select representative coseismic slips from these data. Assumed slips on the megathrust are ~8 m (~300 years of convergence), ~15 m (525 years of convergence), ~22 m (~750 years of convergence), and ~38 m (~1,300 years of convergence) which, if the sources were extended to the entire Cascadia margin, give magnitude values that vary from approximately M_w = 8.3 to 9.3. Additional parameters explored by these scenarios characterize ruptures with a buried megathrust versus splay faulting, local versus regional slip patches, and a seaward skewed versus symmetrical slip distribution. By assigning variable weights to the 25 source scenarios using a logic tree approach, we derived percentile inundation lines that express the confidence level (percentage) that a Cascadia tsunami will *not* exceed the line. Lines of 50, 70, 90, and 99 percent confidence correspond to maximum runup of 9, 11, 16, and 30 m (North American Vertical Datum of 1988 [NAVD 88]) where tsunamis were amplified by local topography; corresponding values without amplification were 8, 10, 13, and 20 m. The tsunami source with highest logic tree weight (preferred scenario) involved rupture of a splay fault with ~15 m slip that produced tsunami inundation near the 70 percent confidence line. The largest tsunami runup (99 percent confidence) was from 38 m slip partitioned to a splay fault. This type of extreme event is considered to be very rare, perhaps once in 10,000 years based on offshore paleoseismic evidence, but it can produce waves rivaling the 2004 Indian Ocean tsunami. Cascadia coseismic deformation most similar to the Indian Ocean earthquake produced generally smaller tsunamis than at the Indian Ocean due mostly to the 1 km shallower water depth on the Cascadia margin. Minimum inundation consistent with the inland extent of three Cascadia tsunami sand layers deposited east of Cannon Beach within the last 1,000 years was consistent with at least ~14 to 15 m slip on the subduction zone (release of 500 to 530 years of plate motion). However, only 200 to 400 years separates four turbidites deposited over the last 1000 to 1200 years when all turbidites, even a very small volume event, T2, were used to calculate potential coseismic slip. Leaving out T2 provided agreement between minimum coseismic slip and slip inferred from turbidite ages. Inundation from distant tsunami sources was assessed by simulation of only two M_w 9.2 earthquakes in the Gulf of Alaska, a hypothetical maximum considered event developed by the Tsunami Pilot Study Working Group (2006) and the historical maximum, the tsunami from the 1964 Prince William Sound earthquake. Maximum runups were, respectively, 12.4 m and 8.2 m at two points, but maxima along most of the shoreline were ~1 m lower than these two values.

INTRODUCTION

OBJECTIVES AND INTENDED AUDIENCE FOR THE REPORT

Tsunami runup on the order of 30 to 35 m near the epicenter of the great Sumatra–Andaman Islands earthquake of December 26, 2004 (Tsuji and others, 2005) and geologic similarities between the Cascadia subduction zone and the Sunda-Andaman subduction zone (Dengler, 2006; Goldfinger and McNeill, 2006) prompted the questions: Could local tsunamis of this size be generated by the Cascadia subduction zone? Can the wealth of new data from the 2004 earthquake and recent studies of Cascadia help us improve the assessment of local tsunami hazard? An ancillary question is how large is the hazard posed by distant tsunamis? This paper addresses the Cascadia tsunami hazard through comprehensive earthquake source characterization of the north-central Cascadia subduction zone combined with numerical simulations of tsunami inundation at Cannon Beach, Oregon (Figure 1). Cannon Beach was chosen for its relatively small size, variety of topography, rich record of Cascadia tsunami deposits,

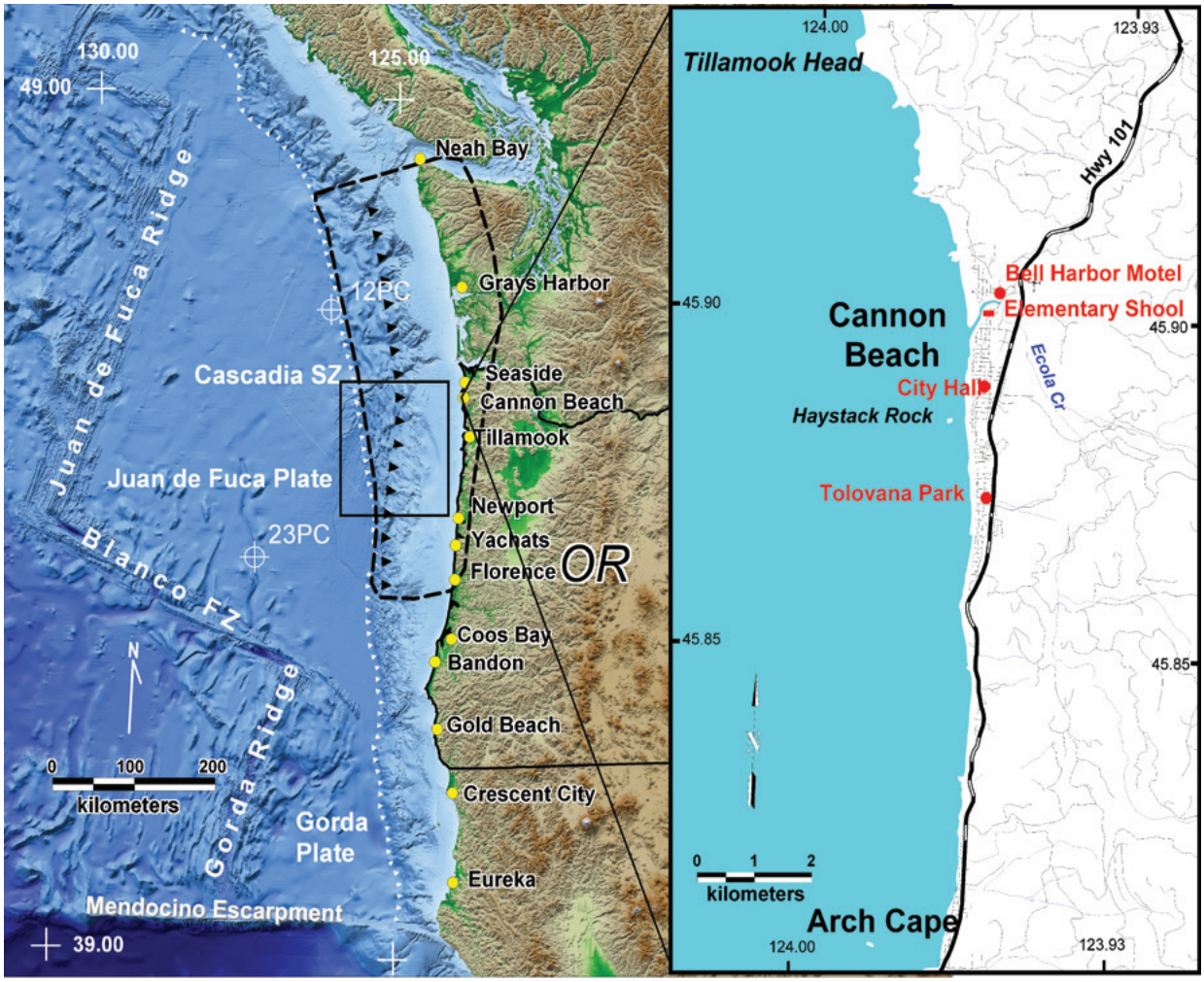

Figure 1. Location of the Cannon Beach study area (right panel) relative to major offshore tectonic plates and plate boundaries (left panel). Small white triangles mark the Cascadia subduction zone megathrust; large black triangles mark a splay fault used for tsunami simulations; solid black rectangle is the map area of Figure 8; white circles with crosses are core sites for turbidite data of Table 1. Dashed line in left panel is the portion of the Cascadia subduction zone simulated for coseismic deformation. FZ = Fracture Zone; SZ = subduction zone.

and detailed historical observations of tsunami inundation from the 1964 tsunami generated by the Prince William Sound earthquake in the Gulf of Alaska. The ultimate objective was development of a cost-effective, improved approach for tsunami hazard assessment of the Oregon coast by the Oregon Department of Geology and Mineral Industries (DOGAMI). This work is being complemented by a similar investigation of the southern Cascadia margin centered on the Bradley Lake-Bandon area where a similarly rich record of paleotsunami deposits exists. When complete, the two investigations will provide a powerful, quantitative framework for estimation of tsunami hazards.

The intended audience of this report is scientists and engineers who wish to understand the approach. Digital data and documentation provided with the report empower technical users to do a similar tsunami hazard assessment within the central part of the area simulated for Cascadia coseismic deformation (dashed line in Figure 1).

LARGEST HISTORICAL TSUNAMI

Satake and others (2003) inferred from historical records in Japan that the Cascadia subduction zone produced a trans-Pacific tsunami that caused destruction in Japan in AD 1700. They estimated that the earthquake most likely had a moment magnitude of ~9.0 and ~19 m of coseismic slip on an offshore, full-slip zone 1,100 km long. Numerous paleoseismic investigations have verified that this event and ~19 to 20 other earthquakes occurred on the northern part of the Cascadia subduction zone over the last 10,000 years (Atwater and others, 1995; Goldfinger and others, 2003a, 2003b, 2008, 2009). Holocene recurrence along the northern Cascadia margin is on average ~500 years (Goldfinger and others, 2008, 2009).

The largest historical tsunami produced by a distant source struck March 28, 1964, reaching Cannon Beach approximately 4 hours after the M_w 9.2 Prince William Sound earthquake in the Gulf of Alaska. The tsunami flooded parts of downtown Cannon Beach, floated a building from its foundation, and destroyed a bridge (Figure 2).

APPROACH

In this investigation we test a new multi-deterministic approach for evaluation of tsunami hazards. For local Cascadia subduction zone earthquakes, we use new geologic data on the subduction zone and new understandings of size and frequency of earthquakes from the offshore turbidite record, supported by the extensive but shorter land paleoseismic record (Goldfinger and others, 2003a, 2003b, 2008, 2009; new interpretations in this paper) to construct plausible sources for tsunamis affecting Washington and northern Oregon (Figure 1). A key assumption is that time intervals between earthquakes can be directly translated into a record of variable slip on the Cascadia megathrust. We then use the paleoseismic record to pick four representative slip magnitudes for a parametric analysis of the effect of slip distribution on vertical coseismic deformation of the North American Plate.

These coseismic deformation scenarios serve as the initial conditions for simulation of tsunami propagation and inundation using a new but carefully benchmarked tsunami code, SELFE [a semi-implicit Eulerian–Lagrangian finite-element model for cross-scale ocean circulation] (Zhang and Baptista, 2008). After weighting each tsunami scenario through a logic tree, the resulting inundations are depicted on maps in terms of percent confidence that a local Cascadia tsunami will reach no farther inland than each boundary line. In effect, the maps represent the spatial distribution of hazard posed by a tsunami from an M_w 8.3 to 9.3 Cascadia megathrust earthquake with a recurrence of ~500 years. The probability of an earthquake along the north-central Cascadia margin capable of triggering a tsunami in the next 50 years is 10 to 14 percent based on 3,500 years of paleoseismic record in coastal marshes (Petersen and others, 2002) or 7 to 9 percent based on the 10,000-year turbidite record (Goldfinger and others, 2009). This approach is a robust way of depicting tsunami hazard dominated by a large local earthquake source like Cascadia.

We examine the hazard from distant tsunamis only for extreme cases, as these tsunamis are relatively small, even for M_w ~9 earthquakes, and have done only modest damage to the Oregon and Washington coasts (see, e.g., data compiled by Lander and Lockridge, 1989). We explore the largest historic event, the 1964 Alaska tsunami, and a hypothetical maximum con-

sidered event from the Gulf of Alaska taken from the Tsunami Pilot Study Working Group (TPSW) (2006) investigation of Seaside, Oregon (Figure 1).

Comparison of simulations to observations served as a quality check. Simulated Cascadia inundation and coseismic deformation were compared to paleoseismic estimates. Standard hydrodynamic benchmark testing (Zhang and Baptista, 2008) and comparison of simulated flow depth and inundation from the 1964 Alaska tsunami to observations assessed the accuracy of the numerical model, SELFE, and model inputs.

GENERAL FINDINGS

We find that largest Cascadia tsunami inundation and runup exceed previous estimates for State of Oregon-sponsored assessments. This finding results from consideration of a broader range of slip for prehistoric Cascadia subduction zone earthquakes consistent with turbidite recurrence as a proxy for earthquake recurrence. Larger coseismic deformation in the current source scenarios results from more realistic slip distributions that concentrate slip instead of distributing it

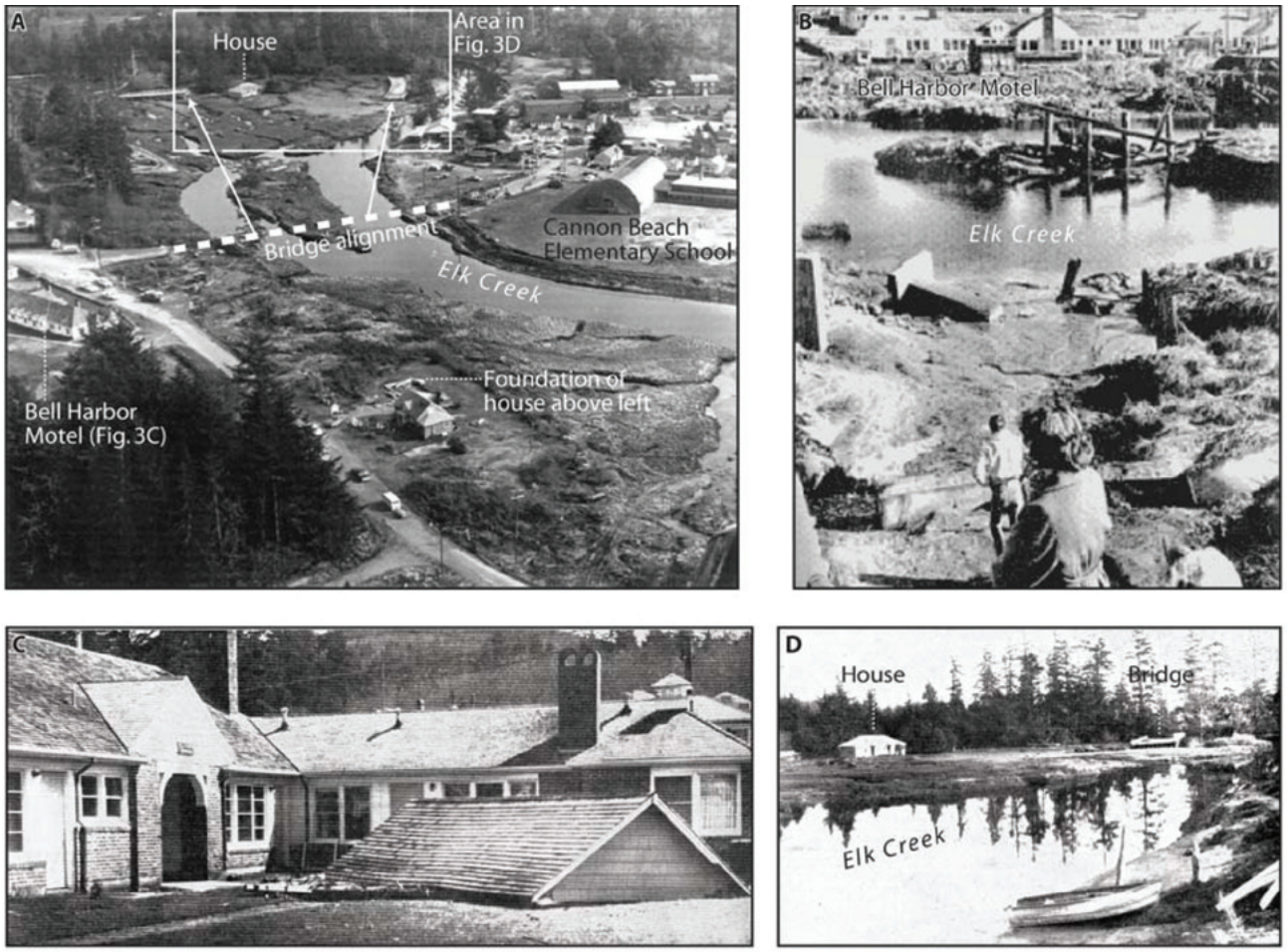

Figure 2. Photographs showing the impact of the 1964 Alaska tsunami (courtesy of the Cannon Beach Historical Society). (A) Oblique aerial photograph of the lower Elk Creek valley (now Ecola Creek) that flows through downtown Cannon Beach. Decking from the old Elk Creek bridge was torn from its abutments and transported 300 m upstream. A foundation in the lower part of the photo marks the original position of a house that was carried 400 m upstream and deposited between the bridge sections. (B) View to the northwest across Elk Creek showing bridge pilings and piers, all that remain after the tsunami destroyed the Elk Creek bridge in 1964. Bell Harbor Motel can be seen in the distance across the creek. (C) Bell Harbor Motel suffered considerable damage from flooding during the tsunami, including broken windows, water damage, and destruction caused by drift logs. The roof of a different building was left in the front yard of the motel after being carried several hundred yards by the waves. (D) View to the southeast looking across Elk Creek at the bridge remains and house transported hundreds of meters inland by the tsunami. Figure is from Witter (2008).

uniformly as in most previous studies. We detail why the resulting variability in tsunami inundation is best depicted as isolines of percent confidence that tsunami flooding will be less than each isoline. We show the advantages of a multi-deterministic approach for estimation of tsunami hazard dominated by a large local tsunami source with high uncertainty in the geometry of the coseismic deformation. We found that it is possible for the Cascadia subduction zone to generate tsunamis nearly as large as the one that struck Sumatra in December 2004, although this would be an extremely rare event. We also explore the hazard posed by a theoretical maximum considered tsunami from the Gulf of Alaska that rivals some Cascadia tsunami scenarios.

RELATIONSHIP TO PREVIOUS TSUNAMI MODELING STUDIES

Unlike previous studies of Cascadia tsunami hazard (Hebenstreit and Murty, 1989; Ng and others, 1990; Preuss and Hebenstreit, 1998; Priest, 1995a; Priest and others, 1997, 1998, 1999a, 1999b, 2000a, 2000b, 2004, 2007; TPSW, 2006; Walsh and others, 2000; Whitmore, 1993; see also review by Mofjeld and others, 1999), this investigation evaluates many Cascadia earthquake sources using a logic tree to systematically explore a wide spectrum of geologically reasonable variations in source parameters. For example, the most sophisticated previous study, the TPSW (2006) investigation, used 12 variations in slip distribution but only one earthquake magnitude, albeit one that was derived from observational data of the AD 1700 tsunami impact in Japan. We found from analysis of turbidite and other paleoseismic data that Cascadia earthquake magnitude likely varied widely from that of AD 1700; hence, we investigated source models with four different estimates of slip. Like previous investigations, we model one regional locked width for the Cascadia subduction zone based on geophysical, geodetic, and geologic data, but we also explore additional locked widths that vary from this regional pattern, concentrating slip under submarine structural highs or forearc basins. Unlike most previous studies, we also explore the effect of slip partitioning from the mega-thrust to a mapped splay fault.

Slip distributions used in this investigation were developed following the method of Wang and He (2008) and differ markedly from previous work. Previous tsunami hazard assessments by the State of Oregon (e.g., Priest and others, 1997, 1998, 1999a, 1999b, 2000a, 2000b, 2002, 2004) have for the most part simulated three Cascadia earthquake sources, two using uniform slip and one maximum event using a Gaussian uplift patterned after uplift at the largest asperity inferred from seismic data on the 1964 Prince William Sound earthquake. The Gaussian uplift was added to the largest of the two uniform slip scenarios to attain a peak uplift of about 6 m centered roughly on the continental shelf-slope break. Tsunami inundation maps for the coast of southern Washington were prepared using a similar Gaussian source model (Walsh and others, 2000) and using a simplified source by Preuss and Hebenstreit (1998). All of these investigations used the Okada (1985) fault dislocation model that we also use but only to simulate uniform slip. Geist and Yoshioka (1996) also used uniform slip models to examine the effect that variations in earthquake source parameters have on Cascadia tsunamis. Geist (2005) examined various types of uncertainties in Cascadia earthquake sources for an investigation aimed at a probabilistic tsunami hazard assessment for Seaside, Oregon (TPSW, 2006). Geist (2005) concluded from global data on subduction zones (Thatcher, 1990; Boyd and others, 1995) that most uncertainty is irreducible and inherent to the rupture process. He emphasized the need to use distributed slip models to avoid underestimating tsunami amplitude and wave steepness. These conclusions were the foundation for a stochastic analysis of Cascadia tsunami sources for a probabilistic tsunami hazard assessment at Seaside, Oregon (TPSW, 2006). TPSW varied slip randomly within a zone on the megathrust consistent with the "long-wide" model of Satake and others (2003) while maintaining a constant moment magnitude of ~9. The 19 m of uniform slip used in the Satake and others (2003) model produced much smaller maximum uplift than the magnitude ~9 earthquakes in the stochastic slip models of the TPSW (2006). The stochastic slip models placed large amounts of slip in small patches of the updip portion of the megathrust in order to maintain a constant moment while still abiding by the seaward skew of slip inherent in the distributed slip assumption. The net effect was that all 12 of the TPSW sources simulated earthquakes with slip much larger

than 19 m in patches mostly along a narrow, ~30-km-wide zone, near the trench. The resulting high slip gradients and uplifts in deep water generally produce larger local tsunamis than do scenarios with uniform slip or the slip distributions used in this investigation.
Most previous investigations focused on the Cascadia tsunami hazard as does this investigation; one exception is the TPSW (2006) study that explored 14 distant sources. The probabilistic tsunami hazard assessment of the TPSW (2006) at Seaside demonstrated that all but the most extreme distant sources pose little threat to the nearby town of Seaside, Oregon; hence, our decision to explore only a maximum teletsunami of the TPSW (their Gulf of Alaska source 3) and the largest historic teletsunami, the 1964 tsunami from the Prince William Sound earthquake (source parameters from Johnson and others [1996]).

METHODS

The main objective of this investigation is assessment of the serious hazard posed by tsunamis from the Cascadia subduction zone We first thoroughly explore the geological constraints on the megathrust slip, locked width of the subduction zone, potential slip patches, and location of a master splay fault. We then explain how this information is used to create fault dislocation scenarios and Cascadia tsunami simulations. To address the ancillary objective of assessment of the distant tsunami hazard, we briefly describe two deterministic sources that in the judgment of the scientific team are near worst-case events for far-field earthquakes. Methods for ground truth check of simulations is the final topic in this section.

GEOLOGICAL CONSTRAINTS ON CASCADIA EARTHQUAKE SOURCE PARAMETERS

Paleoseismicity and Recurrence Model

Paleoseismicity in Cascadia has been investigated using a variety of methods both onshore and offshore. In this project we establish Cascadia earthquake recurrence using best-fitting mean ages for the central Cascadia margin for offshore and onshore events. Onshore, geologic evidence of subsided marshes buried by tsunami deposits are ubiquitous and have been investigated with varying degrees of success at virtually every bay and estuary along the Oregon, Washington, and northern California coast. Offshore, we use turbidite ages and data from Goldfinger and others (2003a, 2003b, 2008, 2009). The onshore paleoseismic record along the central margin extends to ~3,700 years BP (e.g., Atwater and others, 2004), while offshore data extend reliably to ~10,000 years (Goldfinger and others, 2008, 2009).

OFFSHORE TURBIDITE RECORD

The Holocene turbidite stratigraphy of submarine channels along the Cascadia margin (Figure 3) includes Mazama ash from the eruption of Mount Mazama forming Crater Lake, Oregon (Nelson and others, 1988). This marker bed allows correlation and age calibration of the turbidite record. The calendrical age of the eruption of Mount Mazama has recently been re-dated at 7,627± 150 cal. yr BP from the GISP-2 ice core (Zdanowicz and others, 1999). The Mount Mazama eruption airfall was distributed northeastward from southern Oregon mainly over the Columbia drainage and some of the coastal rivers. It is also found in the Puget lowland, British Columbia (Hallett and others, 1997), and in inlets on the west coast of Vancouver Island (Dallimore and others, 2005). From these rivers, Mazama ash was transported to temporary depocenters in canyon heads of the Cascadia continental margin, much as Mount St. Helens ash was transported following the 1980 eruption (Nelson and others, 1988). Subsequent turbidity currents transported the ash into Cascadia Basin canyon and channel floor depocenters.

Using the Mazama marker bed, ^{14}C ages, and stratigraphic correlation, the offshore turbidite record has been demonstrated to be largely if not entirely composed of synchronous turbidites; 19 of these are margin wide, while others span shorter segments along southern Cascadia (Adams, 1990; Goldfinger and others, 2003a, 2003b, 2008, 2009). The synchroneity of the ~10,000-year turbidite event record for 500 km along the northern half of the Cascadia Subduction Zone is best explained by triggering by great earthquakes. The average recurrence interval for long ruptures is ~500 years based on isotopic age data and thickness of hemi-

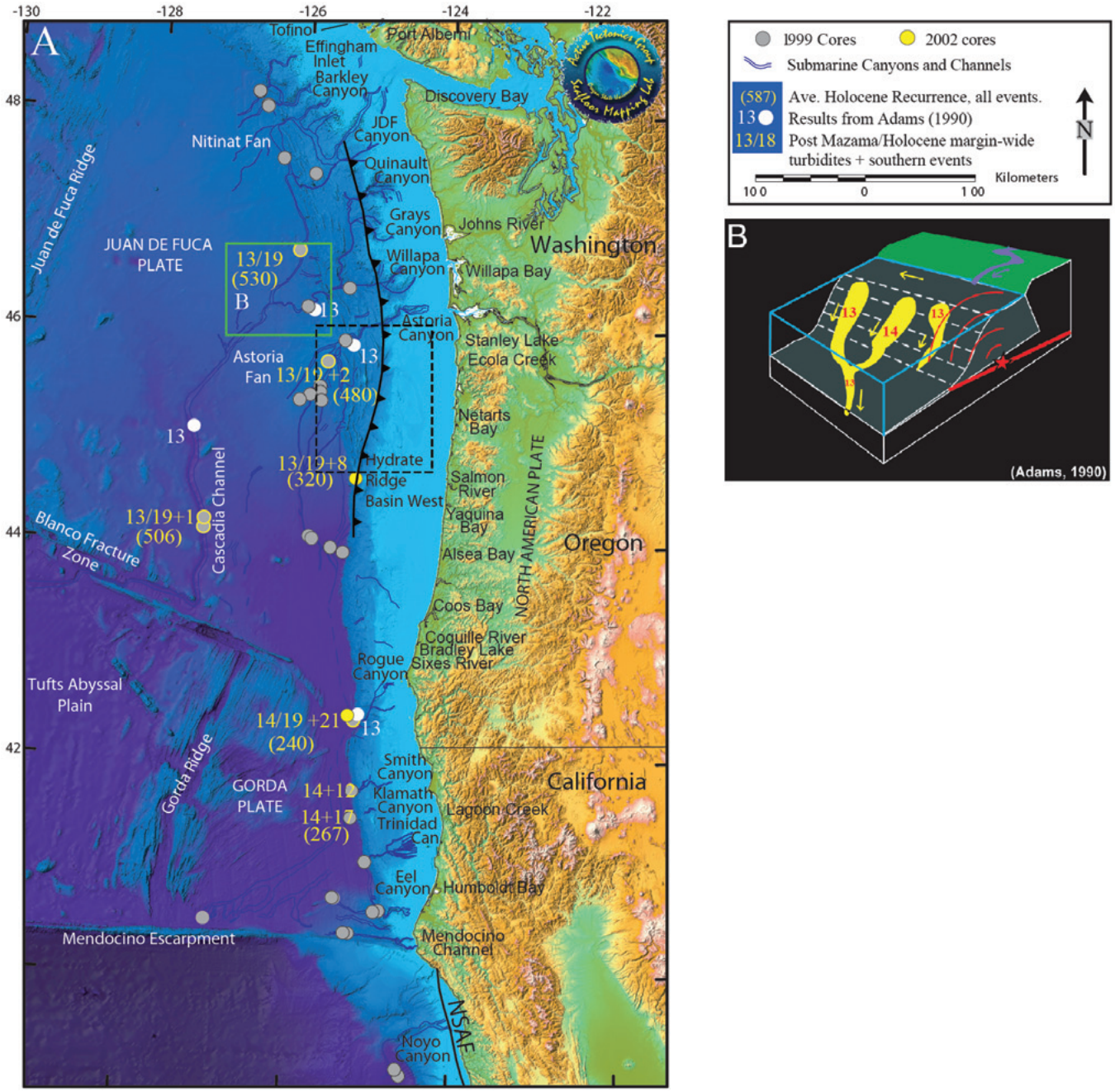

Figure 3. Cascadia margin turbidite canyons, channels, and 1999 and 2002 core locations. Major canyon/channel systems are outlined in blue. Bathymetric grid constructed from multibeam data collected in 1999, Gorda Plate swath bathymetry collected in 1997 (Dziak and others, 2001), and archival data available from the National Geophysical Data Center (NGDC). Primary core sites are shown with yellow rims; all other 1999 and 2002 cores are grey. (B) Synchroneity test at a channel confluence as applied where Washington channels merge into the Cascadia Deep Sea Channel, indicated by green box. The number of events downstream should be the sum of events in the tributaries, unless the turbidity currents were triggered simultaneously. Dashed line is location of the detailed map of Figure 8; line with triangles marks an inferred splay fault separating Pleistocene and Tertiary material of the accretionary wedge.

pelagic sediment deposited between turbidite beds (Goldfinger and others, 2008, 2009).

Offshore data can be used to correlate individual events between sites based on accepted subsurface log correlation techniques. The correlation is done using primarily magnetic susceptibility and gamma density, much as electronic logs are correlated in the oil industry (McCubbin, 1982; Lovlie and van Veen, 1995). Physical property correlations of this type are also common practice with academic, Ocean Drilling Program (ODP), and Integrated Ocean Drilling Program (IODP) cores (e.g., Fukuma, 1998) and have recently come into use for paleoseismology (i.e., Abdelayem and others, 2004; Karlin and others, 2004; St-Onge and others, 2004; Hagstrum and others, 2004; Iwaki and others, 2004; Schnellman and others, 2002). In this context, magnetic susceptibility and density traces are proxies for grain size distribution, and therefore depositional history of each turbidite (Goldfinger and others, 2007a, 2008, 2009). The correlated signatures are composed of stacked coarse sand pulses that exhibit magnetic susceptibility, density, and grain size trends within each event that are closely correlated. This is straightforward but important because we can use in most cases the high-resolution density and magnetic data as grain size proxies, at least for lithologies along the Cascadia and northern San Andreas fault systems (Goldfinger and others, 2007a, 2008). In addition to local site correlation, Goldfinger and others (2008) have found that it is possible to correlate unique physical property signatures of individual turbidites from different sites within individual channels. This relationship suggests that the processes controlling deposition of the turbidite maintain consistency for some considerable distance within a channel. They have also found it possible to correlate event signatures not only down individual channels and past confluences but between channel systems separated by considerable distance, some of which never meet (Goldfinger and others, 2007a, 2008). These turbidite "fingerprints" form the basis of long-distance correlations and are beginning to be recognized and used for regional correlation (e.g., Lake Baikal [Lees and others, 1998]; off Morocco [Wynn and others, 2002]; Cascadia [Goldfinger and others, 2003a]; Laptev Sea in the Russian Arctic [Rivera and others, 2006]). Recently, the "event signatures" of Cascadia turbidites have been linked to coastal fjord records on Vancouver Island (Goldfinger and others, 2009; Dallimore and others, 2005). Goldfinger and others (2006a, 2006b, 2007a, 2007b, 2008, 2009) report detailed stratigraphic cor-

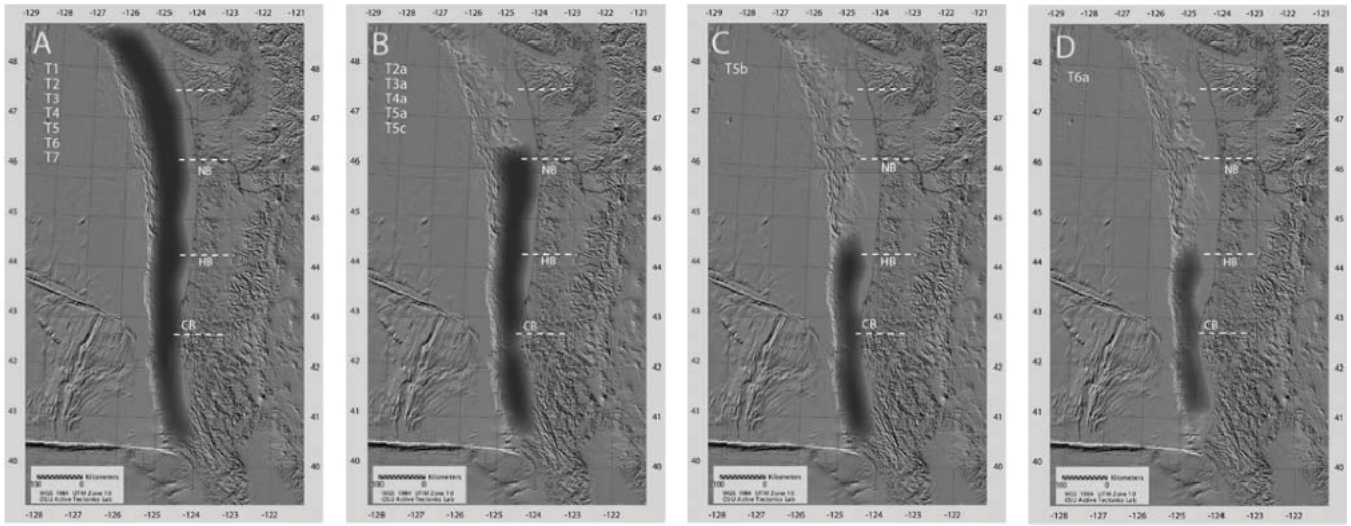

Figure 4. Four panels showing preliminary rupture modes identified using turbidite correlation of Goldfinger and others (2008) for a ~3,000-year period; additional events for the last ~10,000 years are described by Goldfinger and others (2009). (A) Full rupture, represented at all sites by seven events. (B) Mid-southern rupture, represented at all sites as far south as 40.7° N by five events. (C) Southern rupture from central Oregon southward to at least 41° N, represented by one event. (D) Southern Oregon/northern California events, represented by one event. Rupture terminations appear to occur at three forearc structural uplifts: Nehalem Bank (NB), Heceta Bank (HB), and Coquille Bank (CB). Latitudinal boundaries of episodic tremor and slip (ETS) events proposed for the downdip subduction interface (Brudzinski and Allen, 2007) are shown by white dashed lines. Figure is taken from Goldfinger and others (2008).

relations and use them to evaluate rupture lengths of Cascadia paleoearthquakes (Figure 4); a brief summary is included here.

On close inspection of physical property logs, Goldfinger and others (2008, 2009) sometimes see remarkable similarities between correlative turbidites that are separated by as much as 500 km (Cascadia) and 280 km (northern San Andreas fault). Figure 5 shows several typical examples of correlative events in detail along strike over a distance of 280 km. They see a general correspondence of relative turbidite size downcore that is reflected in separate channels, as well as correlative details such as the number of coarse sandy pulses (density and magnetic peaks). The correlation of these signatures indicates that the integrity of the signatures, and thus the pattern of coarse fraction deposition, is maintained to some extent over time and distance during the sediment transport process of the turbidity current.

The fact that turbidites correlate over large distances is strong evidence that the turbidity currents were earthquake generated and is robust regardless of the reasons for the correlation (Goldfinger and others, 2003a, 2007a, 2008, 2009). Japanese investigators have similarly shown that the only plausible mechanism for multiple, simultaneous, regional landslide triggering is an earthquake (Shiki and others, 2000). Goldfinger and others (2007a, 2008, 2009) conclude that the physical property signatures most likely record the shaking signal imparted to the sediment failure region by the earthquake itself; in effect, the physical property signatures are crude paleoseismograms. As such, the earthquake may impart some information about magnitude, source character, or aftershocks to the depositional history of each turbidite (Goldfinger and others, 2007a, 2008). This is an observation used in the next section.

When we consider all offshore paleoseismic data, the along-strike correlations described above, and relevant high-precision onshore data, including those of Witter (2008), we infer that the northern and central Cascadia margin records a minimum of 19 Holocene earthquakes that are correlated between multiple sites and thus define a maximum average late Holocene recurrence interval for the central margin of ~530 years. The combined stratigraphic correlations, hemipelagic analysis, and ^{14}C framework for the entire margin suggest that the Cascadia subduction zone effectively has four rupture modes during the Holocene: 19 long ruptures with variable southern limits (some of which are imposed by data availability); two ruptures comprising the southern 60 percent of the margin, and 18 smaller southern margin ruptures during the Holocene that have variable northern and southern limits (Goldfinger and others, 2008, 2009). There is some uncertainty as to the northern limits of some of these events. One of the large southern ruptures (T10f) and two of the smaller ones (T5b and T9a) may reach the latitude of Cannon Beach. We assume that at least one of these (T5b) reaches Cannon Beach and therefore use 20 events here to determine local interseismic intervals and calculate the local earthquake recurrence of ~500 years (Table 1). Erring on the side of caution, we calculate slip for a maximum considered Cascadia event from the maximum recurrence of the 19 full margin events (i.e., excluding event T5b) plus the 2σ error in age data. This maximum interval is between events T5 and T6 and equals ~1,300 years, once 2σ error is added. In this investigation, we also do not consider the smaller more distant southern Oregon events. The study site at Cannon Beach is located north of inferred southern Oregon segment ruptures (Goldfinger and others, 2008) and would not be expected to experience significant tsunamis from such events, given the directivity of tsunami energy away from the long axes of subduction zone ruptures (Titov and others, 1999). One caveat is the conclusion of Myers (1999) that tsunami energy is more efficiently radiated north from southern segment ruptures than toward the south from northern segment ruptures. We also do not consider tsunamis from sources within the Gorda Plate, along the Northern San Andreas Fault, or Queen Charlotte strike slip faults, because these sources are unlikely to have large enough vertical displacement to create significant tsunamis.

Considering the 19 events that have affected the entire northern and central Oregon margin during the Holocene, the average repeat time these events is ~530 years (versus ~500 years at Cannon Beach), with a minimum repeat time of ~160 years, and a maximum repeat time of ~1,000 years. The events also appear to cluster in time, including a cluster comprising the last four events averaging only ~350 years between events. The three tsunami sand layers mapped at Cannon Beach by Witter (2008) have ages overlapping this cluster of events.

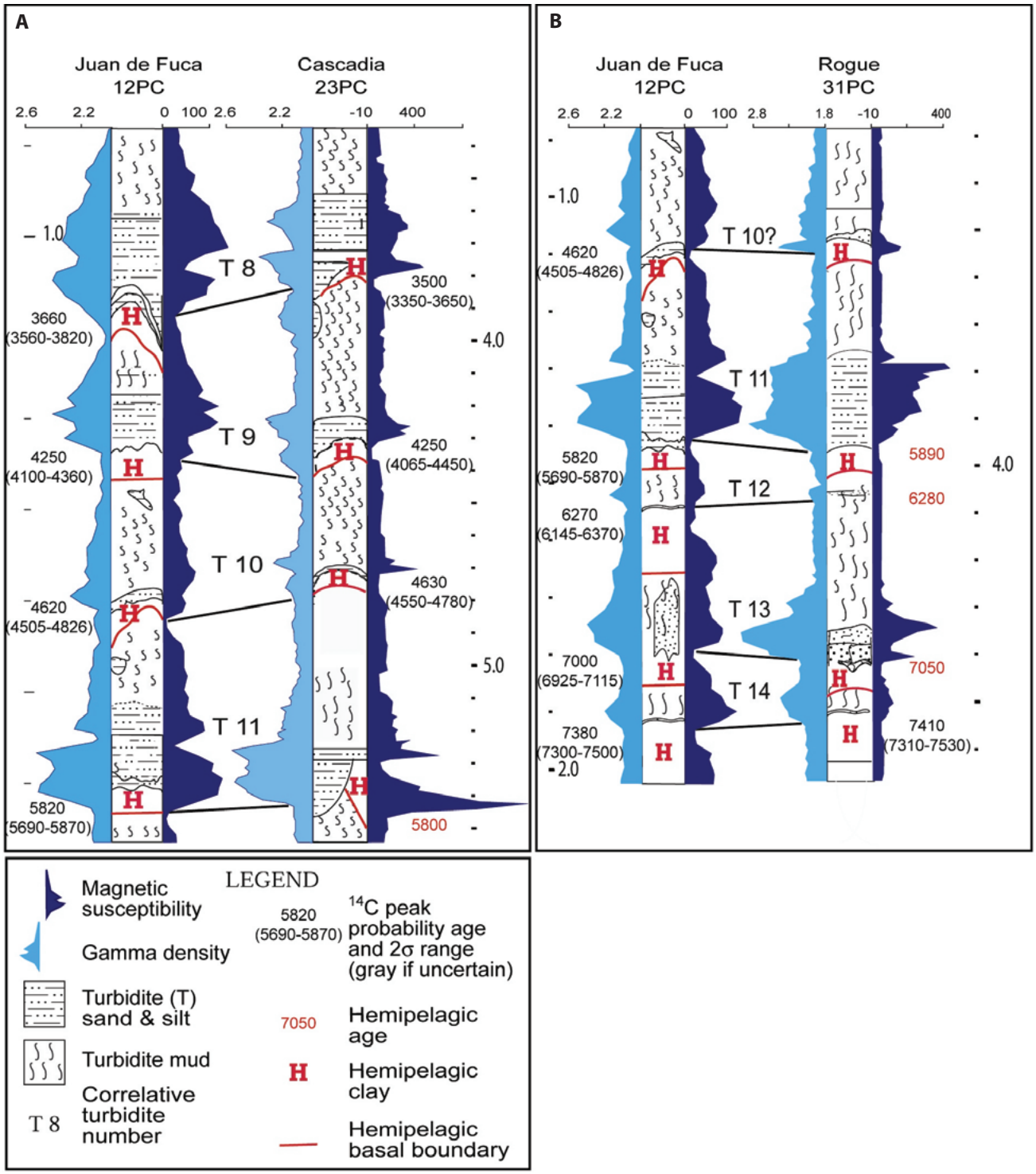

Figure 5. Correlation details from two representative pairs of cores on the Cascadia margin. (A) Events 8 to 11 in cores from Juan de Fuca Channel (left) and Cascadia Channel (right). Left traces are raw gamma density; right traces are magnetic susceptibility. Lithologic logs are also shown. Note correspondence of size, spacing, number of peaks, and trends of physical property traces between these cores. (B) Events T10 to T14 in Juan de Fuca Channel (left) and T10d to T14 in Rogue Channel (right). Panel A cores are part of the same channel system; distance = 475 km. Panel B cores are in channels that do not meet; distance = 500 km. Detailed stratigraphic correlations are used to evaluate rupture lengths of Cascadia paleoearthquakes, and a brief summary is included here. The methods for both earthquake determination and stratigraphic correlation are given by Goldfinger and others (2007a, 2008, 2009).

Table 1. Turbidite mass versus interevent time, either time following or preceding each turbidite.

Turbidite No.	Turb. Mean Age (yr)	Turb. Age Error +2σ (yr)	Turb. Age Error −2σ (yr)	Turb. Follow Time (yr)	Turb. Preceding Time (yr)	Hemipelagic Interevent (Cascadia Channel) Follow Time	Hemipelagic Interevent (Cascadia Channel) Preceding Time	12PC Norm. Mass	23PC Norm. Mass	12PC and 23PC Avg. Mass	Qual. Event Size (Turb.)	Qual. Event Size (Follow Time)
T1	269*	96	100	>309	196	n.d.	149	175	155	165	avg.	n.d.
T2	446	85	89	196	338	149	456	115	60	87.5	small	small
T3	784	103	112	338	414	456	309	155	135	145	avg.	small
T4	1198	122	113	414	369	309	480	110	135	122.5	avg.	avg.
T5	1567	176	167	369	453	480	190	115	235	175	avg.	small
T5b	2020	163	159	453	530	190	645	105	100	102.5	small	avg.
T6	2550	137	147	530	484	835	530	295	225	260	avg.	avg.
T7	3034	134	163	484	480	530	525	340	315	327.5	large	avg.
T8	3514	168	176	480	644	525	642	390	170	280	large	avg.
T9	4158	165	184	644	586	642	686	290	140	215	avg.	avg.
T10	4744	173	189	586	849	686	1017	150	75	112.5	avg.	avg.
T11	5593	148	135	849	696	1017	203	460	625	542.5	large	large
T12	6289	151	138	696	853	203	557	40	45	42.5	small	large
T13	7142	124	118	853	482	557	457	260	110	185	avg.	largest
T14	7624	139	139	482	563	457	639	105	105	105	avg.	avg.
T15	8187	138	143	563	702	639	683	100	60	80	small	avg.
T16	8889	197	187	702	253	683	311	450	1110	780	largest	large
T17	9142	259	292	253	61	311	434	90	195	142.5	avg.	small
T17a	9203	177	193	61	616	434	124	60	55	57.5	small	small
T18	9819	184	232	616	n.d.	124	n.d.	95	195	145	avg.	avg.

Data from Goldfinger and others (in revision; data released June 23, 2009). Mean ages are before AD 1950. Turb. = turbidite; Casc. = Cascadia; ; Norm. = normalized; avg. = average; qual. = qualitative; n.d. = no data. Cascadia Channel refers to a turbidite transport channel in the abyssal plain off the northern Oregon coast.

CASCADIA MEGATHRUST SLIP INFERRED FROM OFFSHORE TURBIDITES

The single largest variable in computing tsunamis is the slip magnitude and distribution for the source earthquake. Having no actual slip distribution from a Cascadia great earthquake, we attempted to assess both the relative sizes of paleoearthquakes and geologic evidence of the position of the coupled plate interface to constrain possible slip distributions to those consistent with geological and geophysical data. To address the size of paleoearthquakes, we use the observed properties of offshore earthquake-generated turbidites and rupture lengths to help estimate the relative sizes of past earthquakes.

We have noted in the preceding section that relative mass of the turbidites correlates between remote sites, regardless of local sedimentation rate. That is, large turbidites are large at all sites, and small turbidites are small at all sites. This correlation suggests that the source earthquake magnitude may control turbidite mass and thickness. If we make the assumption that larger turbidites represent the greater shaking expected during larger earthquakes, we can use the relative sizes and interevent times to address the relative magnitudes of paleoearthquakes. Goldfinger and others (2009) demonstrate that there is a relationship between interevent time intervals and the relative size of the turbidites. Here we briefly summarize this result. As previously noted, we examine only the longer ruptures that affect the north-central region and do not consider smaller, more frequent ruptures common along the southern margin.

To quantify turbidite size, we calculate the dimensionless area under the gamma density curve relative to the baseline hemipelagic density for each Holocene turbidite in cores 12PC and 23PC from the Juan de Fuca and Cascadia channels, respectively. The cross sectional area of the density plot is a dimensionless representation of the mass of each turbidite (multiply-

ing by the cross section of the core tube yields the true mass in grams per cubic centimeter). Table 1 summarizes the relationship between turbidite mass for each correlated event and the interevent times, including both cores, the average of the two cores, and the preceding and following time intervals. We scale turbidite mass with an arbitrary scale factor to plot on the same scale as interevent time in years for visual comparison (Figure 6). Table 2 shows the correlation matrix for following time and prior time intervals to turbidite mass. A Pearson correlation coefficient of 0.73 for the mass values between the two sites (Table 2) indicates a moderately strong correlation for the two turbidite series. The strong correlation of mass and number of pulses between sites supports the earthquake link between sites (Goldfinger and others, 2009). We also find a significant relationship between the mass of each event and the time following that event, with Pearson correlation coefficient of 0.48 between the averaged masses and the following interevent times for the 20 event series (T5b is included). The hemipelagic sediment thickness above each turbidite is also correlated to turbidite mass, with a coefficient of 0.60. The prior interevent time and sediment thickness below each turbidite are negatively correlated to turbidite mass (Table 2). Figures 7a and 7b similarly illustrate the positive correlation of turbidite mass to following time or sediment thickness above turbidites and the near zero correlation for prior time. A moderately strong correlation between turbidite mass and following interevent time supports the inference that the relative size relationship suggested by the mass correlation has physical meaning. Further, the temporal correspondence supports a hypothesis in which turbidite size, assumed to represent earthquake size, and the time between earthquakes are related. The relationship between turbidite size and earthquake size is implicit in the along-strike correlation of turbidites (it is one of the parameters used for correlation), which is unlikely to be related to external factors such as sediment supply (Goldfinger and others, 2009).

An earthquake model in which the interevent time after an earthquake is proportional to the size of the event is known as a "time predictable" model because the time of the next event (but not its size) can be predicted from the size of the preceding event (Shimazaki and Nakata, 1980). The Cascadia turbidite data appear to fit this model to a modest extent. The negative correlation with prior time intervals suggests that a slip-predictable model does not fit the Cascadia data. Several exceptions to the general relationship seen in Figure 6 are that T16, the largest event by mass, is followed by an ~700-year interval, while T12, a small event, and T13, a moderate event, were followed by similarly long intervals.

In the family of Holocene Cascadia earthquakes shown in Table 1, we note that only one of them, T1 (the AD 1700 earthquake), has an independent estimate of magnitude. T1 is in the grouping of "average" events from the turbidite perspective, but independent estimates of this event center around a full margin rupture of M_w ~9.0 (Satake and others, 2003). Although we cannot assign magnitudes to the remainder of the Cascadia earthquakes, we conclude that turbidite mass and following time correlations imply there were events larger than the AD 1700 earthquake, such as T8, T11, and T16; a group of events of about the same size, T3, T4, T5, T6, T7, T9, T13; and numerous events that were smaller, i.e., T2, T10, T12, T14, T17, and T17a. The groupings of relative size from Table 1 were used to establish the relative weights of earthquake sizes used in the decision tree for scenario tsunami runs for the Cannon Beach study area.

The slip values used in the tsunami simulations are derived directly from the time intervals between paleoearthquakes. To estimate fault slip at the latitude of Cannon Beach, we convert the time intervals to fault slip based on Euler poles of Wang and others (2003) and assume that all interplate convergence is released in coseismic slip. Real fault slips are likely smaller due to less than 100 percent locking observed in most subduction zones (McCaffrey, 1997). This approximation, while inexact, offers at least a weak constraint on the possible slips of past earthquakes and on the frequency distribution of earthquakes of different size through the Holocene. We note that Goldfinger and others (2008) observed that when all segmented ruptures are considered, turbidite mass also correlates with rupture length in Cascadia. This observation supports the inference that turbidite mass is related to earthquake "size" (the convolution of magnitude, duration, peak acceleration, etc.) as used in this report.

Few localities in the world offer the opportunity to explore the size and frequency distribution of great earthquakes with even weak constraints. One other is the Tokai-Nankai subduction zone in Japan, where historical records of uplift and tsunamis have been used to

examine the ~1,500 year record available there. Rikitake (1999) modeled fault slip based simply on time intervals and plate motion as we have done and concluded that the slips were not significantly different from those inferred from geodetic, seismologic, and tsunami data, though the tsunami data tended to imply larger slips than from other methods.

The apparent fit to a time predictable model is an outcome of this study and is explored further by Goldfinger and others (2009). The potential recurrence relationship is noted and is supportive of the relationship between time and slip, but not used to predict other parameters in this investigation.

GEOLOGIC EVIDENCE OF INTERPLATE LOCKING

In Cascadia, there are no seismicity data from which to construct actual coseismic slip distributions for great earthquakes to use in tsunami modeling. We therefore use geologic, geodetic, and geophysical constraints to define the most probable family of models from which we expect past and future ruptures to originate. Estimates of the position of the locked plate interface have been made on the basis of thermal and geodetic data (Hyndman and Wang, 1995; Flück and others, 1997), Global Positioning System (GPS) strain data (Wang and others, 2003; McCaffrey and others, 2007), and the evidence of landward tilting found in leveling data from the past ~80 years (Mitchell and others, 1994; Burgette and others, 2009). The models have considerable variability among them, and, because most are land based, place little constraint on the seaward part of the subduction interface, a region important for tsunami generation. For these reasons, we pursued further evidence of the offshore position of the locked plate boundary in Cascadia that could be used to constrain tsunami generation models.

UPDIP LIMIT OF INTERPLATE LOCKING

We used geologic data to map the boundary between landward and seaward vergent structures as a proxy for weak/strong interplate coupling along the seaward part of the central Cascadia margin. Several models of Cascadia interplate coupling have been proposed that suggest the coupled interface extends to the deformation front (Hyndman and Wang, 1995; Flück and others, 1997). These models were primarily based on thermal considerations, which imply that the outer accretionary wedge is hot enough to sustain stick-slip behavior. These models do not exclude other factors that may influence laboratory stick-slip behavior. Geologic evidence suggests that shear stress on the interface between much of the outer accretionary wedge in central and northern Cascadia and the subducting Juan de Fuca plate is very low (Figures 8 and 9). Much of the Pleistocene accretionary prism in this region is landward vergent, that is, the individual faults dip seaward (MacKay, 1995). As the development of landward-vergent thrusts is commonly linked to the properties of incoming sediments (overpressured sediments producing low shear-stress along the basal detachment) and/or to properties of the older deeper prism (high-competency backstop materials), the geometry of these thrusts may in the former case be correlated with the coupling stress (Goldfinger and others, 1992, 1996). Landward vergence is a common expression of very low coupling stress on the underlying décollement (Seely, 1977; MacKay, 1995), requiring pore fluid pressures to be high or near lithostatic on the underlying faults. In some settings, landward vergence may also be attributed to backstop geometry or other factors (e.g., northern California [Gulick and others, 1998]). Further evidence of low coupling stress is a wide fold spacing and open folding style. Overpressuring may be an episodic condition (e.g. Maltman, 1998; Saffer and Bekins, 1999) during earthquakes or may be semi-permanent condition of interplate convergence. The widespread landward vergent province in Cascadia coincides with widely spaced, open folds, suggesting poor interplate coupling underlying this region (Goldfinger and others, 1992, 1996, 1997; Mandal and others, 1997). The evidence is supported by observations of a mud volcano seaward of the Washington deformation front (Goldfinger, 1994) and the variable signature of lower-plate strike-slip faults that breach only the upper plate in regions of inferred strong coupling (Goldfinger and others, 1992, 1996, 1997).

The source of fluid overpressuring is thought to be the rapid late Pleistocene deposition of the Astoria and Nitinat submarine fans, which correspond spatially to the latitudinal position of the landward vergent province within the prism (Goldfinger and others, 1996). The rapid deposition of these two fan systems has resulted in high pore fluid pressures during the Holocene, as insufficient time has elapsed to allow the accreting fans to equilibrate to hydrostatic condi-

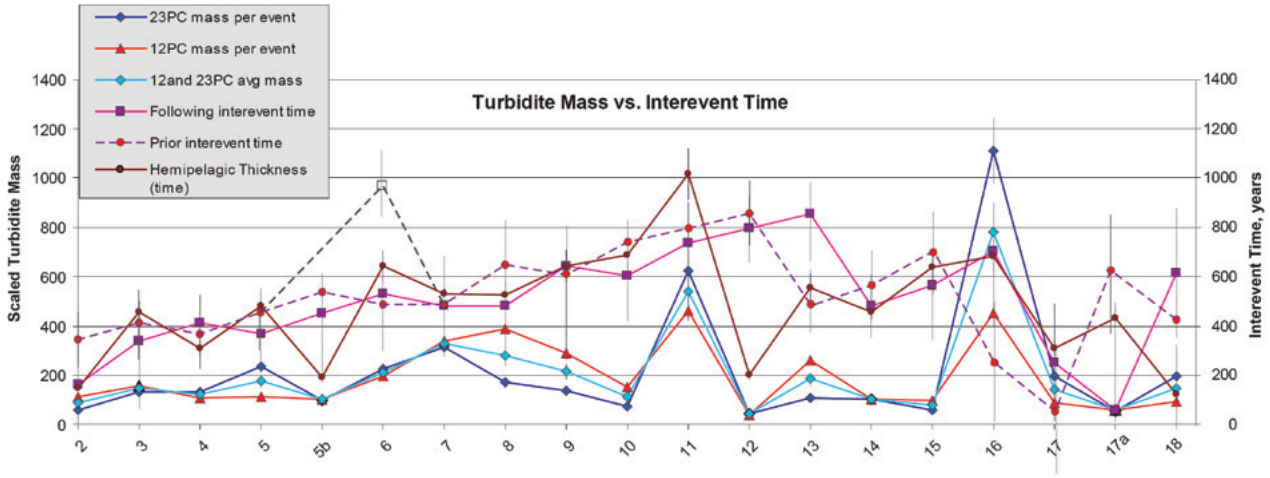

Figure 6. Relationship between turbidite mass per event at Juan de Fuca and Cascadia Channels, and interseismic time, northern Cascadia margin. Mass values for each turbidite from two cores, M9907-12PC from Juan de Fuca Channel, and M9907-23PC Cascadia Channel are plotted separately, and as their average mass. Local turbidite mass determined from gamma density traces and scaled by an arbitrary factor to plot at same scale with interevent time in years (see methods). Time (right Y axis) is the interevent time between turbidites taken from the mean peak PDF (probability density function) ages of the turbidites margin wide (Table 1; Goldfinger and others, 2009). Also plotted are the hemipelagic time equivalents from M9907-25PC. The northern extent of event T5b is uncertain. Following time interval shown assuming T5b extends to the latitude of JDF (Juan de Fuca) channel. Grey dashed following time plot shows alternate interpretation without T5b. Error ranges shown for interevent times are 1σ.

Table 2. Pearson product-moment correlation matrix: Turbidite mass versus prior and following interevent time for data of Table 1 but using 250 years as the age of the last event, T1.

	Following Interevent Time (yr)	Prior Interevent Time (yr)	Hemi-pelagic Follow-ing Time (Cascadia Channel)	Hemi-pelagic Preced-ing Time	12PC Mass	23PC Mass	Average Mass
Following Interevent Time (yr)	1.00	—	—	—	—	—	—
Prior Interevent Time (yr)	0.38	1.00	—	—	—	—	—
Hemipelagic Following Time	0.56	0.26	1.00	—	—	—	—
Hemipelagic Preceding Time	0.25	0.41	-0.03	1.00	—	—	—
12PC mass	0.56	-0.04	0.71	-0.11	1.00	—	—
23PC Mass	0.39	-0.31	0.49	-0.38	0.73	1.00	—
Average Mass	0.48	-0.23	0.60	-0.31	0.88	0.97	1

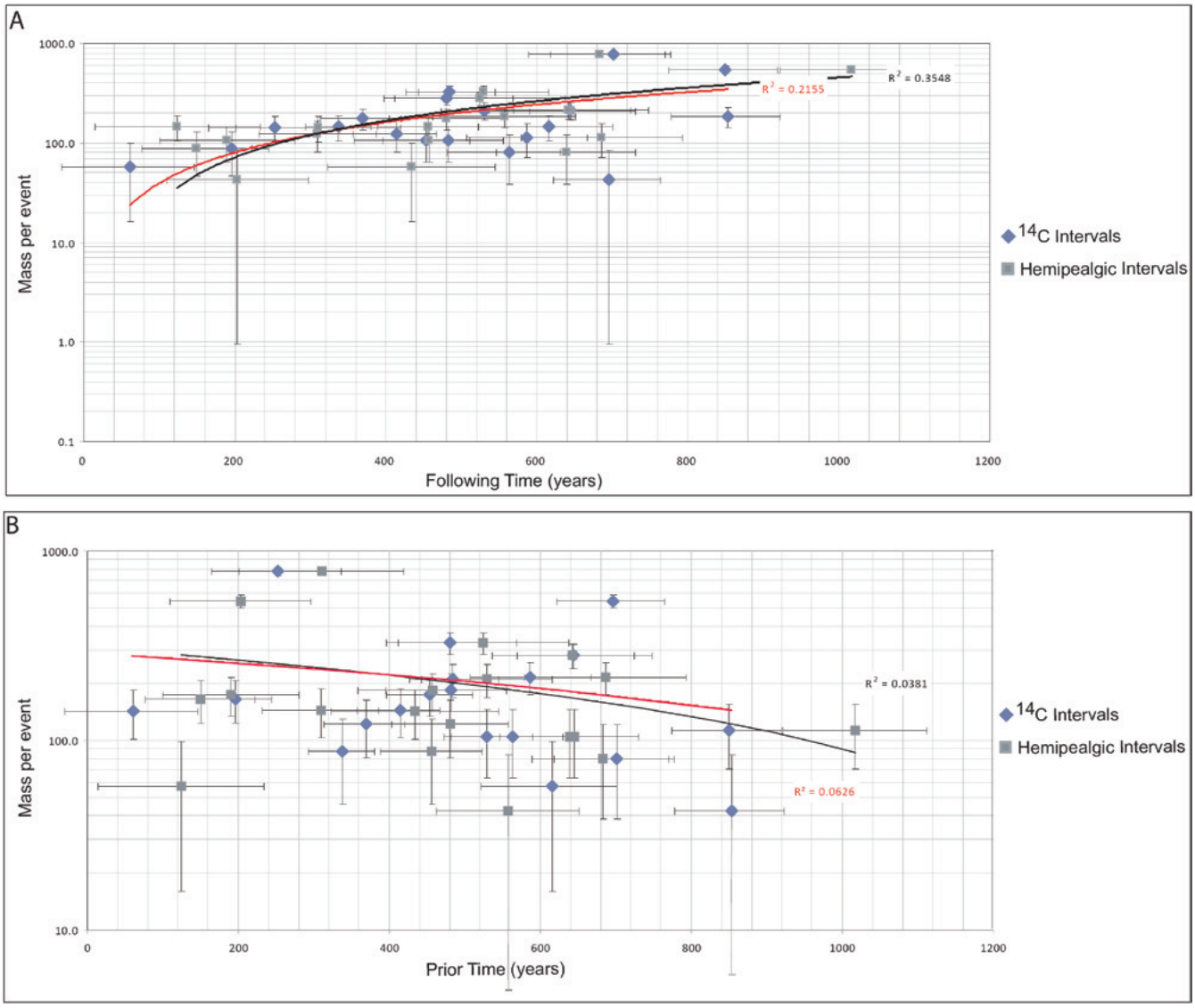

Figure 7. Plot of interseismic intervals versus mass per event for (A) time-predictable and (B) slip-predictable models for the northern and central Cascadia margin. Time intervals based on hemipelagic sediment thickness and sedimentation rates are also shown. Time predictable model is weak positive fit to the data, with regression fit R^2 of 0.22 for ^{14}C data, and 0.36 for hemipelagic data. The poorer fit here shows that while the trends based on a Pearson statistic shown in Table 2 and Figure 6 are moderately good, a direct numerical relationship is weaker. The slip-predictable model however is uncorrelated.

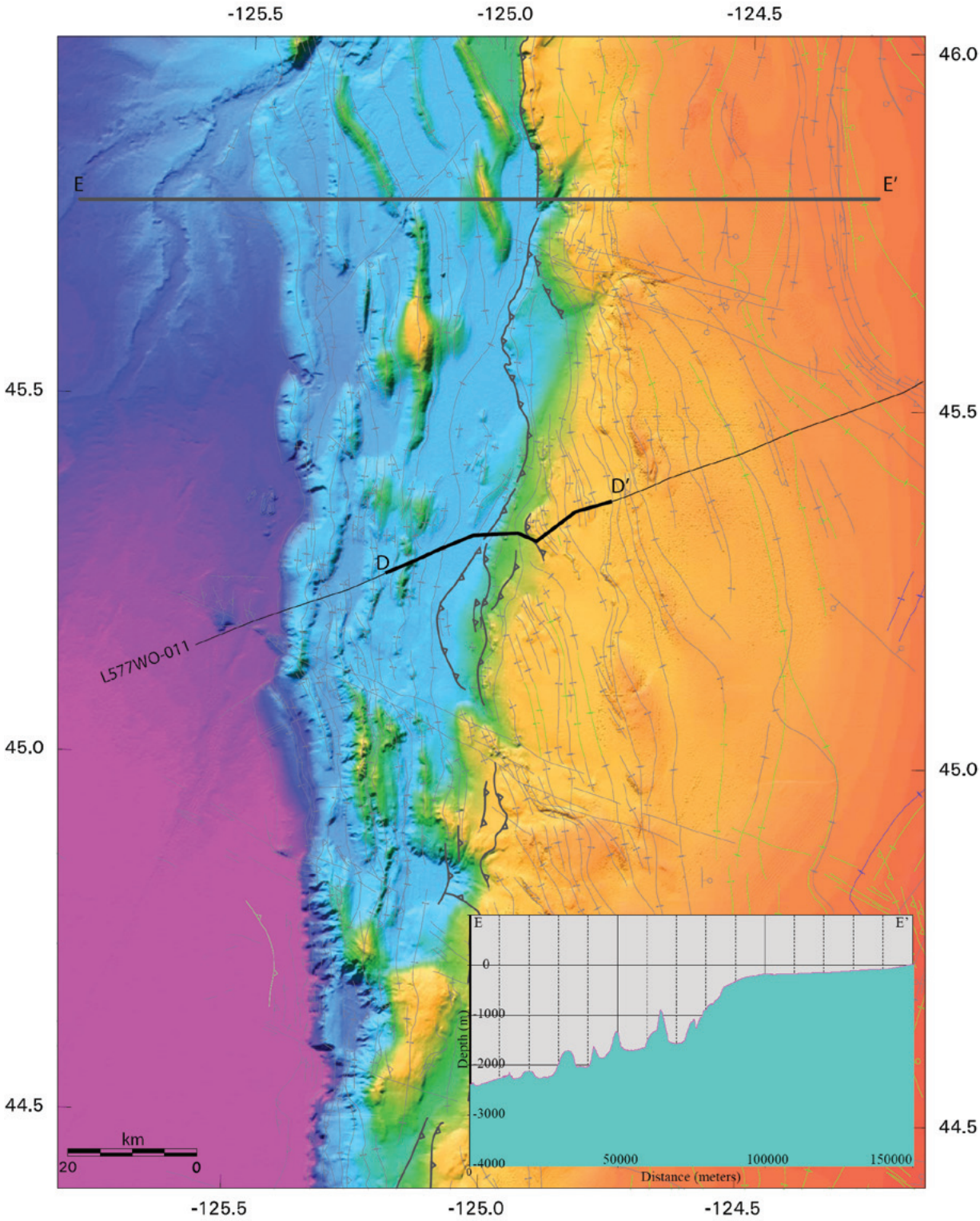

Figure 8. Shaded bathymetry of the Oregon margin, with structural map overlain (Goldfinger 1994). Light blue lower slope is characterized by landward vergence, low surface taper (profile E-E′), and wide fold spacing and is dominated by margin-parallel folds. Older accretionary complex in orange, dominated by convergence-normal fold trends landward vergence, and steep mid-slope defining a steeper wedge taper. The two provinces are separated by a seaward vergent splay fault (bold gray lines with triangles pointing down the thrust fault dip) and abrupt break in surface slope. Mapped traces of the splay fault scarps are shown here; generalized location of the model fault used for the tsunami source models is depicted on Figure 3. Splay fault is imaged by U.S. Geological Survey reflection profile L-5-WO77-12, shown in Figure 14. Bathymetric profile (profile E-E′) shows low surface wedge taper and steep upper slope separated by the splay fault scarps. See Figures 1 and 3 for location of this map.

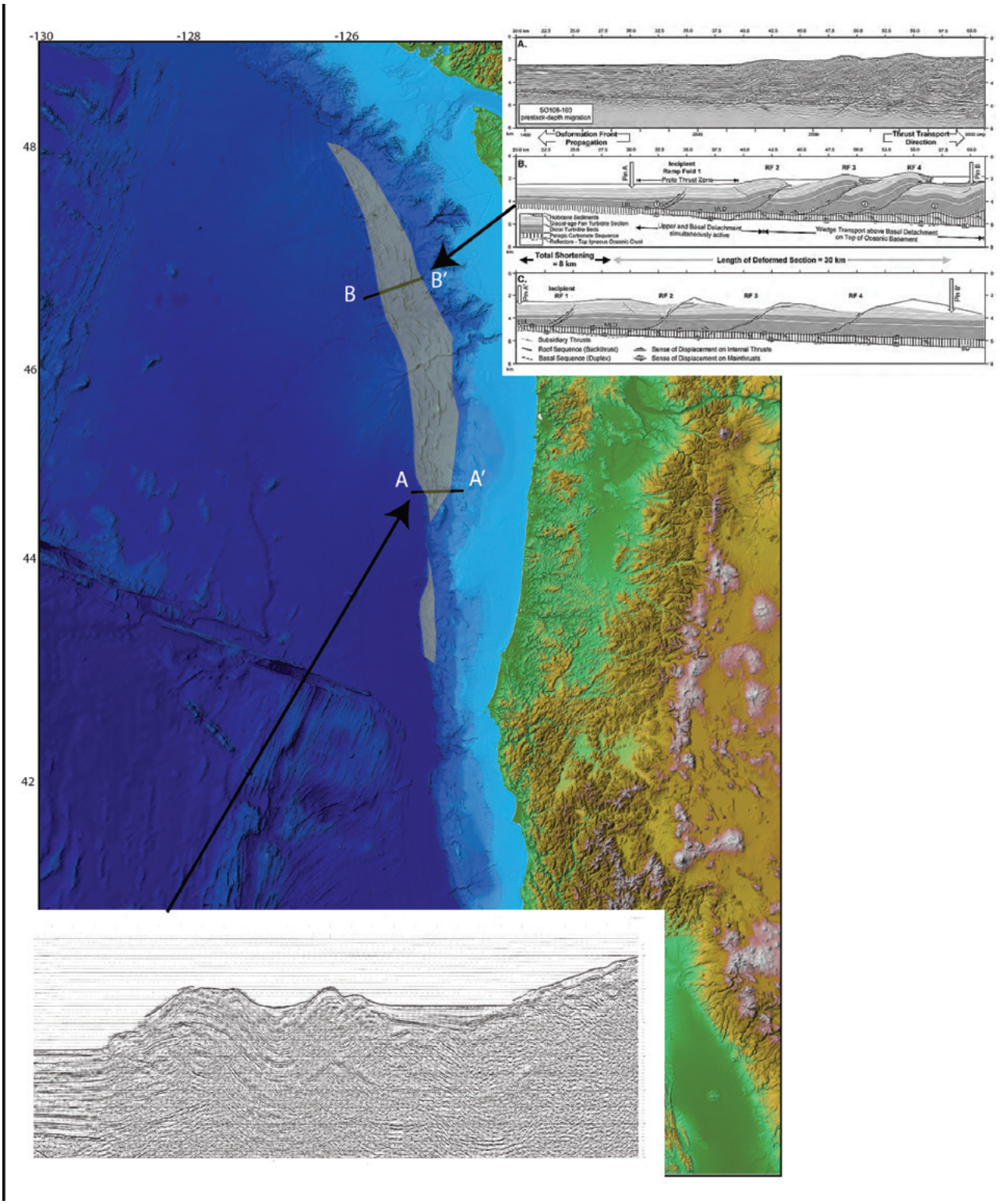

Figure 9. Decoupled regions of the central Cascadia margin mapped from multiple proxies for interplate coupling. Contrast between landward vergent (upper panel, B-B′, R/V *Sonne* lines 103 and 108) and seaward vergent (lower panel, A-A′) structures coincides with break in slope, age contrast, and boundary of structural trends shown in Figure 7. Landward vergent region shown in shaded polygon in map view. Southern shaded polygon is also a decoupled region of landsliding (Goldfinger and others, 2000). Upper inset from Adam and others (2004); lower inset from Johnson (2004).

tion. The sediment supply to the Sumatra prism bears resemblance to Cascadia, in that thick fan sequences supplied from the north are accreting to the outer forearc. This could promote low basal shear stress and landward vergence, as is likely in Cascadia (Seely, 1977; MacKay, 1995; Goldfinger and others, 1996; Goldfinger and McNeill, 2006). Alternatively, the Sumatran landward vergence may be controlled by a backstop of high-velocity material (McNeill and others, 2006) accreted as a duplex beneath the slope cover (Ladage and others, 2006; Fisher and others, 2007). In Cascadia, evidence of backstop-controlled landward vergence can be found along the northern California margin (Gulick and others, 1998) and off southern Oregon (Goldfinger and others, 2000). However, in northern and central Cascadia, the geologic evidence does not support a landward dipping backstop, and the extensive landward vergent province is more consistent with a fluid pressure control. R/V *Sonne* lines 103 and 108 (Adam and others, 2004; cross section B-B′ in Figure 9) image the width and depth extent of the landward vergent province, where as many as seven landward vergent folds comprise the Pleistocene section, revealing no evidence of a backstop control of these structures.

Further evidence of weak coupling in the outermost accretionary prism of northern Oregon comes from structural observations of fold trends in map view. Seaward of a major break in slope and wedge taper (also marked by a splay fault discussed in a subsequent section), fold trends are margin parallel and clearly follow variations in the strike of the splay fault tip (Figure 8). Goldfinger and others (1997) interpret this relationship as clear evidence of the backstop nature of the older accretionary complex in the hanging wall of this structure. The stress orientations that primarily control fold trends respond to the map pattern of the slope break/splay fault. Arcward of the splay, fold trends vary between arc parallel and convergence normal along much of the central margin, a contrast in strike. Over most of the map in Figure 8 the upper slope (yellow-orange) and lower slope (blue) boundary corresponds to a ~30° change in fold strike with some folds truncated at the boundary. The slope break, vergence change, splay fault, and boundary between the low tapering lower slope wedge and steeper tapering upper slope and shelf accretionary complex all coincide, as shown in Figure 8.

This secondary evidence supports a change from strong to weak coupling at the slope break boundary. In contrast to models implying large seismogenic coupling in the seaward accretionary wedge, most subduction earthquakes in accretionary systems have a gradational transition at their updip ends consistent with reduced coupling and higher pore fluid pressures in the outer prism. The fault slip model shown in Figure 10 for the Sumatra–Andaman Islands earthquake of December 26, 2004, is broadly consistent with these observations (Chlieh and others, 2007). Based on the preceding analysis, we map the boundary between landward and seaward vergent structures as a proxy for weak/strong interplate coupling along the seaward part of the central Cascadia margin (Figures 8 and 9). While this boundary is likely to be gradational, there is not presently enough constraint to further develop the model of the updip limit in Cascadia.

DOWNDIP LIMIT OF INTERPLATE COUPLING

In many subduction zones, locating the downdip limit (in the absence of great earthquakes) has been attempted using elastic and viscoelastic models of GPS strain data, leveling data, and with thermal models. Although these methods always produce a result, it is difficult to compare these results to the actual seismogenic zone, which is very poorly defined. In Sumatra, with the 2004 event, we now have a good opportunity to assess possible relationships between forearc structures based on the well constrained slip models.

In this report, in addition to published thermal and GPS based models, we examine the use of an apparent structural transition from contraction to extension on the Cascadia margin that is observable in offshore seismic reflection data, focal mechanisms, and borehole breakouts as a proxy for long-term interplate coupling. Although there is no certainty that the structural data actually represent plate coupling, several lines of reasoning suggest that this may be the case. We then compare these results to published GPS and thermal results. First we briefly discuss the origins of forearc structure.

The actual origin of forearc basins and highs is presently not known. Early models of forearc structure attempted to relate the presence of forearc highs, basins, and intervening deformation zones directly to

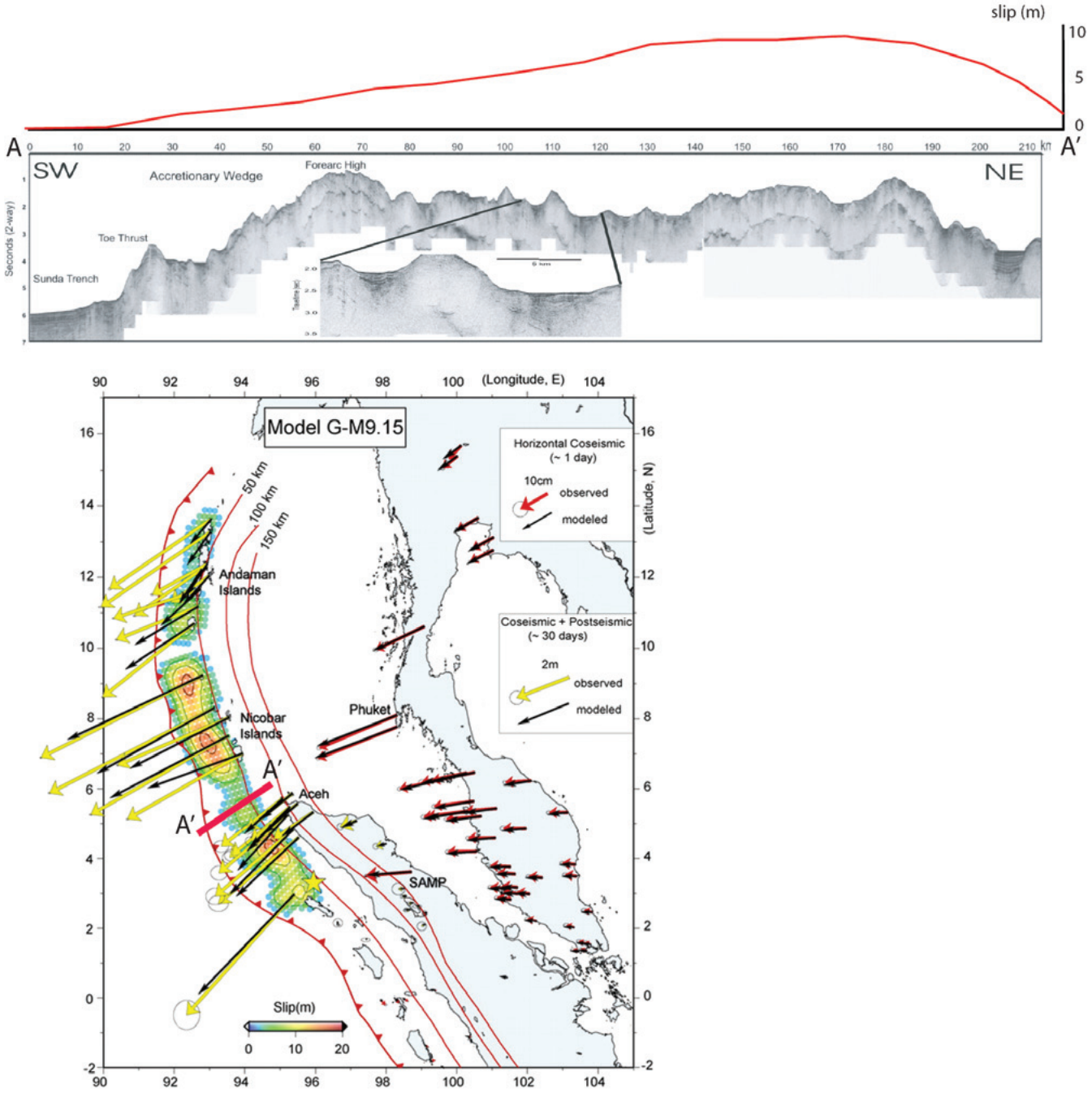

Figure 10. Sumatra forearc shown by single-channel profile (A-A′) Sumatra Earthquake and Tsunami Offshore Survey (SEATOS) line 1 (Fisher and others, 2007). Forearc basin at right, forearc high in center, and subduction thrust (labeled Toe Trust) and the abyssal plain (Sunda Trench) at left. Lower panel shows preferred slip distribution from Chlieh and others (2007) for the Sumatra–Andaman Islands earthquake of December 26, 2004, in map view based on Global Positioning System data. Profile of the Chlieh and others (2007) slip distribution along cross section A-A′ shown above the single-channel seismic (SCS) profile. Slip (m) scale at right of profile. Map location of the subduction zone megathrust is the red line with triangles pointing down the fault dip; red lines to the east are depth contours on the megathrust. Colored regions on lower map are inferred coseismic slip; arrows show direction and magnitude of observed and modeled coseismic and post-seismic slip, as indicated in the map legend.

the mechanical consequences of "backstop" geometry. In these models, the forearc basin overlies the tip of the backstop and thus is undeformed, because it is "shielded" from interplate stress by the presence of the strong backstop (i.e., Byrne and others, 1993). Although forearc highs and basins are ubiquitous, their origins cannot always be explained so simply, the actual structure is typically more complex, and many exceptions to the early models exist.

Models of the Sumatra slip distribution such as those derived from GPS (Chlieh and others, 2007; Figure 10) and seismologically (Ammon and others, 2005) suggest that the downdip extent of seismogenic slip roughly corresponds to the transition from the arcward part of the forearc high to the lightly deformed forearc basin (Goldfinger and McNeill, 2006; Figure 10). Because the Sumatra forearc uniquely has islands above sea level in this zone, this transition is well expressed as a landward tilting of the islands, namely, Simeulue and Nias for the 2004 and 2005 subduction earthquakes, respectively (Meltzner and others, 2006). The strong coseismic tilt is semi-permanent and was mapped by the uplift and subsidence of coral heads and entire coastlines. Because the tilt changed sign from positive to negative on the islands, modeling the source slip zone was relatively straightforward and matched the seismologic models reasonably well. These models also indicate that the downdip transition from slip to no slip roughly underlies the seaward side of the forearc basin. These observations are unprecedented in any great subduction earthquake and lead us to hypothesize that the downdip termination of the seismogenic zone may, at least in some subduction zones, be expressed in the upper plate as the transition from the highly deformed outer arc high to the undeformed forearc basin. In much of Sumatra, the seaward part of the forearc basin is characterized by a transition from a seaward part that exhibits contractional deformation to an undeformed or slightly extensional normal faulted basin farther arcward. This transition suggests a stress change across the basin from horizontal arc normal compression to tension. Whether this transition is coincidence in Sumatra is not yet known, as this locality could well be underlain by the seaward edge of a backstop as in the original forearc models. However, the change in deformation style overlies a transition from seismogenic to aseismic slip based on the 2004 earthquake. A review of other great earthquakes such as Kamchatka (1952), Alaska (1964), and Chile (1960) yields ambiguous interpretations, slightly favoring a similar interpretation (Goldfinger and others, 2007b) except for the Chile 1960 earthquake, which clearly ruptured beneath the forearc basin (Barrientos and Ward, 1990).

In Cascadia, we can map a transition similar to that of Sumatra by examining the numerous available industry multichannel reflection profiles (Goldfinger and others, 1992, 1997). We note that this transition does not coincide with a "backstop" as in the Byrne and others (1993) models. The backstop in Cascadia is the Siletzia terrane, the boundary of which is shown in Figure 11 located beneath the center of the outer arc high. Its position varies along strike, but the western boundary seems to be unrelated to the position of the forearc high-basin transition, which is approximately parallel to the coastline.

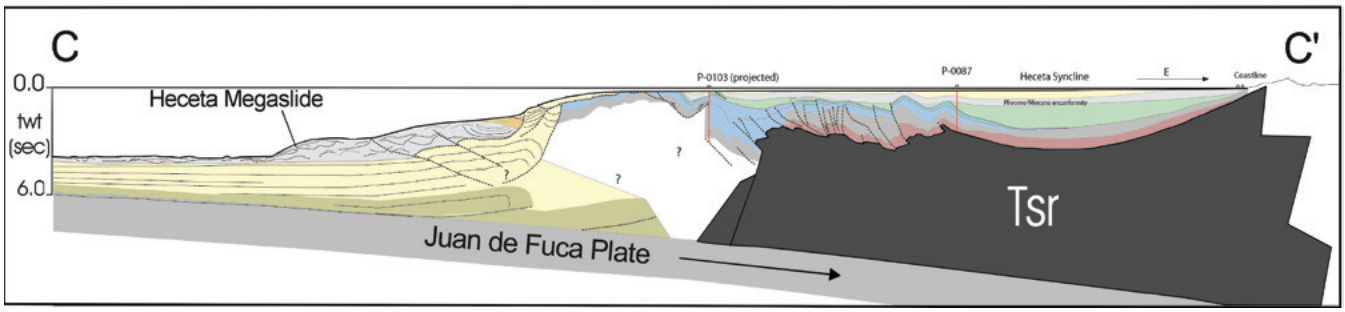

Figure 11. Cross section across Heceta Bank, Oregon from Chevron seismic line HOG-15 and Western Geco seismic line WO-18. This typical forearc section shows the compressional nature of the forearc basin (contrast with section of Wells and others [2003] along the same profile). Flexural slip faulting controls the basin western margin, the eastern margin is undeformed or extensional. Boundary between extension and compression is mapped for numerous similar profiles in Figure 12. See Figure 12 for location of this cross section. Bedded units are sedimentary rocks. Unit Tsr (dark gray) is Tertiary Siletz River Volcanics of the Siletzia terrane considered to be a hard rock backstop in contact with sedimentary rocks of the accretionary prism (yellow and tan deformed units) to the west. Twt is two-way travel time.

We use an industry data set of seismic reflection profiles acquired by Oregon State University (OSU) to assess the structural evidence for landward waning of contractional deformation related to interplate coupling. These data are proprietary in part. Figure 11 shows a typical cross section through Heceta Bank, Oregon, based on industry profiles Western Geco line WO-18 (http://walrus.wr.usgs.gov/NAMSS/) and proprietary line HOG-15. This profile reveals the structure of the forearc basin and outer arc high, supported by age and lithologic data from test wells P-0087 and P-0103. The structure of the forearc high consists of seaward vergent thrust faults in an imbricate stack that serve to uplift the outer arc high. These faults also form the western limb of the forearc basin and are observed as flexural slip faults developed within stratigraphic horizons of the forearc basin stratigraphy.

Figure 11 also reveals that typical structure of the forearc basin is that of a structural basin created by the uplift of the western limb along the outer arc high. Contractional deformation of the basin is limited to the western edge and gives way to undeformed stratigraphy in the basin center and gentle extensional faulting on the landward limb. This general pattern of deformation remains virtually the same throughout the central Cascadia margin. In detail, the axes of the basins are en echelon in map view (Goldfinger and others, 1997; McNeill and others, 2000) and have variable styles of structures linking individual basins (e.g., Yeats and others, 1998).

We map the structural transition from contraction to extension along the Cascadia margin from geologic structure, borehole breakout data, and earthquake focal mechanisms (Figure 12). We used 129 Western Geco multichannel reflection profiles (now available through USGS at http://walrus.wr.usgs.gov/NAMSS/) and mapped in a geographic information system (GIS) the transition from contraction (the direction of which varies from bearings of 060° to 100° based on fold axes) to undeformed or extensional basin strata across the forearc basin. Many profiles exhibited the structural relationships illustrated in Figure 11. Along southern Oregon and Washington, the transition must occur onshore, as structures were contractional up to the landward limit of the reflection data. Evidence of extension of the Washington shelf shown in Figure 12 as a cluster of green symbols is related to shallow listric normal faulting (McNeill and others, 1997) and is probably not relevant to coupling on the megathrust. The structural boundaries mapped with multichannel reflection data showed modest variation with time, suggesting that structures active in the Miocene through present have had a relatively consistent stress relationship. We infer from this that our mapping across this large span of time yields a spatial result that would be similar for other periods of post-Miocene time. We used the youngest structures available, although only approximate temporal control is available from a few test wells (McNeill and others, 2000). Onshore, we supplemented the offshore data with limited evidence from borehole breakouts as indicators of crustal stress (Werner and others, 1991) and from focal mechanisms (Global Centroid Moment Tensor Database; Trehu and others, 2008; Western Geco multichannel reflection profiles, available through USGS at http://walrus.wr.usgs.gov/NAMSS/). Each of these indicators cannot strictly be compared to the others as they represent different physical properties and different time scales. Nevertheless, the combined data are consistent and seem to represent a coherent transition from convergence-related compression to arc-parallel compression that is well known in the Cascadia forearc (Wang and He, 1999).

We note that the precise meaning of the transition line mapped in Figure 12 is not presently known. Although it represents an average structural/stress transition zone over the span of time represented by the data sets used, we cannot assign to it a specific numerical value. We use this mapping only as a general guide, to be considered with other data, to assist in evaluating the downdip and along-strike map pattern of plate coupling in Cascadia. This analysis also assumes that the transition boundary represents long-term features, as it is mostly structurally based, and that these long-lived features are relevant to plate locking, an inference we draw, but also one that requires further study. We are encouraged however that despite these caveats, the stress boundary in Figure 12 is quite compatible with other downdip estimates of coupling based on thermal models (Hyndman and Wang, 1995), leveling data (Mitchell and others, 1994; Schmidt and others, 2007, Burgette and others, 2009), and GPS data (McCaffrey and others, 2007). In particular, the most recent GPS models based on a dense array of campaign data and continuous sites include along-strike variability that closely mirrors that in Figure 12. Also

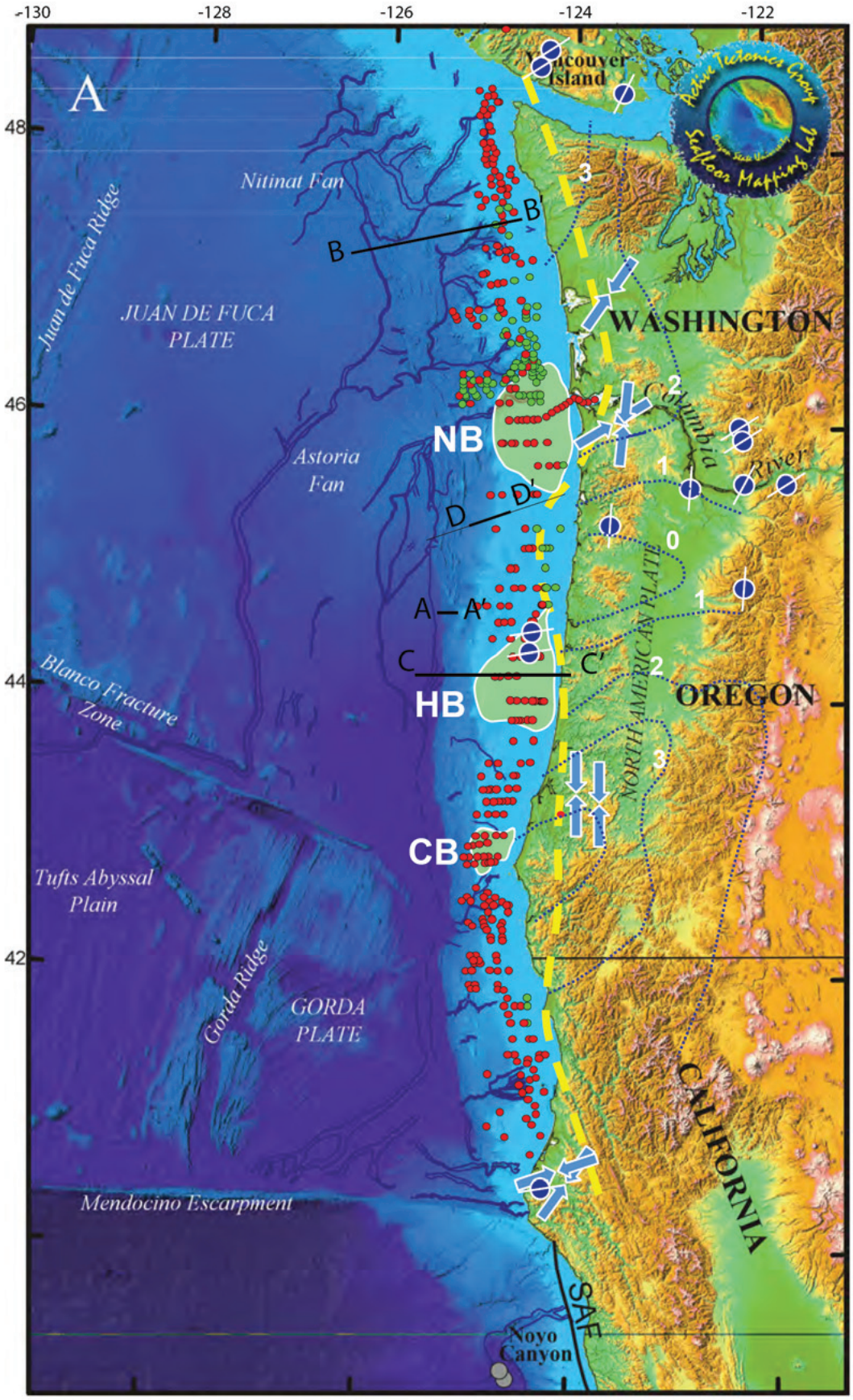

Figure 12. Evidence of extension of the Washington shelf, shown as a cluster of green symbols, is related to shallow listric normal faulting (McNeill and others, 1997) and is probably not relevant to coupling on the megathrust. The structural boundaries mapped with multichannel reflection data showed modest variation with time, suggesting that structures active in the Miocene through present have had a relatively consistent stress relationship. We infer from this that our mapping across this large span of time yields a spatial result that would be similar for other periods of post-Miocene time. We used the youngest structures available, although only approximate temporal control is available from a few test wells (McNeill and others, 2000). Onshore, we supplemented the offshore data with limited evidence from borehole breakouts as indicators of crustal stress (Werner and others, 1991) and from focal mechanisms (Global Centroid Moment Tensor Database; Trehu and others, 2008; and various sources).

compatible with the stress boundary is evidence presented by Mitchell and others (1994), who contoured uplift rates along the Cascadia coast based on repeated leveling surveys. These contours, also shown in Figure 12, suggest an area of low uplift in central-northern Oregon adjacent to a corresponding region where our stress line swings offshore. An ongoing reanalysis of the leveling data (Schmidt and others, 2007) supports the original models of Mitchell and others (1994). An alternative model presented by Hyndman and Wang (1995) uses some of the same data but smooths the uplift variability that we interpret as most likely signal rather than noise. Onshore evidence of coseismic subsidence also suggests a reduced coseismic subsidence from the AD 1700 and three previous earthquakes in this area of central Oregon (Leonard and others, 2004; Nelson and others, 2008).

Finally, we note that the stress boundary shown in Figure 12 suggests that broad regions of the upper plate where the stress line swings landward coincide with major structural uplifts. The central Oregon region where the stress line swings seaward coincides with a deep structural and gravity low (McNeill and others, 2000). In Oregon, the structural uplifts are known as Coquille Bank, Heceta Bank, and Nehalem Bank (Figure 12). These uplifts are known to have been active since the Miocene, with uplift of over 1 km based on biostratigraphic data at Heceta Bank (Kulm and Fowler, 1974). Contractional structures that comprise the banks have greater throw in the banks and reduced throw and more open folding where they are mapped between the banks (Goldfinger and others, 1992, 1997). The present lack of relief between these rapidly deforming regions relative to the slower deforming interbank areas is due to Pleistocene transgressive-regressive erosion. We suggest that the uplifted, highly deformed bank/structural highs outlined by the mapped stress transition line may represent regions of strong coupling averaged over many seismic cycles. The relationship between interplate coupling and structural growth is discussed by Goldfinger and others (1992, 1996, 1997), and thus upper plate structural growth, absent obvious backstop effects, may reflect the strength of interplate coupling. In particular, the Heceta Bank-Nehalem Bank pair bound the region of low uplift onshore and seaward position of the stress line (Figure 12), consistent evidence of a semi-permanent forearc control on plate coupling. Recent results from offshore experiments in Costa Rica suggest that highly stressed regions of the subduction interface, indicated by low *b*-values from onshore-offshore seismic experiments, correlate well to geodetically mapped locked patches (Ghosh and others, 2008). These same areas correspond to free-air gravity highs in the forearc.

The combined evidence of variability of strain along strike spans multiple time ranges from Miocene to Holocene in the case of structural development, spans ~80 years in the case of leveling data, and spans ~12 years for GPS data, yet the map patterns of strain are quite similar, despite the first being permanent and the latter two being elastic. We suggest that the map pattern of inferred higher coupling corresponding to the submarine banks may indicate regions of high slip during subduction earthquakes because the GPS and leveling data suggest greater present interseismic elastic strain that must be released in earthquakes, while the stress line indicates greater long-term strain. We use this conclusion in later sections of this paper, but we also test another proposed model, that the forearc basins are asperities as suggested by Wells and others (2003). These authors argue on the basis of global comparisons of earthquake slip models with gravity data that seismic moment is concentrated beneath forearc basins. While this model appears to work well for several well-known cases such as Nankai and Chile, it failed to predict the Sumatra 2004 distribution of slip or slip distributions of the other largest known earthquakes such as Kamchatka (1952) and Alaska (1964). The basin model proposed by Wells and others (2003) is also incompatible with the structural data outlined above. A related model by Song and Simons (2003) suggests that slip is concentrated in trench-parallel gravity lows, a proposal similar to but distinct from that of Wells and others (2003). Though these models are commonly linked, the Song and Simons model subtracts an average gravity profile and identifies lows from the resulting data, something not done in the Wells and others model. The Song and Simons model also fails to predict slip distributions in Sumatra.

At present, it is not possible to determine which of these models, if any, is operative in Cascadia. Determination of future slip distributions is beyond the cutting edge in subduction zone research at present. However, we presently favor the coseismic slip concentrated under areas of tectonic uplift based on the above discussion and an apparent good performance of these models for match of tsunami inundation to distribution of Cascadia tsunami deposits at Cannon Beach.

SPLAY FAULT

Common along subduction margins with thick incoming sedimentary sections is a major splay fault that separates the active accretionary wedge from an older accretionary complex. The young wedge of Pleistocene age in Cascadia is separated from a Pliocene-Eocene complex by such a fault, similar to the one that has been extensively investigated along the Nankai margin (Figure 13). Along the central Cascadia margin, this fault is well expressed and marks the boundary between the low tapering lower slope wedge and steeper tapering upper slope and shelf accretionary complex (Figures 3, 8, and 14). This fault becomes less distinct to the north on the Washington shelf, where the fault is obscured by extensive listric normal faulting (green dots in Figure 12; McNeill and others, 1997), and to the south where it is similarly obscured by extensive landslide failures (Goldfinger and others, 2000). Along the central Cascadia margin from latitude ~45° N. to 47° N., the splay fault boundary is well expressed and exhibits evidence of a seafloor scarp on OSU line 100, one of the few crossing lines with enough resolution to image the near-surface fault. The fault is well imaged on R/V *Sonne* lines 103 and 108 in on the Washington margin and USGS line 12 (Figure 14; Mann and Snavely, 1984). On a northern Oregon proprietary profile the fault dip can be determined to be ~30°, as the surface map position and the position at which the fault intersects the down-going plate are both imaged. Using

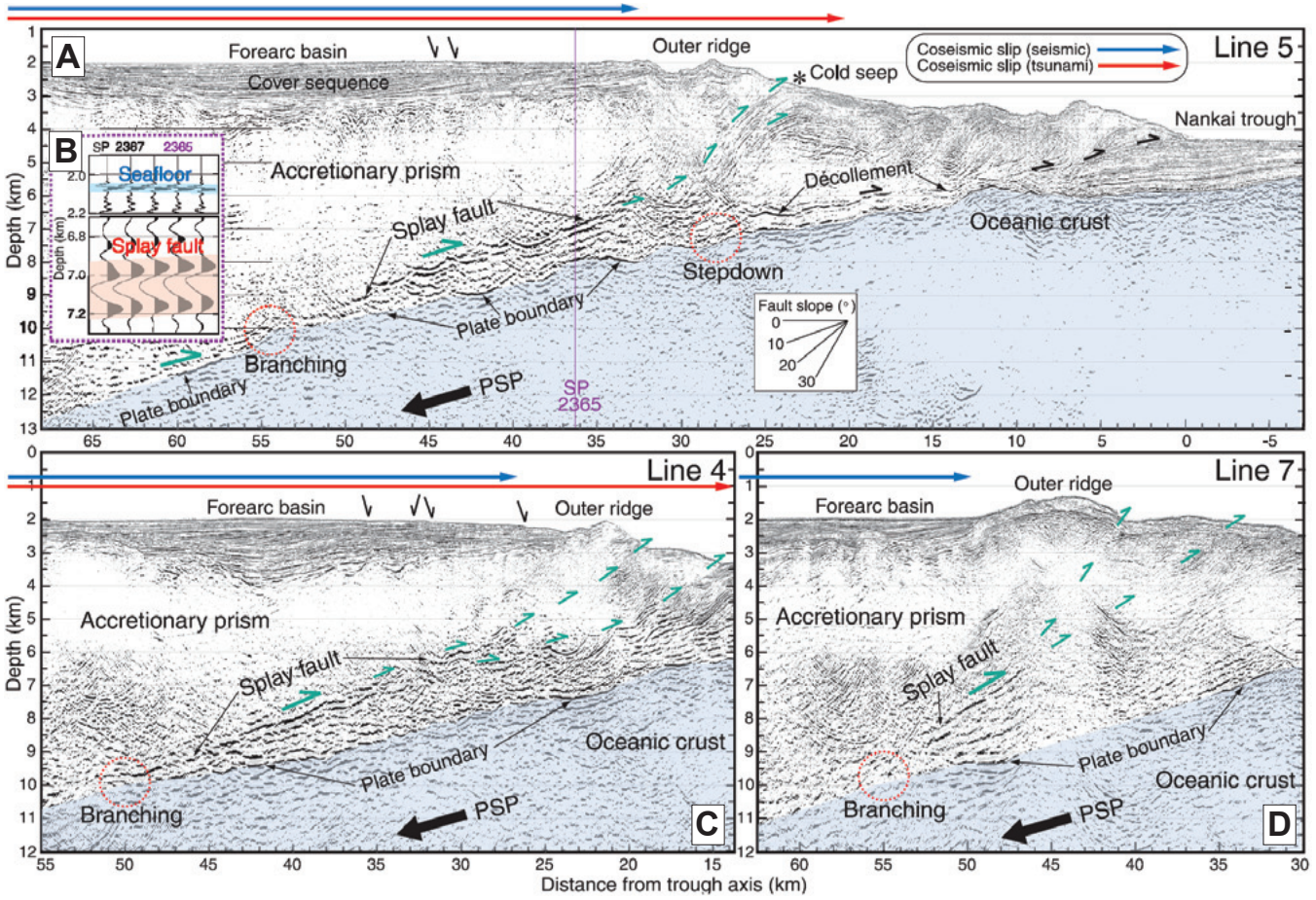

Figure 13. Poststack depth-migrated multichannel seismic (MCS) profiles showing the splay fault off the Kii peninsula, Nankai subduction zone (from Park and others, 2002). The subducting oceanic crust is shaded light blue. The seaward distribution of the 1944 Tonankai coseismic slips estimated from tsunami (red arrows) and seismic (blue arrows) inversions is projected in the profiles. Locations of both the initial branching of the splay fault and the décollement stepdown to the top of the oceanic basement are marked by red dotted circles. Green and black arrows show motions of the splay fault slip and the décollement or normal fault, respectively. Vertical exaggeration is 2×. (A) MCS profile on line 5. (B) Inset of the splay fault at a depth of 7 km, shot point (SP) 2365. The splay fault is also identified on line 7 (D), which is separated from line 4 (C) by an ~80-km distance. PSP is Philippine Sea Plate.

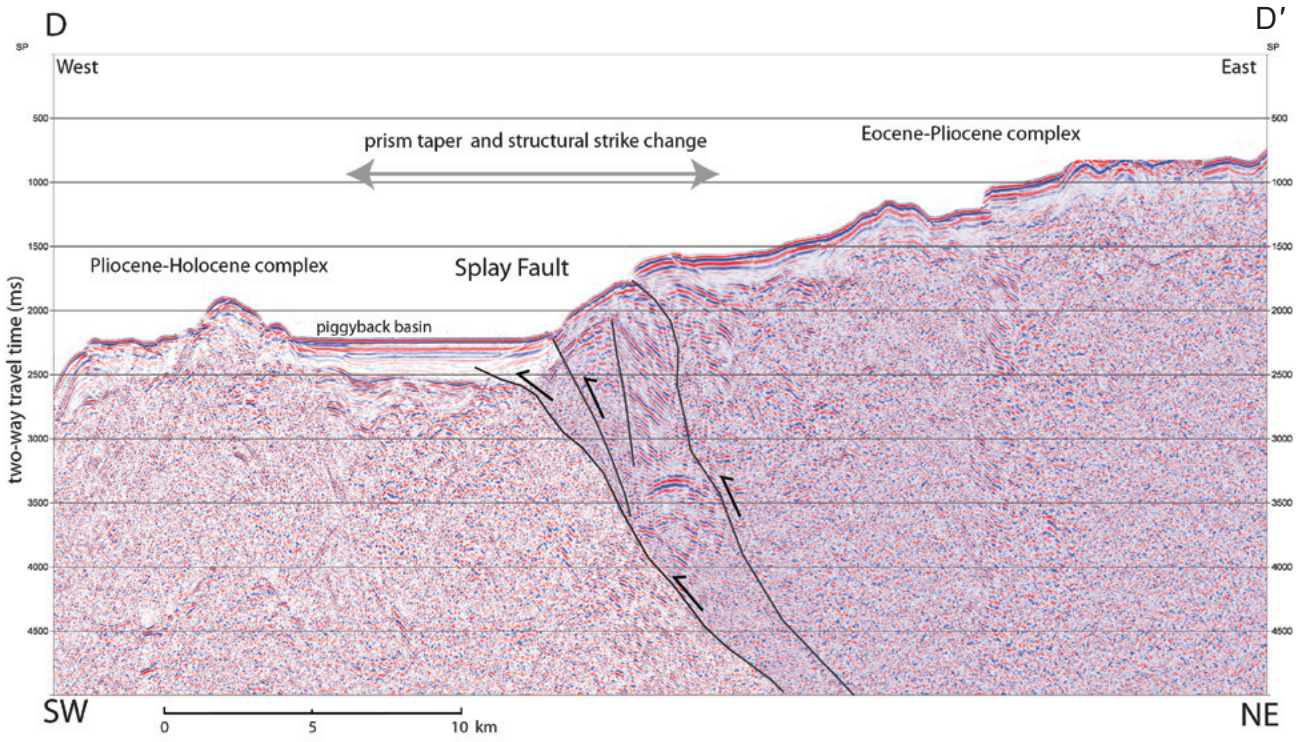

Figure 14. Unmigrated U.S. Geological Survey reflection profile L-5-WO77-12 across the mid slope off north-central Oregon (Mann and Snavely, 1984). Splay fault separating young wedge from older accretionary complex (blue shading) is imaged as a zone with two major traces and active upward branches. Young basin fill is deformed by the upward branching fault, and the upper trace breaks the seafloor at this location. The lower slope is characterized by a more open fold style and landward vergence as discussed in the text (Downdip Limit of Interplate Coupling section) with respect to interplate coupling. See Figures 8 and 12 for location.

the slab contours of McCrory and others (2004) to fix the depth of the slab, the approximate average dip can be determined. On R/V *Sonne* lines 103 and 108 the approximate dip can also be determined as these lines have been processed with prestack depth migration and thus have depth scales rather than two-way travel time scales (Adam and others, 2004). The 30° dip is also consistent with these depth-migrated lines. The splay fault is well imaged in bathymetry as well, appearing as irregular surface scarps in shaded relief bathymetric data (Figure 8). Some profile crossings such as that of Figure 14 suggest recent seafloor offset, and thus recent fault activity. The fault marks not only a bathymetric break on the continental slope but also a map view boundary between fold and fault trends of different orientations previously discussed (Figure 8).

Given the evidence for recent movement, the clear domain boundary between older and younger accretionary complexes, and the structural indications of a significant difference in deformation style, we infer that the Cascadia splay fault is a significant structure capable of diverting slip from the décollement to the surface as has been suggested for the Nankai margin. This makes it potentially significant in tsunami modeling scenarios that include significant slip. We use a generalized fault deformation model of this fault (Figure 3) to explore the effect on tsunami runup and inundation.

Fault Deformation Modeling

Because of a lack of direct observations of coseismic seafloor deformation associated with a great Cascadia megathrust earthquake, deformation scenarios are developed from our current knowledge of the seismogenic behavior of the Cascadia subduction zone and other subduction zones that have experienced great earthquakes. Three types of information contribute to the construction of the rupture and deformation scenarios considered in this investigation.

- Geological structural information. This includes the plate convergence direction and rate from Wang and others (2003), geometry of the Cascadia megathrust, the master splay fault, and width

of the coupled plate interface. Geometry of the megathrust is taken from McCrory and others (2004). Geometry of the splay fault is from interpretation of the previously explained geologic and geophysical data. Slip direction of the coseismic rupture is assumed to be exactly opposite plate convergence between the Juan de Fuca plate and the forearc block after removal of forearc rotation. Slip magnitude and direction take into account oblique convergence and resulting forearc deformation as determined by Wang and others (2003). The resulting convergence rate at the latitude of Cannon Beach is 28.9 mm/yr.

- Paleoseismic data, primarily the offshore turbidite record as proxy for earthquake recurrence, rupture length, and slip (Goldfinger and others, 2003a, 2008, 2009; Table 1); coseismic paleosubsidence data associated with the 1700 Cascadia earthquake as compiled by Leonard and others (2004) and Nelson and others (2008); and information deduced from Japanese historical records of the 1700 Cascadia earthquake and tsunami (Satake and others, 2003) help constrain coseismic slip for a typical magnitude ~9 event.
- Knowledge and hypotheses based on the studies of megathrust earthquakes in other subduction zones. Examples include the possible involvement of coseismic splay faulting that enhances tsunami generation (Plafker, 1972; Park and others, 2002), a reported correlation between the locations of the seismogenic zone and forearc basins (Wells and others, 2003), coseismic slip concentrated in the landward part of the forearc high (Goldfinger and others, 2007a), coseismic slip concentrated under offshore banks (discussions above), and aseismic behavior of the most seaward segment of the megathrust (e.g., Wang and Hu, 2006; Wang and He, 2008; discussion above). Published coseismic slip patterns of the 2004 and 2005 Sumatra earthquakes (e.g., Chlieh and others, 2007; Hsu and others, 2006; Subarya and others, 2006) provide references that serve to validate some of the assumed Cascadia rupture models.

These source parameters informed construction of a logic tree used to explore variation in coseismic deformation and consequent Cascadia tsunami impact to Cannon Beach. All simulations of surface deformation from fault rupture scenarios employ the point source solution from the Okada (1985) dislocation model and emulate coseismic deformation between latitude 43.9° N on the central Oregon coast near Florence to Neah Bay at ~47.9° N on the Washington coast (dashed line in Figure 1). All fault ruptures are simulated using the slip function of Wang and He (2008) modified from Freund and Barnett (1976). Fundamental to the Wang and He approach is recognition that the seismogenic zone of subduction faults has an updip limit, seaward of which the fault exhibits velocity-strengthening behavior, supported by observed and inferred coseismic seafloor deformation of great subduction zone earthquakes, particularly that associated with the 2004 and 2005 Sumatra events. This recognition makes slip patches like those used in the TPSW (2006) study as well as geodetic models such as McCaffrey and others (2007) and Burgette and others (2009) that place large amounts of slip near the deformation front much less likely scenarios. These models were stochastic (TPSW, 2006) or based on onshore geodesy (McCaffrey and others [2007]; Burgette and others [2009]), neither technique is sensitive to the behavior of the seaward part of the accretionary prism. All rupture simulations in this investigation incorporate coseismic slip tapering to zero at the deformation front, albeit one set of simulations incorporates moderate seaward skew of slip (q = 0.3). Another implication of the Wang and He model is that coseismic horizontal compression above the updip limit of the seismogenic zone can activate splay faults (Wang and Hu, 2006); hence, we incorporate splay faulting and assume that the tendency to partition slip to a splay fault increases with increased slip (moment).

In a real megathrust earthquake, the slip varies tremendously along strike giving rise to the concept of asperities. Because we cannot predict where the maximum slip will occur along strike, we use a "regional slip patch" model to approximate a generic representation of along strike slip behavior. The downdip boundary of the regional slip patch was constrained by both the previously discussed "stress boundary" and by a best fit to available coseismic subsidence data of Leonard and others (2004). Local slip patches are assumed to be at either basins or banks and are simulated by quadratically scaling maximum slip with downdip patch width. Each assumed slip distribution on the megathrust for splay fault models is simply cut off at the surface trace of the splay fault. Appendix A summarizes details of the approach and map boundaries of simulated geological structures

Logic Tree Evaluation of Cascadia Earthquake Source Parameters

The parametric analysis of tsunami sources was guided by a logic tree with branches arranged from most to least important controls on vertical coseismic deformation for Cascadia earthquakes (Figure 15). The four earthquake source parameters chosen, from most to least important, are relative earthquake size (coseismic slip), the presence or absence of a splay fault, fault rupture extent (regional rupture or local basin/bank rupture), and slip distribution (symmetrical within banks or basins and symmetrical or seaward skewed within regional slip patches). Weighting factors were assigned by the authors to each branch of the logic tree based on consensus and observational geologic data at Cascadia and other analogous subduction zones. Therefore, weights represent the relative confidence or preference of the authors related to alternative source parameters. The weights do not reflect the temporal probability of the next tsunami. Table 3 is a summary of the weighting factors assigned to the various parameters used to characterize the source scenarios. Figure 16 illustrates map views of the eight coseismic deformation scenarios for slip equaling 525 years of plate convergence (the "Average" scenarios in the logic tree). Figure 16 also illustrates location of the modeled splay fault relative to the coseismic deformation. Figure 12 illustrates the location of the "stress line" used as a critical constraint on the downdip limit of rupture for the regional slip patch scenarios. The downdip limit for regional slip patches was also adjusted to achieve a best match to paleosubsidence patterns of the AD 1700 Cascadia earthquake from Leonard and others (2004; see Appendix A). Implicit in this is the assumption that slip patterns are relatively long-lived features of the megathrust at the time scale of interest here, the Holocene.

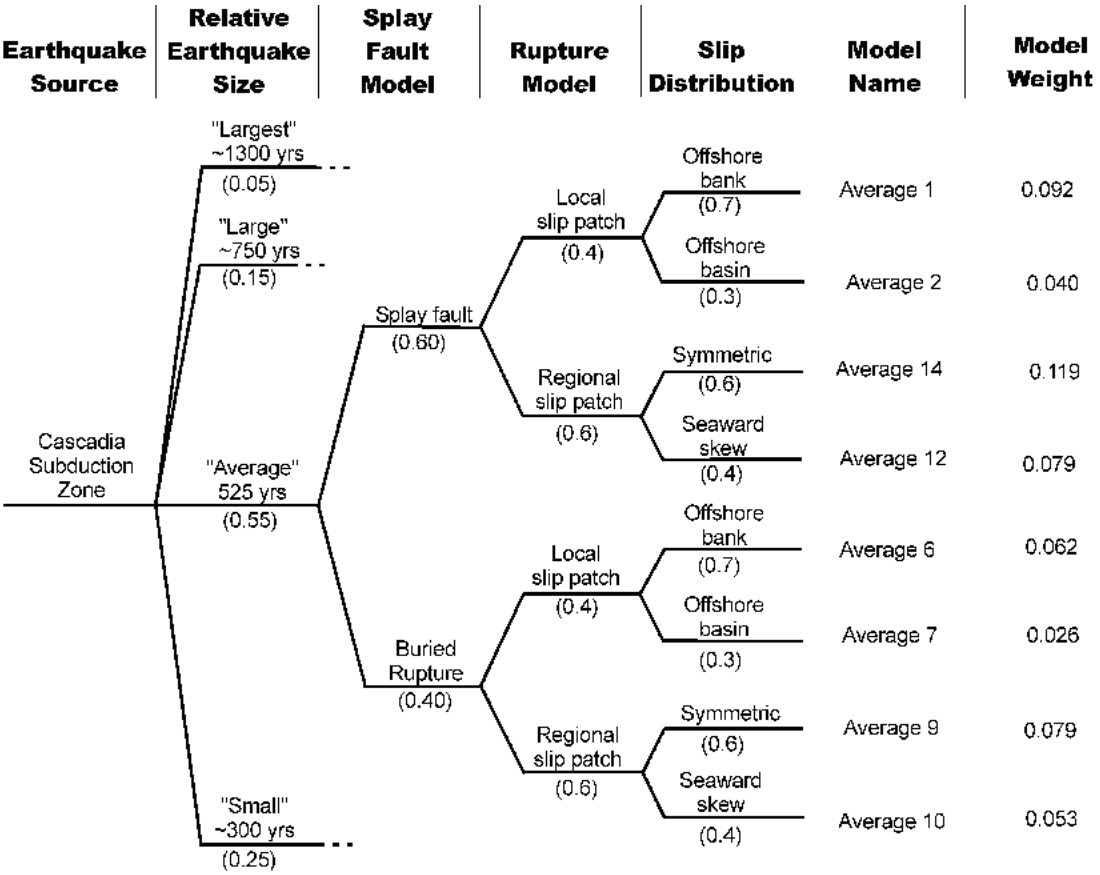

Figure 15. Logic tree for "Average" source scenarios and trunk branches of "Small," "Large," and "Largest" scenarios for Cascadia tsunami simulations. See the text for detailed summaries of the weighting factors (numbers in parentheses) for all branches.

EARTHQUAKE SIZE AND COSEISMIC SLIP

The first branch of the logic tree evaluates the relative size of a Cascadia subduction zone earthquake as a function of slip on the megathrust. Moment magnitudes for each fault slip are listed in Table 3 but are somewhat difficult to determine, as the calculation requires specification of rupture length beyond the boundaries of the modeled portion of the subduction zone (Figure 1). Magnitudes for regional slip patches are based on extrapolation to the entire length of the Cascadia subduction zone. Magnitudes for local slip patches assume a rupture length limited by the source domain boundary (Figure 1), because local slip patches outside of the domain boundary have not as yet been specified.

Tsunami energy is directional away from the long axis of subduction zone ruptures (Titov and others, 1999), so fault length is not usually a significant factor in estimation of local tsunami impact and plays no part

Table 3. Earthquake source parameters and weighting factors used in logic tree for Cascadia tsunami sources (Figure 15).

Rupture Scenario	Slip (m)	M_w	Splay Fault/ Buried Rupture	Rupture Model	Slip Distribution	Total Weight Factor
Largest 1 (0.05)	~38	~8.8	splay (0.8)	local (0.4)	offshore bank (0.7)	0.011
Largest 2 (0.05)	~38	~8.8	splay (0.8)	local (0.4)	offshore basin (0.3)	0.005
Largest 14 (0.05)	~38	~9.2	splay (0.8)	regional (0.6)	symmetric (0.6)	0.014
Largest 12 (0.05)	~38	~9.2	splay (0.8)	regional (0.6)	seaward skew (0.4)	0.010
Largest 6 (0.05)	~38	8.8	buried rupture (0.2)	local (0.4)	offshore bank (0.7)	0.003
Largest 7 (0.05)	~38	8.8	buried rupture (0.2)	local (0.4)	offshore basin (0.3)	0.001
Largest 9 (0.05)	~38	9.3	buried rupture (0.2)	regional (0.6)	symmetric (0.6)	0.004
Largest 10 (0.05)	~38	9.3	buried rupture (0.2)	regional (0.6)	seaward skew (0.4)	0.002
Large 1 (0.15)	~22	~8.6	splay (0.8)	local (0.4)	offshore bank (0.7)	0.034
Large 2 (0.15)	~22	~8.6	splay (0.8)	local (0.4)	offshore basin (0.3)	0.014
Large 14 (0.15)	~22	~9.1	splay (0.8)	regional (0.6)	symmetric (0.6)	0.043
Large 12 (0.15)	~22	~9.1	splay (0.8)	regional (0.6)	seaward skew (0.4)	0.029
Large 6 (0.15)	~22	8.6	buried rupture (0.2)	local (0.4)	offshore bank (0.7)	0.008
Large 7 (0.15)	~22	8.6	buried rupture (0.2)	local (0.4)	offshore basin (0.3)	0.004
Large 9 (0.15)	~22	9.1	buried rupture (0.2)	regional (0.6)	symmetric (0.6)	0.011
Large 10 (0.15)	~22	9.1	buried rupture (0.2)	regional (0.6)	seaward skew (0.4)	0.007
Average 1 (0.55)	~15	~8.5	splay (0.6)	local (0.4)	offshore bank (0.7)	0.092
Average 2 (0.55)	~15	~8.5	splay (0.6)	local (0.4)	offshore basin (0.3)	0.040
Average 14 (0.55)	~15	~9.0	splay (0.6)	regional (0.6)	symmetric (0.6)	0.119
Average 12 (0.55)	~15	~9.0	splay (0.6)	regional (0.6)	seaward skew (0.4)	0.079
Average 6 (0.55)	~15	8.5	buried rupture (0.4)	local (0.4)	offshore bank (0.7)	0.062
Average 7 (0.55)	~15	8.5	buried rupture (0.4)	local (0.4)	offshore basin (0.3)	0.026
Average 9 (0.55)	~15	9.0	buried rupture (0.4)	regional (0.6)	symmetric (0.6)	0.079
Average 10 (0.55)	~15	9.0	buried rupture (0.4)	regional (0.6)	seaward skew (0.4)	0.053
Small 1 (0.25)	~8	~8.3	splay (0.2)	local (0.4)	offshore bank (0.7)	0.000 [0.014]*
Small 2 (0.25)	~8	~8.3	splay (0.2)	local (0.4)	offshore basin (0.3)	0.000 [0.006]*
Small 14 (0.25)	~8	~8.9	splay (0.2)	regional (0.6)	symmetric (0.6)	0.000 [0.018]*
Small 12 (0.25)	~8	~8.9	splay (0.2)	regional (0.6)	seaward skew (0.4)	0.000 [0.012]*
Small 6 (0.25)	~8	8.3	buried rupture (0.8)	local (0.4)	offshore bank (0.7)	0.000 [0.056]*
Small 7 (0.25)	~8	8.3	buried rupture (0.8)	local (0.4)	offshore basin (0.3)	0.000 [0.024]*
Small 9 (0.25)	~8	8.9	buried rupture (0.8)	regional (0.6)	symmetric (0.6)	0.250 [0.072]*
Small 10 (0.25)	~8	8.9	buried rupture (0.8)	regional (0.6)	seaward skew (0.4)	0.000 [0.048]*

Slip listed in the table is maximum slip for each slip distribution and is estimated for the latitude of Cannon Beach. Slip at other latitudes is calculated in the fault deformation models from estimates of plate convergence rate using a Euler pole from Wang and others (2003) and the recurrence times listed in Figure 15. Convergence rate used to estimate slip at Cannon Beach is 28.9 mm/yr. Symbol ~ with M_w values means estimated rather than calculated based on similarity of slip amount between splay fault and buried rupture sources.

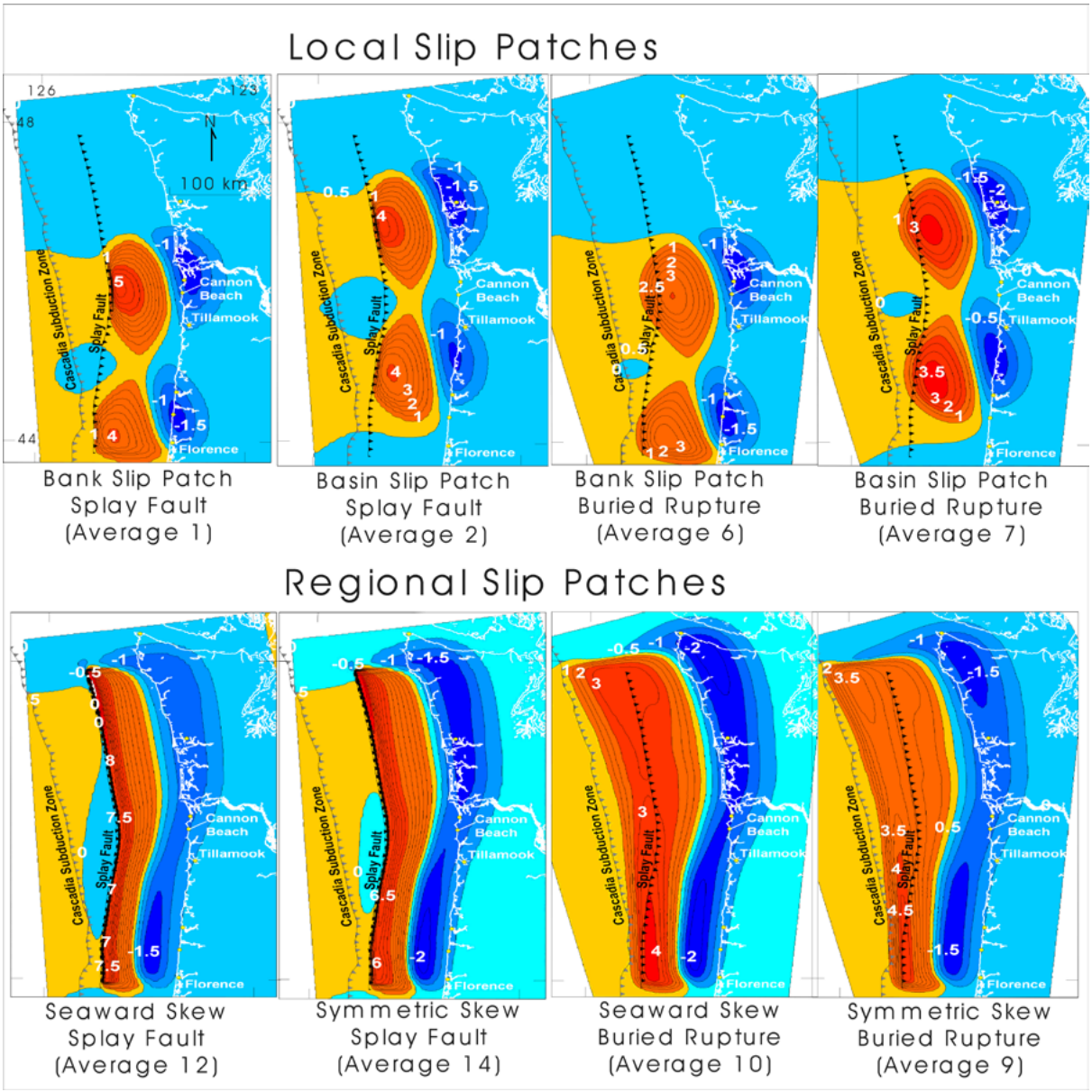

Figure 16. Vertical coseismic deformation patterns for release of 525 years of convergence on the Cascadia subduction zone. White numbers are deformation in meters: positive is uplift; negative is subsidence; contours are at 0.5 m. Bank slip patch models place slip under submarine banks; basin models under submarine basins; slip is quadratically scaled to the width of the basin or bank. Regional slip patch models place slip west of the "stress line" in Figure 12 in either a symmetric (q = 0.5) or seaward-skewed (q = 0.3) distribution. Splay fault scenarios truncate the slip distribution at the splay fault, amplifying uplift from an increase of fault dip to 30°.

in the logic tree. The four alternatives considered for the basal branch include the following earthquake scenarios and corresponding coseismic slip at the latitude of Cannon Beach: The "largest" earthquakes with ~38 m of slip (~1,300 years of plate convergence), "large" earthquakes with ~22 m of slip (~750 years of plate convergence), "average" earthquakes with ~15 m of slip (525 years of plate convergence), and "small" earthquakes with ~8 m of slip (~300 years of plate convergence). Earthquake size was inferred on the basis of correlations between turbidite mass and time intervals between turbidites from data available in 2007. Table 1 is a 2009 update of that data, but, regardless of the data set used, scenario recurrence and slip remain close to 2007 estimates used in our model runs (see Uncertainties section). Coseismic slip amounts were calculated from mean following times in the 2007 data for events assigned to each size category. As previously explained, slip varied by latitude, taking into account the pole of rotation between the plates and internal deformation of the North American Plate. Table 4 lists scenario slips at the latitude of Cannon Beach and demonstrates that the 2007 slip scenarios and logic tree weights are unchanged or well within uncertainties of the 2009 follow time data. (We note that using pre-event intervals would not change the slip data or size bins because the interevent time population remains the same).

Each scenario is assigned a weight according to the number of earthquakes of a particular size that are recorded in the 9,850-year record of ~20 Cascadia turbidites triggered by past great earthquakes. For example, we assigned a weight of 0.05 to the "largest" scenario because one of the ~20 events in Cascadia turbidite record exhibited an exceptionally long following time of ~1,300 years in an analysis of the data available in 2007. Further analysis in 2009 reduced the longest interval to ~850 years for all 20 events (Table 1). When considering only the 19 margin-wide events (excluding T5b), the longest interval is ~980 years with a range of ~660 to 1,290 years at 2σ error (rounded from the interval between T5 and T6 in Table 1). The presence or absence of T5b at the latitude of Cannon Beach strongly influences the time-based maximum slip, reducing the T5-T6 interval of ~980 years to ~530 years. However this illustrates the uncertainties in the time based model, as T5b was not large enough to be recorded as a tsunami or coastal subsidence, and therefore probably played a minor role in strain accumulation during

Table 4. Four scenario time intervals and resulting coseismic slips and logic tree weights used in 2007 compared to similar data from 2009 follow time data of Table 1.

	Qualitative Size Category	Largest*	Large	Average	Small
2007 (used)	Time interval (yr)	1298	748	525	290
	Coseismic slip (m)	37.5	21.6	15.2	8.4
	Logic tree weight (percent)	5	15	55	25
2009	Follow times (percent)	5	15	55	25
	Post-event time interval range (yr) with 2σ error	660–1287	377–1186	118–993	0–699
	Mean post-event time interval (yr)	983	749	525	243
	Coseismic slip range estimate (m) with 2σ error	19.1–37.2	10.9–34.3	3.4–28.7	0–20.2
	Mean coseismic slip estimate (m)	28.4	21.6	15.2	7.0

Table demonstrates that 2007 slips fall well within the uncertainties of 2009 estimates of slip. Ranges of 2009 interturbidite time intervals and equivalent coseismic slips are calculated at the extreme ranges of 2σ error listed in Table 1. Numbers of follow times assigned to each qualitative size category are based on these assignments in Table 1. Follow times were used as proxies for coseismic slips instead of preceding times, because Goldfinger and others (in review) found a better correlation to turbidite size; nevertheless, preceding times are essentially the same as follow times (Table 1) so there would be little difference which are used. Slips are calculated assuming a plate convergence rate of 28.9 mm/yr and coupling ratio of 1.0. Note: For more precise comparisons, slip is listed to 0.1 m and time to 1 year but values are rounded to 1 m and 10 years in the text and summary tables.

* Calculation of time intervals and slips for the "Largest" category for 2009 data uses only the 19 margin-wide turbidite events (i.e., excludes the small turbidite T5b).

the T5-T6 interval, yet it has a disproportionate effect on our time-based maximum slip model. As explained below (Uncertainties and Paleotsunami Deposits sections), comparison of simulated inundation to distribution of Cascadia tsunami deposits demonstrated that inclusion of all small volume turbidites probably causes underestimation of coseismic slip. Therefore, we retain ~1,300 years for calculation of the largest slip in order to err on the side of caution consistent with standard engineering practice and to implicitly recognize our uncertainties about the influence of smaller events like T5b and others on potential coseismic slip. Weights for the other scenarios were calculated as follows: 3 of 20 events were "large" events assigned a weight of 0.15; 11 out of 20 were moderate in size, or "average" events assigned a weight of 0.55; and 5 of 20 were considered "small" events and weighted at 0.25 (Table 4).

SLIP PARTITIONED TO A SPLAY FAULT

The second branch of the logic tree evaluates the possibility that rupture of the Cascadia plate interface is partitioned to a splay fault, which directs the rupture to the surface and results in significantly higher seafloor uplift. As explained above, the splay fault dips landward about 30° and follows the slope break. Weighting factors assigned in this branch reflect greater likelihood that larger slip events will trigger coseismic slip on a splay fault. For the "largest" and "large" scenarios the ratio of weights assigned to splay fault versus buried rupture events is 0.8:0.2. For "average" scenarios the ratio is 0.6:0.4. For "small" events the ratio is the opposite of that used for the largest scenarios, or 0.2:0.8. Therefore, splay fault scenarios have the largest logic tree weights within each slip category except for "small" slip (Table 3). Another consequence is that splay fault scenario Average 14 has the largest logic tree weight of any scenario and is thus the "preferred" event (Table 3).

The weighting factors are based on the hypothesis that smaller slip events on the megathrust are less likely to ramp upward to the surface on a splay fault than larger events owing to less horizontal compression inherent to velocity strengthening assumption of the Wang and He (2008) model. Observational data supporting this hypothesis are meager. Clarke and Carver (1992) found that probable splay faults from the southern Cascadia megathrust had three offsets of 5 to 7 m each and likely accompanied Cascadia earthquakes with magnitudes of 8.4 or greater, but they also suggested that this thrusting did not occur on every megathrust event. The largest mapped reverse fault during the M_w 9.2 (~20 m slip) Alaskan earthquake in 1964 had at least 8 m of dip-slip (Plafker, 1972) and may have had vertical displacement exceeding 10 m in a submarine extension of the fault (Plafker, 1965). Cummins and others (2001) noted that vertical displacements inferred from tsunami inversions of Nankai subduction zone earthquakes with just a few meters of displacement may be explained by splay faulting 100 km landward of the trench; however, they also speculated that the splays may not break the surface of the accretionary wedge. Sibuet and others (2007) hypothesized that splay faulting from the megathrust may have played a role in the 2004 Sumatran earthquake, but Fisher and others (2007) explained much of the thrust faulting in terms of a duplex structure consisting of roof thrusts in young accreted sediment above a stronger backstop of older material.

RUPTURE MODEL

Two rupture models are considered in the third branch of the logic tree, (1) a single regional slip patch that ruptures the entire modeled length of the megathrust, and (2) local slip patches associated with upper-plate structures in the Cascadia forearc. The regional rupture model was assigned a higher weight (0.6) than local ruptures (0.4) localized at either submarine banks or basins, because (1) the trench-parallel length of local slip patches is highly uncertain, whereas the regional model places slip along the entire margin and thus substantially includes all local slip patches; and (2) the landward extent of the regional rupture is approximately limited to the "stress line" where upper plate stress changes from compression to tension, as well as observing thermal limits, whereas local basin or bank ruptures are defined by the extents of banks or basins and associated gravity anomalies. The "stress line" is probably a somewhat better geologic basis for estimation of the downdip limit of the rupture (interseismic locked zone) and is in reasonable agreement with GPS and leveling based models.

SLIP DISTRIBUTION

The fourth branch of the logic tree considers two parameters for distribution of slip: location in a local basin, local bank or regional slip patch, and amount of seaward skew of slip from a symmetrical, bell shape. We used the following rationale to assign weighting factors to local slip patches located beneath two fundamentally different forearc structures: submarine banks versus submarine basins. We assigned a higher weight (0.7) to slip patches concentrating slip at submarine banks because mapped structures within the banks are contractional, indicating greater strain accumulation possibly linked to strong coupling on the locked zone beneath the banks. This assignment is based on the assessment of independent lines of evidence for stress heterogeneity in Cascadia and is guided by results from Sumatra as discussed in previous sections. In our study, we are most interested in local areas of high slip where tsunamis will be generated as opposed to broad regions that cumulatively may have high moment release; thus we weight potential high-slip areas independently of models that propose mechanisms for regions of high moment release.

The hypothesis that local slip patches concentrate slip below submarine basins was assigned a weight of 0.3. This alternative model is considered because of global correlations between regions of high moment release and offshore gravity lows attributed to forearc basins (Wells and others, 2003). As explained previously, submarine basins in the Cascadia forearc have extensional faulting on the landward limb of each basin suggestive of low rather than high plate coupling; hence, the lower weight for the basin slip patch model. The 0.7:0.3 weight ratio for these two models reflects the majority view of the author team. A minority view was to assign a ratio of 0.5:0.5. Slip was quadratically scaled to the width of the basin or bank, achieving essentially a symmetrical taper of slip scaled to the geometry of the geologic feature rather than the "stress line" considered for the regional rupture.

Also considered in the fourth branch of the logic tree are two alternative downdip distributions for slip on regional ruptures. A symmetric slip function (q = 0.5) of the distribution calculation of Wang and He (2008) based on Freund and Barnett (1976) and a seaward skew (q = 0.3). Coastal subsidence predicted by the seaward skewed slip distribution is systematically less than that predicted by symmetric slip on the same fault patch (for further discussion, see Appendix A). The symmetric slip distribution was judged somewhat more likely than the seaward skewed slip, because the skewed distribution results in poorer fit to coastal paleosubsidence data of Leonard and others (2004) for the 1700 AD Cascadia event (Appendix A). The ratio of symmetric to seaward skew weights is thus 0.6:0.4.

Distant Tsunami Sources

We investigated two distant tsunami scenarios in order to simulate the largest historical event and a hypothetical maximum considered event; both tsunamis are triggered by M_w ~9.2 earthquakes in the Gulf of Alaska (Figures 16 and 17). The vertical deformation inferred by Johnson and others (1996) from a tsunami inversion provided the initial condition for simulation of the largest historical event, the 1964 Prince William Sound earthquake (Figure 17). The hypothetical source of the TPSW (2006) causing the largest distant tsunami at Seaside, Oregon (their source 3) was used as an approximate maximum considered event (Figure 18). This source has four segments with 15, 20, 25 and 30 m of slip (see TPSW's Table 6, p. 41) and maximum uplift over twice as high as that inferred for the 1964 earthquake (Figures 17 and 18). This large uplift is in a relatively narrow "spike" near the surface trace of the fault and is caused by a singularity in the Okada (1985) uniform slip model (Titov, 2008, personal communication). The "spike" has little effect on the resulting tsunami relative to the broader area of 3-5 m uplift to the northwest (Titov, 2008, personal communication). TPSW (2006) demonstrated that the larger size of this tsunami relative to the 1964 event is caused by better directivity to the northern Oregon coast.

Hydrodynamic Tsunami Modeling

Vertical components of deformation from selected Cascadia and the two Alaska earthquake sources provided the initial conditions for final tsunami simulations. Fifty-five simulations were completed for the final exercise but ~250 earlier simulations provided information on sensitivity to numerical grid spacing and source characteristics. All simulations assumed an instantaneous static deformation as the initial condition. The finite element model SELFE (Zhang and Bap-

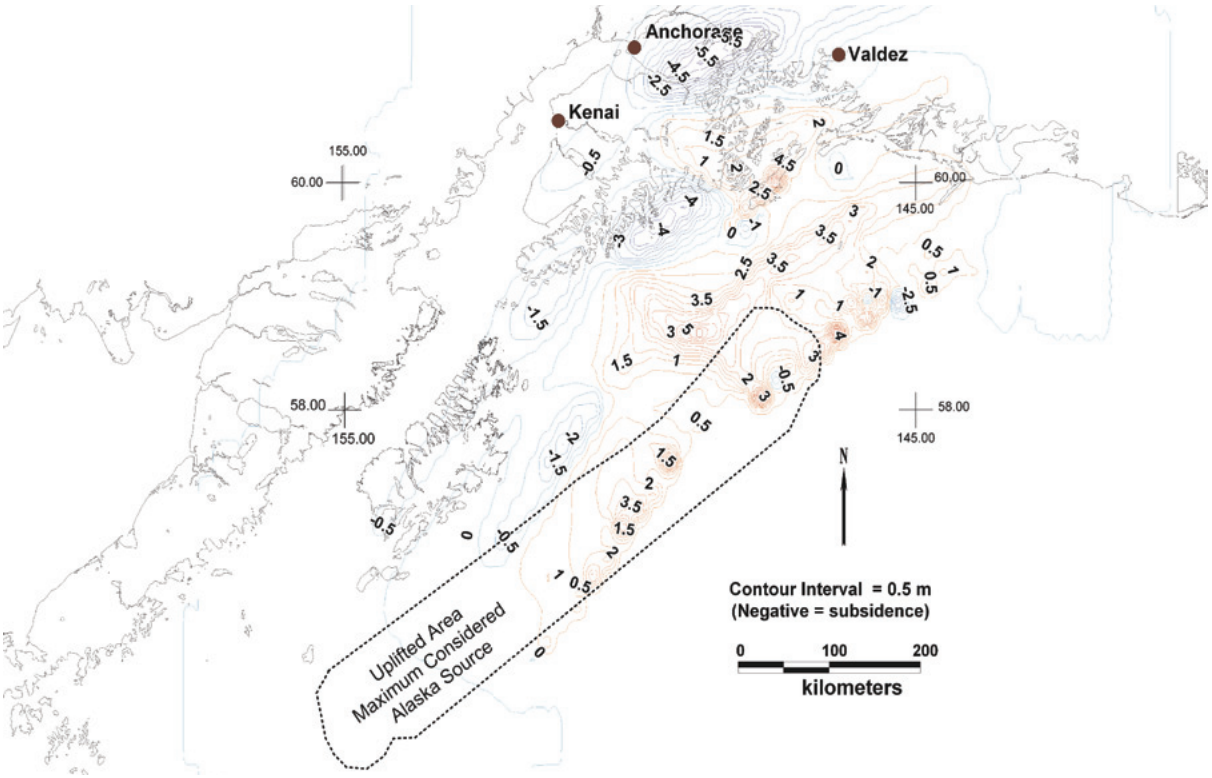

Figure 17. Coseismic deformation from the 1964 Prince William Sound earthquake from Johnson and others (1996); blue isolines with negative values indicate coseismic subsidence; red isolines indicate coseismic uplift. Shown for comparison is the area of uplift from the theoretical maximum considered distant tsunami source of Figure 18.

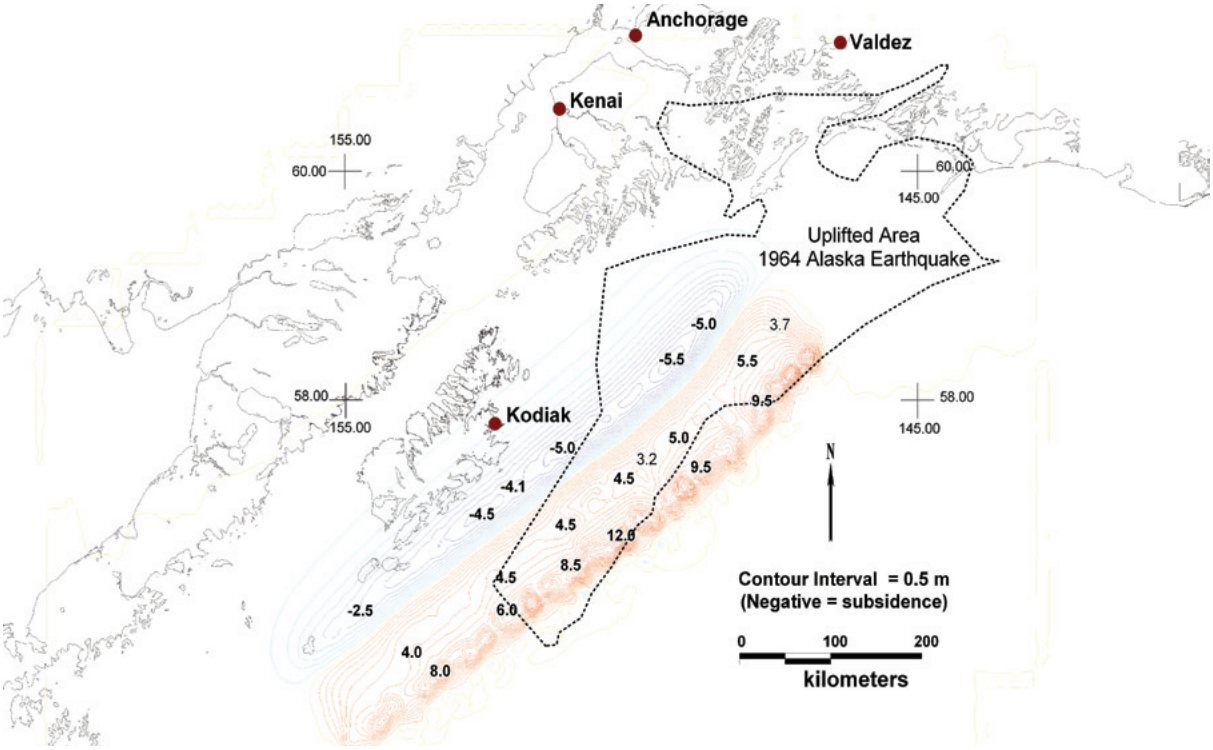

Figure 18. Maximum considered distant tsunami source from the Tsunami Pilot Study Working Group (TPSW, 2006) analysis for Seaside, Oregon; blue isolines with negative values indicate coseismic subsidence; red isolines indicate coseismic uplift. Shown for comparison is the area of uplift from the 1964 M_w 9.2 earthquake.

tista, 2008) simulated propagation and inundation with an unstructured numerical grid using post-earthquake topography. Grid spacing for simulation of local Cascadia sources varied from 200 m at the source to 2.2 m in parts of Cannon Beach with detailed topographic data (Figures 19 and 20). Deep ocean propagation of the distant tsunamis used grid spacing on the order of ~11 km. Each Cascadia simulation was run for at least two hours of "tsunami time." Some simulations were run longer (up to 8 hours of "tsunami time") in order to check the importance of inundation from later refracted waves and to accommodate propagation from the two distant tsunami sources in Alaska. An 8-hour simulation of a Cascadia source revealed that wave height decreased significantly after 2 hours, so later arriving waves were smaller and did not "stack" in lowlands (Ecola Creek).

Tides

Tidal effects can be an important factor in simulation of inundation (Myers and Baptista, 2001). All simulations in this investigation were run at 2.711 m above geodetic mean sea level NAVD 1988 based on mean higher high water (MHHW) at the Astoria, Oregon, tide gauge. Neglecting nonlinear effects, TPSW (2006) did a probabilistic analysis of tides for Seaside, Oregon, and concluded that the effect of tides for a 500-year Cascadia tsunami decreased open coastal runup by 0.7 m from their assumption of tide at mean high water. Our assumption of MHHW for the Cascadia tsunami simulations is therefore conservative.

With regard to simulation of the distant tsunami from Alaska, no local tide gauge data are available to compare how closely the assumption of MHHW is to the actual tide on March 28, 1964. The peak of the tsunami arrived at Neah Bay, Washington, at 7:28 AM GMT and at 8:48 AM GMT at Crescent City, California, (tide gauge data from NOAA West Coast and Alaska Tsunami Warning Center website, http://wcatwc.arh.noaa.gov/). Cannon Beach is 38 percent of the distance between Neah Bay and Crescent City, so arrival was probably close to 8:00 AM GMT. Our simulation predicts arrival in 4 hours 4 minutes (7:39 AM) for an initial 5-m wave followed 6 minutes later by a 6-m wave. Tide at the nearest tide gauge at Garibaldi, Oregon, was ~0.9 m above local mean sea level at these two times, corresponding to 0.3 m lower than the MHHW of the simulation. According to tide gauge data at Garibaldi, the Alaska wave arrived about one hour before the high tide. Myers (1999) found that such flood tides could amplify locally generated tsunamis beyond simple addition of the tidal elevation to the tsunami elevation. Using the 1964 Alaska tsunami as an example, Myers and Baptista (2001) demonstrated these nonlinear effects decrease with distance from the source. It is likely that there was some nonlinear amplification of the Alaska tsunami by the flood tide, but determining whether MHHW (0.3-m higher than in 1964) approximates it requires a simulation with dynamic effect of tide. This exercise was beyond the scope of the investigation.

Comparison of Simulated Tsunami to Observations

Distribution of three prehistoric (paleotsunami) deposits and observations of historic tsunami inundation from Witter (2008) served as ground truth checks of the tsunami modeling approach. Inland reach of paleotsunami deposits marks the minimum inundation of tsunamis. Match of simulated inundation, runup, and flow depths to observations of the tsunami from the 1964 Prince William Sound earthquake tested accuracy of the hydrodynamic model and inputs. Tsunami simulations used as inputs digital elevation models of the modern topography for the 1964 simulation and prehistoric landscapes for paleotsunami simulations.

Observations of the March 27, 1964, Tsunami

Eyewitness reports in newspaper stories released days after the 1964 tsunami afford credible information from which to estimate the extent of inundation, flow depths, and the elevation of wave runup. See Witter (2008) for detailed discussion of data collection methods.

Paleotsunami Deposits

Observations of subsurface stratigraphy beneath the lower Ecola Creek valley and, to a limited extent, an upland swale in the vicinity of the Cannon Beach City Hall formed the basis for mapping the extent of paleotsunami deposits. Field teams used 2.5-cm-diameter gouge cores to determine the presence or absence of sand layers interrupting sequences of freshwater peat and mud deposited beneath the floodplain and wetlands of Ecola Creek. Sediment attributed to tsunami deposition met the following ten criteria:

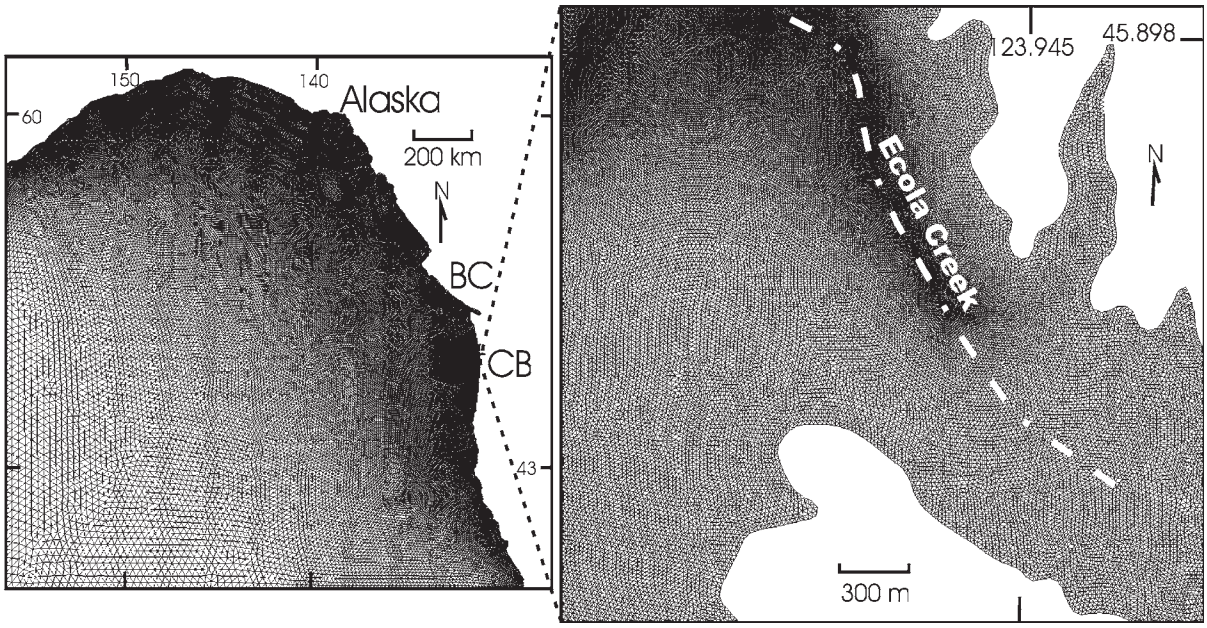

Figure 19. Unstructured computational grid used in tsunami simulations. The left panel shows the full grid. The right panel is the area near Ecola Creek. BC = British Columbia; CB = Cannon Beach.

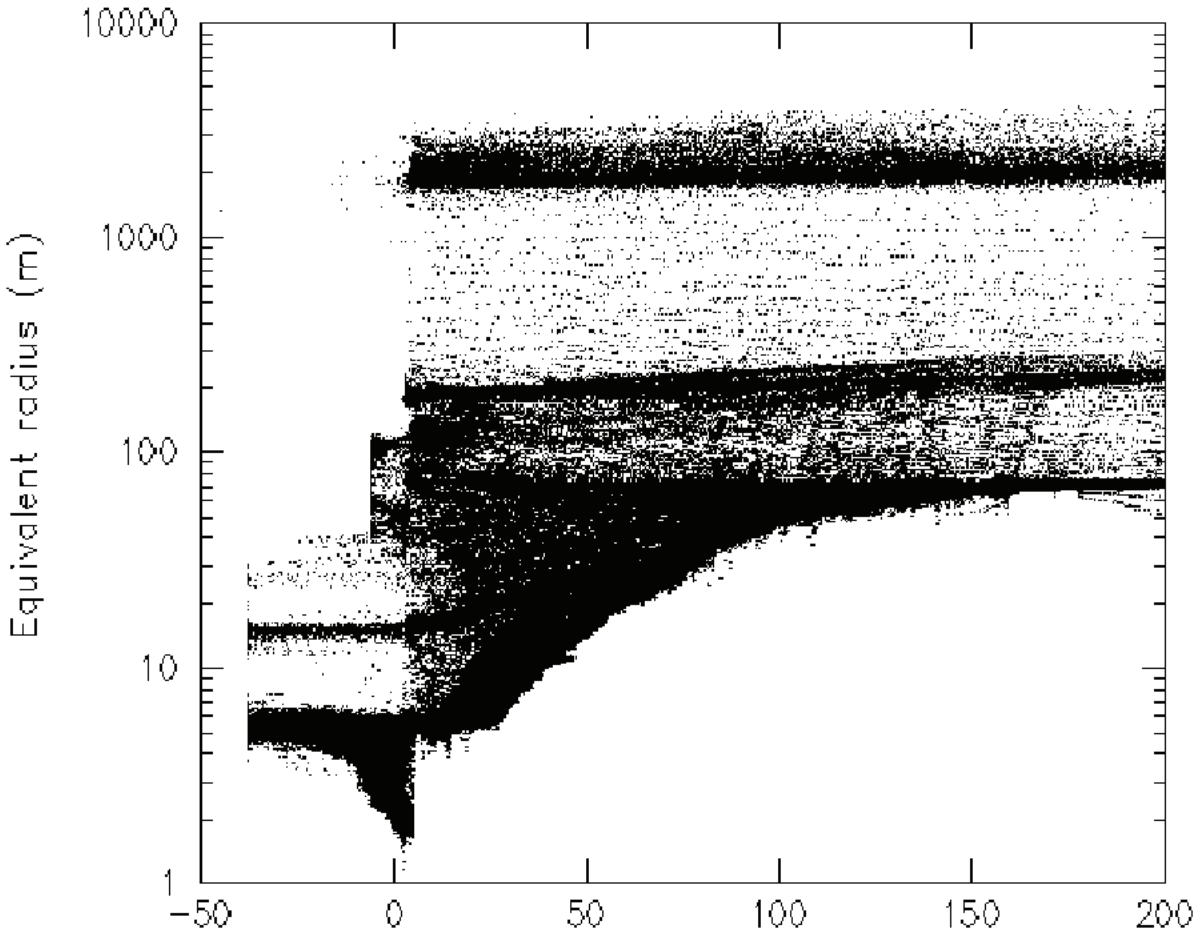

Figure 20. Grid resolution expressed as the equivalent radius of each numerical grid element plotted against bathymetric depth (negative depths are above mean higher high water [MHHW]). Graph demonstrates that resolution changes gradationally from tens of kilometers in the deep ocean to a few meters on land.

- Sand deposit consists of well-sorted, quartz-rich sand and rounded augite grains;
- Brackish-marine diatoms present;
- Deposit thins and/or sand grain size fines in a landward direction;
- Normally graded beds and/or mud lamina present;
- Ripup clasts present in the deposit;
- Lower contact of deposit is sharp or shows evidence of erosion;
- Organic debris present at top of deposit;
- Deposit is extensive over hundreds of meters;
- Deposit is coincident with a buried soil subsided by an earthquake;
- Deposit age overlaps with regional evidence for a Cascadia earthquake or tsunami.

For further details on paleotsunami investigation methods, see Witter (2008).

Reconstructing the Prehistoric Landscape

Comparison of inundation to distribution of paleotsunami deposits from Cascadia tsunami was accomplished by simulations run on a 1000-year B.P. landscape (digital elevation model) reconstructed by removal of artificial fills from the modern landscape and inferring the paleolandscape from analysis of coastal erosion data, cores, and ground penetrating radar surveys (Peterson and others, 2008). 1,000 years corresponds approximately with the age of the tsunami deposit that reaches farthest inland of the three deposits mapped in the Ecola Creek valley by Witter (2008). Because sea level ~1,000 years ago was ~1 m lower (Witter, 2008) and sedimentation in coastal Oregon estuaries keeps pace with rising sea level, terrain underlain by Holocene sedimentary deposits was assumed to be ~1 m lower than the modern surface. The net result is a 1-m increase in relief between Holocene deposits and older rock uplands. Lowering the valley floor of Ecola Creek or raising adjacent uplands by 1 m simulates prehistoric relief; we chose the latter approach in order to simplify numerical grid construction. The former option would have required modification of the entire offshore bathymetric grid.

Sensitivity of simulated inundation to removal of 1,000 years of coastal erosion was examined by moving the shoreline at sedimentary rock bluffs and attached sand spits 70 m west. This value was calculated by assuming a conservatively high erosion rate from historical data on the northern and central Oregon coast taken from Allan and Priest (2001) and Priest and Allan (2004). Modern erosion rates are highly variable, 6 ± 7.6 cm/yr, for sedimentary rock bluffs on the northern Oregon coast, generally decreasing from the central coast to the north (Allan and Priest, 2001). Coseismic subsidence probably augments erosion after each of the three tsunamis; however, we found no definitive observational data on how long such erosion persists or how rapid it might be. We assumed that erosion rates during these intervals approximate rates in sand-starved littoral cells of the central Oregon coast that experience wave strike for most of the year. An erosion rate of 24 ± 12 cm/yr measured on a sedimentary rock bluff fully exposed to waves at Beverly Beach in Lincoln County, Oregon (Priest and Allan, 2004), was used to approximate the conditions after coseismic subsidence. Retreat of the coast would be ~15 ± 6 m from coseismic subsidence, assuming ~20 years of higher sea level after each of three earthquakes. Assuming that gradual coastal erosion in between these three 20-yr intervals was 6 ± 7.6 cm/yr, this amounts to an additional 56 ± 72 m, for a total of 71 ± 72 m of erosion. We assumed ~70 m. Basalt bluffs were not similarly translated because of negligible erosion rates at crystalline rock headlands (Allan and Priest, 2001; Priest and Allan, 2004).

Because there were no definitive data constraining prehistoric dune height, we tested sensitivity to barrier dune height by constructing two digital elevation models (DEMs) to represent the two extremes for prehistoric dune height. One landscape included a barrier dune with the same topographic relief as the present foredune. The current dune is probably at the maximum height for the last 1,000 years as introduction of European beach grass has generally increased dune height in modern times. The second landscape had no barrier dune fronting the estuary.

Comparison of Simulated Coseismic Deformation to Observations

Another means of testing validity of the simulations is to compare simulated coseismic subsidence for Cascadia scenarios to subsidence estimated from paleosubsidence data. We used data compiled by Leonard and others (2004) and Nelson and others (2008) for the AD 1700 Cascadia earthquake, a magnitude ~9 event (Satake and others, 2003).

RESULTS

CASCADIA EARTHQUAKE SOURCES

Modeled coseismic vertical deformation from Cascadia earthquakes at the latitude of Cannon Beach ranged from nearly 17 m to ~2 m (Figure 21). The 25 Cascadia source scenarios selected for tsunami hazard assessment are compared in Figure 21 to the 12 scenarios of TPSW (2006). We simulated tsunami runup and inundation from all of the sources depicted in Figure 21 using post-earthquake topography. The final 25 source scenarios were selected after elimination of some source parameters from an early version of the logic tree and after elimination of some sources that produced small tsunamis of similar size.

SOURCE SCENARIOS ELIMINATED FROM THE ANALYSES

We eliminated all but one of the "Small" source scenarios in order to save computational time simulating low-impact tsunamis. Initial tests of "Small" scenarios revealed that all have runup at the open coast of ≤ 8.4 m (NAVD 88) and generally below 7.7 m over 90 percent of the area. Variations in seismic parameters for these scenarios contributed little to the overall hazard owing to low weighting factors and small inundation. Only the "Small" scenario with the highest weight, Small 9 with open coastal runup of 5.5 to 6.0 m, was simulated for tsunami propagation and inundation. This source has symmetric slip of ~8 m on a regional buried rupture. This reduced the number of Cascadia scenarios in the logic tree (Figure 15) from 32 to 25. To calculate percentile inundation lines based on weighting factors summed for all runs at each grid cell in the composite hazard map, the most probable small scenario, Small 9, was assigned the entire weight of all "Small" scenarios, 0.25. Figure 22 illustrates the weighting factors for 32 versus 25 scenarios.

SOURCE PARAMETERS ELIMINATED FROM THE ANALYSES

Increasing or decreasing the regional rupture width from the best fit to paleoseismic data (see Figure 4 of Appendix A) did not produce enough change in tsunami inundation or wave arrival to justify inclusion in the logic tree. Increasing rupture width of regional rupture scenarios by 20 km produced no significant difference in inundation, runup (Figure 23; Table 5), or peak wave arrival but did decrease the time of first significant rise of water level at the coastline (Figures 24 and 25). Decreasing rupture width by 20 km amplified water elevation at the open coast (Figure 24; Table 5) owing to the larger amplitude of the deformation, but had little effect on inundation (Figure 23; Table 5) or peak wave arrival time (Figure 24). Increasing seaward skew of slip made a significant difference in open coastal runup but little difference in inundation (Figure 23; Table 5) or wave arrival time (Figure 24). Changes in tsunami inundation from narrowing the rupture by 20 km are approximately duplicated by changing skew from q = 0.5 (symmetric) to q = 0.3 (seaward skewed) (Figure 23; Table 5). Freund and Barnett (1976) preferred a q value (skewness) of 0.3 on the basis of limited observations of coseismic vertical deformation caused by the M_w 9.2 Alaska earthquake of 1964. For these reasons, we retained the seaward skew parameter in the logic tree but eliminated the variation in rupture width.

TSUNAMI ELEVATION AND INUNDATION FOR FINAL CASCADIA SCENARIOS

Water depth at the open coast (at 0 m NAVD 88, Station cb009, Figure 25) for scenario tsunamis varied from 3 to 18 m (Figures 26 and 27), while inundation up Ecola Creek varied from ~1.5 to 3.8 km (Figure 28). The cumulative logic tree weights for overlapping scenario tsunamis are illustrated in two ways: (1) Percent confidence that each scenario water depth or inundation is equal to or larger than a potential Cascadia tsunami (Figures 26 and 29) and (2) cumulative weighting factor for overlapping scenario inundations (Figures 27 and 28). The latter, more standard representation is simply the inverse of the former and provides a crude means of comparing how Cascadia wave elevations and inundations at Cannon Beach compare to those of the TPSW (2006) by assuming that all twelve of the TPSW stochastic sources have equal logic tree weights within the TPSW framework for Cascadia tsunami scenarios. Tsunami inundation and runup of the TPSW (2006) generally explore a narrower range of extreme inundation and runup relative to scenarios of this investigation

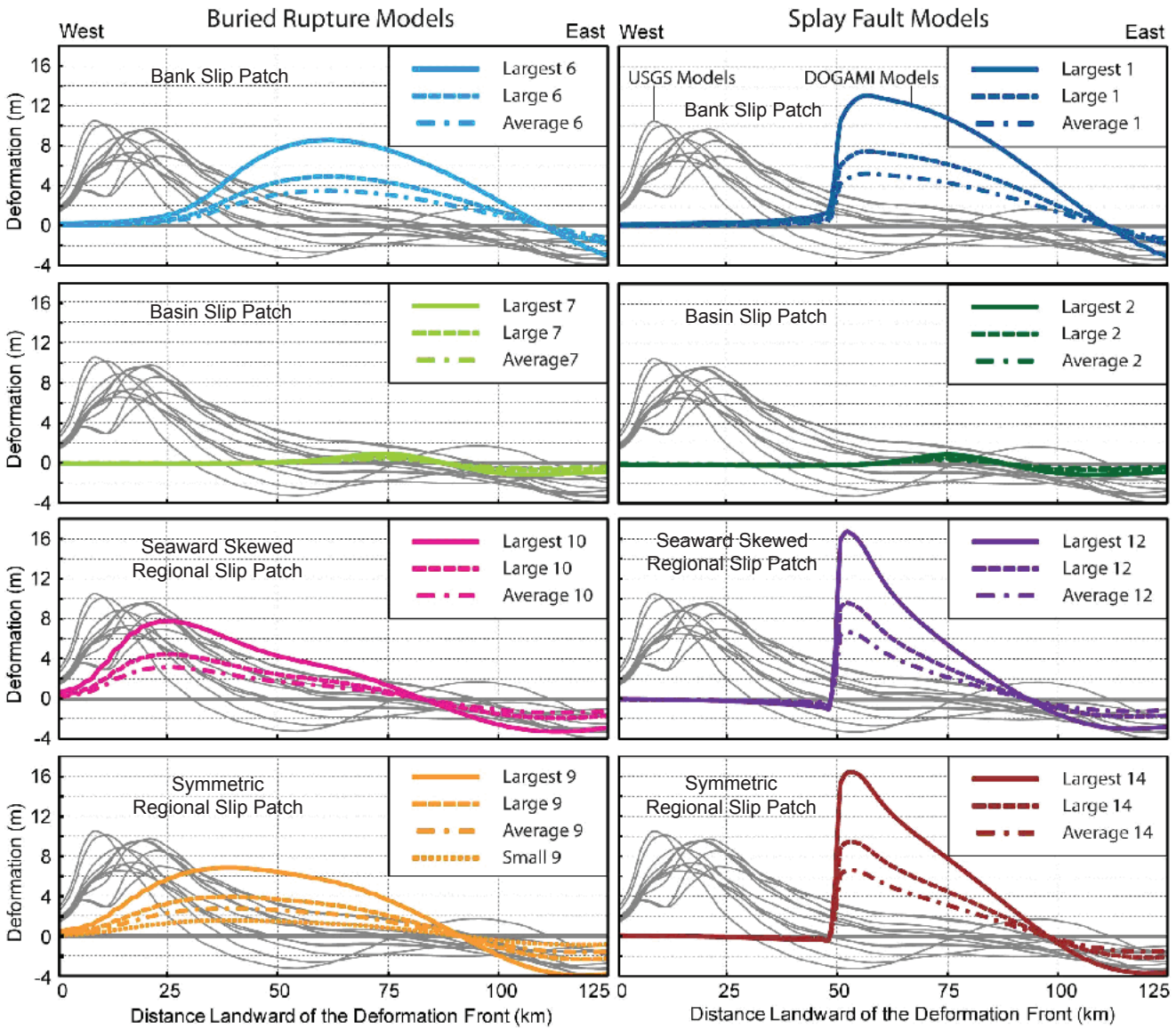

Figure 21. West-to-east cross sections of coseismic deformation for all Cascadia earthquake source scenarios. Cross sections extend from the deformation front to the shoreline at Cannon Beach, Oregon. The final 25 tsunami sources used for this investigation (colored lines) have major uplift mostly landward (east) of stochastic scenarios developed by the U.S. Geological Survey for the Tsunami Pilot Study Working Group (2006) (gray lines). Scenarios of the same color but decreasing deformation have decreasing fault slip at values of ~38, ~22, and ~15 m with one scenario, Small 9, at ~8 m. Titles on each graph explain the type of slip distribution used; see also the logic tree (Fig. 15) for explanation of source scenario names in each legend.

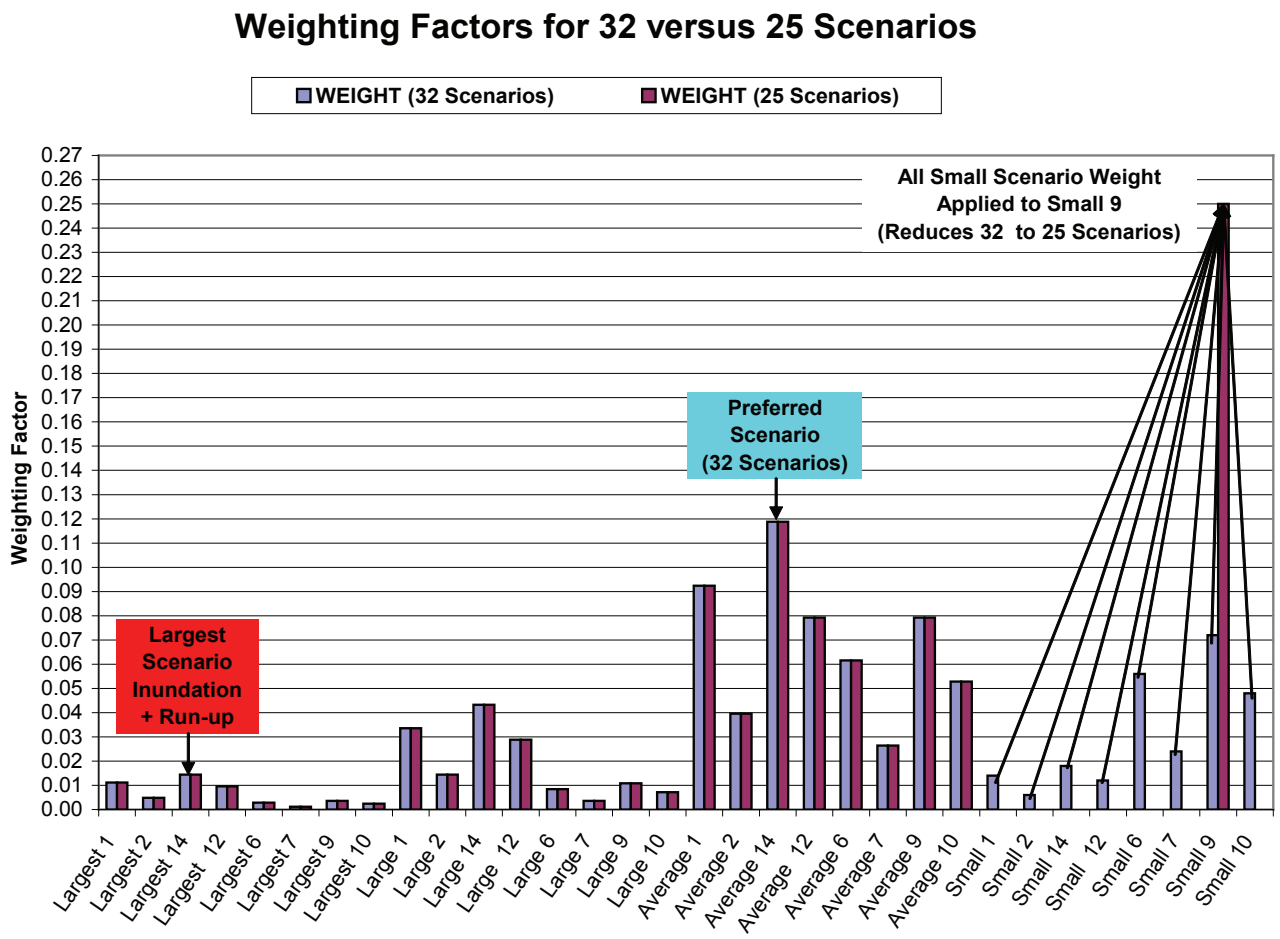

Figure 22. Logic tree weights for 32 versus 25 tsunami source scenarios. Note that the most probable scenario for the original logic tree of 32 scenarios is Average 14. Reduction to 25 scenarios causes Small 9 to have an artificially high weight from adding all weighting factors from the other "small" scenarios. This reduction to 25 scenarios does not change the judgment of the authors that Average 14 is the most probable (preferred) scenario.

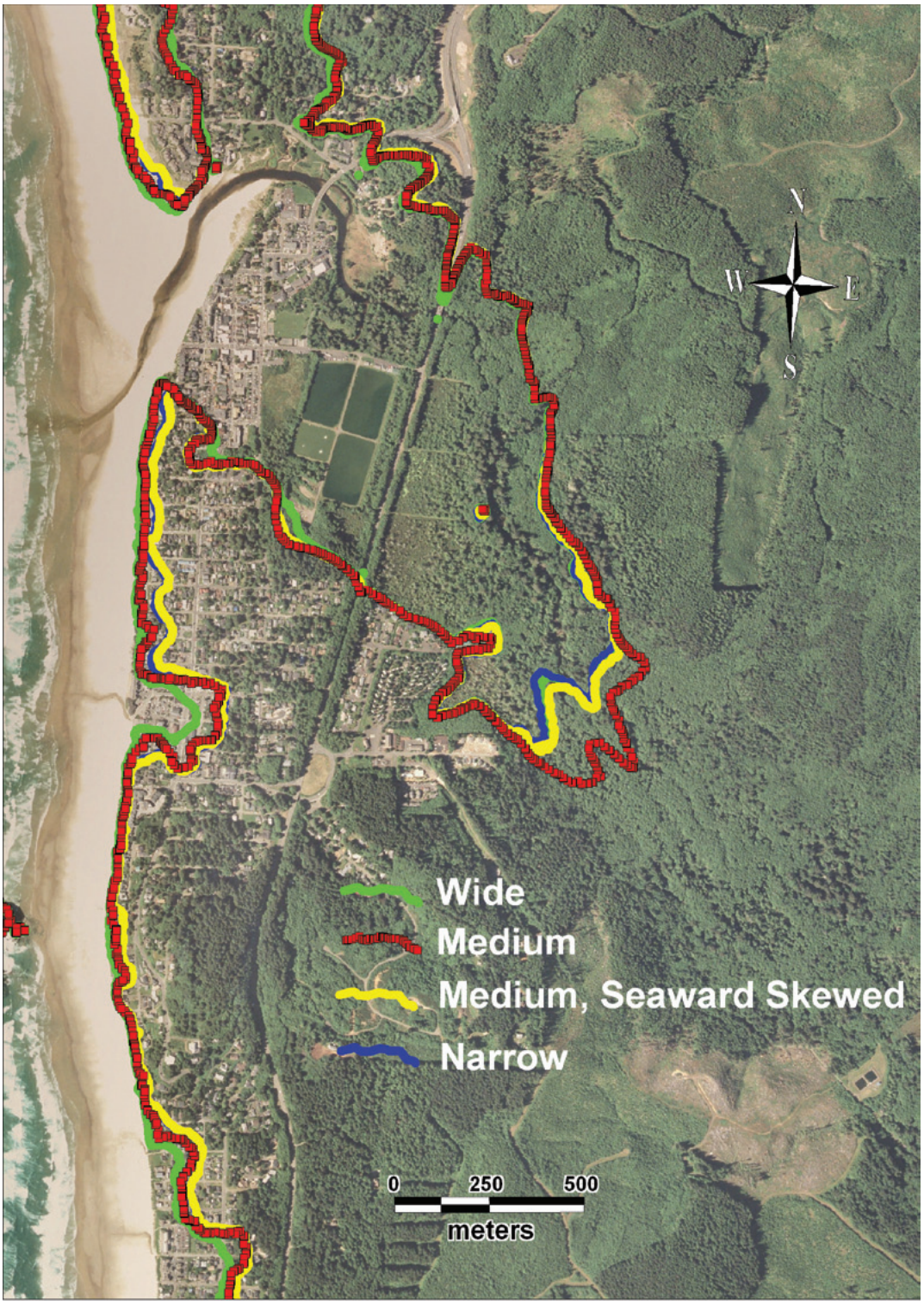

Figure 23. Difference at Cannon Beach, Oregon, between inundation for regional splay fault slip patch scenarios with differing rupture width and skew. All simulations use sources with "Average" fault slip of ~15 m. Simulations use an early numerical grid and early version of the SELFE hydrodynamic model, so inundations are significantly different from those used for the final inundation map but still useful for comparison. Medium = best-fit rupture width to geological data with symmetrical skew of slip (q = 0.5); wide = medium rupture width plus 20 km; narrow = medium rupture width minus 20 km; medium seaward skewed = medium rupture width with q = 0.3.

Table 5. Tsunami water elevation and inundation differences resulting from changes in rupture width and skew.

Rupture Width Scenario	Skew (*q*)	Maximum Slip (m)	Maximum Offshore Uplift (m)	Maximum Offshore Subsidence (m)	Open Coastal Water Elevation (m, NAVD 88)	Maximum Inundation at Ecola Creek (km)
Wide	0.5	~15	3.0	-1.3	9.6	1.6
Average	0.5	~15	2.9	-1.5	10.2	1.8
Average	0.3	~15	3.1	-1.0	13.3	1.6
Narrow	0.5	~15	3.8	-0.8	12.7	1.6

All values are for "Average" slip of ~15 m on a Cascadia rupture without partition of slip to a splay fault (buried ruptures). Skew (*q*) of 0.5 is symmetric and for 0.3, seaward skewed; average rupture width is a best fit to AD 1700 paleosubsidence data and stress transition of Figure 12; wide and narrow widths are plus and minus 20 km from this average, respectively. Water elevations are measured at the open coastal shoreline at the point labeled "observation point for water elevations" in Figure 22; inundation is measured along the dashed line in Figure 22. These preliminary tsunami simulations used an early version the SELFE hydrodynamic model (v1.5e14); final simulations used a later version of SELFE (v1.5i11). Note: Only maximum offshore or coastal uplift and subsidence is listed, because inland deformation has no effect on the tsunami inundation or runup. NAVD 88 is North American Vertical Datum of 1988.

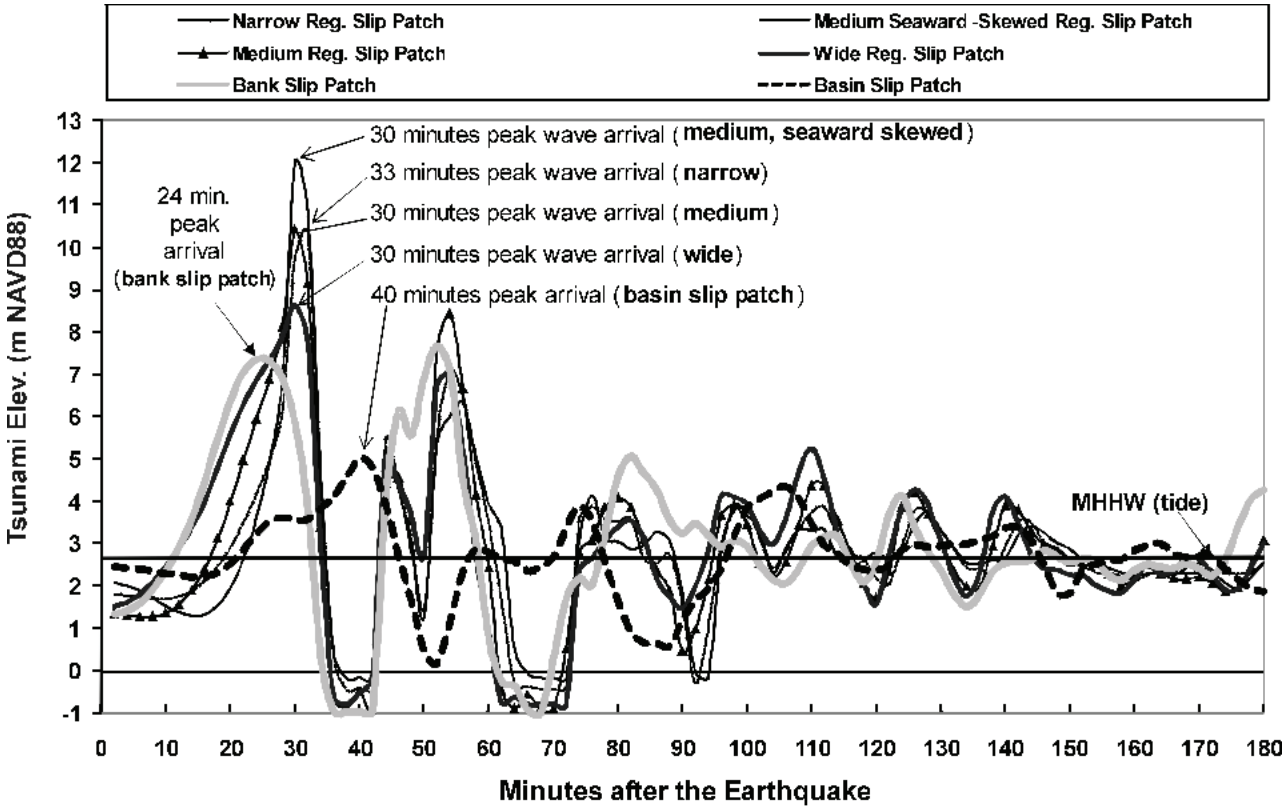

Figure 24. Sensitivity of wave arrival at Cannon Beach, Oregon, to Cascadia fault rupture width and slip distribution for splay fault scenarios with "average" slip of ~15 m. The "wide" and "narrow" regional ruptures are regional slip patches with symmetric slip but rupture width increased or decreased by 20 km, respectively. Mean higher high water (MHHW) = 2.71 m NAVD 88. MHHW is the tidal level for all simulations. Note how all simulations start with some degree of instantaneous drop in water level. This drop is caused by coseismic subsidence from the earthquake source scenario. Both the earthquake deformation and MHHW tide are initial conditions for simulations. Data are from near the open coastal shoreline (Station cb009, Figure 25). Simulations use an early fault dislocation model (fb76 slip distribution without the modification by Wang and He [2008] and early version of the SELFE hydrodynamic model, so elevations and arrival times are slightly different from those used for the final inundation map.

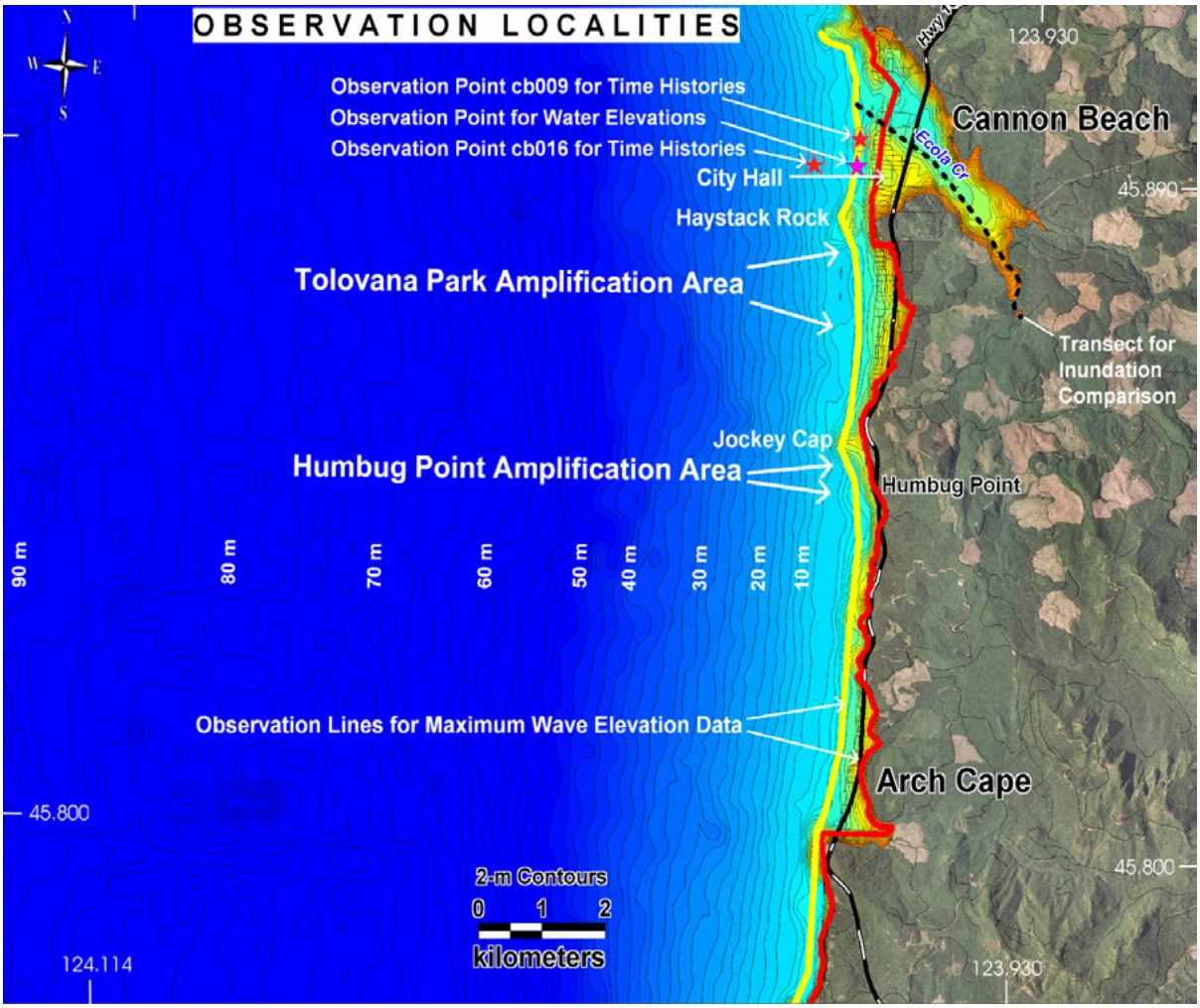

Figure 25. Observation lines and points for inundation, maximum wave elevations, and time histories of wave arrivals. Red observation line for maximum wave elevation data approximates the limit of inundation on steep slopes at the open coast; yellow line approximates the shoreline (0.0 m NAVD 88). Blue to orange colors bounded by black lines illustrate elevation and water depth in 2-m intervals; labels in white indicate water depth relative to the NAVD 88 datum.

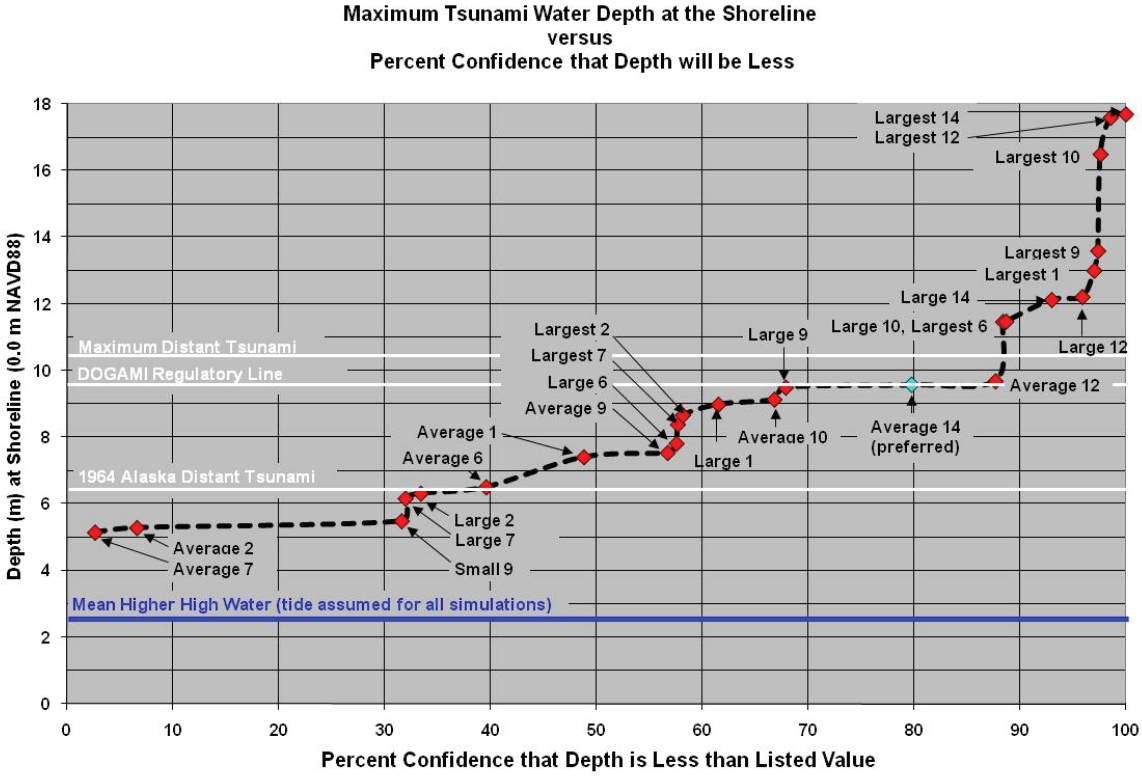

Figure 26. Cumulative percent confidence that tsunami water depth will be less than the scenario depth for a Cascadia tsunami (~500-yr event). Average 14 is the preferred scenario that received the highest logic tree weight for the full 32-scenario analysis. Water depths of the maximum distant tsunami scenario (source 3 of Tsunami Pilot Study Working Group [2006]), the 1964 Alaska distant tsunami, Oregon Department of Geology and Mineral Industries (DOGAMI) regulatory tsunami line (Priest, 1995a; Olmstead, 2003) used for implementation of the 1995 Oregon State Senate Bill 379, and tide assumed for all simulations are shown for comparison. All tsunami water depths are from a point located on the open coastal shoreline at 123.966586° W, 45.891190° N at approximately 0.0 m elevation NAVD 88 (purple star in Figure 25).

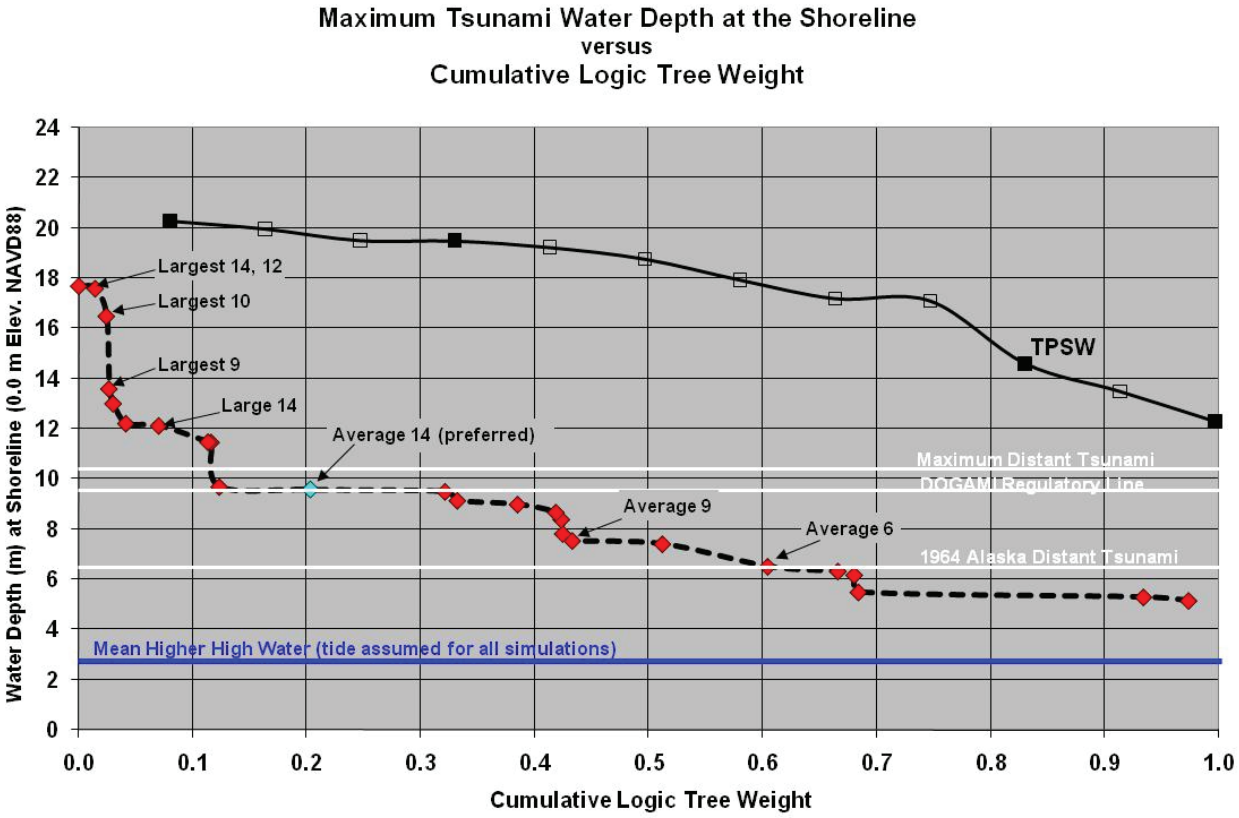

Figure 27. Water depth data as in Figure 26 but in terms of cumulative logic tree weight instead of percent confidence. Lowest depth scenario in each case is overlapped by all other scenarios, so it has a cumulative weight of ~1.0; hence, this chart is the inverse of the one in Figure 26. Included for comparison are data for the 12 stochastic sources used by the Tsunami Pilot Study Working Group (TPSW, 2006); each is assumed to have one twelfth of the total logic tree weight of 1.0. Note: TPSW water depths shown by open squares are inferred from results of an earlier version of the SELFE hydrodynamic model compared to four 2008 simulations (solid squares)

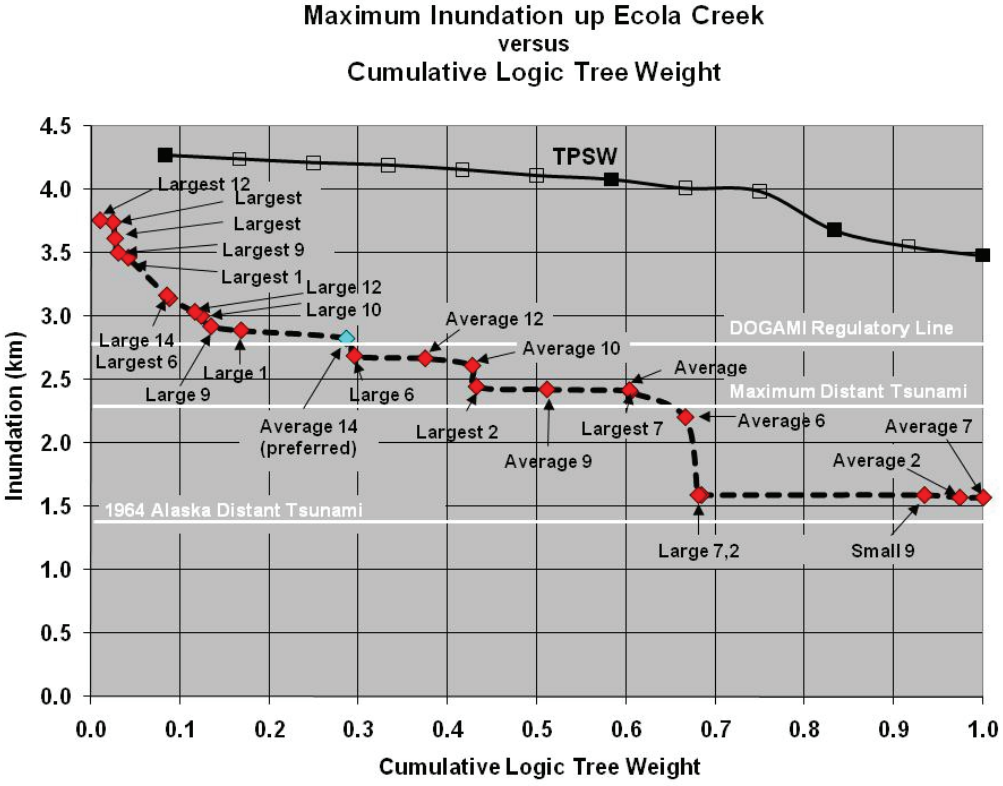

Figure 28. Inundation up the Ecola Creek channel versus cumulative logic tree weight versus scenarios of the TPSW (2006). The same method of calculation is used as for Figure 27. Also shown for comparison are maximum inundation from the 1964 Alaska tsunami and maximum considered distant tsunami from the Gulf of Alaska (source 3 of Tsunami Pilot Study Working Group [TPSW], 2006). Note: Inundation for the TPSW scenarios is inferred from four 2008 simulations (solid black squares) and scaling linearly between these four inundations corresponding open coastal water levels estimated from a 2007 version of the SELFE hydrodynamic model (open black squares).

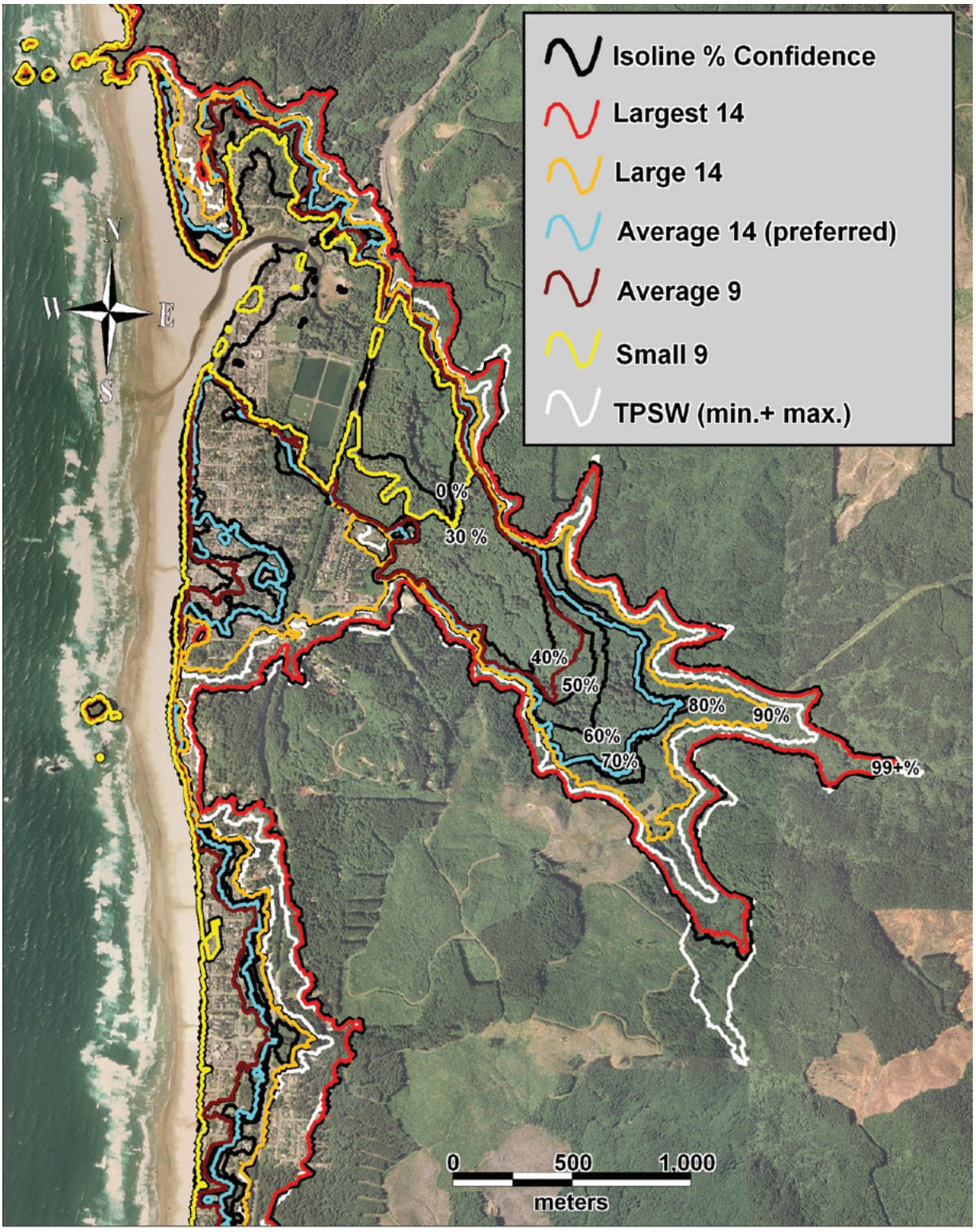

Figure 29. Relationship between inundation for selected regional slip patch scenarios, minimum and maximum inundation for Tsunami Pilot Study Working Group (TPSW, 2006) scenarios, and isolines of percent confidence. The isolines depict confidence that inundation for a 500-yr Cascadia tsunami will be less than the isoline. Note the close correspondence of some regional slip patch scenarios to isolines and extension of largest Tsunami Pilot Study Working Group scenario past the largest inundation of this investigation. The minimum Tsunami Pilot Study Working Group scenario approximates the 96 percent inundation line (not plotted).

(Figures 27 and 28). Most of the 12 tsunami scenarios of TPSW are skewed toward "Largest" scenarios of this investigation, equivalent to ≤0.04 cumulative weight in Figures 27 and 28 (≥96 percent confidence, Figures 26 and 29). Scenario Largest 14 approximates the ~99 percent isoline, Large 14 the 90 percent isoline, Average 14 the 70 percent isoline, and Small 9 at the 10 to 30 percent isolines (Figure 29). The latter correspondence is an artifact, because Small 9 has all of the logic tree weight for "Small" scenarios (Figure 22); thus isolines for 10 to 30 percent are collapsed together. Simulating the other seven "Small" scenarios would have spread out these isolines.

EFFECT ON INUNDATION AND RUNUP OF SLIP, SPLAY FAULTING, AND SLIP PATCHES

Slip magnitude was the most important control of inundation and runup, both of which increased linearly with scenario slip (Figure 30). The next largest differences between scenarios were caused by increasing uplift through splay faulting and distributing slip into regional versus local bank or basin slip patches (Figure 31; Table 6). Local basin slip patch scenarios produced much smaller runup or inundation relative to all other scenarios (Table 6), because the nearest basin slip patch simulated is ~100 km south of Cannon Beach (Figure 16).

For scenarios with significant coseismic deformation, amplification from greater uplift on the splay fault relative to a buried megathrust rupture varied widely depending on how much of the slip was distributed seaward of the splay. Slip distribution on the megathrust for splay fault models is simply cut off at the splay fault, so the potential slip distributed seaward of the splay does not participate in the coseismic deformation. Amplification by splay faulting was 6 to 31 percent for tsunami water level at the open coast and 2 to 20 percent for inundation up Ecola Creek (Figure 31). Amplification by incorporation of a splay was negligible for basin slip patches owing to low slip everywhere in basins, increased with seaward skewed regional slip patches, further increased for bank slip patches, and was largest for regional slip patches with symmetri-

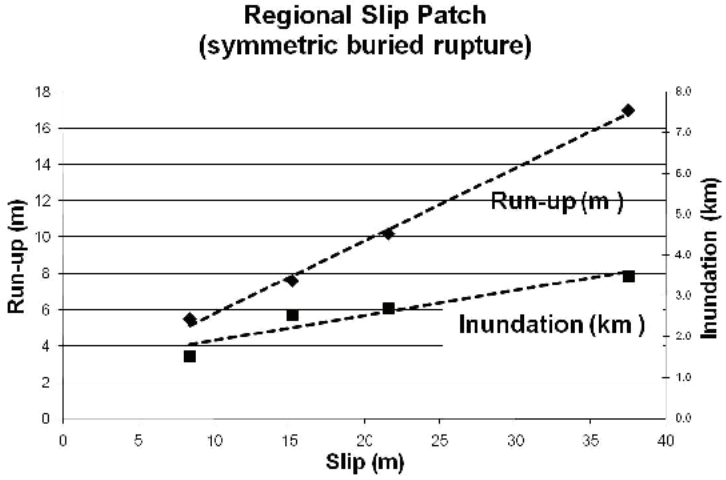

Figure 30. Linear relationship between fault slip and tsunami inundation or tsunami elevation at the shoreline (0.0 m NAVD 88). Tsunami elevation is labeled "run-up" on the graph. Water elevations are measured at observation point cb009 on Figure 25; inundation is measured along the transect shown in Figure 25.

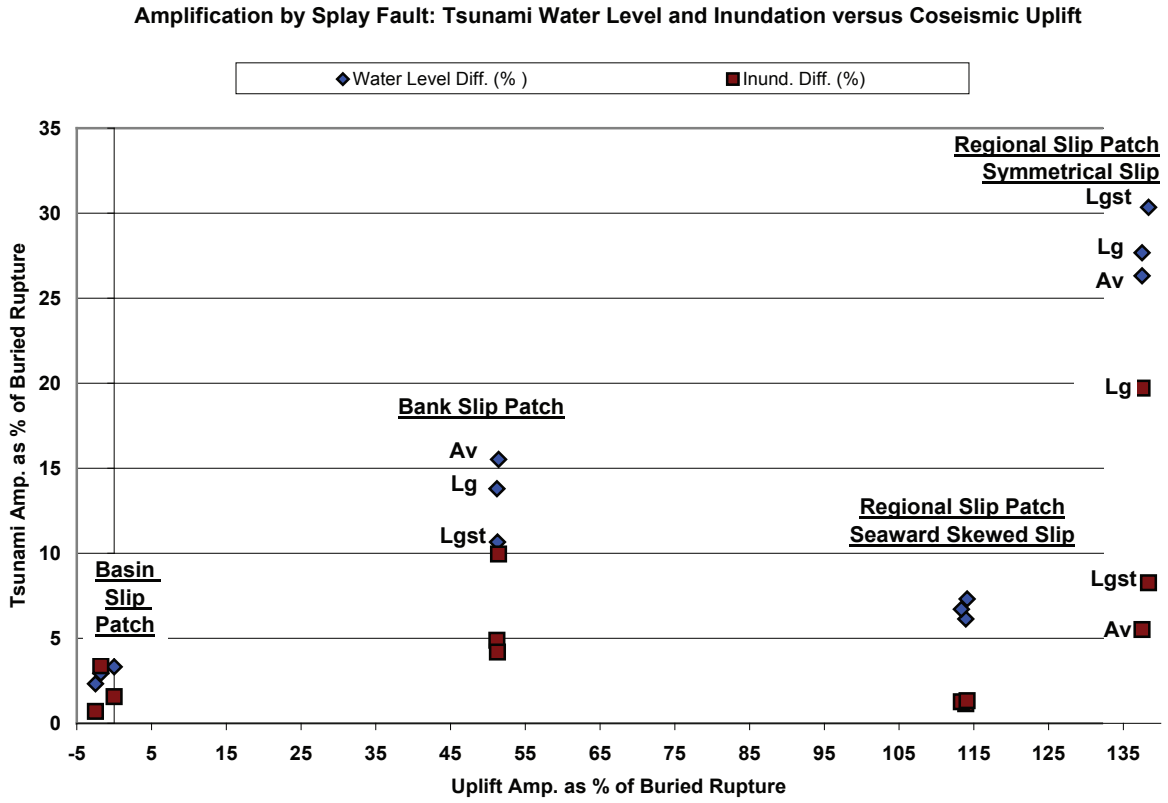

Figure 31. Percent amplification by the splay fault relative to buried rupture source of water level at the shoreline and inundation up Ecola Creek versus percent amplification of seafloor uplift by the splay fault. Av is Average; Lg is Large; Lgst is Largest; Amp. is amplification; Diff. is Difference.

Table 6. Tsunami water elevation and inundation differences between regional versus local (bank or basin) slip patches and splay fault versus buried rupture scenarios.

Scenario	Rupture Type	Slip Patch Type	Maximum Slip (m)	Maximum Offshore Uplift (m)	Maximum Offshore Subsidence (m)	Open Coastal Water Elevation (m, NAVD 88)	Maximum Inundation at Ecola Creek (km)
Average 1	splay fault	local bank	~15	5.3	-1.3	8.5	2.4
Average 2	splay fault	local basin	~15	0.4	-0.4	5.3	1.5
Average 6	buried fault	local basin	~15	3.4	-1.3	7.7	2.2
Average 9	buried fault	regional	~15	2.8	-1.6	7.6	2.5
Average 14	splay fault	regional	~15	6.7	-1.5	9.8	2.7

All source scenarios use an "average" maximum slip corresponding to 525 years of convergence on the Cascadia subduction zone (~15 m at the latitude of Cannon Beach). Observation points for water elevation at the open coast (labeled runup) and inundation are the same as in Table 5 (see Figure 25). Only maximum offshore or coastal uplift and subsidence is listed, because inland deformation has no effect on the tsunami inundation or runup. NAVD 88 is North American Vertical Datum of 1988.

cal slip distributions (Figure 31). The seaward skewed slip scenarios had only ~2 percent amplification of inundation and 6 to 7 percent for water level at the open coast even though the splay fault amplified offshore uplift by 114 percent (Figure 31). The reason for the complex relationship between uplift and tsunami impact is that total water displaced is as important as maximum uplift. Cross sections in Figure 21 illustrate that the seaward skewed slip on buried ruptures (e.g., Largest 10) produces large amounts of slip and uplift west of the splay fault where water is deeper, but splay fault amplification affects just the slip in shallow water where the seaward skewed model has less slip than the symmetrical model (e.g., compare Largest 12 to Largest 14 in Figure 21).

Alaska 1964 Tsunami Simulation

Inundation from the 1964 Alaska tsunami (Figure 32) was generally near the lower threshold for all Cascadia tsunami scenarios (Figures 28 and 33) at ~6.5 m NAVD 88. Flow depth and inundation from the simulation closely matched observations gleaned from historical records (Witter, 2008) (Table 7; Figure 32). Match to observed inundation was improved in two trials by refining the numerical grid defining the Ecola Creek channel and highway embankments. The unstructured numerical grid of the SELFE model made such local refinements relatively easy. Localities with highest quality historic observations were Bell Harbor Motel with 1.5 m (5 ft) maximum flow depth and Steidel House with 0.8 m (2.5 ft) maximum flow depth (Figure 32). The simulation predicted flow depths of 1.6 m at Bell Harbor Motel and 0.8 m at Steidel House. The simulation also matched all but one of the localities along Spruce Street (Table 7). In front of the foredune in downtown Cannon Beach, 1964 tsunami runup reached an estimated elevation of 6.1 m (NAVD 88); the simulation predicted 6.7 m. Simulated inundation on the landward side of the foredune is slightly less than that estimated from historical accounts (Figure 32), but the historical inundation is highly uncertain in this area. There also have been some alterations to the landscape in this same area since 1964. Considering uncertainties in geometry of the Prince William Sound earthquake source, previously mentioned nonlinear effects of tidal flow, and the 0.3-m difference in tide between the simulation and estimated tide, the simulated and observed inundations are remarkably close.

Theoretical Maximum Considered Distant Tsunami Simulation

Water elevation at the open coastal shoreline for the maximum considered Gulf of Alaska tsunami reached ~11 m, similar to the Cascadia splay fault scenarios, Average 12 and 14 (Figure 26). Inundation at Ecola Creek from this Alaska tsunami was lower than these two splay fault scenarios, falling at the ~35 to 40 percent confidence isolines for Cascadia tsunamis (Figures 28 and 33). An exception is in a small drainage through the coastal bluff near the Cannon Beach City Hall where this scenario inundates to the ~60 percent confidence boundary with water elevation of 11.5 m (Figure 33).

Local Amplification of Open Coastal Runup

Runup was amplified by up to 40 percent at nearshore bathymetric lows, especially if combined with small U- or V-shaped valleys where the ~30 m contour penetrates < 1 km inland (Figures 25 and 34). Maximum open coastal runup was 30.3 m in the Tolovana area. Cascadia sources of the TPSW (2006) reached a maximum runup of 34.7 m in the same area. Below is a summary of runup and approximately matching isolines of percent confidence for Cascadia tsunamis from regional slip patch scenarios. Values are representative of most open coastal sites with maximum values in parentheses:

- Largest 14 (~99% isoline): ~20 m runup (30.3 m)
- Large 14 (~90 % isoline): ~13 m runup (15.9 m)
- Average 14 (~70% isoline, preferred scenario): ~10 m runup (12.2 m)
- Average 9 (~50% isoline): ~8 m runup (9.4 m)
- Small 9 (~6–10% isoline): ~5.5 m (6.1 m)

The 1964 Alaska teletsunami was amplified where funneled into the mouth of Ecola Creek where it reached 7.5 m (NAVD 88). The maximum-considered teletsunami from Alaska was amplified in the same places as the Cascadia tsunamis, reaching a maximum of 12.5 m.

Tsunami Arrival Time and Velocities

Cascadia coseismic uplift closer to shore caused sooner tsunami arrival onshore. The first tsunami peak is the largest wave in all of the Cascadia simulations, arriving between 24 and 34 minutes after the earthquake (Figures 35 and 36). Local bank slip patch scenarios always have the earliest wave arrival (Figure 36), because the source uplifts extend farther toward

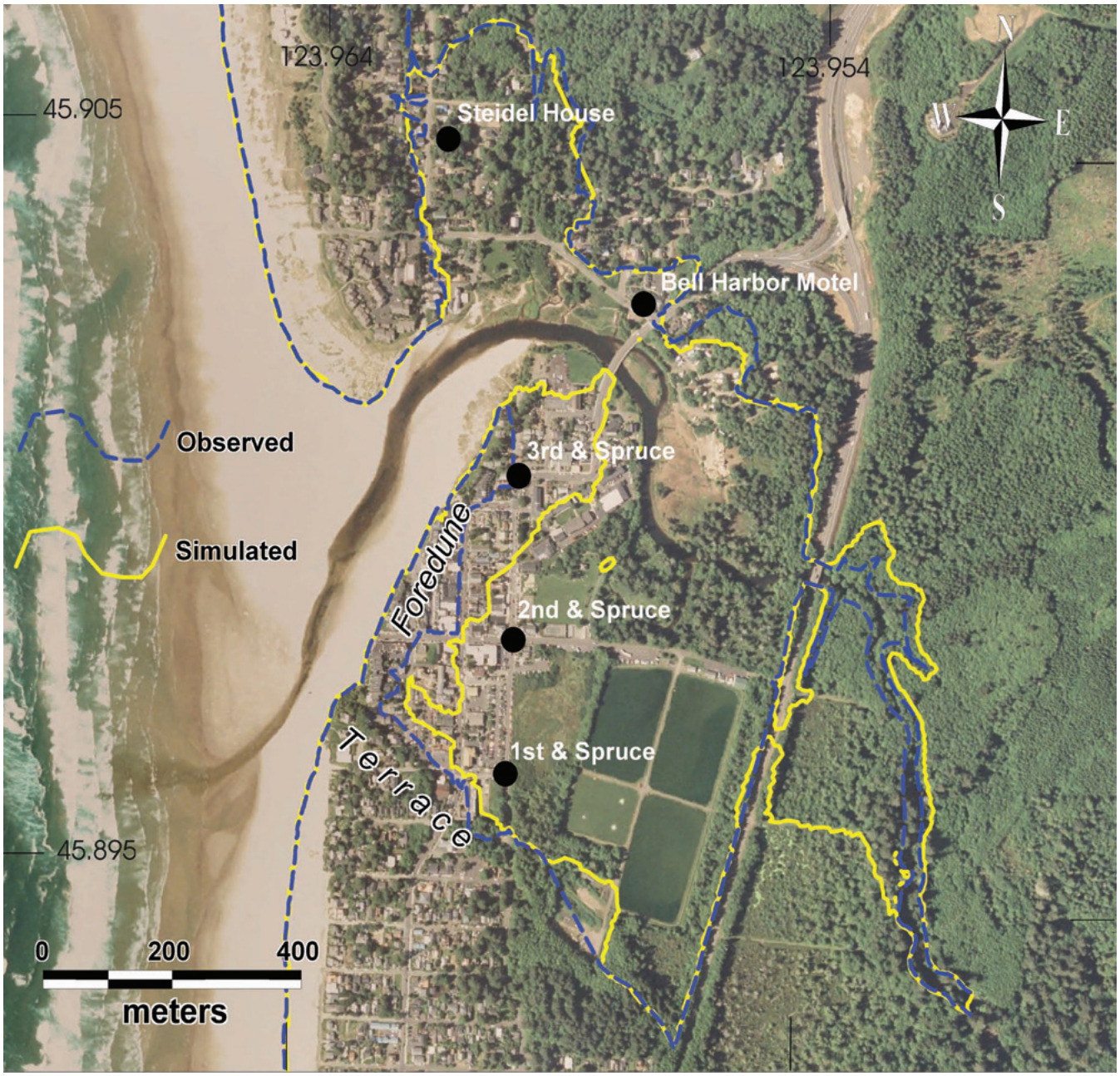

Figure 32. Simulated versus observed inundation from the 1964 teletsunami at Cannon Beach. Steidel House and Bell Harbor Motel are localities with high-quality estimates of tsunami flow depth. Observed inundation on the east side of the foredune is highly uncertain and is based on estimates of flow depth near the creek channel.

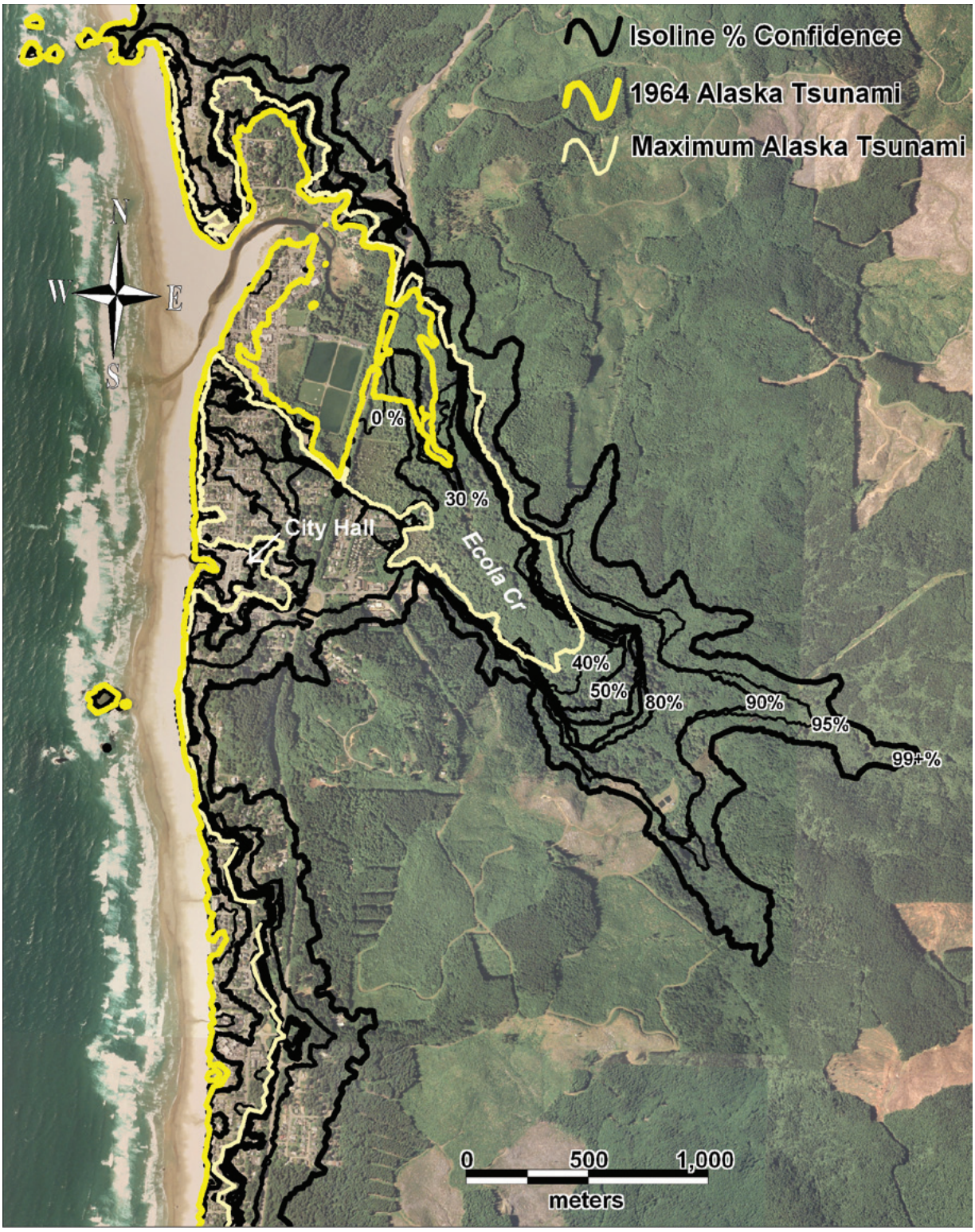

Figure 33. Inundation from the 1964 and maximum considered distant tsunami compared to isolines of percent confidence for capturing all variability in Cascadia inundation.

Table 7. Comparison of observed water depths and elevations during the 1964 Alaska tsunami at Cannon Beach, Oregon, to results of tsunami simulations.

	Tsunami Flow Observations		Simulation Results	
Site	Depth (m)*	Elevation (m, NAVD 88)#	Depth (m)	Elevation (m, NAVD 88)
Bell Harbor Motel	1.5	6.2	1.6	6.2
Steidel House	0.8	5.8	0.8	5.9
3rd and Spruce St.	0.3	5.6	0	<5.3 (~4.2)
2nd and Spruce St.	0.3	3.8	0.3	3.8
1st and Spruce St.	0.3	4.1	0.1–0.3	3.8

Elevation of simulation in parentheses is tsunami elevation nearest to an observation point that was dry in the simulation; < symbol indicates that simulation was less than this ground elevation at the observation point.

* Water depth estimates are based on eyewitness observations noting water damage and water marks on buildings and depth of flooding along the main street in downtown Cannon Beach (Witter, 2008).

Minimum water level elevation estimate relative to the mean lower low water (MLLW) tidal datum is equal to the sum of the observed water depth and the North American Vertical Datum of 1988 (NAVD 88) elevation of the site.

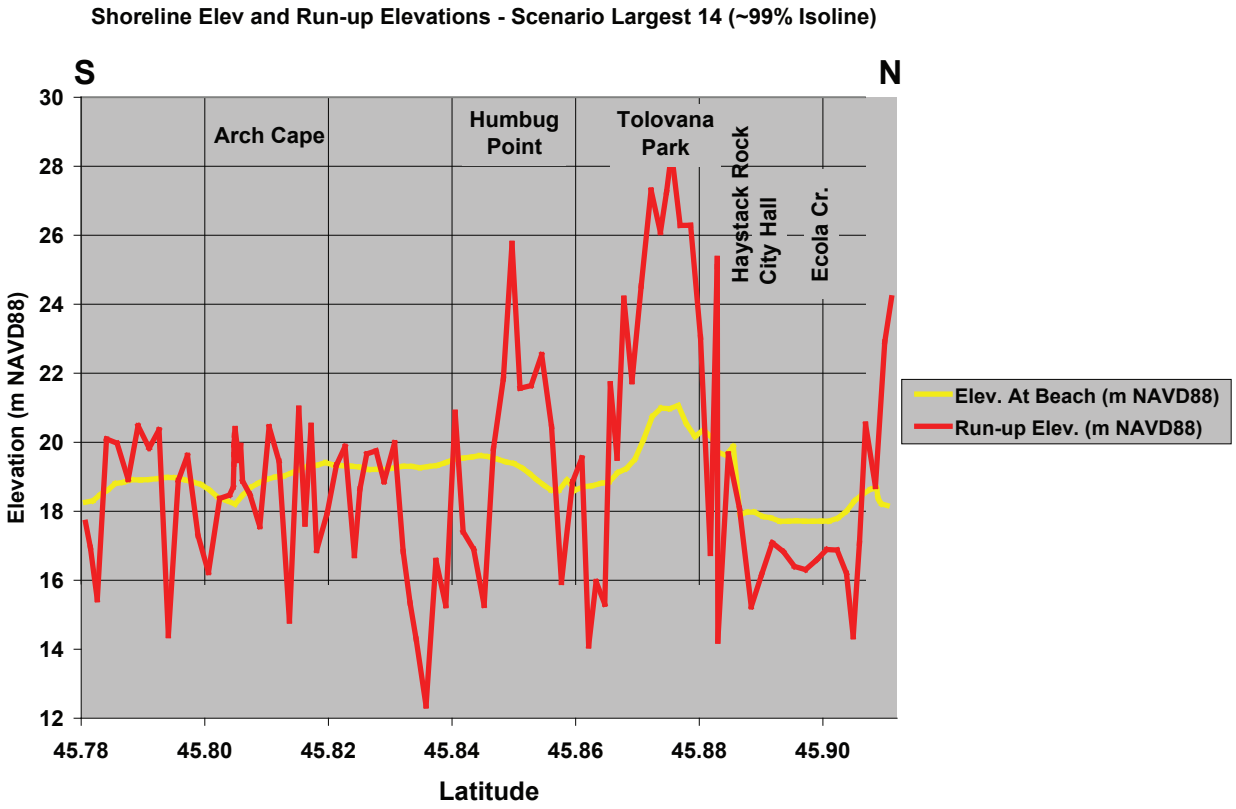

Figure 34. South-north (S-N) variation of open coastal tsunami wave elevations for scenario Largest 14, approximating the 99 percent isoline for all potential Cascadia tsunamis. Locations of observation lines are shown in Figure 25. Runup elevations are sometimes lower than maximum wave height at the beach because the elevations are taken near the limit of inundation on coastal bluffs where the water level decreases inland. In the vicinity of Ecola Creek the "Runup" elevation is actually the maximum wave height above the open coastal foredune (Figure 25). Actual maximum elevations may differ slightly from these values because they are based on a cross section through a numerical grid that averages data using a nearest-neighbor approach.

the shore than the regional rupture scenarios (Figure 21). Water begins to rise immediately after the earthquake at a bank slip patch scenarios (Figure 36). First rise of water level for all Cascadia scenarios was at 2 to 14 minutes, reaching half of the peak height at 14 to 30 minutes (Figures 35 and 36). Half the peak height for Cascadia tsunamis was equal to or less than ~5 to 14 m. For the regional rupture scenarios, the splay fault cases arrive earlier than equivalent buried rupture cases (Figures 35, 36, and 37), because the buried ruptures have peak uplifts west of the splay faults (Figure 21). Peak water levels for tsunami scenarios of TPSW (2006) arrive a few minutes later than most of our Cascadia tsunamis (Figure 35) because peak uplifts are farther offshore (Figure 21). Cascadia source scenarios with identical slip distribution but increasing slip produce tsunamis that have decreasing arrival times for first rise of water but nearly synchronous peak arrival (Figure 37), because larger slip produces wider uplift (Figure 21).

Source scenarios with seaward skew of slip (scenarios 10 and 12) and the basin slip patch sources (scenarios 2 and 7) created small leading depression waves owing to offshore subsidence (Figure 21); all others had leading elevation waves (Figures 35, 36, and 37). A leading depression wave amplifies runup at the open coast (Tadepalli and Synolakis, 1994), but these small leading depression waves had little effect on tsunami impact compared to degree of uplift in deep water (e.g., compare seaward skewed to symmetric distributions for regional slip patches in Figures 35 and 36).

The two distant tsunamis differed little in first wave arrival time but showed contrasting patterns of wave height. The maximum considered distant tsunami scenario had highest runup during the first wave, at 4 hours 6 minutes after the earthquake (Figure 38); first rise in water level was 5 minutes prior. In contrast, the 1964 Alaska tsunami had a 5-m wave arrival at 4 hours 4 minutes followed 6 minutes later by a 6-m wave (Figure 39). First rise of water level for the 1964 tsunami was 6 minutes before the first wave peak (Figure 39). The maximum considered distant event had a slight leading depression wave (Figure 38); the 1964 tsunami had a leading elevation wave (Figure 39).

Velocities varied in concert with wave elevations (Figure 40) but were largest in the Ecola Creek channel and where the tsunami plunges down the back (east) side of the foredune at the mouth of Ecola Creek (Figure 41). Peak Cascadia tsunami velocities at the open coastal shoreline were generally quite modest from initial Cascadia tsunami surge (≤ 3 m/sec), peaking on the withdrawing wave or the second arrival at ~40 to 45 minutes after the earthquake (≤ 8 m/sec; Figure 40). Landward surge velocities increased from the shoreline to the foredune in downtown Cannon Beach; for example, compare scenario Average 14 velocities at the shoreline in Figure 40 to maximum velocities immediately east in Figure 41. Maximum velocities inside Ecola Creek were as large as 22 m/sec for the largest Cascadia tsunamis (see maximum velocity data files on the DVD) owing to the funneling effect of water into the channel and large coseismic deformation for these earthquake sources. Distant tsunami velocities followed a similar pattern after they arrived but had lower velocities than the largest Cascadia tsunamis (Figures 42 and 43).

Correspondence of Cascadia Simulations to Paleotsunami Inundation

The inland extent of the three tsunami deposits mapped by Witter (2008) is 1.6 km and marks minimum inundation where Cascadia tsunamis over the last 1,000 years (Table 8) stopped transporting and depositing sand. Sand deposition occurs when water velocity and turbulence reach a threshold minimum for transport. Any simulated tsunami inundation extending inland of mapped paleodeposits can therefore be consistent with the extent of sand sheets. Comparing the paleosand sheets to tsunami simulations is also made difficult by the unknown value and applicability of bottom friction (the simulation assumes zero friction) and unknown tide at the time of deposition (the simulation assumes mean higher high water). With these caveats in mind, we compared sand sheet distribution to inundation on paleolandscapes for two relatively small Cascadia tsunami scenarios that use regional ruptures, Small 9 and Average 9. These two were chosen because they are regional ruptures, and they apply to a wider part of the coast than equivalent local slip patches. Scenario 9 is a buried rupture (no splay fault) on the Cascadia subduction zone. The "Small" version has ~8 m slip and "Average" ~15 m slip at the latitude of Cannon Beach. The small slip scenario produces a tsunami with ~5.5 m water elevation (NAVD 88) at the open coast (Figure 26) and inundation insufficient to cover the ~1,000-year tsunami deposits with or without the foredune at the estuary mouth (Figure 44). The "Average" slip sce-

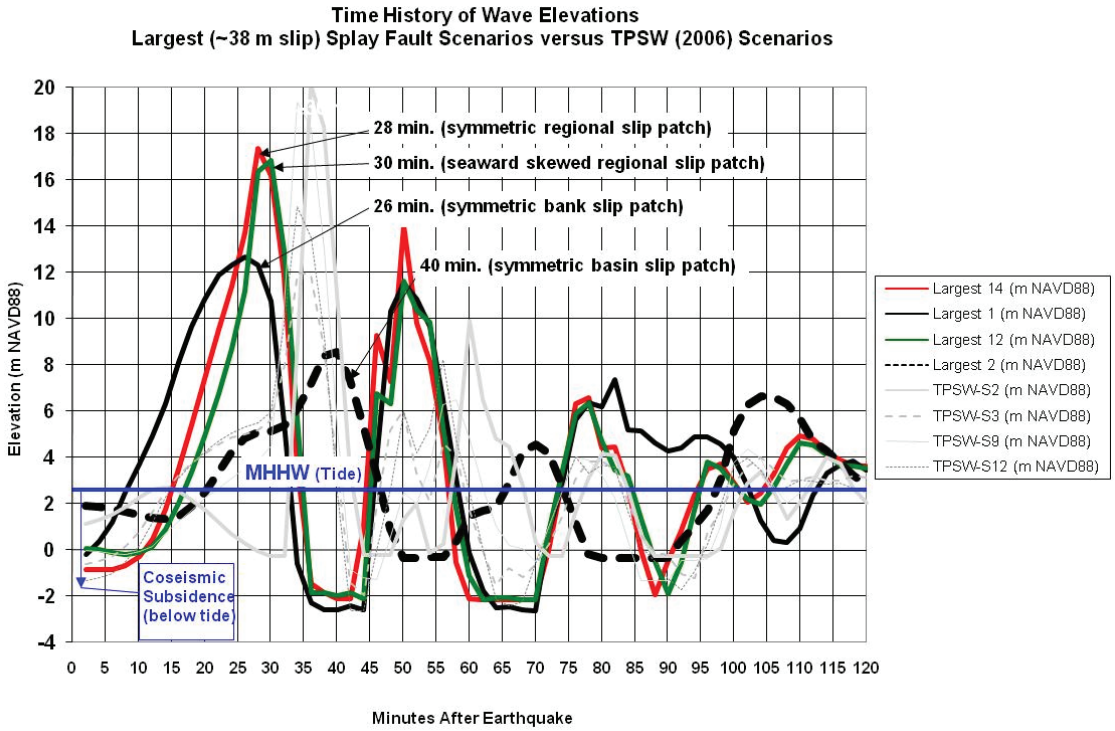

Figure 35. Tsunami arrival times for Cascadia splay fault sources (colored lines) relative to earliest and latest arriving tsunamis from Tsunami Pilot Study Working Group (TPSW, 2006) earthquake sources (light gray lines). Observation point is at the shoreline at point cb009 in Figure 25. Initial arrival times are identical within the 2-minute sampling interval for locations up to 10-m water depth offshore (e.g., see time history data on CD-ROM for point cb016, Figure 25). Largest 14 = symmetric slip distribution, regional slip patch; Largest 1 = local bank slip patch; Largest 12 = seaward skewed slip distribution, regional slip patch; Largest 2 = local basin slip patch. All water elevations start below the prevailing tidal level owing to coseismic subsidence. Note that some water levels continue to decrease in the first 10 minutes after the earthquake; this indicates water withdrawal during arrival of a leading depression wave. (Note: Because time histories for TPSW scenarios were extracted from 2007 simulations, the numerical grid and version of SELFE differs from that used for the other plotted time histories simulated in 2008; however, initial wave arrival times for 2007 simulations are within ±1 minute for 2008 simulations of the same earthquake source).

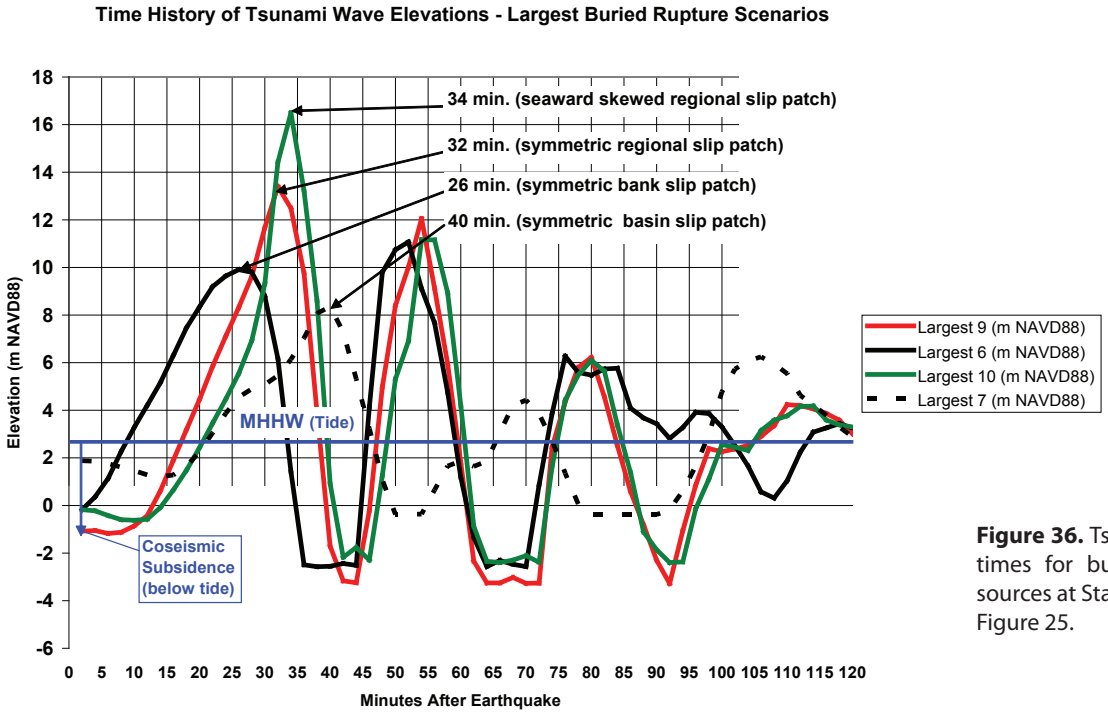

Figure 36. Tsunami arrival times for buried rupture sources at Station cb009 in Figure 25.

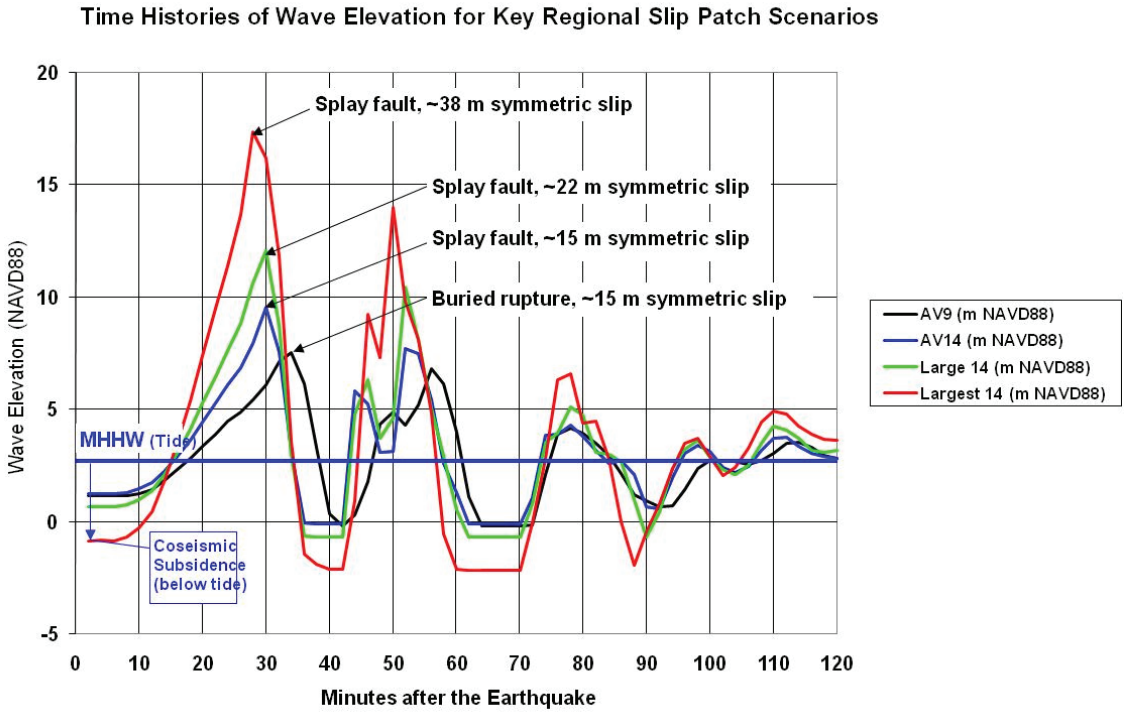

Figure 37. Time histories of wave elevation for key regional slip patch scenarios; observation point at Station cb009 in Figure 25. AV is average.

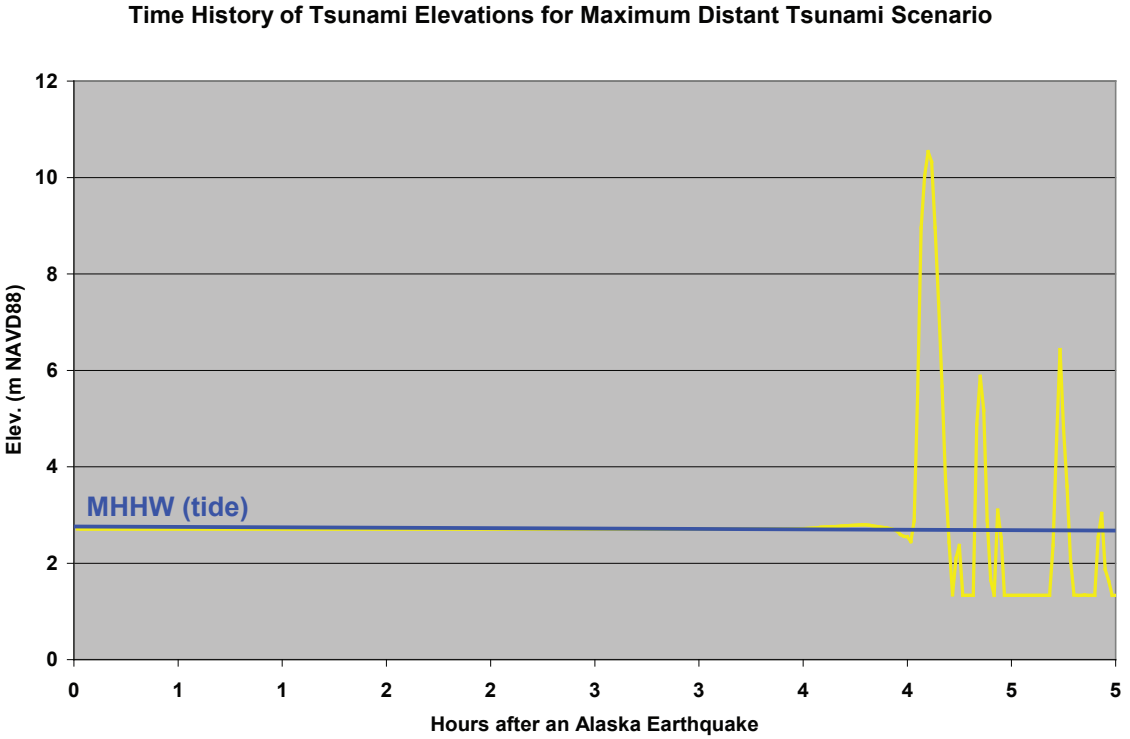

Figure 38. Time history of wave elevation for the maximum considered Alaska tsunami scenario; 5-hour simulation at Station cb009 in Figure 25.

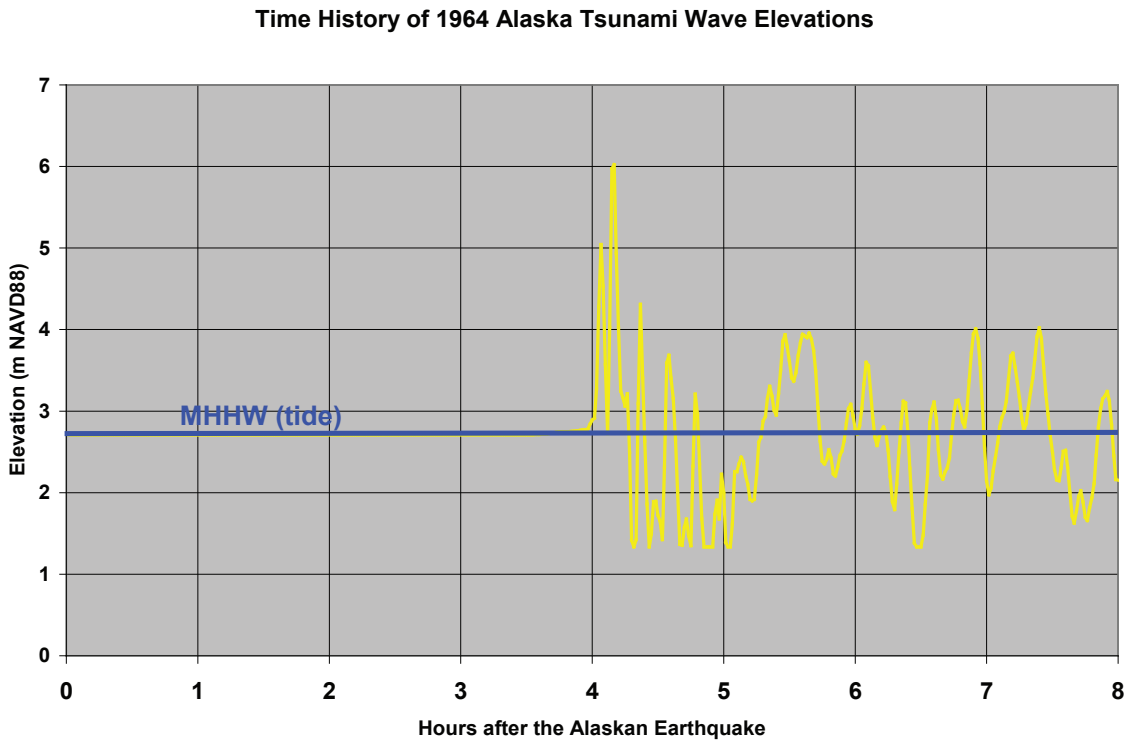

Figure 39. Time history of wave elevation for the 1964 Alaska tsunami scenario; 8-hour simulation at Station cb009 in Figure 25.

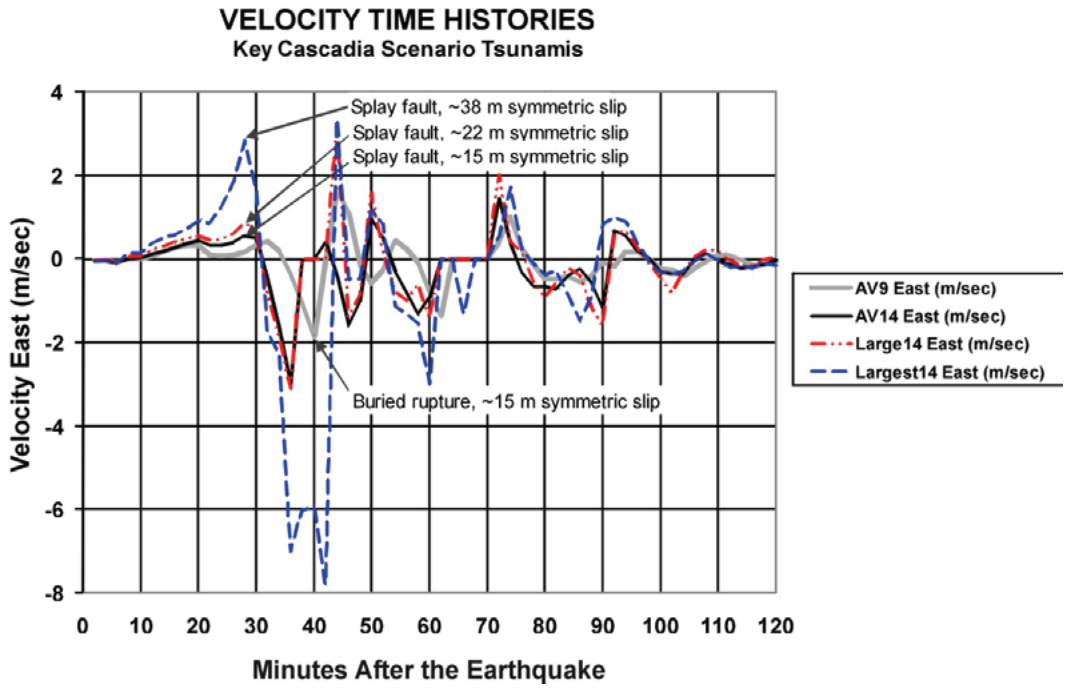

Figure 40. Time histories of tsunami velocity for key Cascadia tsunami scenarios at the open coastal shoreline (Station cb009 in Figure 25). East (landward) = positive velocity; west = negative velocity. One meter per second equals approximately two knots, so maximum velocities vary from ~4 knots for scenario Average 9 to ~16 knots for Scenario Largest 14. AV refers to an "Average" source scenario with ~15 m slip.

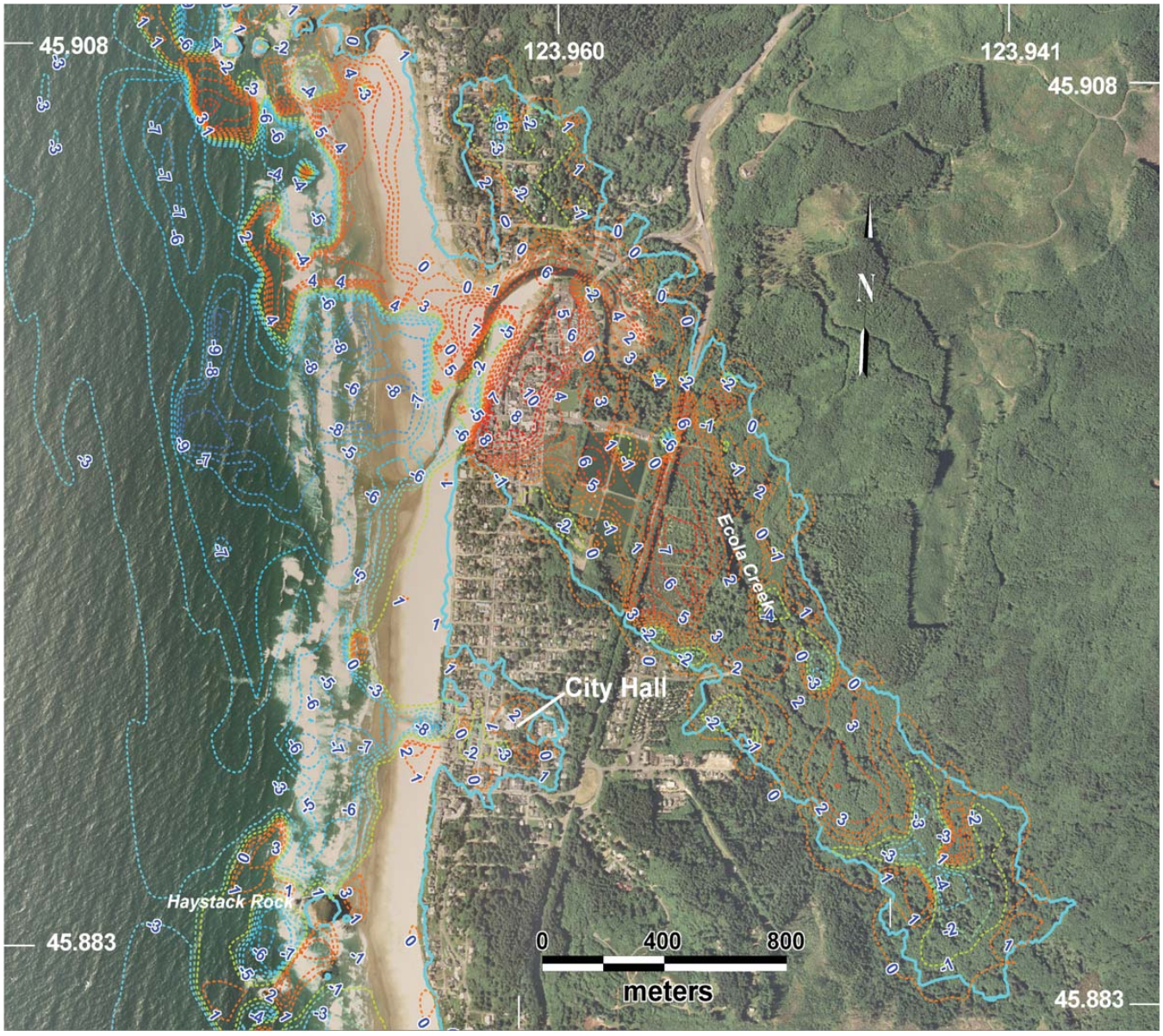

Figure 41. Maximum velocity map for the Average 14 (preferred) tsunami scenario, approximating the ~70 percent confidence level for all variability in velocity for Cascadia tsunami; contoured at 1 m/sec intervals (dashed lines); positive values indicate east velocity; negative values indicate west velocity; thick turquoise blue line indicates maximum inundation for the Average 14 scenario. (Note: Convert meters per second to knots by multiplying by 1.944; to miles per hour by multiplying by 2.237.) The 0 m/sec contour near the beach is an artifact of the change in direction of maximum current velocity between offshore and onshore. This contour marks the boundary where maximum current velocities of the withdrawing waves (negative values) are larger than maximum current velocities of landward surging waves (positive values).

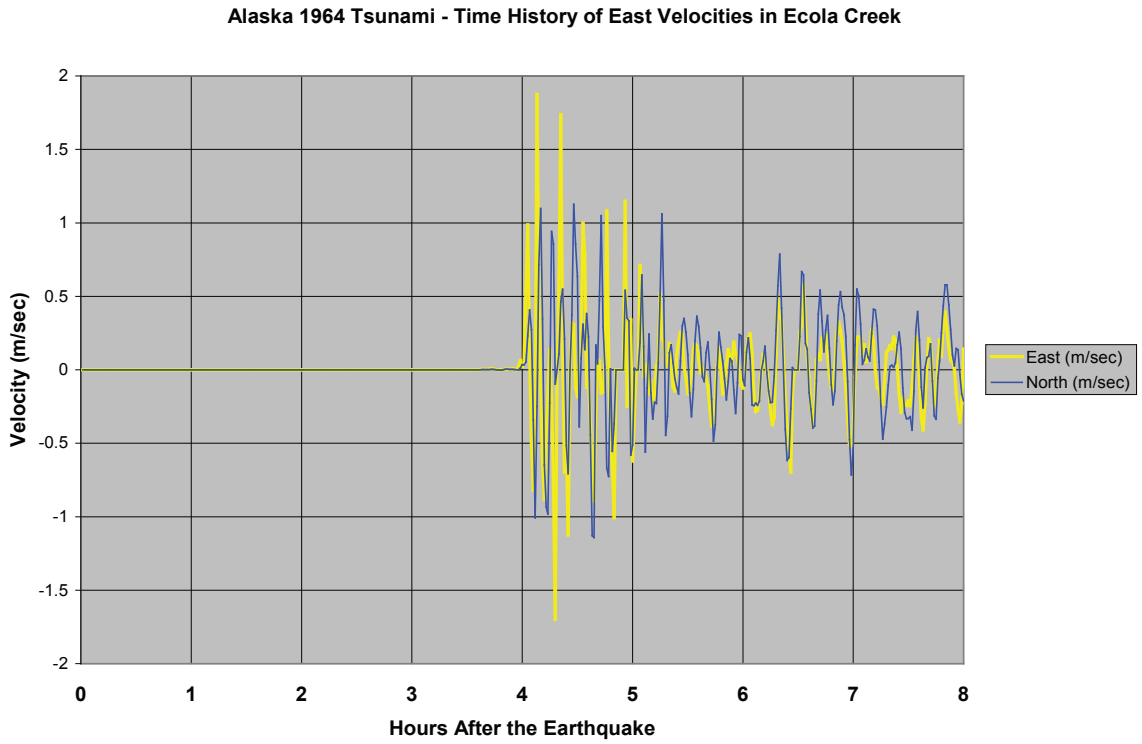

Figure 42. Time history of 1964 tsunami velocities at the open coastal shoreline (Station cb009 in Figure 25); 8-hour simulation. Negative values are west and south vector velocities.

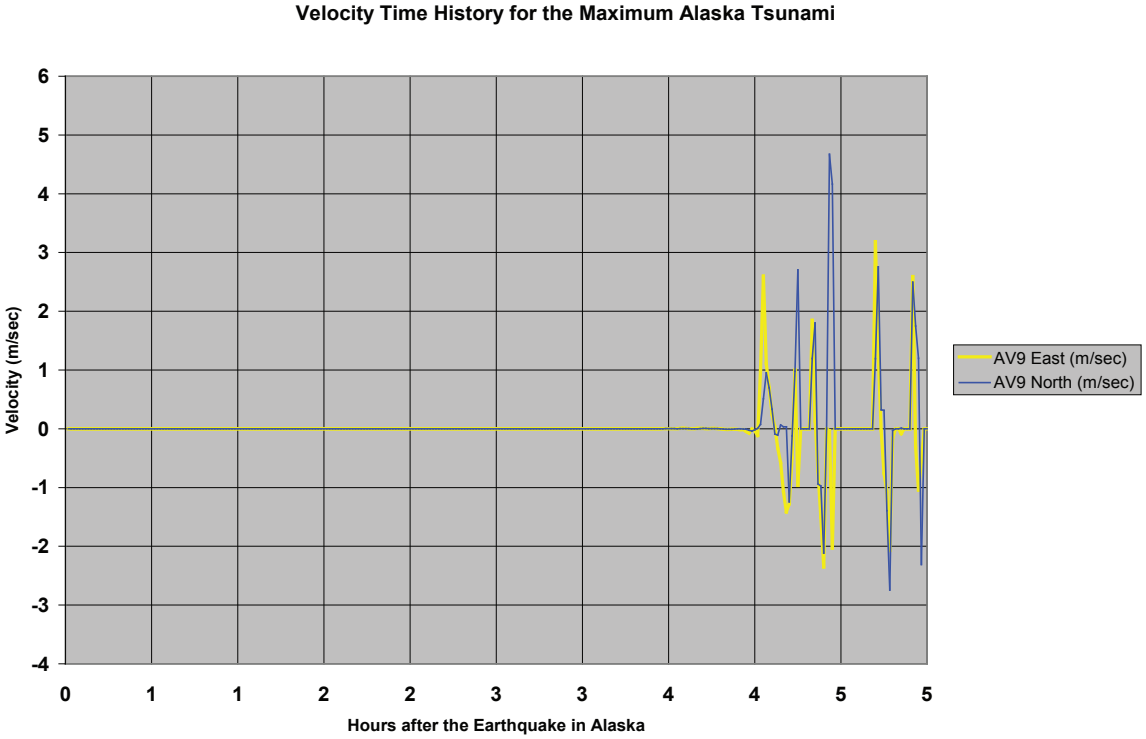

Figure 43. Time history of velocity changes for the maximum distant tsunami scenario at Station cb009 in Figure 25; 5-hour simulation. Negative values are west and south vector velocities.

Table 8. Preferred radiocarbon ages for three sand layers identified as tsunami sands at Cannon Beach, Oregon (data from Witter, 2008).

Sand Layer	Depth (m)	Preferred Age (years before 1950)*
1	0.46	144–270**
2	0.96–1.25	520–800***
3	0.62–1.39	910–980****

* Age ranges rounded to the nearest decade except for historical constraints on the estimate for sand layer 1.
** Upper bound of age range constrained by the year 1806 when Lewis and Clark reached Ecola Creek and written history began in coastal Oregon.
*** Age range represents the sum of probabilities for both ^{14}C ages for sand layer 2. Two samples were dated and met a Xi-square test that shows statistical difference at the 95 percent level.
**** Age range represents 97 percent of the relative area of the calibrated age distribution for the pooled mean age of three ^{14}C dates for sand layer 3. The three ages are indistinguishable based on a Xi-square test for statistical difference at the 95 percent level.

narios with buried ruptures for local bank slip patch (Average 6) or a regional slip patch(Average 9 produced maximum tsunami inundation at or beyond tsunami sand deposits even with a foredune (Figure 44).

We found that basin slip patch scenarios are incompatible with the paleotsunami data. Basin slip patch sources require slip of ~38 m (scenarios Largest 2 and 7) to achieve similar inundation to the "Average" (~15 m slip) buried rupture scenarios (Figure 28). While this scenario is possible, and would be consistent with the distribution of the deposits, it is inconsistent with the slip inferred from times between turbidites in the last ~1,200 years (Table 1).

Other Cascadia scenarios with tsunamis larger than the "Average" buried rupture scenarios are also consistent with paleotsunami deposits (Figures 28 and 29), but only the "Average" bank or regional slip patch scenarios are consistent with both paleotsunami deposits and slip inferred from turbidite data of Table 1. All these "Average" scenarios would be $M_w \geq$ ~8.5 earthquakes (Table 3), but, in reality, the last four Cascadia earthquakes were probably full-margin ruptures based on correlation of turbidites (T1–T4, Figure 4) and were separated by interseismic intervals of ~200 to 400 years (Table 1). Three of the last four turbidites (T1, T3, and T4) are of similar size (Table 1), T1 being associated with a M_w ~9 earthquake, according to Satake and others (2003). Since actual recurrence is less than the 525 years used in the simulations, it may be that splay faulting or some other factor (e.g., slip> turbidite recurrence) amplified uplift during these earthquakes, or that coseismic slip is not simply related to these interseismic intervals. One caveat is that follow time for the last event, T1, is unknown, except that the minimum time is >309 years at the time of this writing. We can infer from Figure 31 that splay fault amplification of inundation for buried ruptures is ~6 percent for "average" slip on a regional slip patch with symmetrical slip. Since inundation is a linear function of slip (Figure 30), we can further infer that involvement of a splay fault would lower the minimum slip from ~15 m to ~14 m and recurrence from 525 years to ~500 years. This recurrence still exceeds the observed interseismic intervals. Turbidite T2 is quite small and the associated earthquake left little record of subsidence or tsunami deposits in estuaries; for example it left no record in southwest Washington (Atwater and others, 1995, 2004). If T2 does not have significant influence on the available coseismic slip, then it suggests that most of the plate motion between T3 and T1 (~530 years) was released in the AD 1700 earthquake, consistent with paleotsunami inundation. The twelve scenarios of the TPSW (2006) have inundation exceeding all of our "Average" scenarios (Figures 28 and 29), so they extend well past the tsunami deposits; hence none can be ruled out by extent of the deposits. However, slip in the high slip patches of these scenarios generally exceeds their average value of 19 m (equivalent to >660 years of plate convergence at the latitude of Cannon Beach), so they would all exceed the slip inferred from interevent times for the last four turbidites contemporaneous with the three paleotsunami deposits, even if turbidite T2 is removed from the recurrence calculations (Tables 1 and 8).

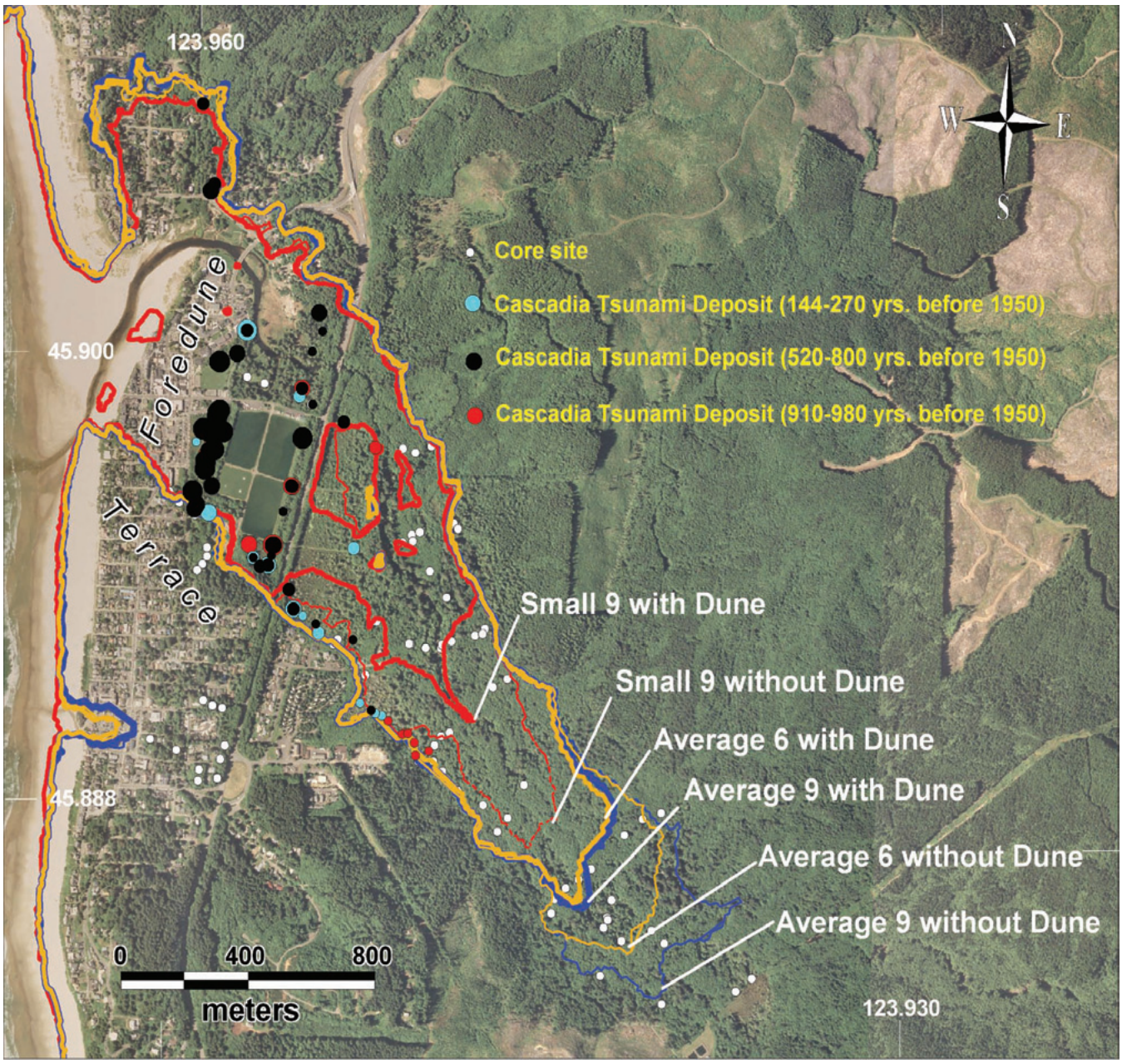

Figure 44. Map of core sites used for the paleoseismic investigation (white dots) and tsunami deposits (colored dots) versus tsunami inundation simulated on a paleolandscape with a foredune and without a foredune. Sizes of dots correspond to relative deposit thickness; all paleotsunami data are from Witter (2008). Note that simulated inundation is ~70 m seaward of the modern coastline; this is caused by translation of the coastline seaward to account for 1,000 years of coastal retreat. Earthquake source scenarios: Small 9 = ~8 m slip, regional slip patch, buried rupture; Average 9 = ~15 m slip, regional slip patch, buried rupture; Average 6 = ~15 m slip, local bank slip patch, buried rupture.

The paleotsunami data, being limited to only three events and compared to simulations of only the 1,000-year event, do not place strong constraints on the full range of scenarios that are possible, given the unknowns such as tide, local bottom friction on land, and unknown characteristics of the causative earthquake. In the offshore paleoseismic record for the last 10,000 years there are turbidites thicker and thinner and with larger and smaller follow times than those contemporaneous with the three Cascadia tsunami deposits (Table 1). Thus it is reasonable to assume that smaller and larger tsunamis than those that deposited

these three sand layers have probably occurred in the last ~10,000 years.

The AD 1700 tsunami deposit is the least widespread of the three mapped in Ecola Creek (Figure 44), whereas the AD 1700 turbidite has the largest thickness/mass of the last four, although it is only slightly larger than two of them (Table 1). If turbidite thickness/mass correlates with earthquake size, then some other factor must account for the mismatch. We speculate that this factor is contemporary tide. Mofjeld and others (1997) inferred that the AD 1700 tsunami (youngest Cascadia deposit) occurred during a relatively low, neap tide all along the West Coast. We estimate from his data that the AD 1700 tsunami arrived at Cannon Beach on a neap tide at ~0.8 m NAVD 88, ~1.9 m lower than our simulated static tide. Myers (1999) and Myers and Baptista (2001) showed that a dynamic tide has strong nonlinear effects on tsunamis, so the combined effect of a withdrawing tidal current and lower tidal elevation should decrease inundation in AD 1700 relative to our simulations and relative to tsunamis with higher or flood tides. It is beyond the scope of this investigation to do dynamic simulations of tsunamis and tides to test more fully this hypothesis.

Coseismic Subsidence

At the latitude of Cannon Beach simulated offshore coseismic subsidence for all Cascadia scenarios ranged from 0.3 to 3.9 m, increasing with more slip (Figures 21 and 45). Simulated subsidence at Cannon Beach was in the same range. For the preferred scenario, Average 14, coseismic subsidence was 1.4 m at Cannon Beach (Figure 45).

Paleoseismic subsidence for the AD 1700 event from Leonard and others (2004) generally matched Large to Average slip scenarios better than Small or Largest slip cases (Figure 45). The one Small scenario used in the investigation, Small 9, matched best to the coseismic subsidence estimates of Nelson and others (2008) for the last four Cascadia earthquakes (Figure 45). The paleoseismic subsidence appears less variable from north to south than is predicted by the local slip patch scenarios (top four graphs in Figure 45), matching regional rupture scenarios somewhat better (bottom four graphs in Figure 45). However, the northern limit of our northernmost local bank slip patch scenario, centered on Nehalem Bank (Figures 12 and 16), is arbitrary and not defined by geophysical data offshore. This slip patch may extend farther north or may become a long regional patch as suggested by GPS and leveling data (McCaffrey and others, 2007; Burgette and others, 2007, 2009). If this is the case, fit to the bank models is improved. Most of the TPSW scenarios exceeded paleoseismic deformation along the coast (Figure 45). Neither the TPSW nor our scenarios closely match the pattern of paleosubsidence in the east-west cross section up the Columbia River (Figure 46). This may be due to too broad of a landward transition zone on the megathrust, interaction with other upper plate faults and structures, or other factors. Alternatively, some of these paleosubsidence data may be of low quality according to the rating system of Leonard and others (2004).

However, reanalysis of contemporary leveling data led Schmidt and others (2007) and Burgette and others (2007, 2009) to conclude that the modern interseismic data support a downdip locked zone boundary similar (at least in map pattern) to that suggested from paleosubsidence data for the AD 1700 earthquake of Leonard and others (2004). Residuals from that study indicate that the locked/transition zone, which swings shoreward in northern Oregon (as it does in our models), would satisfy the data somewhat better if it swung farther shoreward in northern Oregon (opposite Nehalem Bank). The GPS models of McCaffrey and others (2007) are substantially similar in indicating an onshore trend of the locked zone in northern Oregon. If this is the case, and the leveling, GPS, stress, and structural data are correct, the bank and regional rupture models would be consistent, fitting the form if not the details of the Columbia River data well, while the basin models do not. Alternatively, Nelson and others (2008) suggested a narrow offshore position of the locked zone based on improved paleoseismic subsidence data; however, we consider that the preponderance of the evidence presently suggests the opposite case for northern Oregon and southwest Washington. For these reasons, and the previously mentioned poor match of basin slip patch scenarios to paleotsunami inundation, we placed a lower logic tree weight on those scenarios relative to both regional rupture and local bank slip patch cases.

Data Files

One objective of the investigation is to establish a template for tsunami hazard assessment on the northern Oregon coast. To this end, we provide digital data

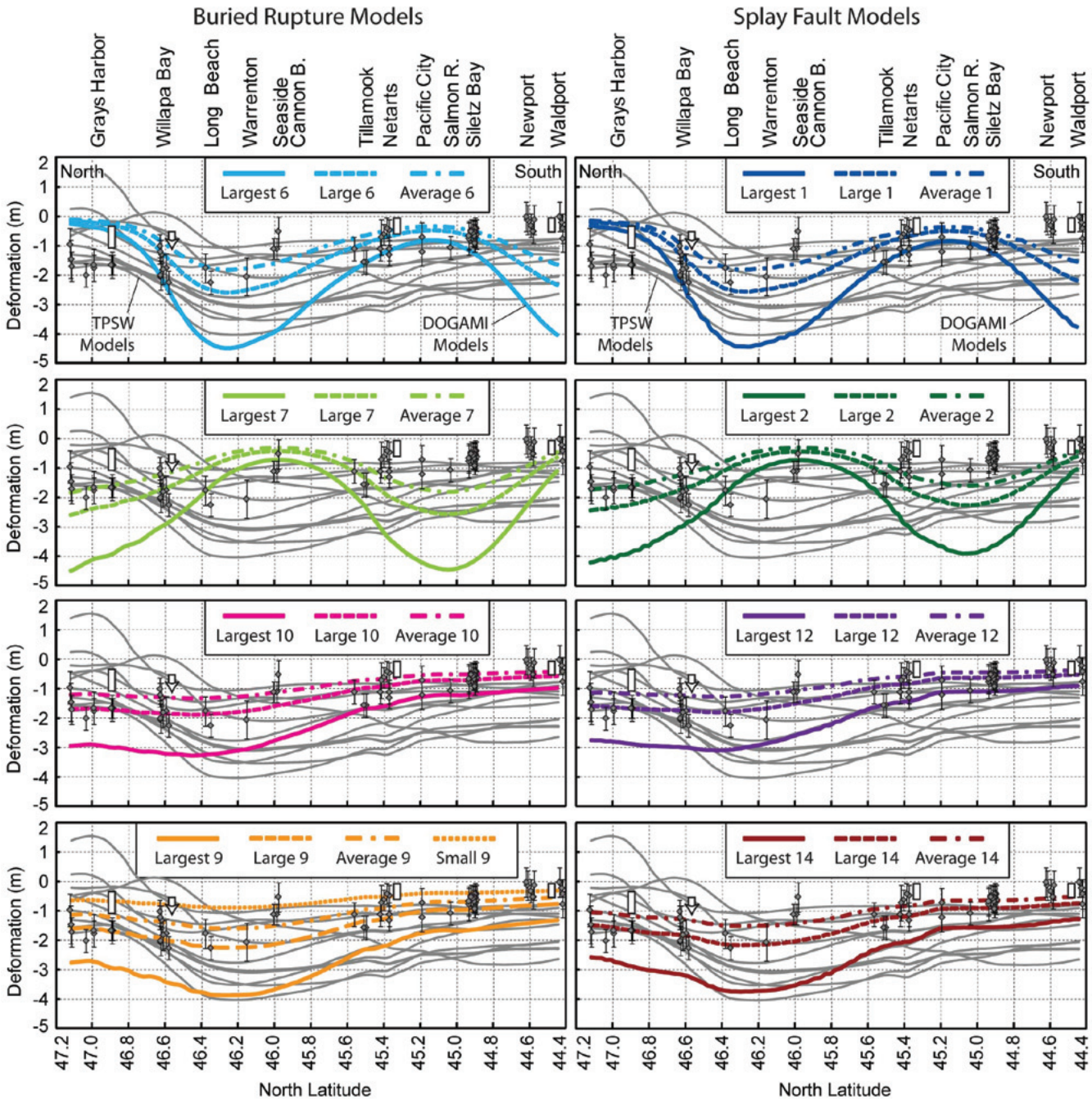

Figure 45. Correspondence at the outer coast of scenario coseismic deformation to paleosubsidence data for the AD 1700 Cascadia earthquake of Leonard and others (2004) (diamonds with error bars) and Nelson and others (2008) (open bars; one open arrow indicating that value is a minimum for the locality). Scenarios S1 to S12 (gray lines) are from TPSW (2006); colored lines are from scenarios of this investigation. Note that many TPSW scenarios overestimate subsidence as do many of the "Largest" scenarios of this investigation. B is beach; R is river.

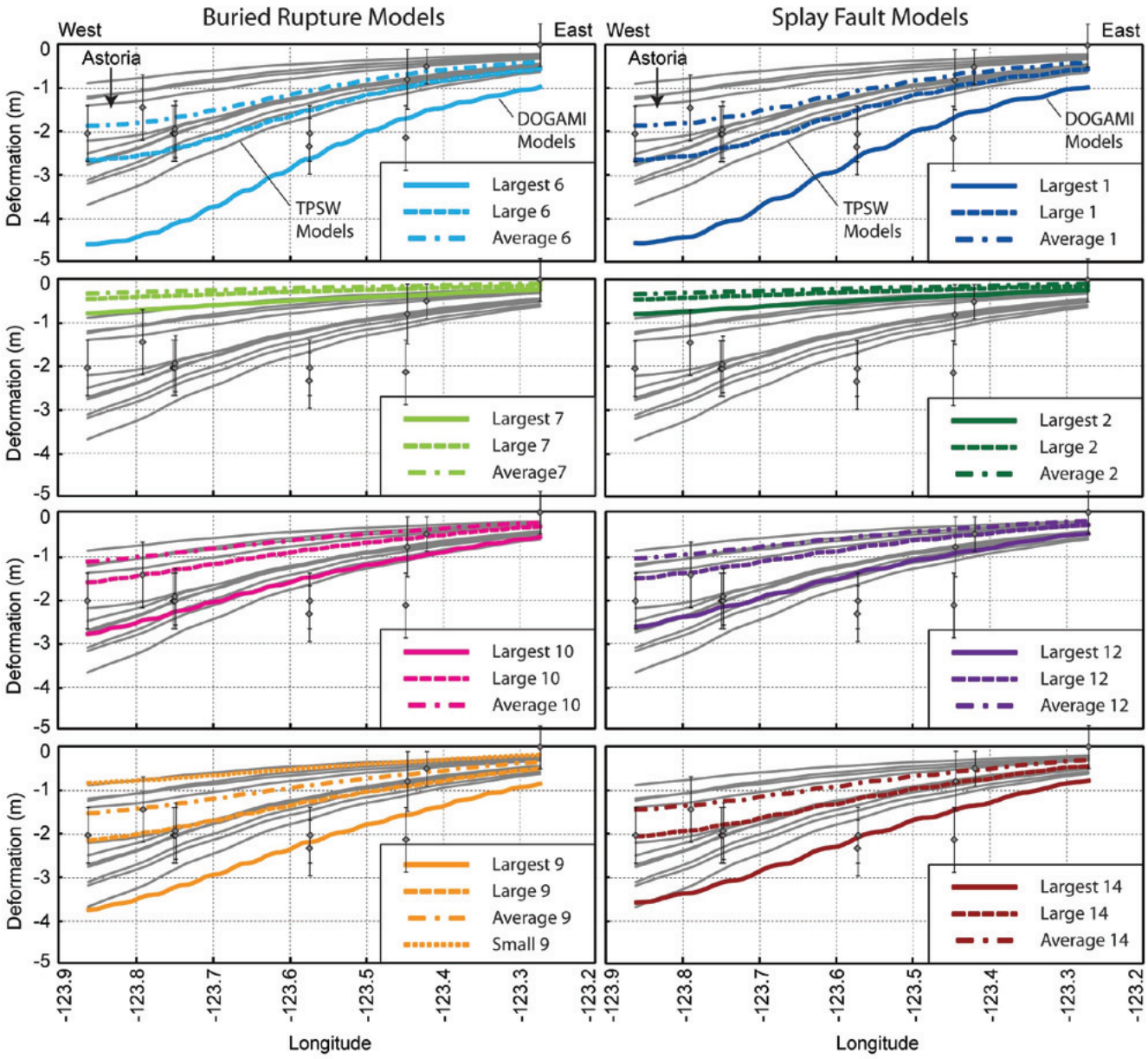

Figure 46. Correspondence from Youngs Bay east along the Columbia River of scenario coseismic deformation to paleosubsidence data of Leonard and others (2004) for the AD 1700 Cascadia earthquake (diamonds with error bars). Scenarios S1 to S12 (gray lines) are from TPSW (2006); colored lines are this investigation. None of the scenarios fully capture the pattern of subsidence in the paleosubsidence data, but the "Largest" scenarios of this investigation and many of TPSW scenarios overestimate subsidence toward the west (open coast).

files of all earthquake source deformations. We also provide the source code for SELFE, numerical grids, and output data to empower other investigators to compare their results to ours.

In addition to tsunami time histories and animations, the DVD contains data files and metadata in standard ASCII format for:

- initial conditions (coseismic deformations) for tsunami simulations
- maximum tsunami elevations and flow depths (flow depth listed as "inundation")
- maximum tsunami velocities
- numerical grid for modern topography
- numerical grid for paleotopography with the foredune
- numerical grid for paleotopography without the foredune
- *x*-*y* data for time history graphs of velocity and wave elevation

The DVD also contains vector GIS files for:

- computer-generated inundation boundaries for all scenario tsunamis
- isolines of cumulative logic tree weight for inundation

COMPARISON OF RESULTS TO PREVIOUS STUDIES

RELATIONSHIP TO PROBABILISTIC TSUNAMI HAZARD ASSESSMENTS

In Figure 29, we show a map of percent confidence that we have captured variability in Cascadia tsunami inundation. Figure 29 is not a map of probability of inundation. The map depicts the variation in extent of inundation from a range of deterministic Cascadia earthquake scenarios, all with $M_w \geq 8.3$, that fall within the uncertainties of the tsunami source parameters. The probability of a Cascadia tsunami is directly related to the recurrence interval of great Cascadia subduction zone earthquakes, ~500 to 530 years for the northern margin (Petersen and others, 2002; Goldfinger and others, 2009). This recurrence amounts to a probability of 10 to 14 percent (Petersen and others, 2002) or 7 to 9 percent (Goldfinger and others, 2009) in the next 50 years and possibly lower if the clustering model of Goldfinger and others (2009) is applicable

The approach employed by this study does not follow standard methods applied in probabilistic tsunami hazard assessments (PTHA) performed along other coastlines facing tsunami risks. PTHA methods have been derived from the probabilistic seismic hazard analysis (PSHA) method originally developed by Cornell (1968), which is now considered the standard of practice for projects that require seismic hazard analyses (Senior Seismic Hazard Analysis Committee, 1997) and in developing the U.S. national seismic hazard maps (Frankel and others, 2002). The primary difference between the two methods is that PTHA uses numerical tsunami propagation models to predict runup height, whereas PSHA employs empirical attenuation models to determine ground motions. For example, Geist and Parsons (2006) used empirical methods and Monte Carlo simulations to compute the probabilistic tsunami hazards for Acapulco, Mexico and the U.S. Pacific Northwest. Annaka and others (2007) used a logic tree approach to calculate tsunami hazard curves to quantify the risk to important coastal facilities in Japan. Power and others (2007) used Monte Carlo techniques to estimate probabilistic tsunami hazards along the coastline of New Zealand caused by South American subduction zone earthquakes.

Our approach differs from a PTHA performed for Seaside, Oregon (TPSW, 2006). As part of FEMA's Map Modernization Program, the purpose of the Seaside pilot study was to produce maps showing tsunami wave heights with 1 percent and 0.2 percent annual probability of exceedance and thereby demonstrate a methodology to improve FEMA Flood Insurance Rate Maps (FIRMs). Source specifications for the tsunami simulations included 14 far-field earthquake sources using parameters from the NOAA/PMEL FACTS database (Titov and others, 2005) and an additional 12 Cascadia earthquake source models that compute stochastic slip distributions that are constrained by a constant seismic moment (e.g., Geist, 2002). Departing from standard PTHA methods that compute a hazard curve for a point on the coastline (e.g., Geist and Parsons, 2006; Annaka and others, 2007; Power and others, 2007), the TPSW (2006) developed a probabilistic tsunami inundation map of the City of Seaside and surrounding communities. Generation of 100- and 500-year maps

proceeded by calculating a hazard curve for each grid cell and then mapping exceedance wave heights for the 1- and 0.2-percent annual probabilities using GIS techniques.

We see two limitations to the approach used for the Seaside pilot study (TPSW, 2006) for depiction of the tsunami hazard dominated by a large local source like the Cascadia subduction zone. First, the maps do not express the range of tsunami inundation and runup that is a product of the uncertainty associated with alternative models for Alaska and Cascadia subduction zone earthquakes. For example, only one, relatively large magnitude of earthquake is explored for Cascadia, albeit with many slip distributions. Second, as a result of this approach, the maximum tsunami wave heights plotted on the 100- and 500-year maps are determined by the smallest tsunami inundations. This may be an appropriate method to use for independent far-field earthquake sources but it biases the maps toward the smallest tsunami scenarios when depicting uncertainty in source parameters for a single local earthquake source like the Cascadia megathrust. Because a tsunami flows from the ocean toward the land, hazard curves for grid cells at the shoreline naturally predict higher flow depths than inland grid cells for the same recurrence rate. Therefore, maps developed using alternative source models for a particular earthquake source with a 500-year average recurrence interval will depict only the results of the minimum tsunami scenario on the 500-year probabilistic inundation map. In other words, inundation and flow-depth hazard maps at the 500-year exceedance level will not show equally or more likely larger tsunami scenarios, because grid cells flooded only by these scenarios will have less than a cumulative probability of 1.0 for all 500-year events considered. The size of the minimum scenario tsunami thus determines the degree of underestimation of potential hazard at the 500-year exceedance isoline, but hazard will always be underestimated relative to the preferred or most likely event. In contrast, for most PTHA of far-field tsunamis, each scenario is an independent preferred or most likely scenario for each seismic source assigned a certain probability, so areas of overlapping inundation from multiple sources have the sum of these probabilities, resulting in a somewhat more reasonable assessment of hazard.

COMPARISON TO PREVIOUS TSUNAMI HAZARD ASSESSMENTS FOR OREGON

Previous tsunami inundation mapping for Cannon Beach was based on source scenarios that approximate our "Average" to "Small" slip models. Whitmore (1993) provided the City of Cannon Beach with an estimate of Cascadia tsunami open coastal wave elevation on the order of 6 m (NAVD 88) from an M_w 8.8 earthquake with 9 m of slip. This scenario had broad areas with ~1.5 m uplift, corresponding most closely to our Small 9 scenario (Figure 21). Priest (1995a) in collaboration with the Oregon Graduate Institute of Science and Technology simulated open coastal wave elevations for the Whitmore source and for Cascadia sources with 11.5 and 10.5 m slip on a planar fault dipping 12.1°. Priest (1995a) used open coastal tsunami elevation data for the source with 11.5 m slip, a fully locked width of 66 km, and broad uplift of ~2.5 to 3 m to map inundation for the entire Oregon coast for implementation in 1995 of Oregon Senate Bill 379 (now Oregon Revised Statutes 455.446 and 455.447). The bill limited new construction of critical, essential, and hazardous facilities in potential tsunami inundation areas (Olmstead, 2003). Maximum tsunami elevation at the open coastal shoreline (Priest, 1995a, Appendix B, model 2 data) is essentially the same as the preferred Cascadia scenario of this study, Average 14 (Figure 26), about 9.6 m NAVD 88 (8.5 m NGVD29 in the original publication). We cannot compare our simulated maximum runup to the 1995 data, because the older study did not have enough grid refinement to simulate runup or inundation. Inundation mapped by Priest (1995b, 1995c) differs from Average 14 in detail (Figure 47) because the 1995 inundation was not numerically simulated but estimated from a simulation of open coastal wave height.

Priest and others (1997) used a more realistic, curving Cascadia subduction zone fault with linear landward taper of slip for construction of 11 Cascadia sources, four of which were used for State of Oregon inundation mapping in subsequent years (i.e., Priest and others 1998, 1999a, 1999b, 2000a, 2000b, 2004, 2007) to construct inundation maps from simulation of tsunamis from three earthquake sources per map. The sources were: (1) a segment rupture 450 km long with slip equaling 225 years of plate convergence (model 2Cn for a segment north of Cape Foulweather; model 2Cs to the south); (2) a rupture 1,050 km long

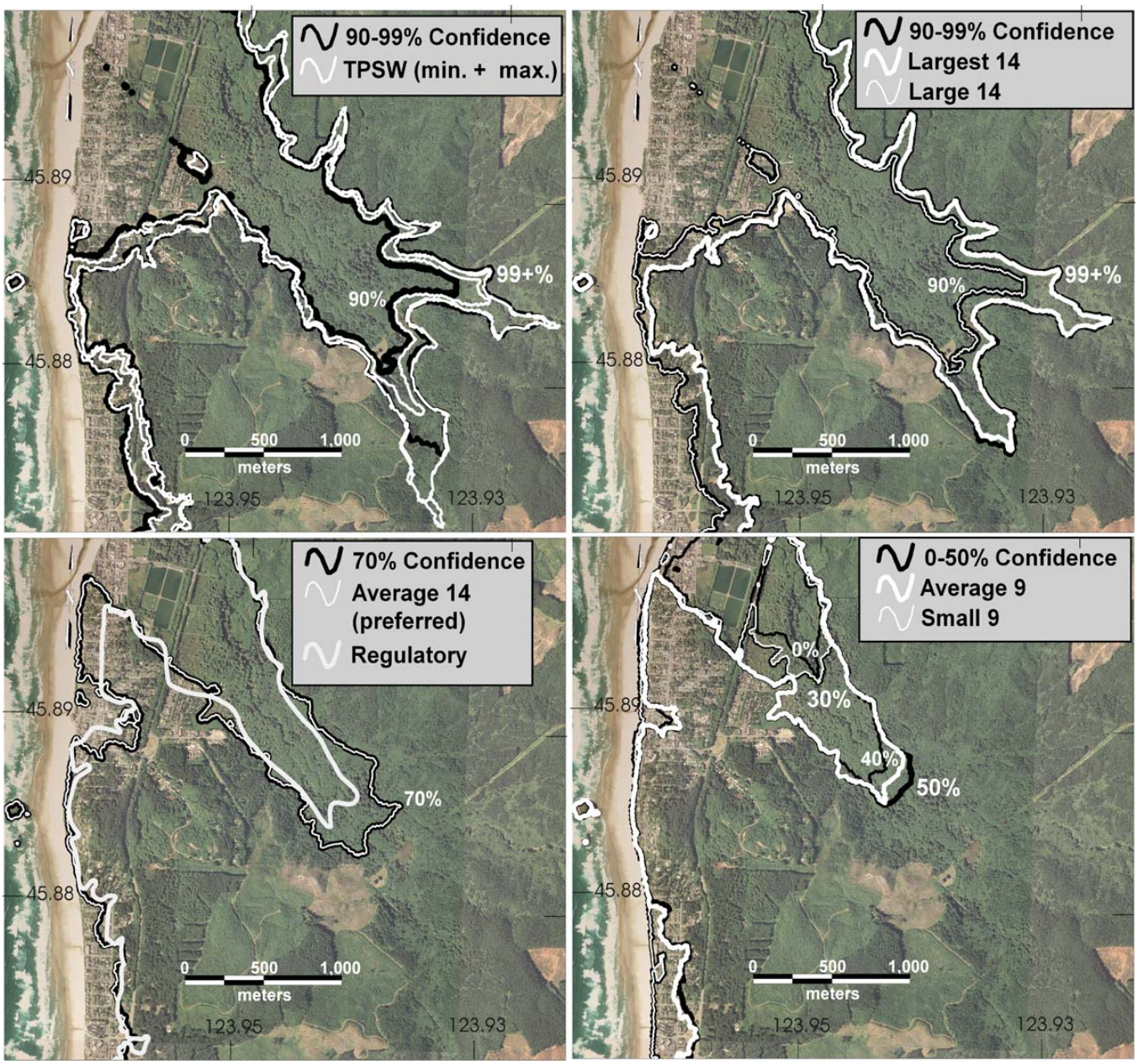

Figure 47. Relationship between isolines of percent confidence and key inundation boundaries. The isolines depict confidence that inundation for a Cascadia tsunami with ~500-year recurrence will be less than the isoline. Upper left map illustrates extension of largest TPSW scenarios past the largest inundation of this investigation (99 percent isoline). The minimum inundation from TPSW sources is also plotted on the upper left map and approximates the 96 percent inundation line (not plotted). Upper right map shows the close correspondence of the Large 14 scenario to the 90 percent isoline and the Largest 14 scenario to the 99 percent isoline. Lower left map demonstrates the exact correspondence of the 70 percent isoline with the Average 14 (preferred) scenario and similarity of both to the tsunami regulatory line affecting the building code in Oregon. Lower right map illustrates the relationship of inundation from the Average 9 source (~15 m slip on buried subduction zone rupture) and the Small 9 source (~8 m slip) to isolines.

with slip equaling 450 years of convergence (model 1A); and (3) a maximum event simulating the largest uplift from the 1964 Prince William Sound earthquake (model 1A-Asperity). The latter source was constructed in central Oregon by placing a Gaussian uplift of 3 m centered about 60 to 80 km offshore on the model 1A source. Model 1A in central Oregon is a Cascadia rupture approximately 70 km wide with 35 km of uniform slip and 35 km of linear landward taper of slip. Model 1A uplifted a broad area about 3 m, so adding the 3-m Gaussian mound achieved the 6 m uplift estimated by Holdahl and Sauber (1994) for the largest asperity in the Alaska earthquake. This uplift is smaller than several of the largest sources of this study and lies at about the same distance offshore as the maximum uplift in our scenarios (Figure 21). This degree of uplift corresponds to "Average" splay fault scenarios and "Large" buried rupture scenarios but is smaller than "Large" splay fault and "Largest" scenarios with ~38 m of slip (Figure 21). Tsunami wave elevation at the open coast was generally about 20 to 50 percent higher for the 1A-Aperity relative to the 1A scenario (e.g., Priest and others, 1997, 2002). Simulation of the 1A-Asperity scenario at Cannon Beach in early trials produced runup similar to the 1A. The reasons for this are not entirely clear but appear to be from complex wave refraction and interference. The two segment ruptures, models 2Cn and 2Cs, caused ~1.5 m uplift over broad areas and are most similar to the Small 9 scenario (Figure 21).

Comparison to Cascadia Scenarios of Tsunami Pilot Study Working Group

TPSW (2006) Cascadia earthquake sources produced tsunamis much larger than most of Cascadia tsunamis of this investigation. Tsunami simulations of the 12 Cascadia earthquake sources of TPSW (2006) allowed direct comparison of tsunamis produced from our sources to that study. TPSW sources simulate coseismic deformations from magnitude 9 earthquakes with a constant moment but stochastically varied slip distribution. These scenarios generally concentrate slip within 30 km of the deformation front, producing corresponding uplift and subsidence in deeper water than most of the scenarios considered here (Figure 21). Nearly all TPSW scenarios produce a leading depression wave (e.g., Figure 35) that amplifies runup (Tadepalli and Synolakis, 1994). The leading depression wave combined with deformation in deeper water produces runup and inundation equal to or larger than the "Largest" source scenarios of this investigation with ~38 m of slip (Figures 27 and 28). All TPSW inundations equal or exceed our isolines of percent confidence at the 96th percentile(Figures 28 and 29). As previously mentioned, all TPSW inundations exceed the extent of the three Cascadia paleotsunami sand deposits, some by a wide margin. All are at least not inconsistent with extent of paleotsunami deposits for the last ~1,000 years, since we do not know the degree to which inundation exceeds sand transport. As previously explained, the TPSW mean slip of 19 m and larger maximum slips exceed slip inferred from turbidite interevent times over the last 1000 years.

TPSW Cascadia earthquake sources produced coseismic deformation with a poorer match to paleoseismic data than our sources. We used paleoseismic estimates of coseismic subsidence for the AD 1700 Cascadia earthquake to evaluate our scenarios and those of TPSW. Relative to previous events, this earthquake was probably close to an "average" magnitude 9 event based on thickness of the offshore turbidite and inland reach of the tsunami deposit at Cannon Beach. The TPSW sources generally show much greater coastal deformation relative to paleoseismic estimates for this event, whereas deformation for all but our "Largest" scenarios overlapped the paleoseismic estimates more closely (Figure 45). This is no surprise, as our source scenarios for the regional rupture cases were constrained to match paleosubsidence, but a more fundamental reason is that TPSW sources use much less down dip taper of slip than do our scenarios (E. L. Geist, personal communication, 2007). Relative to the highest quality paleosubsidence estimates for the AD 1700 earthquake (Leonard and others, 2004; Nelson and others, 2008), nearly all scenarios (ours and TPSW) predict greater coseismic deformation to some extent (Figure 45). Better correspondence to these high-quality data in central Oregon could probably be achieved by narrower scenario ruptures (moving deformation offshore) or wider ruptures (moving the "hinge line" between subsidence and uplift nearer the coast). The latter conflicts with estimates of the width of the locked zone from thermal, geologic, geophysical, and geodetic data for central Oregon (e.g., Hyndman and Wang, 1995) but is consistent with these data in northern Oregon and southwest Washington. As previously explained, a relatively wide locked zone at the Columbia River is consistent with the large paleosubsidence inferred from the Leonard and others (2004) data (Figure 46) and modern geodetic data of Schmidt and others (2007), Burgette and others (2009), and McCaffrey and others (2007).

Our inferred sharp change in width of the coseismic rupture in northern Oregon ("stress line" of Figure 12 and regional slip patch scenarios of Figure 16), is thus consistent with the overall pattern of geodetic and paleoseismic observations but could probably be somewhat larger, swinging somewhat farther inland at the Columbia River and slightly farther offshore to the south. These modest changes in rupture width are unlikely to cause large changes in tsunamis, because changes of rupture width of ±20 km produced similar tsunami (Figures 23 and 24).

COMPARISON OF CASCADIA TSUNAMI TO THE 2004 SUMATRA TSUNAMI

One of the objectives of the investigation was to assess whether a Cascadia earthquake similar to the December 26, 2004, Sumatra-Andaman earthquake could occur and, if so, what tsunamis might be produced. "Large" (~22 m slip) splay fault scenarios and a few "Largest" (~38 m slip) buried rupture scenarios roughly match coseismic deformation inferred from two tsunami inversions for the Sumatra earthquake (Figure 48). Open coastal runup from these Cascadia analogues to Sumatra generally fall between the 95 and 99 percent confidence isolines for capturing all variability for a Cascadia event, so an event as severe as the 2004 Indian Ocean tsunami would be considered rare but possible. Coseismic uplift inferred from tsunami inversions of the Indian Ocean tsunami appears more consistent with our source scenarios than sources with extreme seaward skew of slip like those of TPSW (2006). Coseismic deformation for many of the TPSW (2006) scenarios was closer to the deformation front than estimated for even the most seaward uplift inferred from Suma-

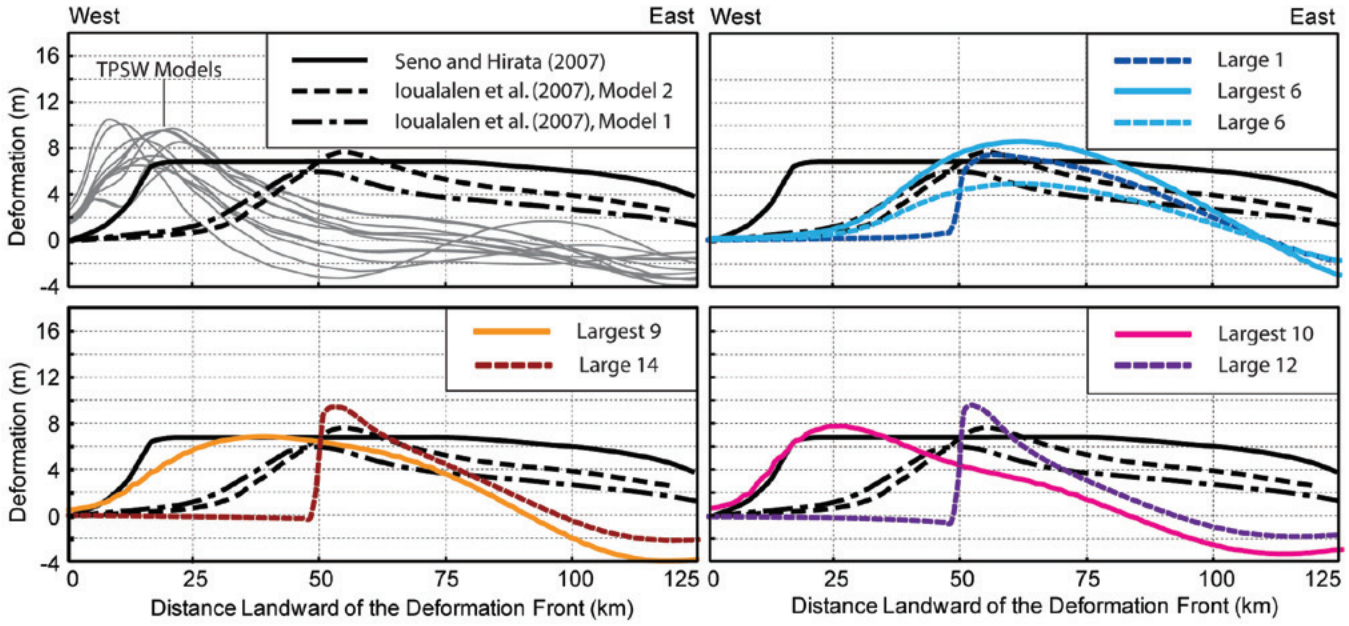

Figure 48. Cross sections of selected coseismic deformation of Cascadia earthquake scenarios of this investigation (colored lines) most similar to inferred deformation for the 2004 Sumatra–Andaman earthquake near the latitude of Banda Aceh, Indonesia (black lines); Cascadia source scenarios of the TPSW (2006) are shown for comparison (gray lines). Cascadia scenarios: Large 1 = ~22 m slip, splay fault, local bank slip patch; Largest 6 = ~38 m slip, buried rupture, local bank slip patch, symmetrical slip; Large 6 = ~22 m slip, buried rupture, local bank slip patch, symmetrical slip; Largest 9 = ~38 m slip, buried rupture, regional slip patch, symmetrical slip; Large 14 = ~22 m slip, splay fault, regional slip patch, symmetrical slip; Largest 10 = ~38 m slip, buried rupture, regional slip patch, seaward -skewed slip; Large 12 = ~22 m slip, splay fault, regional slip patch, seaward-skewed slip.

tra tsunami inversions (i.e., Seno and Hirata, 2007), although some TPSW and few of our largest-slip, buried rupture scenarios were fairly close to this model (Figure 48). Well-constrained tsunami inversions for Sumatra deformation from Ioualalen and others (2007) produce sources with uplift maxima ~50 to 60 km landward of the deformation front, similar to most of our scenarios, though somewhat seaward of the geodetic and seismologic models, and far from the TPSW pattern (Figure 48). Well-constrained geodetic slip models of the 2004, 2005 and 2007 Sumatran earthquakes (Chlieh and others, 2007; Hsu and others, 2006; Konca and others, 2008) show that slip was concentrated in the forearc highs and tapered both updip and downdip (Figure 10), similar to our regional rupture model and bank slip patch models. This was further supported by GPS data showing updip and downdip afterslip into the updip and downdip transition zones respectively. However, considerable uncertainty remains in the link between these models and the actual generation of the 2004 tsunami from coseismic displacement of the seafloor.

Coseismic deformation for the Sumatra earthquake is at ~1 km greater water depths than geologically equivalent areas of the Cascadia subduction zone, and the locked zone width is significantly greater, so more water is displaced and larger tsunamis should be produced in Sumatra for equivalent earthquake deformation. For example, the Cascadia source scenario most similar to the Ioualalen and others (2007) source, Largest 6 (buried rupture with ~38 m slip, Figure 48), produced maximum runup ~10 m lower than observed over most of the Sumatran coast nearest to the 2004 rupture. Most of the Cascadia tsunami simulations of this investigation produced open coastal runup approaching the ~30 m reported on the northwest coast of Sumatra (Tsuji and others, 2005) only when slip was ~38 m on a splay fault. This much slip simulates a very large Cascadia earthquake that may have occurred just once in the last 10,000 years, according to interpretations of turbidite data (Table 1), and like all of our simulations, includes the assumption of full plate locking and full release in each earthquake. A third assumption is that this splay fault source has all slip partitioned to the splay fault. These three assumptions are unlikely to be correct, but we have no basis for modeling alternatives at this time. The emergency planner cannot take too much comfort from the rarity of these extreme Cascadia events, because, as previously mentioned, turbidite data appear consistent with the Cascadia subduction zone following a time-predictable pattern of seismic energy release. This means that 8.9 m of plate convergence since the last Cascadia earthquake 309 years ago does not limit possible earthquakes at present to Cascadia events with only 8.9 m of slip.

DISTANT TSUNAMI SCENARIOS

The maximum considered distant tsunami is similar to many Cascadia tsunami scenarios but is a very low probability event compared to the largest historical event, the 1964 Alaska tsunami. The maximum considered distant tsunami scenario had optimal directivity of tsunami energy toward the northern Oregon coast from the Gulf of Alaska (TPSW, 2006) and produced tsunami inundation and runup corresponding to 40 to 60 percent of the variability in inundation for Cascadia scenarios (Figures 28 and 33). The tsunami reached a maximum 10- to 12-m runup at the open coast and inundated 2.3 km up Ecola Creek. The 1964 event produced runup of only 6 to 7.5 m and inundation of 1.4 km at Ecola Creek, corresponding to the lowest Cascadia tsunami (Figures 26 and 28). The hypothetical earthquake source had an anomalous "spike" of uplift owing to a singularity in the fault dislocation model (Titov, 2008 personal communication) and a highly simplified geometry with no taper of coseismic slip landward or seaward of the simulated locked zone Whereas these shortcomings are of less importance for simulation of distant tsunamis than local events, we concur with the TPSW (2006) assessment that this hypothetical scenario is a very low probability event. The 1964 tsunami is the largest historical event and is probably a more realistic maximum case. The implication for emergency planning is that largest potential distant tsunami inundation could conceivably be similar to median Cascadia inundation, but a real event is far more likely to flood only beaches and waterfront localities. Priorities for evacuation should be set accordingly.

UNCERTAINTIES

UNCERTAINTY OF CASCADIA FAULT SLIP ESTIMATED FROM TURBIDITE DATA

As previously discussed, Cascadia tsunami runup and inundation vary linearly with fault slip, so understanding uncertainties in scenario slip is critical. We estimate variability of slip from variability of times between earthquakes based on the radiocarbon ages of offshore turbidite beds. Two questions arise with regard to our choice of scenario recurrence (fault slip) from these data, (1) how strongly is the choice affected by updates in turbidite data and interpretations, and (2) how strongly is the choice affected by the somewhat speculative assumption that turbidite mass correlates with large slip? Figure 49 illustrates the difference in interevent frequency between the 2009 data

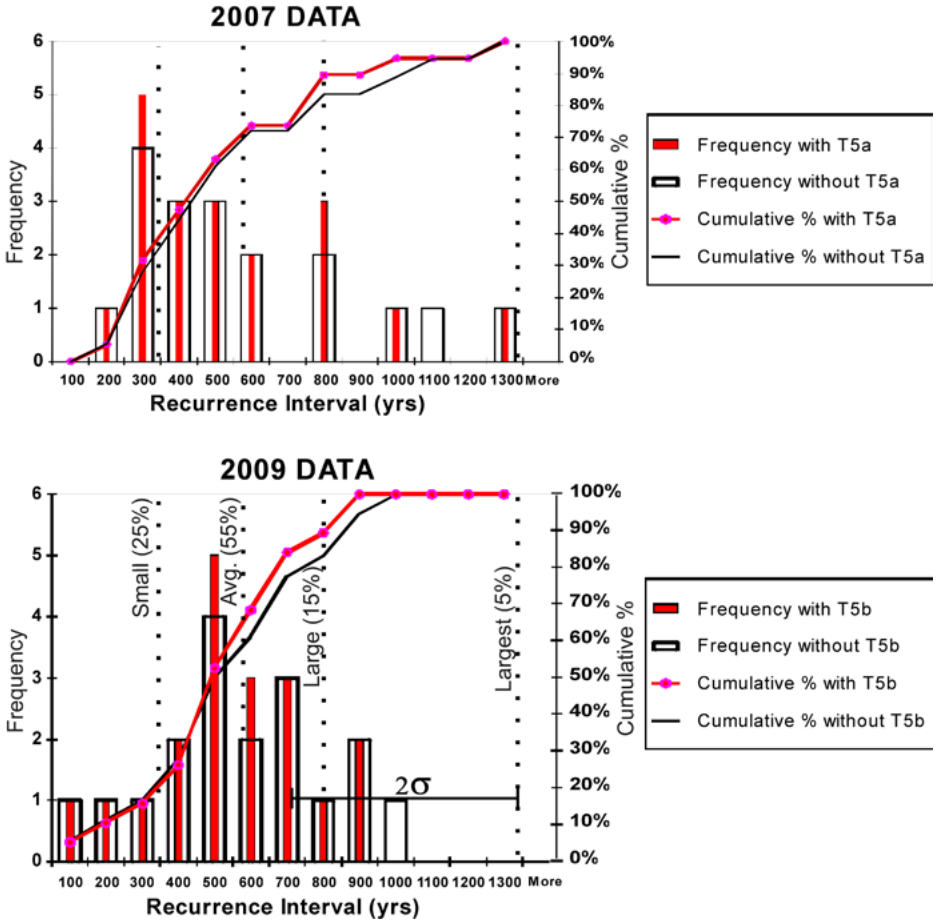

Figure 49. Comparison of data from 2007 (top) and 2009 (bottom) on frequency of inter-turbidite time intervals (100-yr bins) for turbidites deposited in the last ~10,000 years compared to recurrence scenarios (labeled dotted lines) and weights (in parentheses) from the basal four branches of the logic tree. Frequencies and cumulative percentages are shown in two ways: for all 20 turbidites and for intervals between the 19 turbidites extending the entire length of the Cascadia margin (i.e. no turbidite T5b for 2009 data or T5a for 2007 data). The 2σ error on the maximum recurrence interval for 2009 recurrence data without turbidite T5b is shown encompassing the "Largest" scenario recurrence. Turbidite T5b extends only as far north as 44° N, and may extend as far north as Juan de Fuca Canyon, which includes the latitude of Cannon Beach. Note that in 2007 turbidite T5b was originally correlated with a turbidite of a different age, T5a.

and 2007 turbidite data; the 2007 data were the basis for the original slip scenarios and tsunami simulations. The 2009 data included analysis of new ^{14}C data and recalibration of older data using a consistent revised marine calibration and reservoir correction. The final average ages and intervals in Goldfinger and others (2009) reflect decisions made about which ages for each of these events represent the best quality results as opposed to the averaged full range of ^{14}C data for each event. The overall pattern of 2007 and 2009 data is quite similar and assigned logic tree weights compare well with cumulative percentages of recurrence intervals (Figure 49). The largest difference is for the "Largest" scenario recurrence; it is reduced from ~1,300 years to ~980 years for the 19 full margin events (Table 4). As previously explained, ~980 years is the interval between turbidites T5 and T6 (ignoring T5b). One can argue that the original ~1,300 years lies within the 2σ root mean square error of the T5-T6 interval (Tables 1 and 4, Figure 49), but this makes the event of very low probability. The fact that the T5 and T6 turbidites are of average size (Table 1) does not provide support for this interval being associated with an unusually large earthquake. The original 1,300-year maximum interval was from the follow time in 2007 for the T11 turbidite, the largest on the southern Cascadia margin and second largest on the northern margin. This turbidite had ubiquitous basal erosion, increasing the errors involved in dating and interpretation of the age and hence the follow time (Goldfinger and others, 2009). The revised follow time for T11 is ~850 years, expanding to ~1200 years at 2σ. One could argue that 1200 years would be more appropriate for calculation of maximum slip. Our retention of ~1,300 years (slip of ~38 m) is therefore conservative (higher hazard). Nevertheless, this slip is similar to maximum slip of ~40 m inferred for the 1960 Chile earthquake (Barrientos and Ward, 1990), so it is not an unprecedented event.

Mismatches between turbidite size and the prior or following intervals indicate caution in adopting individual intervals as a metric for the largest event. Because the fit to a time predictable model is only a modest one (Table 2; Figures 6 and 7), strict adherence to following times is not warranted. Furthermore, evidence suggests that smaller events use very little energy, and skew the interevent time values inappropriately. For example, event T12 was preceded by ~850 years, and followed by 700 years, yet it was the smallest-mass turbidite of those considered here (Table 1). The ~1,550 year interval between T13 and T11 represents ~45 m of plate motion, yet only T12 occurred during that period. We suspect that much of that strain was released in the very large T11 earthquake, though the preceding and following times for T11 were not extraordinary. As previously discussed, we came to similar conclusions when comparing simulated inundation to distribution of Cascadia tsunami deposits. The small-volume turbidite, T2, provided a very short minimum interevent time (slip) that would be inconsistent with observed tsunami deposits. We conclude that use of any turbidites as small as or smaller than T2 for calculation of interseismic intervals likely causes underestimation of slip. If this is the case, then we might ignore T12 in the T11–T13 interval and assign a maximum interseismic time of 1,550 years rather than 1,300 years. Viewed in this context, 1,300 years is not overly conservative.

The 2009 update in age data left unchanged the basic observation that recurrence is highly variable, a conclusion reached independently from interpretation of paleoseismic data in coastal estuaries (e.g., Atwater and others, 2004; Kelsey and others, 2005). These coastal paleoseismic data (Atwater and others, 2004; Leonard and others, 2004) also support variable coseismic subsidence consistent with variable coseismic slip, so our variable slip approach is supported by observations.

With regard to the second question, Figure 49 illustrates the frequency and cumulative percentage of interseismic intervals of various sizes in the 10,000-year record, ignoring any relationship with turbidite thickness or follow times. The relative weights of each scenario slip compare reasonably well with the cumulative percentage of interevent times on the graphs, whether for 2007 or 2009 data. Table 4, as previously explained, illustrates the same point.

We note also that the calculation of slip is solely based on interevent time (i.e., Rikitake, 1999) and does not depend on turbidite size. Turbidite size is a third variable that apparently supports the use of time to calculate slip by indicating that earthquakes followed by long times also produced large turbidites and, by inference, large earthquakes.

A third source of uncertainty is our assumption that the coupling ratio is 1.0 for calculation from scenario recurrence of maximum slip in each slip distribution. McCaffrey (1997) argues that the closest subduction zone analogues to Cascadia in terms of thermal regime

have a large component of aseismic slip (coupling ratio <1.0). He suggests that much of the slip release at Cascadia could be in the form of "slow earthquakes" that would greatly reduce seismic shaking. He explains the observation by Satake and others (2003) that a large earthquake caused the AD 1700 tsunami by calling on slow earthquakes that can produce significant tsunamis but little seismic shaking. Depending on how much slip is too slow to be tsunamigenic, we could be overestimating tsunimigenic slip based on interevent times.

UNCERTAINTY IN PALEOSEISMIC ESTIMATES OF COSEISMIC SUBSIDENCE

The map position of observed paleoseismic deformation places strong constraints on the position of the underlying locked subduction interface (i.e., Meltzner and others [2006] for the Aceh earthquake). However, at present we have comprehensive paleoseismic data for only one earthquake, the AD 1700 event, compiled by Leonard and others (2004). The locked zone analysis presented here for the most part uses either geological and geophysical data generated over many seismic cycles, and therefore averaged, or geodetic data that relate to a future earthquake. Direct comparison to a single past earthquake of unknown slip distribution in AD 1700 guides but does not strongly constrain our models.

Both the geophysical evidence and paleosubsidence estimates have large uncertainties and inherent limitations. Paleosubsidence is measured in vertical soil profiles from changes of estuarine micro- and macro-fossil assemblages sensitive to local sea level, so it is possible that prompt postseismic deformation could occur before these signals are recorded in the deposits. Postseismic deep fault slip could increase subsidence near the coast, whereas uplift from viscoelastic relaxation could reduce it over hours, days, or a few years after an earthquake (Hyndman and others, 2005; Wang, 2007). Decreasing salinity of estuarine waters upstream can collapse the vertical ranges of salinity-sensitive species used for subsidence estimates. This factor may cause overestimate of paleosubsidence in large estuaries with high-volume rivers like the Columbia River. Potentially larger sources of error in estimating slip are the inherent assumptions of full locking and of complete stress drop. We make these assumptions though they are likely to be incorrect because we cannot determine these parameters at the present time.

UNCERTAINTY IN THE HYDRODYNAMIC MODEL

The hydrodynamic model, SELFE, passed all standard tsunami benchmark tests (Zhang and Baptista, 2008) and reproduced the inundation and flow depths of the 1964 Alaska tsunami in populated areas of Cannon Beach, so it is a reasonably accurate model. Note that flow velocities are depth-averaged from the 3D velocity field, but since a zero bottom drag is used in the model, there is no shear in the 3D velocity field. We do not understand the details of the vertical structure, including the bottom boundary layer for overland flow; hence the use of zero friction for conservative (high) estimates of velocity. Use of zero friction probably causes overestimates of inundation over dry land and wetlands, although match of the simulated and observed inundation for the 1964 tsunami indicates that the overestimate may be small where heavy vegetation is not present. We can speculate that degree of overestimate probably depends on how far inundation proceeds and how many obstacles the flow encounters. In low-lying areas like the Ecola Creek valley where closely spaced trees and other vegetation could slow tsunamis, the overestimate could be significant. A full analysis of the friction parameters relative to empirical observations is beyond the scope of this investigation.

UNCERTAINTY IN THE FAULT DISLOCATION MODEL

The Wang and He (2008) fault dislocation model, as applied here, does not allow significant slip near the deformation front owing to the velocity strengthening assumption, but there is some uncertainty about this assumption. According to Wang and He (2008), there is speculation that in the course of the evolution of pore fluid pressure distribution, parts of the updip segment at some subduction zones may occasionally become moderately velocity weakening and, when triggered to slip, acquire tsunamigenic rupture speed (Seno, 2002). Earthquakes characterized by this type of coseismic slip could have relatively high slip near the deformation front, low felt shaking, and produce relatively large tsunamis. While we cannot rule out the occurrence of

such "tsunami earthquakes" on the Cascadia subduction zone, the widespread occurrence of turbidites offshore (e.g., Goldfinger and others, 2009) and liquefaction features onshore (Obermeier and Dickenson, 2000) is consistent with at least moderate coseismic ground motion over wide areas for the vast majority of Cascadia events for which there is paleoseismic evidence. Because the evidence of strong ground shaking does not preclude the above scenario occurring simultaneously, there will remain some uncertainty in the behavior of the outermost wedge until better observational data are obtained.

UNCERTAINTY IN THE LOCAL BASIN AND BANK SLIP PATCH SOURCES

The local basin slip patch sources (Figure 16) at Nehalem Bank (Figure 12) are accurate representations of the Wells and others (2003) hypothesis that higher coseismic slip will be centered under forearc sedimentary basins, but the Wells and others paper also hypothesized that there would be high slip at the gravity low at Nehalem Bank. This apparent contradiction is caused by the Wells and others hypothesis that gravity lows are proxies for forearc basins. Nehalem Bank, however, is both a structural high and a gravity low due to its youthful development from recently reaccreted materials with a very local Columbia River source (Kulm and others, 1973). We modified our sources such that the bank is an area of low slip in our basin slip patch source to be consistent with the basin model proposed by Wells and others (2003). Alternatively, if the gravity signature is important beyond its use as a basin proxy (Song and Simons, 2003), then our model does not capture that possibility, one for which there is no clear physical explanation. In that case, lack of correspondence of the simulated tsunami inundation and crustal deformation for these sources to paleoseismic estimates could then be taken as an indication that the gravity low is a more important indicator of higher potential coseismic slip than the presence or absence of a sedimentary basin.

MINIMUM TSUNAMI SCENARIOS FOR INUNDATION MAPS

Ideally, tsunami hazard assessments would employ all deterministic earthquake sources used in this investigation, but an adequate assessment can be accomplished with five Cascadia and one or two distant tsunami sources. We recommend Cascadia tsunami scenarios closely matching the 50 (Average 9), 70 (Average 14), 90 (Large 14), and ~99 percent (Largest 14) isolines for wide application to the Oregon coast. In order to evaluate minimum Cascadia tsunami arrival for emergency planning, simulation of a splay fault scenario with either a local bank (Largest 1) or basin slip patch (Largest 2), whichever is the larger uplift, should be accomplished for each map area. These earthquake sources cause offshore deformation that produce tsunami wave arrivals with distinctly different timing from the regional slip patch scenarios. At Cannon Beach, Cascadia earthquakes with bank slip patches caused half of the peak tsunami flooding only 14 minutes after the earthquake; much sooner than scenarios with regional slip patches. Distant tsunami hazard is best depicted by mapping inundation from the hypothetical maximum considered teletsunami from the Gulf of Alaska. If local observational data are available, the tsunami from the 1964 Prince William Sound earthquake should also be simulated as ground truth check on the hydrodynamic modeling approach. The 1964 event is also worth simulating for evaluation of a more realistic maximum considered distant event than the hypothetical case.

The following are key scenarios for hazard assessment:

- ~99 percent confidence isoline (approximated by scenario Largest 14).
- 90 percent confidence isoline (approximated by scenario Large 14)
- 70 percent confidence isoline (approximated by scenario Average 14, the preferred scenario with highest logic tree weight)
- ~50 percent confidence isoline (scenario Average 9, minimum inundation regional rupture scenario consistent with paleotsunami deposits)
- Local bank (Largest 1) or basin slip patch (Largest 2), whichever has largest uplift.
- Maximum considered distant tsunami from the Gulf of Alaska (source 3 of TPSW [2006])

- Optional 1964 distant tsunami from the Prince William Sound earthquake in the Gulf of Alaska. This event should be simulated only if there is enough observational data to serve as a check on the tsunami simulation.

Figures 50 and 51 illustrate inundation maps using the five most critical scenarios from the list above. Similar maps can illustrate maximum water depth (Figure 52) and velocity (Figure 41) that will not be exceeded at these key confidence levels.

Tsunami source scenarios developed for this investigation are useful for tsunami hazard assessment of the northern Cascadia margin from Florence, Oregon (43.9° N) to Neah Bay, Washington (47.9° N) (Figure 1). The sources are not useful for tsunami hazard assessments at the extreme ends of the coseismic deformation, as tsunami waveforms will be incomplete. Assessments aimed at areas near Neah Bay and Florence will need tsunami sources that extend beyond the sources considered here.

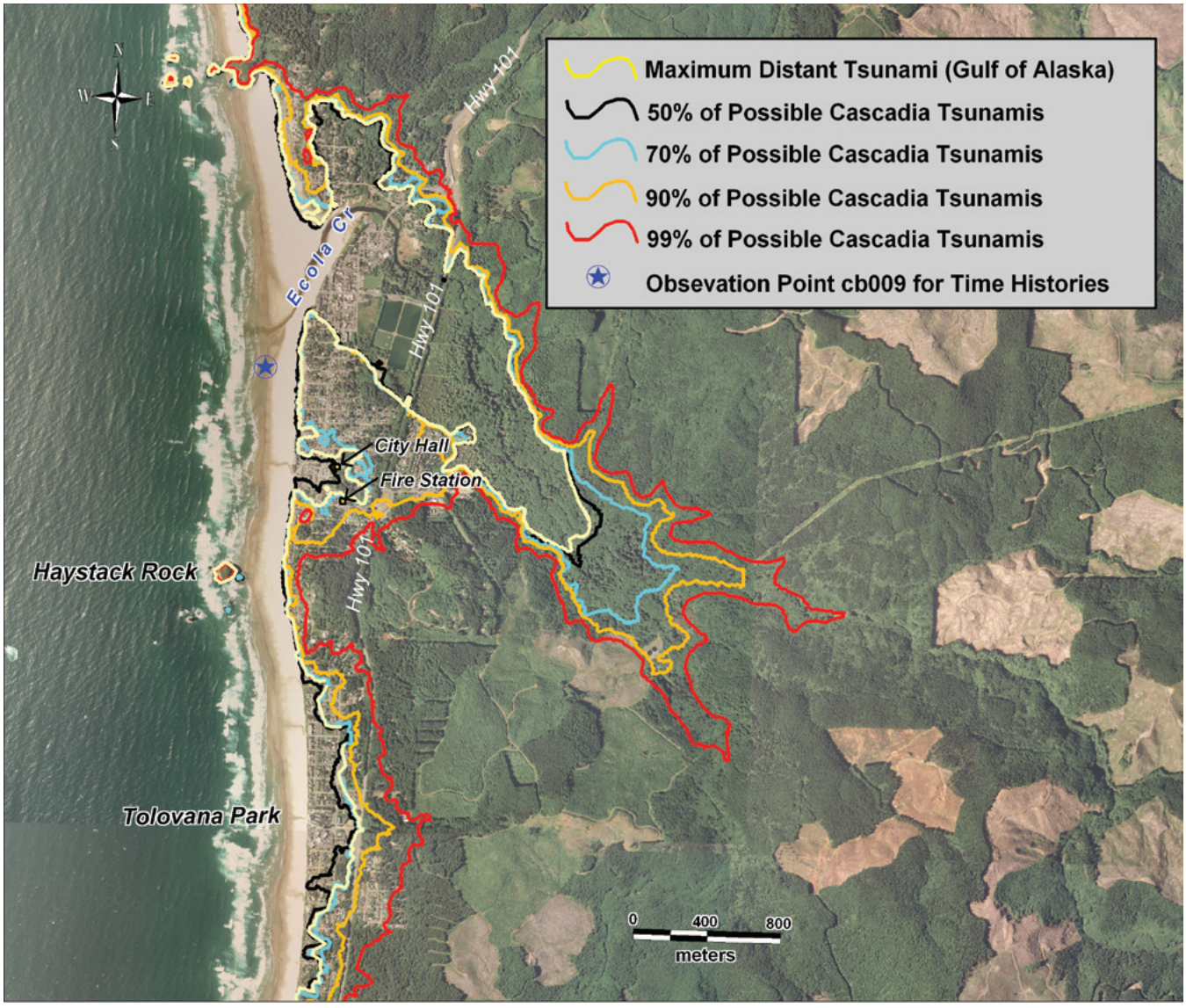

Figure 50. Key scenario inundation scenarios at Cannon Beach, Oregon. All inundation lines are individual tsunami scenarios that most closely match the listed confidence lines (see Figure 47). Mapped scenarios: ~50 percent = Average 9; 70 percent = Average 14; 90 percent = Large 14; ~99 percent = Largest 14.

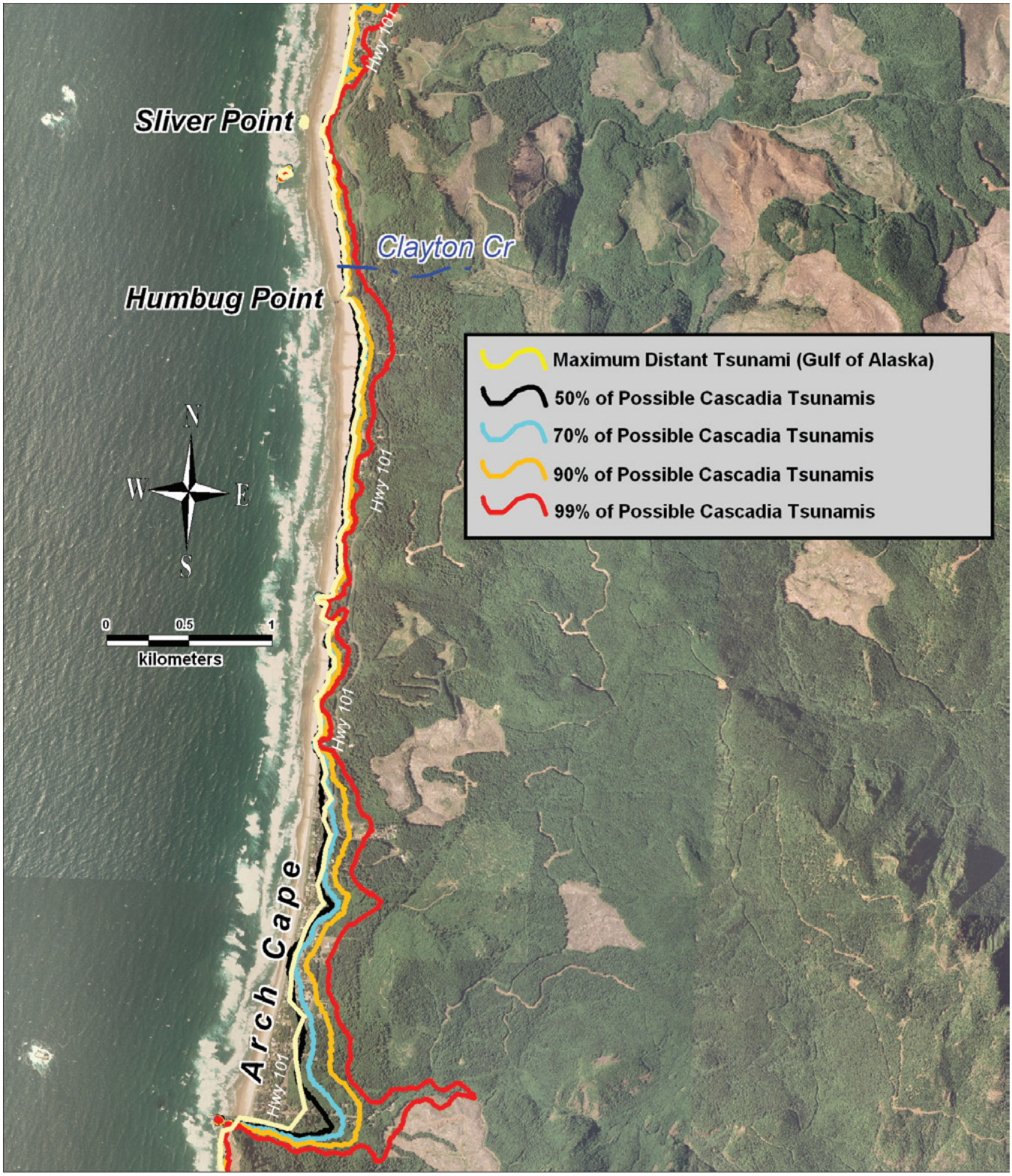

Figure 51. Inundation map as in Figure 50 but for the Arch Cape area immediately south of Cannon Beach, Oregon. Note that inundation in this area is less precise than at Cannon Beach to the north owing to coarser (~10 m) numerical grid.

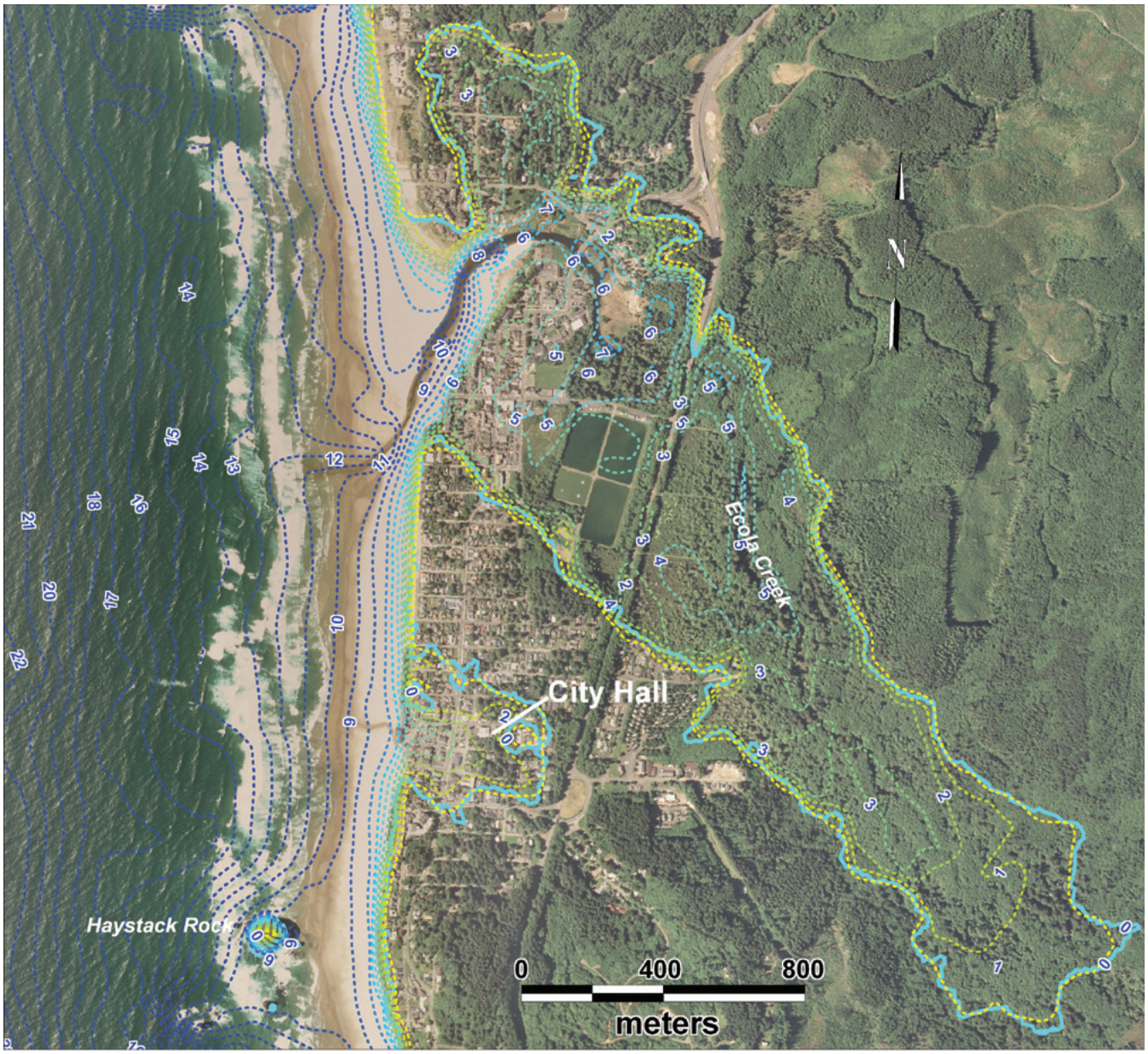

Figure 52. Maximum depth map for Average 14 scenario (preferred), approximating the ~70 percent confidence level for all variability in flow depth for Cascadia tsunami; contour interval (dashed lines) is 1 m; thick turquoise blue line is the maximum inundation for the Average 14 scenario.

TSUNAMI SCENARIOS FOR OREGON EVACUATION MAPS

In 2008 the Oregon Tsunami Advisory Council recommended depiction of two evacuation zones in recognition of the differing emergency planning needs for distant and local tsunami sources. Aside from some possible southern Cascadia earthquakes, the closest distant events are in the Gulf of Alaska with at least 4 hours of travel time to Oregon during which the NOAA West Coast and Alaska Tsunami Warning Center will have time to issue a warning. Local Cascadia earthquakes will produce tsunamis arriving in minutes rather than hours, so the only practical warning will be the earthquake itself. The two zones recommended for Oregon tsunami evacuation maps are the maximum considered distant tsunami inundation from the Gulf of Alaska and the largest inundation from a Cascadia earthquake. For this investigation of the northern Oregon coast, these earthquake source scenarios correspond, respectively, to source 3 of TPSW (2006) and Cascadia source Largest 14. Largest 14 produces inundation approximating the 99 percent confidence boundary for a full multi-deterministic analysis. Figure 53 illustrates this type of evacuation map.

SUMMARY AND CONCLUSIONS

Runup and inundation from locally generated tsunamis are extremely sensitive to details of the source uplift and subsidence, so a thorough parametric analysis of coseismic deformation is needed for tsunami hazard assessment. This investigation accomplished this for estimation of the Cascadia subduction zone tsunami hazard to Cannon Beach, Oregon. Coseismic deformation was explored by constructing source scenarios with the new fault dislocation model of Wang and He (2008) and then simulating tsunamis with a new finite element hydrodynamic model, SELFE (Zhang and Baptista, 2008). We used the marine paleoseismic record to establish recurrence bins from the 10,000-year event record and selected representative coseismic slips from these data. Assumed slips on the megathrust were ~8 m (~300 years of convergence), ~15 m (525 years of convergence), ~22 m (~750 years of convergence), and ~38 m (~1,300 years of convergence) which, if the sources were extended to the entire Cascadia margin, gave M_w varying from approximately 8.3 to 9.3. We further explored how this slip was distributed, including symmetric versus seaward skew of slip, partition to a splay fault or concentration under forearc basins, forearc banks, and seaward of the transition from contractional to extensional deformation of the North American Plate.

Ground truth checking of the simulated inundation against historic observations for the 1964 Alaska tsunami and minimum inundation inferred from three Cascadia tsunami deposits provided a key quality check, as did standard benchmark tests conducted by Zhang and Baptista (2008). Cascadia scenarios ~14-15 m slip and significant slip patches offshore of Cannon Beach were the minimum events needed to inundate beyond the inland reach of three Cascadia tsunami deposits emplaced in the last ~1,000 years. Runup and inundation were linearly correlated with scenario slip on the subduction zone. Presence of a splay fault amplified tsunami water level at the open coast by 6 to 31 percent and inundation in a river valley by 2 to 20 percent. Buried ruptures on the megathrust produced first-arriving tsunamis delayed relative to the splay fault cases. Submarine bank ruptures generated rising ocean levels from the start of the simulation due to the locally large rupture width. Forearc basin slip patches generated much smaller tsunamis, similar to distant tsunamis, because the nearest basin is ~100 km south of Cannon Beach. Changes in rupture width of ±20 km on the regional rupture scenarios had little effect on the tsunamis, but seaward skew of slip produced higher open coastal runup than scenarios with symmetrical slip distributions. In all, 25 Cascadia source scenarios were constructed and were assigned weights using a logic tree that weighted sources according to their fit to relevant geologic, geodetic, and geophysical data. We derived percentile inundation lines that expressed the confidence level (percentage) that a Cascadia tsunami will *not* exceed the line by adding up logic tree weights of overlapping inundation scenarios at each numerical grid cell. Lines of 50, 70, 90, and 99 percent confidence corresponded to maximum runup of 8.9, 10.5, 13.2, and 28.4 m (NAVD 88). The tsunami source with highest

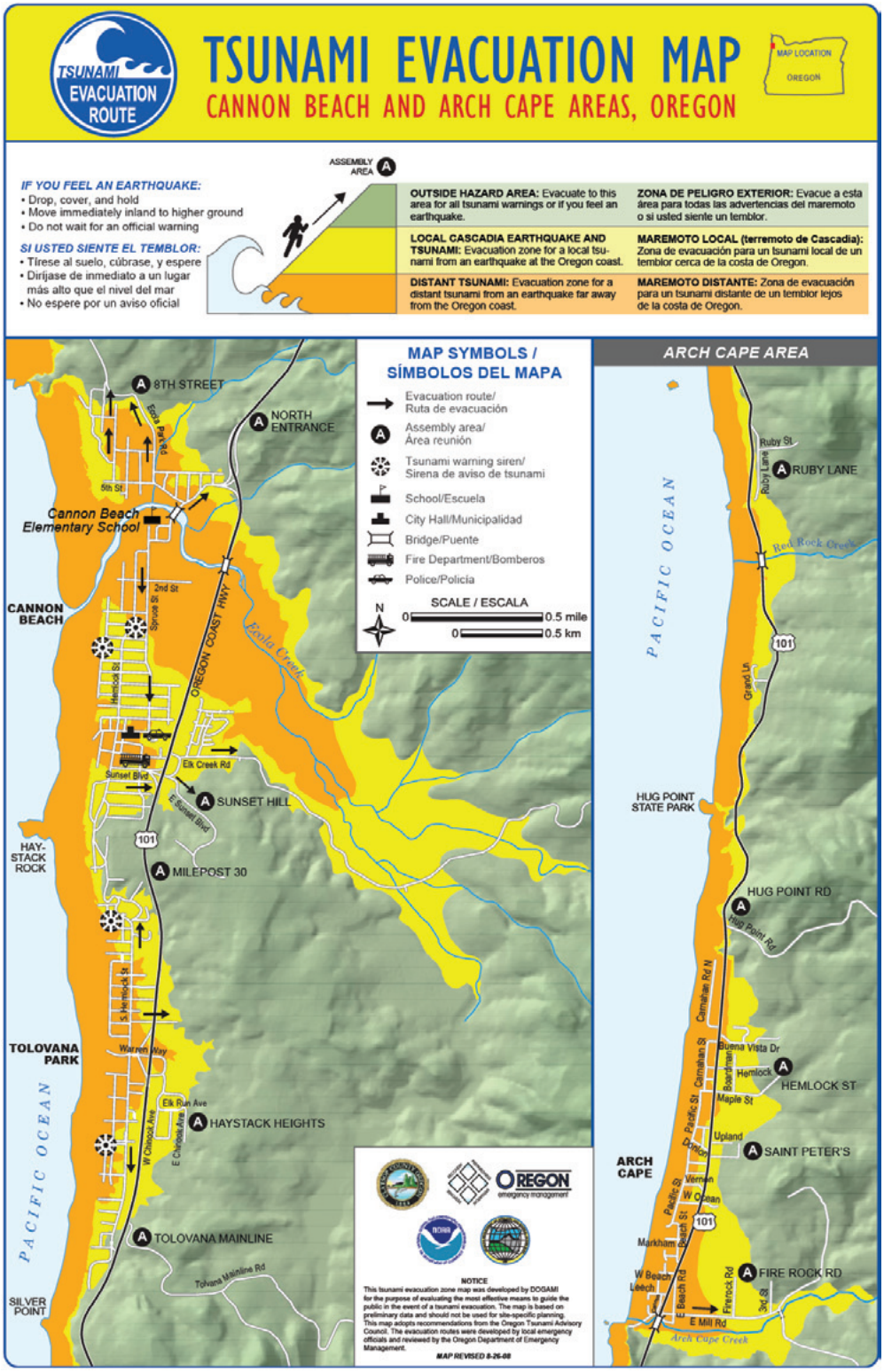

Figure 53. 2008 tsunami evacuation map for Cannon Beach, Oregon, based on theoretical worst-case local and distant tsunami inundation. Note that small differences between inundation for the worst-case distant tsunami (orange zone) and local tsunami (orange plus yellow zone) between this map corresponding inundation from computer-generated inundation of previous figures is from adjustment of the boundaries to more accurately match water elevations to local topography than could be achieved with the grid spacing used by the simulations. This map is available online: http://www.oregongeology.org/pubs/tsubrochures/CannonEvac.pdf

logic tree weight (preferred scenario) involved rupture of a splay fault with ~15 m slip that produced tsunami inundation near the 70 percent confidence line. In a similar fashion, maps of maximum tsunami water depth and velocity for particular isolines illustrate values not exceeded at each confidence level. Five of the 25 Cascadia tsunami scenarios correspond closely to 50, 70, 90, and 99 percent confidence levels and can be used as proxies for a reasonably complete assessment of local tsunami hazard.

Available resources did not permit a complete parametric analysis of the hazard posed by distant tsunami sources. A distant tsunami that struck in 1964 from a M_w 9.2 earthquake in the Gulf of Alaska did damage to the Oregon and Washington coasts but, overall, impact was to beaches and immediate water front areas (e.g., data compiled by Lander and Lockridge, 1989), even though the tsunami arrived during a high tide and was the largest distant event in historic times. In view of these observations, we examined only the 1964 tsunami from the Gulf of Alaska as a check of the modeling approach, and, for a hypothetical maximum, a similar Gulf of Alaska earthquake with optimal tsunami directivity to the Oregon coast. The latter had runup and inundation similar to the 40 to 50 percent confidence isolines for possible Cascadia tsunamis but is a much less likely event than the largest historical tsunami that struck in 1964.

The Tsunami Advisory Council recommended that Oregon evacuation maps use inundations from the theoretical maximum considered distant earthquake and a local Cascadia earthquake approximating the 99 percent confidence level. The rationale for showing both inundation boundaries is the differing evacuation planning for distant versus local events. Distant events arrive at least 4 hours after the earthquake, giving ample time for the national warning system to operate, whereas local tsunamis arrive in minutes so the earthquake itself is the only practical warning.

RECOMMENDATIONS FOR FUTURE WORK

Construction of tsunami source scenarios for the entire Cascadia margin would allow tsunami hazard assessment at and beyond the model limits used here, from Neah Bay to Florence, Oregon. Of particular importance for tsunami hazard assessment in Oregon is the southern Cascadia margin where there were as many as 40 Cascadia earthquakes in the last 10,000 years, giving a probability in the next 50 years as high as ~80 percent (Goldfinger and others, 2009).

Given the observation of Myers (1999) that tsunami energy is more efficiently radiated northward from southern Cascadia segment ruptures than southward from northern ruptures, construction of southern Cascadia segmentation scenarios is also needed to fully explore the hazard to the northern margin. If significant tsunami hazard is posed to areas on the north margin with little felt shaking, then the national warning system would be the only effective warning for those areas. Determination of tsunami travel time to and runup in areas where the earthquake is not an effective warning is a critical sensitivity test.

We recommend that rigorous simulations of the AD 1700 tsunami be accomplished at Ecola Creek or another area where tsunami deposits from AD 1700 are well preserved. The primary objective would be to determine geologically reasonable variation in coseismic deformation needed to produce a tsunami that could deposit the sand. Contemporary tide inferred from data of Mofjeld and others (1997) should be used as an input for dynamic simulations of tsunami-tide interactions. Predictions of velocity and flow depth from three-dimensional tsunami simulations from analysis of sediment particle size and thickness could be compared.

The Cannon Beach experiment did not definitively test whether slip patches are concentrated under forearc basins, banks, or gravity lows, because, as previously explained, the adjacent Nehalem Bank (Figure 12) is anomalous in being located at a gravity low (see gravity map of Wells and others [2003]). We recommend that paleoseismic subsidence and paleotsunami inundation at Siletz Bay be compared to simulated coseismic deformation and inundation from the Cascadia earthquake sources of this investigation. Siletz Bay lies adjacent to a forearc gravity low (Wells and others, 2003) directly opposite the axis of a large forearc basin where geodetic uplift rate is at a minimum (Mitchell and others, 1994).

We recommend acquisition of high-quality (bare earth) lidar data for the entire Cascadia margin. These data will provide a single consistent digital elevation model far more accurate than data now available. Progress of this project was severely hampered at one point by a datum error in one of the two topographic data sets. A single lidar data set would largely eliminate such errors.

Acknowledgments.

This investigation was supported by National Oceanic and Atmospheric Administration (NOAA) Requisition Number NRMAH000-6-01035 through Oregon Department of Geology and Mineral Industries (DOGAMI) Intergovernmental Agreement number 61110-09192006, and support from the City of Cannon Beach, the Cannon Beach Rural Fire Protection District, and the Seaside School District through Intergovernmental Agreement 41180-63006. The Pacific Marine Environmental Laboratory of NOAA kindly provided earthquake source data for the two distant tsunami scenarios and cooperated at every stage of the investigation. Harvey Kelsey of Humboldt State University, Vasily Titov of NOAA, and Eric Geist of the U.S. Geological Survey provided key reviews. The authors acknowledge Western Geco and the U.S. Geological Survey for providing some of the seismic reflection data for the purpose of this research. Angie Venturato of NOAA produced the initial compilation of topographic and bathymetric data. Charles Seaton of the OGI School of Science and Engineering, Oregon Health and Science University, provided key support with data reduction at all stages of the project. Ian Madin, Vicki McConnell, and Don Lewis of DOGAMI provided helpful review and advice. We thank local stakeholders for their wise council and cooperation, particularly Al Aya and Cleve Rooper of the Cannon Beach Rural Fire Protection District, Richard Mays and Jay Raskin of the City of Cannon Beach, and Doug Dougherty, Superintendent of the Seaside School District. Many of the graphics and excerpts in the text of this paper will appear in a summary paper accepted for publication by the journal *Natural Hazards*.

REFERENCES

Abdelayem, A. L., Ikehara, K., and Yamazaki, T., 2004, Flow path of the 1993 Hokkaido-Nansei-Oki earthquake seismoturbidite, southern margin of the Japan Sea north basin, inferred from anisotropy of magnetic susceptibility, Geophysical Journal International, v. 157, p. 15–24.

Adam, J., Klaeschen, D., Kukowski, N., and Flueh, E. 2004, Upward delamination of Cascadia Basin sediment infill with landward frontal accretion thrusting caused by rapid glacial age material flux: Tectonics, v. 23, p. TC3009.

Adams, J., 1990, Paleoseismicity of the Cascadia subduction zone: evidence from turbidites off the Oregon-Washington margin: Tectonics, v. 9, p. 569–584.

Allan, J. C., and Priest, G. R., 2001, Evaluation of coastal erosion hazard zones along the dune and bluff backed shorelines in Tillamook County, Oregon, Cascade Head to Cape Falcon, Preliminary Technical report to Tillamook County: Oregon Department of Geology and Mineral Industries Open-File Report O-01-03, 120 p.

Ammon, C. J., Ji, C., Thio, H.-K., Robinson, D., Ni, S., Hjorleifsdottir, V., Kanamori, H., Lay, T., Das, S., Helmberger, D., Ichinose, G., Polet, J., and Wald, D., 2005, Rupture process of the 2004 Sumatra-Andaman earthquake: Science, v. 308, p. 1,133–1,139.

Annaka, T., Satake, K., Sakakiyama, T., Yanagisawa, K., and Shuto, N., 2007, Logic-tree approach for probabilistic tsunami hazard analysis and its applications to the Japanese coasts, *in* Satake, K., Okal, E.A., and Borrero, J.C., eds., Tsunami and its hazards in the Indian and Pacific oceans: Pure and Applied Geophysics, v. 164, no. 2-3, p. 577–592.

Atwater, B. F., and Hemphill-Haley, E., 1997, Recurrence intervals for great earthquakes of the past 3500 years at Northeastern Willapa Bay, Washington, U.S. Geological Survey Professional Paper 1576, 108 p.

Atwater, B. F., Nelson, A. R., Clague, J. J., Carver, G. A., Yamaguchi, D. K., Bobrowsky, P. T., Bourgeois, J., Darienzo, M. E., Grant, W. C., Hemphill-Haley, E., Kelsey, H. M., Jacoby, G. C., Nishenko, S. P., Palmer, S. P., Peterson, C. D., and Reinhart, M. A., 1995, Summary of coastal geologic evidence for past great earthquakes at the Cascadia subduction zone. Earthquake Spectra, v. 11, no. 1, 1–18.

Barrientos, S. E., and Ward, S. N., 1990, The 1960 Chile earthquake: inversion for slip distribution from surface deformation: Geophysical journal international, v. 103, no. 3, p. 589-598.

Boyd, T. M., Engdahl, E. R., and Spence, W., 1995, Seismic cycles along the Aleutian arc; analysis of seismicity from 1957 through 1991: Journal of Geophysical Research, v. 100, p. 621–644.

Brudzinski, M. R., and Allen, R. A., 2007, Segmentation in episodic tremor and slip all along Cascadia, Geology, v. 35, 907–910.

Burgette, R., Weldon, R. J., and Schmidt, D., 2007, A more accurate vertical velocity field for coastal Oregon reveals variations in extent of locking on the Cascadia Subduction Zone: Eos, Trans. American Geophysical Union, v. 88, abstract G52A-01.

Burgette, R. J., R. J. Weldon II, and D. A. Schmidt, 2009, Interseismic uplift rates for western Oregon and along-strike variation in locking on the Cascadia subduction zone, Journal of Geophysical Research, 114, B01408, doi:10.1029/2008JB005679.

Byrne, D. E., Wang, W., and Davis, D. M., 1993, Mechanical role of backstops in the growth of forearcs: Tectonics, v. 12, p. 123–144.

Chlieh, M., Avouac, J.-P., Hjorleifsdottir, V., Song, T.-R. A., Ji, C., Sieh, K., Sladen, A., Hebert, H., Prawirodirdjo, L., Bock, Y., and Galetzka, J., 2007, Coseismic slip and afterslip of the great (M_w9.15) Sumatra-Andaman earthquake of 2004: Bulletin of the Seismological Society of America, v. 97, no. 1, S152–S173.

Clarke, S. H., Jr., and Carver, G. A., 1992, Late Holocene tectonics and paleoseismicity, southern Cascadia subduction zone: Science, v. 255, p. 188–192.

Cornell, C. A., 1968, Engineering seismic risk analysis: Bulletin of the Seismological Society of America, v. 58, p. 1583–1606.

Cummins, P. R., Hori, T., and Kaneda, Y., 2001, Splay fault and megathrust earthquake slip in the Nankai Trough: Earth and Planetary Science Letters, v. 53, p. 243–248.

Dallimore, A., Thomson, R. E., and Bertram, M. A., 2005, Modern to late Holocene deposition in an anoxic fjord on the west coast of Canada: impli-

cations for regional oceanography, climate and paleoseismic history: Marine Geology, v. 219, no. 1, p. 47–60.

Dengler, L. A., 2006, Awareness and preparedness, *in* Summary report on the Great Sumatra Earthquakes and Indian Ocean Tsunamis of 26 December 2004 and 28 March 2005: Oakland, Calif., Earthquake Engineering Research Institute, p. 51–65.

Dziak R. P., Fox, C. G., Bobbitt, A. M., and Goldfinger, C., 2001, Bathymetric map of the Gorda Plate: structural and geomorphological processes inferred from multibeam surveys: Marine Geophysical Researches, v. 22, p. 235–250.

Fisher, D., Mosher, D., Austin, J. A., Gulick, S. P., Masterlark, T., and Moran, K. 2007, Active deformation across the Sumatran forearc over the December 2004 M_w 9.2 rupture: Geology, v. 35, p. 99–102.

Flück, P., Hyndman, R. D., and Wang, K., 1997, 3-D dislocation model for great earthquakes of the Cascadia subduction zone: Journal of Geophysical Research, v. 102, p. 20,539-20,550.

Frankel, A. D., Petersen, M. D. Mueller, C. S., Haller, K. M., Wheeler, R. L., Leyendecker, E. V., Wesson, R. L. , Harmsen, S. C., Cramer, C. H., Perkins, D. M., and Rukstales, K. S., 2002, Documentation for the 2002 update of the national seismic hazard maps, U.S. Geological Survey Open-File Report 02-420.

Freund, L. B., and Barnett, D. M., 1976, A two-dimensional analysis of surface deformation due to dip-slip faulting: Bulletin of the Seismological Society of America, v. 66, p. 667–675.

Fukuma, K., 1998, Origin and applications of whole-core magnetic susceptibility of sediments and volcanic rocks from Leg 152. Proceedings of the Ocean Drilling Program: Scientific Results, 152, 271-280.

Geist, E. L., 2002, Complex earthquake rupture and local tsunamis: Journal of Geophysical Research, v. 107, doi: 10.1029/2000JB000139.

Geist, E. L., 2005, Local tsunami hazards in the Pacific Northwest from Cascadia Subduction Zone earthquakes: U.S. Geological Survey Professional Paper 1661B, 17 p.

Geist, E. L., and Yoshioka, S., 1996, Source parameters controlling the generation and propagation of potential local tsunamis along the Cascadia margin: Natural Hazards, v. 13, p. 151–177.

Geist, E. L., and Parsons, T., 2006, Probabilistic analysis of tsunami hazards: Natural Hazards, v. 37, p. 277–314.

Ghosh, A., Newman, A.V., Thomas, A.M., and Farmer, G. T., 2008, Interface locking along the subduction megathrust from *b*-value mapping near Nicoya Peninsula, Costa Rica, Geophysical Research Letters, v. 35, no. 1, L01301, doi:10.1029/2007GL031617.

Global Centroid Moment Tensor database, http://www.globalcmt.org/CMTsearch.html.

Goldfinger, C., 1994, Active deformation of the Cascadia forearc: implications for great earthquake potential in Oregon and Washington: Corvallis, Oreg., Oregon State University, Ph.D. dissertation 202 p., 4 pls.

Goldfinger, C., and McNeill, L. C., 2006, Sumatra and Cascadia: parallels explored: Eos, Trans. American Geophysical Union, v. 87, p. 52.

Goldfinger, C., Mackay, M. E., Moore, G. F., Kulm, L. D., Yeats, R. S., and Appelgate, B., 1992, Transverse structural trends along the Oregon convergent margin: implications for Cascadia earthquake potential and crustal rotations: Geology, v. 20, no. 2, pp. 141–144.

Goldfinger, C., Kulm, L.D., Yeats, R.S., Hummon, C., Huftile, G. J., Niem, A. R., Fox, C. G., and McNeill, L. C., 1996, Oblique strike-slip faulting of the Cascadia submarine forearc: the Daisy Bank fault zone off central Oregon, *in* Bebout, G. E., Scholl, D., Kirby, S., and Platt, J. P., eds., Subduction top to bottom, Geophysical Monograph 96: Geophysical Monograph: Washington, D. C., American Geophysical Union, p. 65–74.

Goldfinger, C., Kulm, L. D., Yeats, R. S., McNeill, L. C., and Hummon, C., 1997, Oblique strike-slip faulting of the central Cascadia submarine forearc: Journal of Geophysical Research, v. 102, p. 8,217-8,243.

Goldfinger, C., Kulm, L. D., McNeill, L. C., and Watts, P., 2000, Super-scale failure of the southern Oregon Cascadia margin: Pure and Applied Geophysics, v. 157, p. 1189–1226.

Goldfinger, C., Nelson, C. H., and others, 2003a, Deep-water turbidites as Holocene earthquake proxies: the Cascadia Subduction Zone and Northern San Andreas Fault systems: Annals of Geophysics, v. 46, no. 5, p. 1169–1194.

Goldfinger, C., Nelson, C. H., and others, 2003b, Holo-

cene earthquake records from the Cascadia Subduction Zone and Northern San Andreas Fault based on precise dating of offshore turbidites: Annual Reviews of Earth and Planetary Sciences, v. 31, pp. 555–577.

Goldfinger, C., Morey, A., Erhardt, M., Nelson, C. H., Gutierrez-Pastor, J., Enkin, R., and Dallimore, A., 2006a, Cascadia great earthquake recurrence: rupture lengths, correlations and constrained OxCal analysis of event ages, *in* Diggles, M., Geist, E., and Lee, W. (eds.), Proceedings of the USGS Tsunami Sources Workshop, April 21-22, 2006 (available on CD-ROM).

Goldfinger, C., Morey, A., and Nelson, C. H., 2006b, Deep-water turbidites as Holocene earthquake proxies along the northern San Andreas fault system: Seismological Research Letters, v. 77, no. 2, p. 195–196.

Goldfinger, C., Morey, A. E., Nelson, C. H., Gutierrez-Pastor, J., Johnson, J. E., Karabanov, E., Chaytor, J., and Ericsson, A., 2007a, Rupture lengths and temporal history of significant earthquakes on the offshore and north coast segments of the Northern San Andreas Fault based on turbidite stratigraphy: Earth and Planetary Science Letters, v. 254, p. 9–27.

Goldfinger, C., Nelson, C. H., Morey-Ross, A., Johnson, J. E., Baptista, A., Zhang, J., Wang, K., Witter, R., and Priest, G., 2007b, Interplay of structure and sediment supply may influence subduction zone rupture patches and propagation: Eos, Trans. American Geophysical Union, Fall Meet. Suppl., v. 88, Abstract T52A-07.

Goldfinger, C., Grijalva, K., Bürgmann, R. Morey, A. , Johnson, J. E., Nelson, C. H., Gutiérrez-Pastor, J., Ericsson, A., Karabanov, E., Chaytor, J. D., Patton, J., and Gràcia, E., 2008, Late Holocene rupture of the northern San Andreas Fault and possible stress linkage to the Cascadia Subduction Zone: Bulletin of the Seismological Society of America, v. 98, no. 2, p. 861–889.

Goldfinger, C., Nelson, C. H., , Morey, A., Johnson, J. E., Gutierrez-Pastor, J., Eriksson, A. T., Karabanov, E., Patton, J., Gracia, E., Enkin, R., Dallimore, A., Dunhill, G., Vallier, T., and the shipboard scientific parties, 2009, in preparation, Turbidite event history: methods and implications for Holocene paleoseismicity of the Cascadia Subduction Zone, U.S. Geological Survey Professional Paper.

Gulick, S. P. S., Meltzer, A. M., and Clarke, Jr., S. H., 1998, Seismic structure of the southern Cascadia subduction zone and accretionary prism north of the Mendocino triple junction: Journal of Geophysical Research, v. 103, no. B11, p. 27,207–27,222.

Hagstrum, J. T., Atwater, B. F., and Sherrod, B. L., 2004, Paleomagnetic correlation of late Holocene earthquakes among estuaries in Washington and Oregon, v. G3 , no. 5, doi:10.1029/2004GC000736.

Hallett, D. J., Hills, L. V., and Clague, J. J., 1997, New accelerator mass spectrometry radiocarbon ages for the Mazama tephra layer from Kootenay National Park, British Columbia, Canada: Canadian Journal of Earth Sciences, 34, 1202–1209.

Hebenstreit, G. T., and Murty, T. S., 1989, Tsunami amplitudes from local earthquakes in the Pacific Northwest region of North America, part 1—the outer coast: Marine Geodesy, v. 13, p. 101–146.

Holdahl, S. R., and Sauber, J., 1994, Coseismic slip in the 1964 Prince William Sound Earthquake: a new geodetic inversion: Pure and Applied Geophysics, v. 142, no. 1, p. 55–82.

Hsu, Y.-J., Simons, M., Avouac, J.-P., Galetzka, J., Sieh, K., Chlieh, M., Natawidjaja, D., Prawirodirdjo, L. ,and Bock, Y., 2006, Frictional afterslip following the 2005 Nias-Simeulue earthquake, Sumatra, Science, 312, 1921–1926.

Hyndman, R. D., and Wang, K., 1995, The rupture zone of Cascadia great earthquakes from current deformation and the thermal regime: Journal of Geophysical Research, v. 100, p. 22,133–22,154.

Hyndman, R.D., Leonard, L.J., Currie, C.A., 2005. Test of models for the Cascadia great earthquake rupture area using coastal subsidence estimates for the 1700 earthquake. Final Report, US Geological Survey NEHRP External Grant Award 04HQGR0088, 11 p.

Ioualalen, M., Asavanant, J., Kaewbanjak, N., Grilli, S. T., Kirby, J. T., and Watts, P., 2007, Modeling the 26 December 2004 Indian Ocean tsunami: case study of impact in Thailand, Journal of Geophysical Research, v. 112, no. C7, C07024.1-C07024.21.

Iwaki, H., Hayashida, A., Kitada, N., Ito, H., Suwa, S., and Takemura, K., 2004, Stratigraphic correlation of samples from the Osaka Bay off Kobe based on magnetic properties and its implication for tec-

tonic activity of the Osaka-wan fault for the last 6300 years, Eos, Trans. American Geophysical Union, v. 84, no. 46 (abstract GP41C-0053).

Johnson, J. E., 2004, Deformation, fluid venting, and slope failure at an active margin gas hydrate province, Hydrate Ridge, Cascadia accretionary wedge: Corvallis, Oregon State University, Ph.D. dissertation.

Johnson, J., Satake, K. Holdahl, S., Sauber, J., 1996, The 1964 Prince William Sound earthquake: joint inversion of tsunami and geodetic data: Journal of Geophysical Research, v. 101, no. B1, p. 523–532.

Karlin, R. E., Holmes, M., Abella, S. E. B., and Sylwester, R., 2004, Holocene landslides and a 3500-year record of Pacific Northwest earthquakes from sediments in Lake Washington: Geological Society of America Bulletin, v. 116, no. 1-2, p. 94–108.

Kulm, L. D., and Fowler, G. A., 1974, Oregon continental margin structure and stratigraphy: a test of the imbricate thrust model, *in* Burk, C. A., and Drake, C. L., eds., The geology of continental margins: New York, Springer-Verlag, p. 261–284.

Kulm, L. D., Von Huene, R., and the Shipboard Scientific Party, 1973, Initial reports of the Deep Sea Drilling Project, v. 18: Washington, D.C., U.S. Government Printing Office, p. 97–168.

Ladage, S., Gaedicke, C., Barckhausen, U., Heyde, I., Weinrebe, W., Flueh, E. R., Krabbenhoeft, A., Kopp, H., Fajar, S., and Djajadihardja, Y., 2006, Bathymetric survey images structure off Sumatra: Eos, Trans. American Geophysical Union, v. 87, no. 17, p. 165.

Lander, J. F., and Lockridge, P. A., 1989, United States tsunamis (including United States possessions) 1690–1988: Boulder, Colo., NOAA NGDC Publication 41-2.

Lees, J. A., Fowler, R. J., andAppleby, P. G., 1998, Mineral magnetic and physical properties of surficial sediments and onshore samples from the southern basin of Lake Baikal, Siberia: Journal of Paleolimnology, v. 20, no. 2, p. 175–186.

Leonard, L. J., Hyndman, R. D., and Mazzotti, S., 2004, Coseismic subsidence in the 1700 Great Cascadia earthquake: coastal estimates versus elastic dislocation models: Geological Society of America Bulletin, v. 116, p. 655–670.

Lovlie, R., and van Veen, P., 1995, Magnetic susceptibility of a 180 m sediment core: reliability of incremental sampling and evidence for a relationship between susceptibility and gamma activity, *in* Turner, P., and A. Turner, eds., Palaeomagnetic applications in hydrocarbon exploration and production, Special Publication, 98: London, Geological Society, p. 259–266.

MacKay, M. E., 1995, Structural variation and landward vergence at the toe of the Oregon accretionary prism: Tectonics, v. 14, p. 1309–1320.

Maltman, A. J., 1998, Deformation structures from the toes of active accretionary prisms: Journal of the Geological Society, v. 155, p. 639–650.

Mandal, N., Chattopadhyay, A., and Bose, S., 1997, Imbricate thrust spacing: experimental and theoretical analyses, chap. 8 *of* Sengupta, S., ed., Evolution of geological structures in micro- to macroscales: London, Chapman and Hall, p. 143–165.

Mann, D. M., and Snavely, P. D., Jr., 1984, Multichannel seismic-reflection profiles collected in 1977 in the eastern Pacific Ocean off of the Washington/Oregon coast: U.S. Geological Survey Open-File Report 84-0005, 3 p.

McCaffrey, R., 1997, Influences of recurrence times and fault zone temperatures on the age-rate dependence of subduction zone seismicity: Journal of Geophysical Research, v.102, no. B10, p. 22,839-22,854.

McCaffrey, R., Qamar, A., King, R. W., Wells, R. W., Khazaradze, G., Williams, C., Stevens, C., Vollick, J. J., and Zwick, P. C., 2007, Fault locking, block rotation and crustal deformation in the Pacific Northwest: Geophysical Journal International, v. 169, p. 1315–1340.

McCrory, P. A., Blair, J. L., Oppenheimer, D. H., and Walter, S. R., 2004, Depth to the Juan de Fuca slab beneath the Cascadia subduction margin – a 3-D model for sorting earthquakes: USGS Data Series DS-91; http://pubs.usgs.gov/ds/91/.

McCubbin D. G., 1982, Barrier-island and strandplain facies, *in* Scholle P. A., and Spearing, D., eds., Sandstone depositional environments: Tulsa, Okla., American Association of Petroleum Geologists, Memoir 31, p. 247–279.

McNeill, L. C., Piper, K. A., Goldfinger, C., Kulm, L. D., and Yeats, R. S., 1997, Listric normal faulting on the Cascadia continental margin: Journal of Geophysical Research, v. 102, no. B6, p. 12,123–12,138.

McNeill, L. C., Goldfinger, C., Kulm, L. D., and Yeats,

R. S., 2000, Tectonics of the Neogene Cascadia forearc basin: investigations of a deformed late Miocene unconformity: Geological Society of America Bulletin, v. 112, no. 8, p. 1209–1224.

McNeill, L. C., Henstock, T., Tappin, D., and Curray, J., 2006, Forearc morphology and thrust vergence, Sunda subduction zone: Eos, Trans. American Geophysical Union, Fall Meeting Supplement, v. 87, no. 52.

Meltzner, A. J., K. Sieh, Abrams, M., Agnew, D. C., Hudnut, K. W., Avouac, J.-P., and Natawidjaja, D. H., 2006, Uplift and subsidence associated with the great Aceh-Andaman earthquake of 2004: J. Geophysical Research, v. 111, p. B02407.

Mitchell, C. E., Vincent, P., Weldon II, R. J., and Richards, M. A., 1994, Present-day vertical deformation of the Cascadia margin, Pacific northwest, U.S.A.: Journal of Geophysical Research, v. 99, p. 12,257–12,277.

Mofjeld, H. O., Foreman, M. G. G., and Ruffman A., 1997, West Coast tides during Cascadia subduction zone tsunamis, Geophysical Research Letters, v. 24, no. 17, p. 2215–2218.

Mofjeld, H. O., González, F. I., and Newman, J. C., 1999, Tsunami prediction in U.S. coastal regions: Coastal and Estuarine Studies, v. 56, p. 353–375.

Myers, E. P., III, 1999, Physical and numerical analysis of long wave modeling for tsunamis and tides: Portland, Oreg., Oregon Graduate Institute of Science and Technology, Ph.D. dissertation, 271 p.

Myers, E. P., and Baptista, A. M., 2001, Analysis of factors influencing simulations of the 1993 Hokkaido Nansei-Oki and 1964 Alaska tsunamis: Natural Hazards, v. 23, p. 1–28.

Nelson, A. R., Sawai, Y., Jennings, A. E., Bradley, L., Gerson, L., Sherrod, B. L., Sabean, J., and Horton, B. P., 2008, Great-earthquake paleogeodesy and tsunamis of the past 2000 years at Alsea Bay, central Oregon coast, USA: Quaternary Science Reviews, v. 27, no. 7-8, p. 747–768.

Nelson, H. C., Carlson, P. R., and Bacon, C. R., 1988, The Mount Mazama climactic eruption (~6900 yr B.P.) and resulting convulsive sedimentation on the Crater Lake caldera floor, continent, and ocean basin: Geological Society of America Special Paper 229, p. 37–57.

Ng, M. K.-F., LeBlond, P. H., and Murty, T. S., 1990, Simulation of tsunamis from great earthquakes on the Cascadia subduction zone: Science, v. 250, p. 1248–1251.

Obermeier, S. F., and Dickenson, S. E., 2000, Liquefaction evidence for the strength of ground motions resulting from Late Holocene Cascadia subduction earthquakes, with emphasis on the event of 1700 A.D.: Bulletin of the Seismological Society of America, v. 90, no. 4, p. 876–896.

Okada, Y., 1985, Surface deformation due to shear and tensile faults in a half-space: Bulletin of the Seismological Society of America, v. 75, no. 4, p. 1135–1154.

Olmstead, D., 2003, Development in Oregon's tsunami inundation zone: information guide for developers and local government: Oregon Department of Geology and Mineral Industries Open-File Report O-03-05, 17 p.

Park, J. O., Tsuru, T., Kodaira, S., Cummins, P. R., and Kaneda, Y., 2002, Splay fault branching along the Nankai subduction zone: Science, 297, 1,157–1,160.

Petersen, M. D., Cramer, C. H., and Frankel, A. D., 2002, Simulations of seismic hazard for the Pacific Northwest of the United States from earthquakes associated with the Cascadia Subduction Zone: Pure and Applied Geophysics, v. 159, no. 9, p. 2147–2168.

Peterson, C. D., K. Cruikshank, M., Jol, H. M., and Schlicting, R. B., 2008, Minimum runup heights of paleotsunami from evidence of sand ridge overtopping at Cannon Beach, Oregon, Central Cascadia Margin, U.S.A.: Journal of Sedimentary Research, v. 78, p. 390–409.

Plafker, G., 1965, Tectonic deformation associated with the 1964 Alaska earthquake: Science, v. 148, no. 3678, p. 1675–1687.

Plafker, G.,1972, Alaskan earthquake of 1964 and Chilean earthquake of 1960: implications for arc tectonics, Journal of Geophysical Research, v. 77, p. 901–925.

Power, W., Downes, G., and Stirling, M., 2007, Estimation of tsunami hazard in New Zealand due to South American earthquakes: Pure and Applied Geophysics, v. 164, p. 547–564.

Preuss, J., and Hebenstreit, G. T., 1998, Integrated tsunami-hazard assessment for a coastal community, Grays Harbor, Washington: U.S. Geological Survey Professional Paper 1560, v. 2, p. 517–536.

Priest, G. R., 1995a, Explanation of mapping methods and use of the tsunami hazard maps of the Oregon coast: Oregon Department of Geology and Mineral Industries Open-File Report O-95-67, 95 p.

Priest, G. R., 1995b, Tsunami hazard map of the Tillamook Head quadrangle, Clatsop County, Oregon: Oregon Department of Geology and Mineral Industries Open-File Report O-95-15, scale 1:24,000.

Priest, G. R., 1995c, Tsunami hazard map of the Arch Cape quadrangle, Clatsop and Tillamook counties, Oregon: Oregon Department of Geology and Mineral Industries Open-File Report O-95-16, scale 1:24,000.

Priest, G. R., and Allan, J. C., 2004, Evaluation of coastal erosion hazard zones along dune and bluff backed shorelines in Lincoln County, Oregon: Cascade Head to Seal Rock, Technical report to Lincoln County: Oregon Department of Geology and Mineral Industries Open-File Report O-04-09.

Priest, G. R., Myers, E., Baptista, A., Kamphaus R. A., and Peterson, C. D., 1997, Cascadia subduction zone tsunamis: hazard mapping at Yaquina Bay, Oregon: Oregon Department of Geology and Mineral Industries, Open-File Report O-97-34, 144 p.

Priest, G. R., Myers, E., Baptista, A. M., Kamphaus, R., Peterson, C. D., and Darienzo, M. E., 1998, Tsunami hazard map of the Seaside-Gearhart area, Clatsop County, Oregon: Oregon Department of Geology and Mineral Industries Interpretive Map Series map IMS-3, scale 1:12,000.

Priest, G. R., Myers, E., Baptista, A.M., Erdakos, G., and Kamphaus, R., 1999a, Tsunami hazard map of the Astoria area, Clatsop County, Oregon: Oregon Department of Geology and Mineral Industries Interpretive Map Series map IMS-11, scale 1:24,000.

Priest, G. R., Myers, E., Baptista, A. M., and Kamphaus, R., 1999b, Tsunami hazard map of the Warrenton area, Clatsop County, Oregon: Oregon Department of Geology and Mineral Industries Interpretive Map Series IMS-12, scale 1:24,000.

Priest, G. R., Myers, E., Baptista, A. M., Flück, P., Wang, K., and Peterson, C. D., 2000a, Source simulation for tsunamis: lessons learned from fault rupture modeling of the Cascadia subduction zone: Science of Tsunami Hazards, v. 18, 77–106.

Priest, G. R., Myers, E., Baptista, A. M., and Kamphaus, R., 2000b, Tsunami hazard map of the Gold Beach area, Curry County, Oregon: Oregon Department of Geology and Mineral Industries Interpretive Map Series IMS-13, scale 1:12,000.

Priest, G. R., Allan, J. C., Myers, E., Baptista, A. M., and Kamphaus, R., 2002, Tsunami hazard map of the Coos Bay area, Coos County, Oregon: Oregon Department of Geology and Mineral Industries Interpretive Map Series IMS-21.

Priest, G. R., Chawla, A., and Allan J. C., 2004, Tsunami hazard map of the Alsea Bay (Waldport) area, Lincoln County, Oregon: Oregon Department of Geology and Mineral Industries Interpretive Map Series IMS-23.

Priest, G. R., Chawla, A., and Allan, J. C., 2007, Tsunami hazard map of the Florence-Siuslaw River area, Lane county, Oregon, 42 p., 1 map plate, scale 1:20,000.

Rikitake, T., 1999, Probability of a great earthquake to recur in the Tokai district, Japan: reevaluation based on newly-developed paleoseismology, plate tectonics, tsunami study, micro-seismicity and geodetic measurements: Earth Planets Space, v. 51, p. 147–157.

Rivera, J., Karabanov, E. B., Williams, D. F., Buchinskyi, V., and Kuzmin, M., 2006, Lena River discharge events in sediments of Laptev Sea, Russian Arctic: Estuarine Coastal and Shelf Science, v. 66, p. 185–196.

Saffer, D. M., and Bekins, B. A., 1999, Fluid budgets at convergent plate margins: implications for the extent and duration of fault-zone dilation: Geology, v. 27, p. 1095–1098.

Satake, K., Wang, K., and Atwater, B. F., 2003, Fault slip and seismic moment of the 1700 Cascadia earthquake inferred from Japanese tsunami descriptions: Journal of Geophysical Research, v. 108, p. ESE 7-1–7-17.

Schmidt, D., Burgette, R., and Weldon, R., 2007, The distribution of interseismic locking on the central Cascadia subduction zone Inferred from coastal uplift rates in Oregon: American Geophysical Union, Fall Meeting 2007, abstract #T52A-04.

Schnellmann, M., Anselmetti, F. S., Giardini, D., and Ward, S. N., 2002, Prehistoric earthquake history revealed by lacustrine slump deposits: Geology, v. 30, no. 12, p. 1131-1134.

Seely, D. R., 1977, The significance of landward ver-

gence an oblique structural trends on trench inner slopes, *in* Talwani, M., and Pitman, W.C., eds., Island arcs, deep sea trenches, and back-arc basins: Washington, D.C., American Geophysical Union, Maurice Ewing Series, v. 1, pp. 187–198.

Senior Seismic Hazrd Analysis Committee, 1997, Recommendations for probabilistic seismic hazard analysis: guidance on uncertainty and use of experts: U.S. Nuclear Regulatory Commission, Main Report NUREG/CR-6372 UCRL-ID-122160 v. 1, 256 p.

Seno, T., 2002, Tsunami earthquake as transient phenomena, Geophysical Research Letters, v. 29, doi: 10.029/2002GL014868.

Seno, T., and Hirata, K., 2007, Did the 2004 Sumatra–Andaman earthquake involve a component of tsunami earthquakes?: Bulletin of the Seismological Society of America, v. 97, no. 1A, p. S296–S306.

Sibuet, J-C., Rangin, C., Le Pichon, X., Sing, S., Cattaneo, A., Graindorge, D., Klingelhoefer, F., Lin, J-Y., Malod, J., Maury, T., Schneider, J-L., Sultan, N., Umber, M., Yamaguchi, H., and the "Sumatra aftershocks" team, 2007, 26th December 2004 Great Sumatra-Andaman Earthquake: co-seismic and post-seismic motions in northern Sumatra: Earth and Planetary Science Letters, v. 263, p. 88-103.

Shiki, T., Kumon, F., Inouchi, Y., Kontani, Y., Sakamoto, T., Tateishi, M., Matsubara, H., and Fukuyama, K., 2000, Sedimentary features of the seismo-turbidites, Lake Biwa, Japan: Sedimentary Geology, v. 135, p. 37–50.

Shimazaki, K., and Nakata, T., 1980, Time-predictable recurrence model for large earthquakes: Geophysical Research Letters, v. 7, p. 279–282.

Song, T.-R. A., and Simons, M., 2003, Large trench-parallel gravity variations predict seismogenic behavior in subduction zones: Science, v. 301, p. 630–633.

St-Onge, G., Mulder, T., Piper, D. J. W., Hillaire-Marcel, C., and Stoner, J. S., 2004, Earthquake and flood-induced turbidites in the Saguenay Fjord (Québec): a Holocene paleoseismicity record: Quaternary Science Reviews, v. 23, p. 283–294.

Subarya, C., Chlieh, M., Prawirodirdjo, L., Avouac, J., Bock, Y., Sieh, K., Meltzner, A.J., Natawidjaja, D.H., and McCaffrey, R., 2006, Plate-boundary deformation associated with the great Sumatra–Andaman earthquake: Nature, v. 440, p. 46–51.

Tadepalli, S., and Synolakis, C. E., 1994, The run-up of N-waves on sloping beaches: Proceedings of the Royal Society of London, v. 445, no. 192,3 p. 99–112.

Thatcher, W., 1990, Order and diversity in the modes of circum-Pacific earthquake recurrence: Journal of Geophysical Research, v. 95, p. 2609–2623.

Titov, V. V., Mofjeld, H. O., González, F. I., and Neuman, J. C., 1999, Offshore forecasting of Hawaiian tsunamis generated in Alaskan-Aleutian SubductionZone: NOAA Technical Memorandum ERL PMEL-114, 22 p.

Titov, V. V., González, F. I., Bernard, E.N., Eble, M.C., Mofjeld, H. O., Newman, J. C., and Venturato, A. J., 2005, Real-time tsunami forecasting: challenges and solutions: Natural Hazards, v. 35, no. 1, p. 40–58.

Trehu, A. M., Braunmiller, J., and Nabelek, J. L., 2008, Probable low-angle thrust earthquakes on the Juan de Fuca–North America plate boundary: Geology, v. 36, p. 127–130.

Tsuji, Y., Matsutomi, H., Tanioka, Y., Nishimura, Y., Sakakiyama, T., Kamataki, T., Murakami, Y., Moore, A., and Gelfenbanm, G., 2005, Distribution of the tsunami heights of the 2004 Sumatera tsunami in Banda Aceh measured by the Tsunami Survey Team, http://www.eri.u-tokyo.ac.jp/namegaya/sumatera/surveylog/eindex.htm.

Tsunami Pilot Study Working Group (TPSW), 2006, Seaside, Oregon tsunami pilot study — modernization of FEMA flood hazard maps: Seattle, Wash., National Oceanic and Atmospheric Administration OAR Special Report, NOAA/OAR/PMEL, 92 p. + 7 app.

Walsh, T. J., Caruthers, C. G, Heinitz, A. C., Myers, E. P., III, Baptista, A. M., Erdakos, G. B., and Kamphaus, R. A., 2000, Tsunami hazard map of the southern Washington coast; modeled tsunami inundation from a Cascadia subduction zone earthquake: Washington Division of Geology and Earth Resources Geologic Map GM-49, scale 1:100,000.

Wang, K., 2007, Elastic and viscoelastic models of crustal deformation insubduction earthquake cycles, *in* Dixon, T., and Moore, J.C., eds., The seismogenic zone of subduction thrust faults: New York, Columbia University Press, p. 540–575.

Wang, K., and He, J., 1999, Mechanics of low-stress

forearcs: Nankai and Cascadia: Journal of Geophysical Research, v. 104, no. B7, p. 15,191–15,205.

Wang, K., and He, J., 2008, Effects of frictional behaviour and geometry of subduction fault on coseismic seafloor deformation: Bulletin of Seismological Society of America, v. 98, no. 2, p. 571–579.

Wang, K., and Hu, Y., 2006, Accretionary prisms in subduction earthquake cycles: the theory of dynamic Coulomb wedge: Journal of Geophysical Research, v. 111, B06410.

Wang, K., Wells, R., Mazzotti, S., Hyndman, R. D., and Sagiya, T. 2003, A revised dislocation model of interseismic deformation of the Cascadia subduction zone: Journal of Geophysical Research, v. 108, no. B1, p. 2009, doi:10.1029/2001JB001227.

Wells, R. E., Blakely, R. J., Sugiyama, Y., Scholl, D. W., and Dinterman, P. A., 2003, Basin-centered asperities in great subduction zone earthquakes: a link between slip, subsidence, and subduction erosion: Journal of Geophysical Research, v. 108, no. B10, p. 2507, doi:10.1029/2002JB002072.

Werner, K. S., Graven, E. P., Berkman, T. A., and Parker, M. J., 1991, Direction of maximum horizontal compression in western Oregon determined by borehole breakouts: Tectonics, v. 10, no. 5, p. 948–958.

Whitmore, P. M., 1993, Expected tsunami amplitudes and currents along the North American coast for Cascadia subduction zone earthquakes: Natural Hazards, v. 8, p. 59–73.

Witter, R. C., 2008, Prehistoric Cascadia tsunami inundation and runup at Cannon Beach, Oregon: Oregon Department of Geology and Mineral Industries Open-File Report O-08-12, 42 p.

Wynn, R. B., Weaver, P. P. E., Masson, D. G., and Stow, D. A. V., 2002, Turbidite depositional architecture across three interconnected deep-water basins on the north-west African margin: Sedimentology, v. 49, no. 4, p. 669–695.

Yeats, R. S., Kulm, L. D., Goldfinger, C., and McNeill, L. C., 1998, Stonewall anticline: an active fold on the Oregon continental shelf: Bulletin of the Geological Society of America, v. 110, p. 572–587.

Zdanowicz, C. M., Zielinski, G. A., and Germani, M. S., 1999, Mount Mazama eruption: calendrical age verified and atmospheric impact assessed: Geology, v. 27, p. 621–624.

Zhang, Y., and Baptista, A.M., 2008, An efficient and robust tsunami model on unstructured grids. Part I: inundation benchmarks: Pure and Applied Geophysics, v. 165, no. 11-12, p. 2229–2248.

APPENDIX A:
FAULT DISLOCATION MODELING OF CASCADIA EARTHQUAKE SCENARIOS

by Kelin Wang, Pacific Geoscience Centre, Sidney, British Columbia

FAULT SOURCE MODELING APPROACH

Because of a lack of direct observations of coseismic seafloor deformation associated with a great Cascadia megathrust earthquake, deformation scenarios are "educated guesses" based on our current knowledge of the seismogenic behavior of the Cascadia subduction zone. Three types of information contribute to the construction of the rupture and deformation scenarios considered in this investigation.

Geological structural information. This includes the geometry of the megathrust and splay faults constrained by seismic surveys and locations of other structural features of interest (see main text). Geometry of the megathrust is taken from McCrory and others (2004). Splay fault geometry is constrained by seismic surveys and assumed to coincide with a major fault zone bounding the Pleistocene-Tertiary contact in the accretionary wedge (Figures 3, 7, and 13 of the main text).

Paleoseismic data, primarily coseismic coastal subsidence associated with the AD 1700 Cascadia earthquake as compiled by Leonard and others (2004). Information deduced from Japanese historical records of the AD 1700 Cascadia earthquake and tsunami (Satake and others, 2003) helps constrain coseismic slip for a typical magnitude ~9 event.

Knowledge and hypotheses based on the studies of megathrust earthquakes in other subduction zones. Examples include the possible involvement of coseismic splay faulting that enhances tsunami generation (Plafker, 1972; Park and others, 2002), a reported correlation between the locations of the seismogenic zone and forearc basins (Wells and others, 2003), coseismic slip concentrated in the landward part of the forearc high (Goldfinger and McNeill, 2006), and aseismic behavior of the most seaward segment of the megathrust (e.g., Wang and Hu, 2006; Wang and He, 2008). Published coseismic slip patterns of the 2004 and 2005 Sumatra earthquakes (e.g., Chlieh and others, 2007; Hsu and others, 2006; Subarya and others, 2006) provide references that serve to validate some of the assumed Cascadia rupture models.

These source parameters informed construction of a logic tree in order to explore variation in coseismic deformation and consequent Cascadia tsunami impact to Cannon Beach. All simulations of surface deformation from fault ruptures employ the point source solution from Okada's (1985) model and emulate coseismic deformation between 43.9° N latitude on the central Oregon coast to near the Straits of Juan de Fuca at ~47.9° N latitude.

FAULT SLIP DIRECTION AND MAGNITUDE

Aside from magnitude of coseismic slip, the most important control on tsunamigenic seafloor deformation is spatial distribution of slip. Where the peak slip is located and how the slip decreases from its peak location, especially how it tapers up dip towards the seafloor, strongly control the magnitude and shape of static elastic seafloor deformation. Slip distributions that cause large volumes of seafloor displacement at greater water depth generally have the potential to generate larger tsunami, baring other bathymetrical complications. Compared to the importance of and large uncertainties in the slip distribution, other factors such as material heterogeneity, inelastic behavior, dynamic deformation, and horizontal seafloor motion are of secondary concern. Therefore, the model of a uniform elastic halfspace with a Poisson's ratio of 0.25 is employed in this work. Attention is paid mainly to the most critical issue of how to assign coseismic slip along the fault.

Slip direction of the coseismic rupture is assumed to be exactly opposite of plate convergence. The plate convergence direction and rate are calculated from Euler vectors as explained by Wang and others (2003).

Maximum coseismic slip in all models is derived from four representative interseismic intervals derived from offshore Holocene turbidite data (Table 1, main text).

FAULT GEOMETRY AND FAULT MESHES — CASCADIA SCENARIOS

For the Cannon Beach project, two fault geometry models are used for Cascadia subduction zone scenarios: the model of megathrust without a splay fault (buried rupture) and the model of a splay fault merging into the megathrust. In each geometrical model there is a single fault on which slip is assigned.

The no-splay-fault, buried rupture model employs a megathrust geometry modified from that of McCrory and others (2004). In the McCrory and others (2004) model, because depth is measured from the sea level, the depth of the megathrust is over 5 km at the deformation front, where the actual depth from the seafloor is 2 to 3 km. To let the upper surface of the elastic half-space approximately represent the seafloor, the most updip part of the megathrust is "raised" to 2 to 3 km depth by resetting the 5-km slab surface contour of McCrory and others (2004) (located seaward of the deformation front) to 2 km. This "raised" structure contour line and other contour lines of McCrory and others (2004) at 5-km intervals are used to construct the megathrust geometry using GMT program "surface" (http://gmt.soest.hawaii.edu/). In no-splay-fault models, fault slip always tapers to zero at the deformation front, so all ruptures are "blind" or buried megathrust events. In these models, the exact depth of the shallowest part of the mega-thrust is not important, because most of the slip occurs farther down dip. Figure A1 illustrates the trace of the splay fault and representative structure contours on the subduction zone.

For splay-fault models, the fault geometry at >20-km depths is identical to that of the no-splay-fault (buried rupture) model. The splay fault trace shown in Figure A1 is used as the upper edge of the fault. The geometry of the fault between this upper edge and the 20-km contour is constructed also using GMT program "surface" but with added auxiliary contour lines to ensure that the dip of the shallowest part of the splay fault is about 30° and that it merges into the megathrust smoothly. Geologic data supporting the splay fault location and dip are presented in the Splay Fault section of the main text.

For each fault geometry, a fault mesh is set up which exactly follows the observed three-dimensional shape and is sufficiently large to include all areas of non-zero slip to be modeled. The name of the no-splay-fault mesh is f3, and that of the splay-fault mesh is f4. The mesh (f4) for the splay-fault is dense near its upper edge, with element dimension of about 650 m in the strike direction and about half of this size in the dip direction. Because of the Cannon Beach focus in this project, both fault meshes are limited between 43.9° and 47.9° N latitude.

FAULT PATCHES AND SLIP DISTRIBUTION — CASCADIA SCENARIOS

For each fault mesh, five different slip patches are used, with three of them being regional "asperities" with slip distributed according to simple slip distributions everywhere along the subduction zone (named p2a, p2b, and p2c) and two involving local "asperities" (named p3 and p4) that have limited extent along the subduction zone. Boundaries of p2a, p3, and p4 are shown in Figure A1. The symmetric fb76 slip function (q = 0.5) of Freund and Barnett (1976) modified for distribution of Equation 1 of Wang and He (2008) is considered representative and is used for all five patches. The same slip distribution but with a seaward skew (q = 0.3) is also used

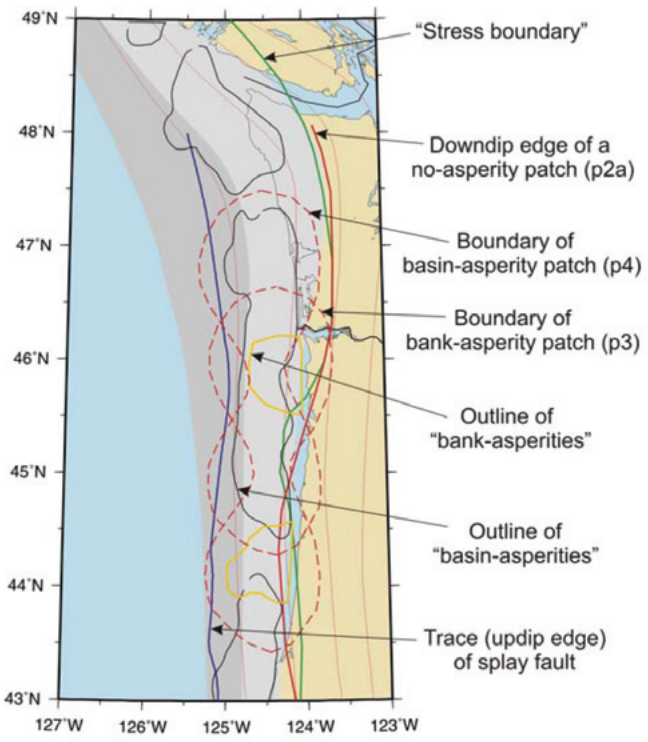

Figure A1. Structural boundaries relevant to this study. The areas of dark and light shading are the full-rupture and linear transition zones used by Satake and others (2003) based on the model of Wang and others (2003). Thin red lines are slab contours at 10-km intervals.

with p2a. This gives a total of six scenarios for each fault mesh. For the regional asperity models, maximum slip at each location is obtained by the local plate convergence rate times the scenario recurrence interval being simulated. For the local asperity models, the maximum slip is quadratically scaled with the local width of the fault patch, so that the slip distribution for each asperity has a three-dimensional bell shape. In plan view, the splay-fault scenarios are simply no-splay-fault (buried rupture) scenarios truncated by the splay-fault trace, although the fault mesh for the splay-fault models is much denser and uplift is amplified by the higher dip of the splay fault. Coseismic uplift/subsidence calculated along an east-west profile crossing Cannon Beach (at latitude 35.9° N) for all eight regional asperity scenarios is shown in Figure A2 for complete release of 500 years of slip deficit on the subduction zone (coupling ratio = 1.0). The splay-fault models (solid lines) predict larger seafloor uplift. Results along the same profile for all four local asperity models are shown in Figure A3. Again, the splay fault models give larger seafloor uplift. For the local basin-asperity fault patch (p4), no asperity is located offshore of Cannon Beach, and therefore the vertical deformation is very small along the Cannon Beach profile.

The updip edge of fault patch p2a is the deformation front (seaward boundary of the darkly shaded area in Figure A1). The downdip edge (shown as a red line in Figure A1) is a best-fit to the "stress boundary" where plate coupling decreases (green line in Figure A1) while still producing deformation patterns with a reasonable fit to paleosubsidence data of Leonard and others (2004) for the AD 1700 Cascadia earthquake (red line in Figure A4). The "stress boundary" marks a transition of structural style (see main text). Seaward of it, the fold and thrust structure of the accretionary prism indicates predominantly east-west compression (main text). Landward of it, the structure indicates much less compression or even east-west tension. The red line boundary in Figure A1 was derived by using the symmetric fb76 slip distribution (q = 0.5) in a trial and error approach with slip consistent with 500 years of plate convergence to obtain the best compromise between the "stress boundary" and the paleosubsidence data.

The symmetric fb76 slip distribution (modified by Wang and He [2008]) on the p2a patch is shown in Figure A5, together with the predicted vertical surface deformation. The splay-fault version of the same distribution and its surface deformation are shown in Figure A6 for comparison. Freund and Barnett (1976) preferred a q value (skewness) of 0.3 on the basis of limited observations of coseismic vertical deformation caused by the M_w 9.2 Alaska earthquake of 1964. An fb76 slip with q = 0.3 is thus used with the p2a patch to test the sensitivity of tsunami models to the skewness of the slip distribution. Coastal subsidence predicted by this seaward skewed slip distribution (green curve in Figure A4) is systematically less than that predicted by the symmetric slip on the same fault patch.

Fault patches p2b and p2c differ from p2a in that the downdip boundary is located 20 km seaward and landward, respectively. They are called "narrow" and "wide" in Figure A4. Only the modified symmetric fb96 slip distribution is used for these two fault patches. Both models fit the AD 1700 coastal subsidence data much more poorly than does the p2a model (Figure A4).

Fault patch p3 is based on the assumption that offshore banks may be the location of rupture asperities (Figure A1). Such asperities were inferred at islands and submarine highs in the December 2004 Sumatra earthquake (Goldfinger and McNeill, 2006).

Fault patch p4 is based on the assumption by Wells and others (2003) that offshore basins may be the location of rupture asperities. Patch p4 is modified from one of the "basin asperities" that Wells and others (2003) inferred from gravity anomalies by letting it be divided into two smaller asperities by the bank directly offshore of Cannon Beach (Figures A1 and A4). Both scenarios are further detailed in the main text. For both asperity models, a symmetric, modified fb76 slip distribution is applied, and the maximum slip is quadratically scaled with downdip patch width. The slip distribution and surface deformation for p3 are shown in Figure A7. Figure A8 depicts the splay-fault version. The p4 deformation is not illustrated but is simply the reverse of the p3 deformation.

All of the illustrations of coseismic deformation assume that 500 years of Cascadia plate convergence is released as slip. The vertical components of coseismic deformation from each scenario were transmitted to the tsunami modeling team as x-y-z data; they then scaled the components up or down linearly to simulate longer or shorter interseismic intervals.

See References section of the main text for publications cited in this appendix.

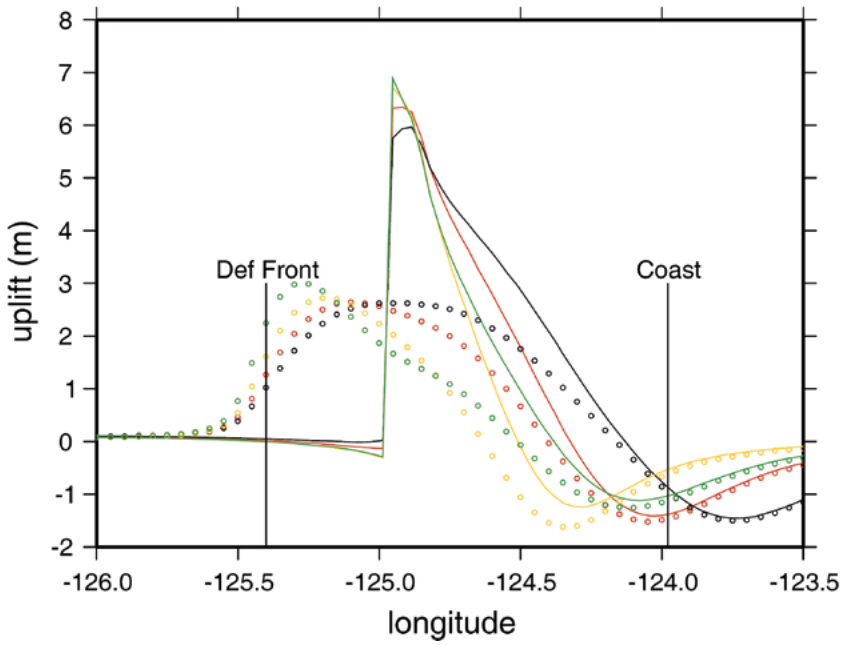

Figure A2. Model results of regional asperity models along an east-west profile at the Cannon Beach, Oregon, latitude. No-splay-fault (buried rupture) profiles are shown using circles. Splay-fault results are shown using solid lines. Deformation is for complete release of 500 years of slip deficit on the subduction zone (coupling ratio = 1.0).

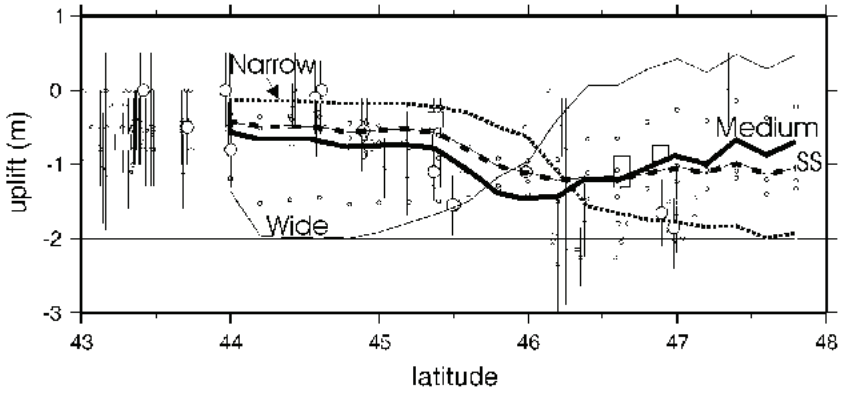

Figure A3. Coastal subsidence predicted by buried rupture, regional slip patch models and comparison with 1700 coseismic subsidence data using 500 years of slip release. 500 years is the approximate mean recurrence of Cascadia earthquakes. Square and large circles indicate best quality and better quality data as explained in Leonard and others (2004). Models use the symmetric fb76 slip modified for Equation 1 of Wang and He (2008) but varying rupture width by ±20 km from the best fit width to geologic data; bold line = preferred medium-width rupture patch), dotted line = 20 km narrower, and thin line = 20 km wider. To test for sensitivity of tsunami simulations to seaward skewed (SS) slip ($q = 0.3$) one model was constructed using a medium patch width (dashed line).

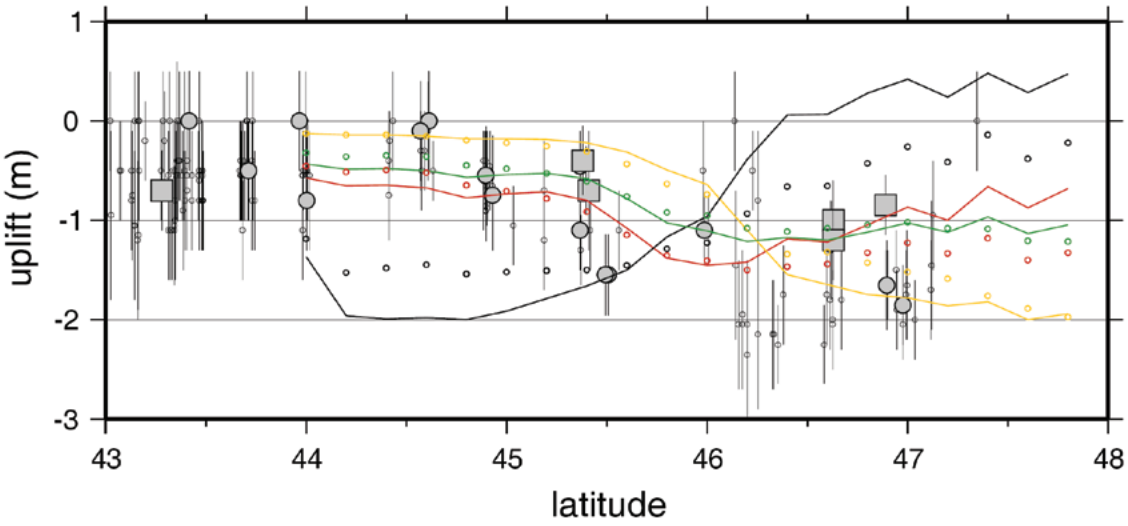

Figure A4. Coastal subsidence predicted by no-splay-fault, regional asperity models and comparison with AD 1700 coseismic subsidence data using 500 years of slip release. 500 years is the approximate mean recurrence of Cascadia earthquakes. Square and large circles indicate best quality and better quality data as explained by Leonard and others (2004). Models use the symmetric fb76 slip modified for Equation 1 of Wang and He (2008) but varying rupture width by ±20 km from the best fit width to geologic data; red line indicates p2a (medium patch width), yellow line indicates p2b (narrow), and black line indicates p2c (wide). To test for sensitivity of tsunami simulations to seaward skewed slip (q = 0.3), one model was constructed using a medium patch width (p2a, green line).

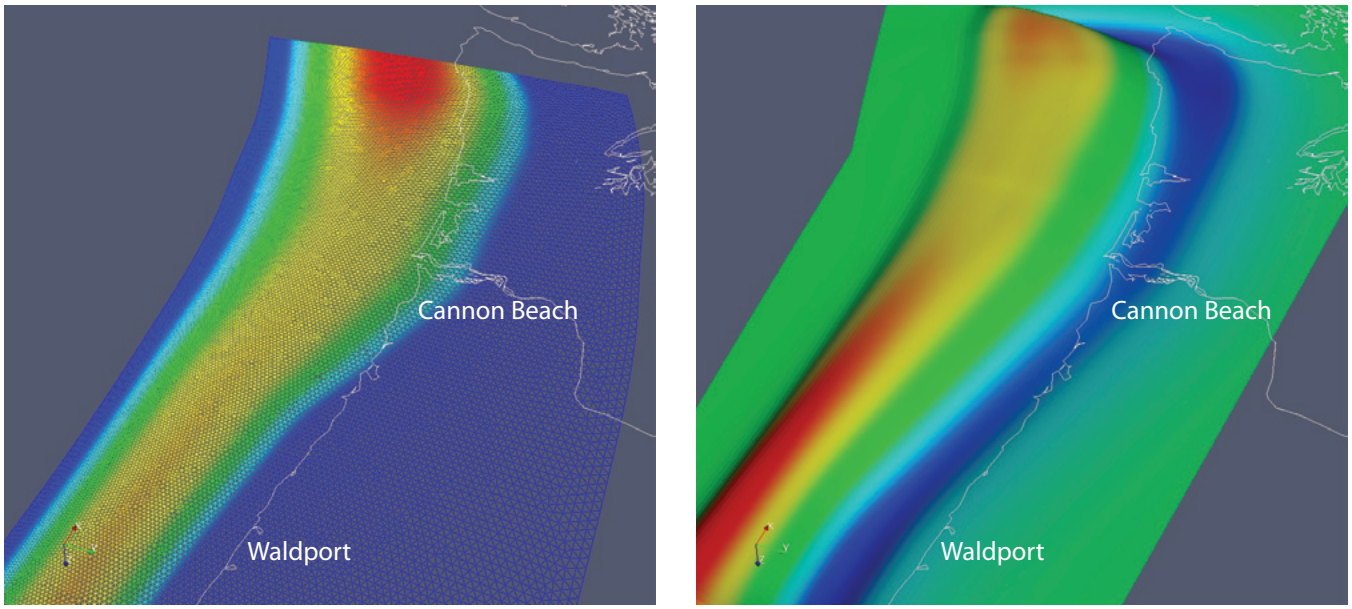

Figure A5. Fault slip distribution (left) and resultant surface vertical deformation (right) for the no-splay-fault model of medium p2a patch with modified symmetric fb76 slip distribution. Red is ~17-18 m slip (left) and ~3 m uplift (right).

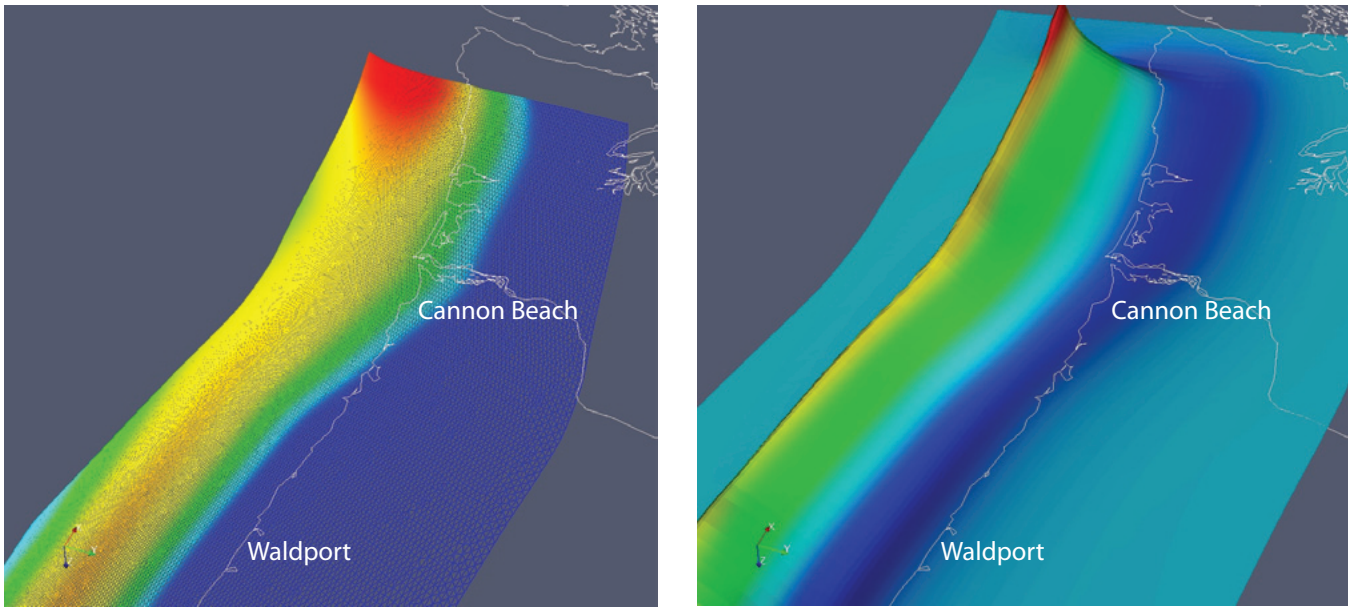

Figure A6. Fault slip distribution (left) and resultant surface vertical deformation (right) for the splay-fault model of medium p2a patch with symmetric fb76 slip distribution using 500 years of plate convergence to simulate coseismic slip. Red is ~17-18 m slip (left) and ~6 m uplift (right).

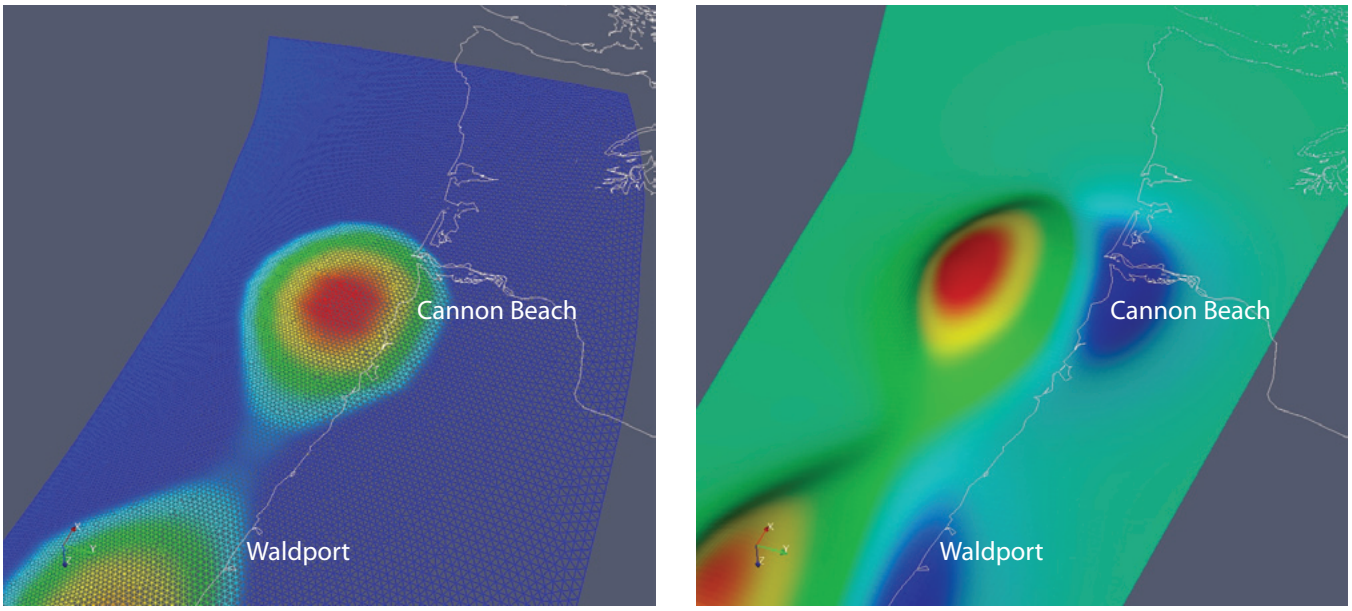

Figure A7. Fault slip distribution (left) and resultant surface vertical deformation (right) for the no-splay-fault "bank asperity" model (p3 patch). Red is ~17-18 m slip (left) and ~3 m uplift (right).

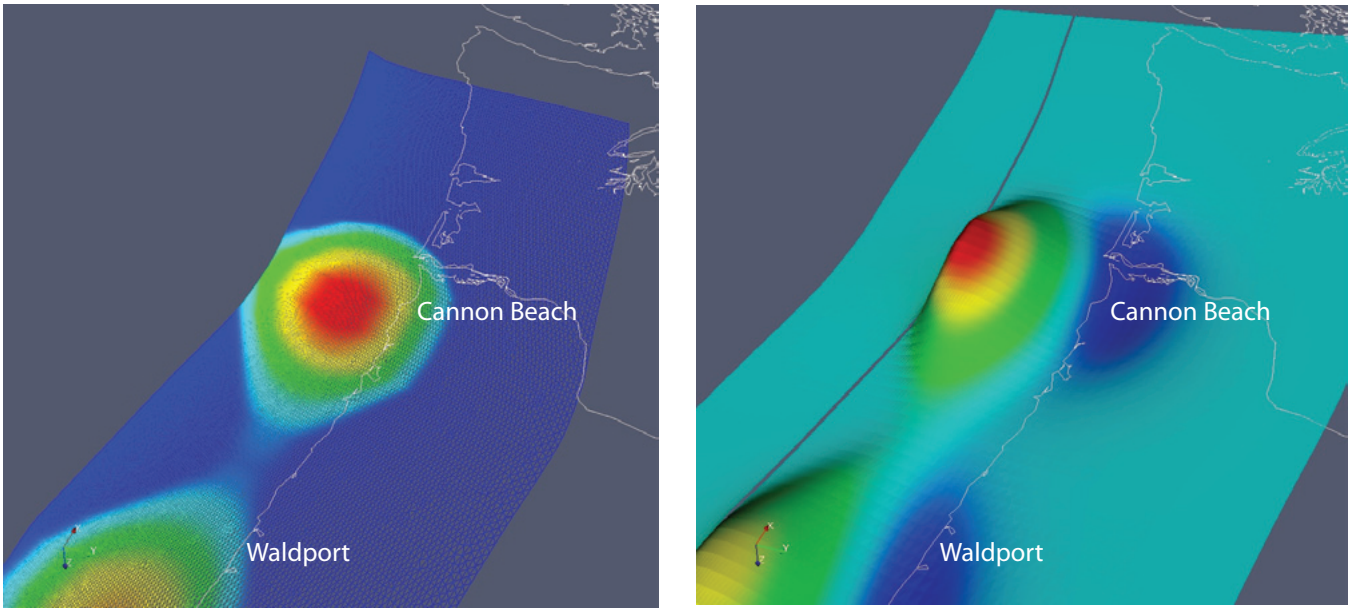

Figure A8. Fault slip distribution (left) and resultant surface vertical deformation (right) for the splay-fault "bank asperity" model (p3 patch). The "gap" in the surface observation grid is the trace of the splay fault. Red is ~17-18 m slip (left) and ~4.5 m uplift (right). The "basin asperity" (p4 patch) model is simply the inverse of this pattern.